Tensor Networks:
From Holography to Quantum Field Theory

Dissertation
zur Erlangung des Grades eines
Doktors der Naturwissenschaften

am Fachbereich Physik
der Freien Universität Berlin

vorgelegt von

JOHANNES KNAUTE

Berlin 2021

Max Planck Institut für Gravitationsphysik (Albert Einstein Institut)

Erstgutachter:	Dr. Michal P. Heller
Zweitgutachter:	Prof. Dr. Jens Eisert

Tag der Disputation: 10.01.2022

Selbstständigkeitserklärung

Name: Knaute
Vorname: Johannes

Ich erkläre gegenüber der Freien Universität Berlin, dass ich die vorliegende Dissertation selbstständig und ohne Benutzung anderer als der angegebenen Quellen und Hilfsmittel angefertigt habe. Die vorliegende Arbeit ist frei von Plagiaten. Alle Ausführungen, die wörtlich oder inhaltlich aus anderen Schriften entnommen sind, habe ich als solche kenntlich gemacht. Diese Dissertation wurde in gleicher oder ähnlicher Form noch in keinem früheren Promotionsverfahren eingereicht. Mit einer Prüfung meiner Arbeit durch ein Plagiatsprüfungsprogramm erkläre ich mich einverstanden.

Datum: 15.09.2021 Unterschrift:

Abstract

In this thesis we study aspects at the interplay of holography, quantum field theory and quantum simulation with tensor network and related techniques. The discussion is divided in three parts. In the first introductory part, we describe the necessary background of the gauge/gravity duality as well as tensor network methods and algorithms for our work.
The second part focuses on simulations of quantum spin chain models to extract properties of (1+1)-dimensional quantum field theories at zero and finite temperature. We review relevant aspects of quantum chromodynamics and heavy-ion collisions, which primarily motivate our work. Subsequently we present a new method that combines matrix product operator simulations with a signal analysis method, allowing us to make ab initio predictions about the thermal response in nonintegrable interacting quantum field theories. We then extend this line of research by employing scaling operators originating from an analytic wavelet solution of the multiscale entanglement renormalization ansatz. Based on this alternative discretization scheme, we calculate dynamical correlation functions in a coarsegrained system and compare them to the ones for the bare Ising model. Partially motivated by these considerations, we subsequently discuss the effect of meson melting, which describes the thermally induced breaking of nonperturbative bound states in a medium. Phenomenological approaches for its understanding from the quantum chromodynamics side as well as holographic models are reviewed. We introduce a new paradigm for the description of meson melting by analyzing entanglement entropies in a static and dynamical setting for the nonintegrable ferromagnetic phase of the Ising quantum field theory. We explain observed features at high enough temperatures through the fact that meson states in the quantum many-body system are melted and argue that the considered entanglement measures can serve as a witness of that process. In the last project of this part of the thesis, we explore the capabilities of analog quantum simulations with trapped ions to detect relativistic meson spectra, and present a method for its experimental realization on current devices via absorption spectroscopy.
The third part of this thesis deals with *complexity* as a quantum information quantity, which quantifies the difficulty of realizing a quantum circuit. We review its computational definition and recently proposed holographic interpretations of it. We then give an overview of two approaches, circuit complexity and path integral optimization, to understand complexity for quantum field theories. We unify these two concepts by showing that path integral complexity arises as an approximation to a particular choice in the circuit approach to complexity. We discuss this result in the context of quantum gravity through discrete tensor network interpretations of the gauge/gravity duality based on the multiscale entanglement renormalization ansatz.

Zusammenfassung

In dieser Dissertation studieren wir Themen an der Schnittstelle von Holographie, Quantenfeldtheorien und Quantensimulationen mittels Tensornetzwerken und verwandten Methoden. Die Diskussion ist in drei Teile aufgeteilt. Im ersten Einleitungsteil beschreiben wir den notwendigen Hintergrund zur sogenannten Eich/Gravitations Dualität sowie Tensornetzwerk-Methoden und Algorithmen, welche relevant für unsere Arbeit sind.
Im zweiten Teil fokussieren wir uns auf Simulationen von Quantenspinketten-Modellen, um Eigenschaften von (1+1)-dimensionalen Quantenfeldtheorien bei verschwindender und endlicher Temperatur zu extrahieren. Dazu geben wir zunächst einen Überblick über relevante Aspekte der Quantenchromodynamik sowie Schwerionenkollisionen, welche unsere Arbeit hauptsächlich motivieren. Anschließend stellen wir eine neue Methode vor, welche Simulationen mittels Matrixprodukt-Operatoren mit einer Signalanalyse-Methode verbindet. Dies erlaubt uns ab-initio Vorhersagen über die thermische Reaktion in nicht-integrablen wechselwirkenden Quantenfeldtheorien zu treffen. Anschließend erweitern wir diese Forschungsrichtung durch den Einsatz von Skalierungsoperatoren, welche aus einer analytischen Wellen-Lösung des Multiskalen-Verschränkungs-Renormierungsansatzes stammen. Auf der Grundlage dieses alternativen Diskretisierungsschemas berechnen wir dynamische Korrelationsfunktionen in einem großskaligen System und vergleichen diese mit denen für das ursprüngliche Ising Modell. In einem verwandten Projekt diskutieren wir im Anschluss den Effekt des Mesonenschmelzens, welcher das thermisch induzierte Auflösen von nichtperturbativ gebundenen Zuständen in einem Medium beschreibt. Wir geben dafür zunächst einen Überblick über phänomenologische Ansätze zum bisherigen Verständnis dieses Prozesses von Seite der Quantenchromodynamik als auch durch holographische Modelle. Wir führen ein neues Paradigma zur Beschreibung dieses Prozesses ein, indem wir Verschränkungsentropien sowohl in einem statischen als auch dynamischen Setting für die nicht-integrable ferromagnetische Phase der Ising Quantenfeldtheorie analysieren. Wir erklären beobachtete Eigenschaften bei hohen Temperaturen durch die Tatsache, dass Mesonen-Zustände im Quanten-Vielkörpersystem geschmolzen sind und argumentieren, dass die betrachteten Verschränkungsmaße zur Charakterisierung dieses Prozesses dienen können. Im letzten Projekt dieses Teils der Dissertation erforschen wir die Möglichkeiten analoger Quantensimulationen mittels gefangenen Ionen relativistische Mesonspektren nachzuweisen und präsentieren eine Methode zur experimentellen Realisierung mittels Absorptionsspektroskopie für bereits existierender Hardware.
Im dritten Teil dieser Dissertation behandeln wir *Komplexität* als eine quanteninformationstheoretische Größe, welche die Schwierigkeit der Realisierung eines Quanten-Schaltkreises quantifiziert. Wir geben einen Überblick über die rechnerische Definition und vorgeschlagene holographische Interpretationen davon. Anschließend geben wir einen Überblick über zwei Ansätze, Schaltkreiskomplexität und Pfadintegraloptimierung, welche vorgeschlagen wurden, um die Komplexität von Quantenfeldtheorien zu definieren. Wir vereinheitlichen diese beiden Konzepte, indem wir zeigen, dass die Pfadintegralkomplexität eine Approximation für eine bestimmte Wahl im Schaltkreisansatz zur Komplexität darstellt. Wir ordnen unser Ergebnis im Zusammenhang mit Quantengravitation durch diskrete Tensornetzwerk-Interpretationen der Eich/Gravitations Dualität basierend auf dem Multiskalen-Verschränkungs-Renormierungsansatzes ein.

Publications

Chapter 4 and 7 in this thesis are respectively based on the results and discussions from the following papers. [1]

[1] M. C. Bañuls, M. P. Heller, K. Jansen, J. Knaute and V. Svensson: *From spin chains to real-time thermal field theory using tensor networks*, Physical Review Research 2, 033301 (2020), doi.org/10.1103/PhysRevResearch.2.033301; arXiv:1912.08836 [hep-th]
My main contributions to the project were the overall development and progression of theoretical ideas to tackle the formulated problem and address its physical implications. It required my code development and numerical calculations as well as interpretation of the results by taking my co-authors input into account. I also contributed to the writing of the paper and managed the publication process.

[2] J. Knaute and P. Hauke: *Relativistic meson spectra on ion-trap quantum simulators*, arXiv:2107.09071 [cond-mat.str-el] (2021)
The project emerged from my initiative based on discussions with my collaborator. I implemented code to perform numerical calculations and interpreted the results with my coauthor. I mainly wrote the paper and now manage the publication process.

The results and discussions presented in chapter 5 and 6 are respectively based on the following projects.

[3] M. P. Heller, J. Knaute, S. Singh and V. Svensson: *in preparation*
The presented real-time simulations are my contributions in a larger project on extracting QFT information from MERA tensors. The content emerged from discussions with my coauthors on interpretations of the results and required my code development and numerical calculations.

[4] M. C. Bañuls, M. P. Heller, K. Jansen, J. Knaute and V. Svensson: *in preparation*
The simulations about non-integrable QFT regimes and quench studies presented in this chapter are my contributions in a project on meson melting. The content emerged from discussions with my coauthors on interpretations of the results and required my code development and numerical calculations.

Part III of this thesis is based on the results and discussions from the following paper.

[5] H. Camargo, M. P. Heller, R. Jefferson and J. Knaute: *Path Integral Optimization as Circuit Complexity*, Physical Review Letters 123, 011601 (2019), doi.org/10.1103/PhysRevLett.123.011601; arXiv:1904.02713 [hep-th]
My main contribution in this project was the central computational trick that lead to the result of the paper as well as its interpretation following the input of the co-authors. I also contributed to the writing of the paper and managed the publication process.

Another paper, which I coauthored during my PhD studies but whose content is not covered in this thesis, is

[6] S. Banerjee, S. Choudhury, S. Chowdhury, J. Knaute, S. Panda, K. Shirish: *Thermalization Phenomena in Quenched Quantum Brownian Motion in De Sitter Space*, arXiv:2104.10692 [hep-th] (2021)

[1] All our publications and papers are available with open access.

Contents

Part I

Introduction

1 Motivation and overview

In modern theoretical physics, one major quest is to understand fundamental matter under extreme conditions. Such circumstances existed for example at the beginning of our universe, and today in the interior of black holes (BHs) – one of the most fascinating objects in our cosmos, which were predicted by Einstein a century ago, but only recently have been directly experimentally observed via gravitational wave measurements [7] or the event horizon telescope [8]. The understanding of such systems necessarily involves the description of many interacting quantum bodies, which appear not only in particle but also condensed matter physics. In this research field, it is one of the most interesting developments of the past decade, that ideas from quantum field theory (QFT), quantum information science and quantum gravity are becoming increasingly important as a joint effort. This research trend is most visible in the field of tensor network (TN) studies.

TNs – a formalism originating from quantum information concepts – are representations of quantum states, which can be visualized graphically through a network of connected tensors. They capture the relevant entanglement properties of a quantum system and are the basis for very efficient algorithms to simulate the dynamics of many-body systems. This is achieved by exploiting properties that circumvent the normal exponential increase of (classical) computational resources with the number of microscopic constituents. While we provide the necessary background of our work in the following chapters, general introductions and reviews into this interdisciplinary field can be found in [9–17].

TNs are useful not only in their original context of condensed matter physics, but also to study QFTs. The latter are the building blocks of the standard model in particle physics, which describes the fundamental interactions in nature, and have been tested with an amazing precision up to very high energies. In more detail, the electroweak theory describes microscopic particle interactions, whereas Quantum Chromodynamics (QCD) is the theory of strong interactions, whose properties and understanding is an important motivation for the topics in this thesis. QCD has quarks and gluons as fundamental degrees of freedom, which carry both an electric and color charge, and appear in nature only as color-neutral hadronic matter states due to color confinement. One relevant type of hadrons are are mesons, which consist of a quark-antiquark pair that form a non-perturbative bound state. At high energies, the QCD coupling strength between particles is decreasing, causing a transition from the confined hadronic phase

to the deconfined quark-gluon plasma (QGP). The QGP at high temperatures or densities is one such extreme matter state as mentioned in the beginning. It existed in the early universe after the big bang when nucleons were formed during the cooling process, and nowadays is expected to be in the interior of neutron stars. Experimentally, the QGP can be created in heavy-ion collisions (HICs) or, more generally, nuclear collisions, at particle accelerators like the Relativistic Heavy Ion Collider in Brookhaven or the Large Hadron Collider at the European Organization for Nuclear Research. At these facilities, it was measured that the QGP is the most perfect [18–21] and also the fastest-rotating fluid [22] ever observed in the universe. The theoretical understanding of HICs as dynamical QFT processes is of upmost importance in modern physics. In this context, TNs allow a study of QFTs in Hamiltonian formulation, and, in contrast to state-of-the-art Monte Carlo based methods, provide the advantage of being free of the famous sign-problem, which prohibits calculations a finite density or in real-time formalism. TN methods therefore have the potential to address physical situations relevant to the description of HICs.

On the other side, holography, also known as gauge/gravity duality, describes a relation between QFTs and gravitational theories. In particular, based on the holographic principle developed by 't Hooft and Susskind [23,24] it was conjectured that a QFT in D dimensions could be related to a gravitational theory in $D+1$ dimensions. It found a concrete realization in the anti-de Sitter/conformal field theory (AdS/CFT) correspondence [25–27], which links a specific superstring theory to a supersymmetric gauge theory. This *duality* exhibited a significant influence on theoretical physics as a whole, becoming one of the most important tools to study strongly coupled systems, and a new quantitative perspective to understand quantum gravity (see e.g. [28–30] for a broad overview of the theoretical background and applications). Holographic methods have been successfully used to describe HICs and lots of other phenomena in particle and condensed matter physics. [2] The main reason for its applicability is the fact, that a strongly coupled QFT is translated into a weakly coupled classical gravitational theory, which is computationally more tractable.

TNs provide several conjectured frameworks for discrete interpretations of this duality, giving insight into the quantum nature of gravity and the emergence of spacetime. As reviewed extensively in [34], this development is mostly driven by the exploration of quantum information measures, which have a dual holographic interpretation. Most prominently, the breakthrough result of Ryu and Takayanagi [35,36] identifies the entanglement entropy in a CFT with the minimal surface in the bulk of AdS spacetime for a chosen entangling area. Another infor-

[2] For example, the complicate dynamics of systems out-of-equilibrium and questions related to the time dependence of their hydrodynamization and isotropization were analyzed in models of HICs. Furthermore, the celebrated holographic result for the shear viscosity to entropy density ratio [31], $\eta/s = 1/4\pi$, is in good agreement with experimental results [18–21]. In a solid-state context, holographic models were developed to describe e.g. superconductors. Comprehensive overviews are given in [32,33] (for QCD related topics) and [28,29] (for all fields).

mation quantity, which has received an enormous amount of attention in the last years, is *complexity* [37]. The general idea behind complexity is to quantify how difficult it is to reach a certain quantum state starting from another one. From a holographic perspective, it has been conjectured to be dual to gravitational volumes and actions [38,39]. Complementary to entanglement entropy, its precise definition on the QFT side of the duality is, however, less understood.

The main theme of this thesis is to use TN and related techniques to study important aspects at the interplay of QFT and holography. Some inspiring and motivating questions in this line of research are:

- *How can we use TN algorithms in combination with (other) numerical tools to model and understand equilibration processes similar to collisions of atomic nuclei at particle accelerators?*

- *What role does complexity as a quantum information measure play in the connection of TNs, QFT and holography?*

Regarding the first question, one major motivation is the understanding of microscopic mechanisms which govern the equilibration of the QGP phase from an initial far-from-equilibrium state in HICs. TN approaches open the novel possibility to access this phenomenon in the most difficult regime of intermediate coupling, where strongly-coupled and weakly-coupled methods are naturally not applicable and do not provide a description. As a limitation, we constrain our studies in this thesis to (relativistic) QFTs which arise as infra-red (IR) descriptions of (1+1)-dimensional quantum spin systems near a critical point. The available algorithms are most advanced in this scenario and allow us to study phenomena which are important across dimensions. In particular, as part of this thesis, a new method is presented that combines TN simulations and signal analysis methods to compute and analyze retarded thermal two-point functions. This allows us to extract their analytic structure and to make fully ab initio predictions for specific non-integrable interacting QFTs at finite temperature. As it will be outlined in this thesis, such analyses are directly motivated by similar holographic studies, which allow to compute transport coefficients or to identify time scales at which the hydrodynamic regime in models of the QGP and HICs applies. From a broader perspective, these analyses can be embedded into a research trend of studying soluble models of phenomena relevant to our actual physical world.
Beyond QFTs emerging as effective descriptions of discrete spin models, TNs allow also a direct implementation of (lattice) gauge theories (LGTs). Such explorations are already very advanced in (1+1) and (2+1) dimensions, as comprehensively reviewed in [40]. Most recently, there has been even a first study of Quantum Electrodynamics in (3+1) dimensions [41]. Moreover, specific TN algorithms allow to describe physical systems directly either in the

thermodynamic or continuum limit. Eventually, one ultimate goal of this entire research direction is the study of full QCD in (3+1) dimensions, which is one of the grand challenges of modern theoretical physics. An important step in this direction are nonperturbative studies which access regimes that are difficult to treat using existing approaches.

The simulation of quantum systems with TN methods that are not directly defined in the continuum implicitly assume a discrete lattice structure as an underlying geometry. For the previously described study of correlation functions we use *matrix product states* (MPS) and *matrix product operator* (MPO) techniques on a line to derive QFT information. The *multiscale entanglement renormalization ansatz* (MERA) [42] is another type of TN ansatz, which combines a renormalization group (RG) flow with entanglement properties. It has a two-dimensional circuit geometry and is particularly well suited to capture CFT information. Based on an analytic wavelet solution [43] for the MERA, we ask the question whether this TN type provides a more faithful encoding of QFT information, which we similarly test in the context of retarded correlation functions and their analytic structure. This effort is related to the more general quest to find suitable discretizations of QFTs, a topic which is not only relevant in the context of TNs and LGTs, but also for quantum simulations (QS) as we will motivate below.

As an extension of this line of research, we then study the phenomenon of meson melting through TN simulations. Mesons, which we already introduced as bound states in QCD, are expected to break apart into their fundamental constituents when the temperature of the environment is heavily increased. The understanding of this process is particularly important for HICs and the QGP in the early universe, where effectively the inverse transition took place. Mesons appear also in the spectrum of spin chain Hamiltonians in specific parameter regimes. Near a quantum critical point, they correspond in the IR limit to bound states of an underlying relativistic QFT. Using TN methods, we study this regime both statically (as properties of a thermal state) and dynamically (through a quantum quench protocol) in different temperature regimes. While phenomenological QCD approaches as well as holographic models typically focus on spectral correlation functions to describe the melting of mesons, we, for the first time, describe this process from properties of entanglement measures, i.e. entropies, which are easily accessible in TN simulations. This analysis provides new insights into the meson melting process in a class of simplified models in lower-dimensional systems. In that vein, we see our investigation as a first step to address entanglement quantities as characteristics of meson melting also in more complicate (gauge) theories, leading eventually to QCD, for which currently no detailed microscopic understanding is known.

TN methods can be seen as an effort intimately related to the larger field of QS with the prospect to understand fundamental physics. Exactly 40 years ago, Richard Feynman envisioned in his seminal keynote address the use of universal quantum computers to simulate physical systems [44]. Due to the unprecedented improvement of experimental capabilities in the last decade, current technologies already allow the simulation of systems with a small

number of qubits. One of these technologies is based on trapped ions, which can perform either digital QS (i.e. the implementation of universal quantum circuits) or analog simulations (i.e. the implementation of specific spin chain Hamiltonians). For the latter case, we develop in this thesis a spectroscopical method to measure a relativistic meson spectrum on such an ion trap quantum simulator. Based on numerical modelling on classical computers, we estimate the capabilities of small current devices to extract properties of QFT mesons, which, as previously described, appear in the scaling limit of spin chain models near its critical point. Due to the enormous theoretical and experimental efforts of the community to develop methods that allow more complicate gauge theory simulations with quantum devices, this project opens the avenue of using ion traps to study fundamental meson physics. With that, we express the hope that in the future QS can answer some of the fundamental questions that motivated the previous projects in this thesis.

In the context of the second main question formulated above, the pioneering contributions [45, 46] used a geometric quantum circuit approach and an associated gate counting procedure to define and analyze complexity for certain QFTs. While this procedure is motivated by quantum information theory concepts, an independent program evolved, known as path integral optimization, which is originating from TN ideas. The latter definition of complexity is based on an optimization of a discretized Euclidean path integral that prepares an operator or state. As part of this thesis, it is shown how the latter path integral optimization program can be understood as a particular choice in the language of circuit complexity. We will show how this unification opened the avenue towards a better understanding of complexity for QFTs and in holography. Since complexity has been discussed as a probe for the BH interior and the emergence of dynamical spacetimes from microscopic quantum mechanical degrees of freedom, these explorations can serve as a starting point for a better understanding of quantum gravity, i.e. the attempt to describe QFTs and gravitational theories within one unified framework.

This thesis is organized in three parts. In this first part, we introduce the necessary background knowledge about holography and the gauge/gravity duality (chapter 2) as well as TN methods and concepts (chapter 3). Since our simulation-based research work is using the latter as computational tools, we keep the holography introduction rather compact. In sections of both of these chapters, which describe well established textbook knowledge, we follow in our discussion the cited reviews or lecture notes and refrain from citing all original publications. Part II contains all discussions related to the TN simulation and QS of QFT properties. In particular, chapter 4 is based on the project [1] in which we develop methods to extract thermal field theory properties from real-time TN simulations and apply them to non-trivial QFT regimes. We also describe necessary elements of QCD and holography, which motivate this line of research. In chapter 5 we extend these analyses based on entanglement renormalization approaches [3] and in chapter 6 we present our studies in the context of meson melting [4].

The explorations of using ion trap QS for meson physics [2] are discussed in chapter 7. In part III we discuss complexity in the context of TNs. At first, chapter 8 motivates holographic complexity proposals, while chapter 9 gives an overview of the different QFT interpretations. In chapter 10 the project [5] is discussed, in which the two QFT approaches for complexity are unified. We provide an overall summary and discussion in chapter 11. Appendix A contains a demonstration of a Prony signal analysis in a non-trivial holographic setup. We list for the reader's convenience all our acronyms in appendix B. Throughout this thesis we standardly assume natural units $\hbar = c = k_{\mathrm{B}} \equiv 1$.

2 The gauge/gravity duality

The gauge/gravity duality identifies a gravitational theory in $D+1$ dimensions with a D-dimensional QFT. Already 't Hoofts early work [47] on planar diagrams provided the starting point for this theoretical idea by identifying the large-N limit of a gauge theory with a dual string. The holographic principle of 't Hooft and Susskind [23,24] then stated that the quantum (gravitational) information within a spacetime volume can be fully encoded on its boundary, generalizing the BH entropy formula of Bekenstein [48], in which gravitational entropy is proportional to the horizon's area (rather than volume, which at least in some cases has been conjecture to be related to complexity). It was Maldacenas original AdS/CFT proposal [25], which gave this idea a concrete realization. Two other foundational papers [26,27] provided a dictionary allowing to translate between the gravity and QFT side by identifying their partition functions (cf. the operator/field map below) and an interpretation of thermal QFT effects via BH thermodynamics. Countless studies explored and used this correspondence in all areas of physics, both from a conceptual standpoint to understand quantum gravity as well as for fundamental problems, e.g., in particle or condensed matter physics, which are experimentally falsifiable. As already alluded in the previous chapter, many of these applications trace back to the fact that a strongly coupled QFT problem is translated into a weakly coupled gravitational problem, which often is more tractable. As we will explain below, the QFT is defined (or "lives") on the boundary of the higher-dimensional gravitational spacetime, giving rise to the term *holographic duality*, which is inspired by the optical phenomenon. Although the AdS/CFT correspondence in its original formulation (cf. section 2.4) relates very specific theories, many *top-down* and *bottom-up* phenomenological approaches have been developed and adjusted to physical problems (like heavy-ion collisions, the quark-gluon plasma, superconductivity and many more) by taking results from other physical methods into account. They are included in the term *gauge/gravity duality* as the more general holographic framework. Such holographic QFTs have a large number of degrees of freedom and strong interactions among them. It can then be an illuminating strategy to analyze how interesting physical effects generalize when lowering the number of degrees of freedom or changing the interaction strength etc. In this vein, we can motivate our explorations about real-time thermal field theory effects in chapter 4.

Many of these foundations, developments and applications are discussed in the textbooks [28–30,49,50]. Following mostly [28] and [30], we intend to give a very compact overview, similar to the presentation style in [51], of the most important aspects of the gauge/gravity du-

ality in this chapter. Detailed aspects of holographic descriptions, which are directly relevant to our research based on TN methods, are discussed in the individual chapters.

2.1 Anti-de Sitter spacetimes

The AdS spacetime is a maximally symmetric solution to the Einstein–Hilbert action

$$S_{\mathrm{EH}} = \frac{1}{16\pi G_N^{(D+1)}} \int \mathrm{d}^{D+1}x\sqrt{-g}\,(R - 2\Lambda) \tag{2.1}$$

for negative cosmological constant $\Lambda = -\frac{D(D-1)}{2L^2} < 0$ with AdS radius L.[3] It can be defined in $(D+1)$ dimensions by a hyperboloid embedded into $(D+2)$-dimensional Minkowski spacetime as

$$-X_0^2 + \sum_{i=1}^{D} X_i^2 - X_{D+1}^2 = -L^2, \qquad \mathrm{d}s^2 = -\,\mathrm{d}X_0^2 + \sum_{i=1}^{D} \mathrm{d}X_i^2 - \mathrm{d}X_{D+1}^2 \tag{2.2}$$

with coordinates $(X_0, \ldots, X_{D+1}) \in \mathbb{R}^{D,2}$.[4] An important property for the identification within the AdS/CFT correspondence is the invariance under the $SO(D,2)$ symmetry group. The compactified D-dimensional Minkowski spacetime can be identified as the conformal boundary of this spacetime. In Poincaré patch coordinates, the line element takes the form

$$\mathrm{d}s^2 = \frac{L^2}{r^2}\,\mathrm{d}r^2 + \frac{r^2}{L^2}\left(-\,\mathrm{d}t^2 + \mathrm{d}\vec{x}^{\,2}\right) = \frac{L^2}{z^2}\left(-\,\mathrm{d}t^2 + \mathrm{d}\vec{x}^{\,2} + \mathrm{d}z^2\right), \tag{2.3}$$

where $t \in \mathbb{R}$, $\vec{x} = (x^1, \ldots, x^{d-1}) \in \mathbb{R}^{D-1}$. The coordinates $0 \le r \le \infty$ or $0 \le z \equiv \frac{L^2}{r} \le \infty$ allow holographic interpretations for the conformal boundary at $r \to \infty$ or $z = 0$.
Within the holographic correspondence, empty AdS spacetimes represent the trivial time development of the vacuum state in a dual CFT. More general solutions of the gravitational field equations in asymptotic AdS spacetimes can be thought of as the time development of other states. For example, thermal deconfined states correspond to BHs, which are encoded as a zero of a blackness function $f(z)$ at the event horizon. Their thermodynamic properties can be associated to the QFT side of the gauge/gravity duality as outlined in section 2.5 below. Most prominently, the Schwarzschild AdS BH solution reads

$$\mathrm{d}s^2 = \frac{L^2}{z^2}\left(-f(z)\,\mathrm{d}t^2 + \mathrm{d}\vec{x}^{\,2} + \frac{\mathrm{d}z^2}{f(z)}\right), \tag{2.4}$$

whereby $f(z) = 1 - (z/z_h)^4$ admits a simple zero at the horizon $z = z_h$. More generally, any solution of the form $\mathrm{d}s^2 = \mathrm{e}^{2A(z)}\left(-f(z)\,\mathrm{d}t^2 + \mathrm{d}\vec{x}^{\,2} + \mathrm{d}z^2/f(z)\right)$, for which the scaling factor

[3] Maximally symmetric means that AdS solutions possess the maximum number of Killing vectors for constant curvature $R = -\frac{D(D+1)}{L^2} = \mathrm{const} < 0$. Here, $G_N^{(D+1)}$ is the $(D+1)$-dimensional Newton constant.
[4] Similarly, de Sitter (dS) spacetimes are given by $-X_0^2 + \sum_{i=1}^{D} X_i^2 + X_{D+1}^2 = L^2$ as sphere-like embeddings.

satisfies $A(z\to 0)\to -\ln(z/L)$ and $f(z\to 0)=1-\mathcal{O}(z^4)$, represents an asymptotic AdS BH metric.

2.2 Foundations of conformal field theories

Conformal field theories (CFTs) play an important role in this thesis: They appear as effective descriptions of lattice models in (1+1) dimensions, which can be studied with TN methods. Relevant deformations of them can give rise to more involved theories with interesting physical features. Moreover, our holographic complexity studies are in the realm of $2D$ CFTs as the most controllable case. In higher dimensions, CFTs are relevant for the deduction of the AdS/CFT correspondence presented in this chapter. By definition, they are QFTs invariant under conformal transformations. They are one way to bypass the Coleman–Mandula theorem [52], which states that extensions of the Poincaré algebra would make the S-matrix vanish and are therefore forbidden. The second way is by introducing graded Lie algebras, which leads to the supersymmetry (SUSY) algebra. Both symmetries are obeyed by $\mathcal{N}=4$ super Yang–Mills (SYM) theory, which appears on the gauge theory side of the holographic duality. We describe in this section the most basic elements of CFTs based on [28,29,53]. For a comprehensive discussion of CFTs we refer to [54].

We start by considering regularization and renormalization methods to cancel divergences in QFTs, which introduce an energy scale μ, whose dependence on the coupling constant g of the theory is described by the β function

$$\beta(g)=\mu\frac{\mathrm{d}g}{\mathrm{d}\mu}. \tag{2.5}$$

While classical theories can be globally scale invariant, anomalies can break this property on the quantum level. Quantum mechanically scale invariant theories therefore require a vanishing β function. This can be realized as $\beta=0$ for all values of g (as in $\mathcal{N}=4$ SYM) or for a nontrivial interacting fixed point $\beta(g_0)=0$ (as in the critical point of a quantum phase transition). All known examples of such theories are additionally also conformally invariant, which is a local generalization. Conformal coordinate transformations locally preserve angles and the causal structure. In terms of a positive conformal factor $\Omega(x)^2$, the metric components and line element satisfy

$$g_{\mu\nu}(x)\mapsto\Omega(x)^{-2}g_{\mu\nu}(x)\quad\Leftrightarrow\quad \mathrm{d}s'^2=\Omega(x)^{-2}\,\mathrm{d}s^2, \tag{2.6}$$

which implies

$$\left(g_{\mu\nu}\partial_\rho\partial^\rho+(D-2)\,\partial_\mu\partial_\nu\right)\partial_\mu\epsilon^\mu=0 \tag{2.7}$$

for infinitesimal conformal transformation $x^\mu\mapsto x^\mu+\epsilon^\mu(x)$.

Due to the factor $(D-2)$, there is an important differentiation between CFTs in two dimensions and higher. We consider at first the conformal algebra in $D = 2$. The condition (2.7) then reads $\partial_0\epsilon_1 = -\partial_1\epsilon_0$ and $\partial_0\epsilon_0 = \partial_1\epsilon_1$ for the two components, being identical to the Cauchy-Riemann differential equations in functional analysis. Introducing complex coordinates as $z \equiv x^0 + ix^1$ and $\bar{z} \equiv x^0 - ix^1$, conformal transformations in two dimensions are thus realized by holomorphic and anti-holomorphic functions as $z \mapsto f(z)$, $\bar{z} \mapsto \bar{f}(\bar{z})$. They form an infinite dimensional Virasoro algebra, generated by the modes of the energy-momentum tensor, which are given as Laurent coefficients

$$T_{zz}(z) = \sum_{n\in\mathbb{Z}} \frac{L_n}{z^{n+2}}, \qquad L_n = \frac{1}{2\pi i} \oint \mathrm{d}z z^{n+1} T_{zz}(z). \tag{2.8}$$

Their commutation relation takes in the quantum theory the form

$$[L_m, L_n] = (m-n)L_{m+n} + \frac{c}{12} m(m^2-1)\delta_{m+n,0}, \tag{2.9}$$

where c is called central charge and specifies the conformal anomaly (or central extension) in the second term. [5] The conformal dimension $(h, \bar{h})$ characterizes how fields in a CFT transform under conformal transformations. A *primary field* (or tensor operator) ϕ satisfies

$$\phi(z,\bar{z}) \mapsto \phi'(z,\bar{z}) = \left(\frac{\partial f}{\partial z}\right)^h \left(\frac{\partial \bar{f}}{\partial \bar{z}}\right)^{\bar{h}} \phi(f(z), \bar{f}(\bar{z})), \tag{2.10}$$

leaving the differential $\phi(z,\bar{z})(\mathrm{d}z)^h(\mathrm{d}\bar{z})^{\bar{h}}$ invariant. Under rescalings $z \mapsto \lambda z$, $\bar{z} \mapsto \lambda\bar{z}$, this implies $\phi \mapsto \lambda^{\Delta_\phi}\phi$, where we defined the scaling dimension $\Delta_\phi \equiv h + \bar{h}$. [6] A so-called *highest-weight state* $|h\rangle$ satisfies $L_0 |h\rangle = h |h\rangle$ and $L_n |h\rangle = 0$ for $n > 0$. It is related to a primary field ϕ by the the *operator-state correspondence* as $|h\rangle = \lim_{z\to 0} \phi(z) |0\rangle$, where $|0\rangle$ is denoting the vacuum. A representation of the Virasoro algebra is then constructed by the method of induced representation, in which *descendant states* of the form $(L_{-n_1} L_{-n_2} \cdots L_{-n_k}) |h\rangle$ follow from the action of modes L_{-n} on the highest-weight state as $L_0 L_{-n} |h\rangle = (h+n) L_{-n} |h\rangle$.
In higher dimensions, $D > 2$, the general solution of eq. (2.7) reads

$$\epsilon^\mu(x) = a^\mu + \omega^\mu{}_\nu x^\nu + \lambda x^\mu + b^\mu x^2 - 2(b\cdot x)x^\mu, \tag{2.11}$$

where a^μ parameterizes translations (generated by the momentum operator P_μ), $\omega^\mu{}_\nu$ corresponds to Lorentz transformations (generated by $J_{\mu\nu}$), λ to dilatations (generated by $\mathfrak{D}$), and b_μ to special conformal transformations (generated by K_μ). In contrast to the two-dimensional case, they form a finite-dimensional Lie algebra with symmetry group $SO(D,2)$. As before,

[5] Note that only the generators $\{L_{-1}, L_0, L_1\}$ define a closing, finite-dimensional subalgebra representing global conformal transformations.
[6] The difference $h - \bar{h}$ is interpreted as the spin of the field, specifying its behavior under rotations.

group representations are constructed inductively, but now from eigenfunctions of the scaling operator $\mathfrak{D}$ with eigenvalue $-i\Delta_\phi$, which is the analogon of L_0.[7] The role of any other L_n and L_{-n} is taken by K_μ (annihilation operator) and P_μ (creation operator), which act on fields as $\mathfrak{D}(X_\mu\phi) = -i(\Delta_\phi \pm 1)(X_\mu\phi)$ for $X_\mu \equiv P_\mu, K_\mu$. Descendants follow from their successive application on the primary operator/state of lowest dimension, defined by $K_\mu\phi_0 = 0$.

Conformal symmetry severely restricts the form of correlation functions and entanglement entropies in CFTs. We discuss these aspects in the relevant sections of the next chapter 3. A way of obtaining nontrivial QFTs is to deform CFTs by relevant operators with $\Delta < D$, which affects the physics at large distances. This property enables us in part II to study interesting physical effects.

The final remarks in this section are devoted to $\mathcal{N} = 4$ SYM theory as a realization of the superconformal group in $D = 4$. SUSY extends the Poincaré algebra by new field contents in a graded Lie algebra representation. $\mathcal{N} = 4$ SYM theory possesses the maximum number of 16 supercharges $Q^a, \bar{Q}^a$ (without gravity), which follow from Noether's theorem as conserved quantities and act as operators transforming fermion fields into bosonic ones and vice versa.[8] The defining action of this maximally supersymmetric and non-Abelian gauge theory can be derived from the $\mathcal{N} = 1$ superspace formalism or by dimensional reduction from 10-dimensional $\mathcal{N} = 1$ SYM theory.[9] It has the following field content: A vector gauge field $A_\mu(x)$ with gauge group $SU(N_c)$, four Weyl fermions $\lambda^a_\alpha(x)$ $(a = 1, \ldots, 4)$ and six real scalars $\phi^i(x)$ $(i = 1, \ldots, 6)$. The coupling is parametrized by the Yang–Mills constant g_{YM} with dimension $[g_{\mathrm{YM}}] = 0$, making this massless theory classically scale invariant. Due to a vanishing β function in all perturbative orders, this holds also for the quantum theory, which can be shown to be invariant under the more general superconformal group.

2.3 Elements of string theories

We motivate the most basic elements of string theory in this section to provide the necessary background of the AdS/CFT derivation in the next section. While our discussion is based on [29], we refer to [53,56,57] as comprehensive textbooks on this topic.

In an attempt to formulate a fundamental theory of quantum gravity, string theory generalizes QFT from relativistic point particles to strings as extended one-dimensional lines or loops with an associated tension, i.e. energy per unit length. By the variational principle, their action needs to minimize the area of the string worldsheet, which is the surface swept out by moving strings. Denoting the string position coordinates as $X^\mu(\sigma, \tau)$, this leads to the Nambu-Goto

[7] The scaling dimension Δ_ϕ is defined as previously as the exponent under field rescalings, i.e. for $x \mapsto \lambda x$ one has $\phi(x) \mapsto \lambda^{\Delta_\phi}\phi(\lambda x)$.

[8] The index $a = 1, \ldots, \mathcal{N}$ enumerates the number of independent supersymmetries.

[9] We refer to, e.g., [28,29,55] for its explicit form and omit the details here, since they are not relevant for the understanding of the gauge/gravity derivation in this chapter nor the actual research part in this thesis.

action $S_{NG} = -T \int \mathrm{d}\sigma\, \mathrm{d}\tau \sqrt{\det(h_{ab})}$ with $T \equiv (2\pi\alpha')^{-1}$ as the string tension, containing the string length l_s via $\alpha' \equiv l_s^2$, and $h_{ab} = \partial_a X^\mu \partial_b X^\nu g_{\mu\nu}(X)$ as the induced spacetime metric. This action can be transformed into the more fundamental Polyakov action of the form

$$S_{\mathrm{P}} = -\frac{T}{2} \int \mathrm{d}\sigma\, \mathrm{d}\tau \sqrt{-\gamma} \gamma^{ab} h_{ab}, \tag{2.12}$$

where γ^{ab} is an independent worldsheet metric. Open strings with Neumann (free endpoints) or Dirichlet (fixed endpoints) boundary conditions as well as closed strings appear as solutions of the resulting equation of motion. After canonical quantization of the bosonic string, it turns out that the vacuum consists of unstable tachyons of negative mass. Massless excitations are consistent only in the critical spacetime dimension $D = 26$. The unstable tachyons can be projected out if the Polyakov action is extended to the supersymmetric form

$$S_{\mathrm{P,SUSY}} = -\frac{T}{2} \int \mathrm{d}\sigma\, \mathrm{d}\tau \sqrt{-\gamma} \gamma^{ab} \left(\partial_a X^\mu \partial_b X^\nu + i \bar{\Psi}^\mu \gamma_a \partial_b \bar{\Psi}^\nu \right) g_{\mu\nu}(X), \tag{2.13}$$

where Ψ^μ are fermionic spinors on the worldsheet and γ_a Dirac matrices. The quantized supersymmetric string is consistent in the critical dimension $D = 10$, which can be reduced to $D = 4$ in our real world by the dimensional reduction procedure of Kaluza–Klein. Depending on the boundary conditions for the individual left- and right moving modes, closed superstring solutions of (2.13) can be projected out in four consistent ways, giving rise to distinct superstring theories, which are related to each other by a set of dualities. It is conjectured that they arise from a more fundamental M-theory in 11 dimensions. One of these superstring theories is denoted as type IIB, which reduces in the low-energy limit ($\alpha' \to 0$) to a supergravity solution, representing a SUSY extension of general relativity.

Amplitudes of scattering processes in type IIB superstring theory (or any other) can be calculated by generalizing Feynman diagrams to a sum over two-dimensional topologies. The interaction strength is parametrized by the coupling constant g_s, which, in fact, can be shown to be given in terms of the asymptotic vacuum expectation value of a scalar field in the spectrum.

We finally introduce p-branes and Dp-branes as important objects in superstring theories. Black p-branes are BH solutions in p spatial dimensions, which can carry a charge Q_p under an antisymmetric tensor field $A_{\mu_1 \cdots \mu_{p+1}}$. They appear as supergravity solutions and are called *extremal* if their tension T_p saturates the bound $T_p \geq \mathrm{const} \cdot Q_p$. D$p$-branes are dynamical, nonperturbative hyperplanes in $(p+1)$ dimensions, on which open strings (i.e. with Dirichlet boundary conditions) end. They contain nontrivial gauge fields and other degrees of freedom by deformations through the open strings.

2.4 The AdS/CFT correspondence

Symmetry properties are one of the most important considerations for physical theories (in the standard model and beyond). From section 2.1 and 2.2, it becomes apparent that a D-dimensional CFT and AdS spacetime in $(D+1)$ dimensions share the same symmetry group, providing a necessary condition to identify very different theories on both sides of the duality with each other. We describe in this section very briefly the original AdS/CFT correspondence, which was found by Maldacena in [25].

Making use of the result that extremal p-branes and Dp-branes are two ways of viewing the same physics [58], the AdS/CFT proposal originates from two different perspectives on these branes, which we explain using Fig. 2.1. We consider type IIB superstring theory in 10 dimensions with coordinates $x^0, x^1, \ldots, x^9$ and a stack of N_c D3-branes along the spacetime directions $x^0, \ldots, x^3$ transversal to $x^4, \ldots, x^9$.

The open string viewpoint, visualized in the left panel, is considered in the perturbative regime of small string coupling $g_s \ll 1$. For small energies $E \ll \alpha'^{-1/2} = l_s^{-1}$, only the massless part of the string spectrum contributes, which contains a gauge field $A_\mu(x)$, six scalar fields $\phi^i(x)$ and their superpartners. The effective action of a D3-brane can be written as $S = S_{\text{open}} + S_{\text{closed}} + S_{\text{int}}$, referring to closed and open string modes and their interactions. If additionally also the limit $\alpha' \to 0$ is considered, open and closed string decouple, i.e. $S_{\text{int}} = 0$, and S_{closed} reduces to the supergravity action in Minkowski spacetime. The relevant action S_{open} reduces to $\mathcal{N} = 4$ SYM theory with gauge group $SU(N_c)$.

In the closed string viewpoint (cf. right panel), one considers the opposite regime of strong coupling, $g_s N_c \to \infty$. Dp-branes are therefore treated as massive gravitating objects. One can show that the supergravity solution for D3-branes reduces in the near-horizon region of the BH to the metric $\mathrm{d}s^2 = \frac{r^2}{L^2}\left(-\mathrm{d}t^2 + \mathrm{d}\vec{x}^2\right) + \frac{L^2}{r^2}\,\mathrm{d}r^2 + L^2\,\mathrm{d}\Omega_5^2$, where we defined $r^2 \equiv \sum_{i=4}^{9} x_i^2$ as a radial coordinate and $L^4 \equiv 4\pi g_s N_c \alpha'^2$. By comparing with eq. 2.3, one identifies this metric as an AdS_5 spacetime times a compact five-sphere S_5. On the other hand, for large distances, the geometry is given by the usual Minkowski metric. In the low-energy limit, these regimes decouple again.

Both perspectives yielded two decoupled regimes, which now can be identified with each other. Since the supergravity solutions in $\mathbb{R}^{9,1}$ agree, Maldacena proposed (by relaxing the low-energy condition) the following theory identification

$$\mathcal{N} = 4\ SU(N_c)\ \text{SYM in}\ \mathbb{R}^{1,3} \quad \Longleftrightarrow \quad \text{IIB superstring theory in}\ \mathrm{AdS}_5 \times S_5 \tag{2.14}$$

where the parameters are mapped to each other as $g_{\text{YM}}^2 = 2\pi g_s$ and $2g_{\text{YM}}^2 N_c = (L/l_s)^4$.

In the strongest form, the parameter mapping is expected to be valid for any values. In a strong version, the string theory is assumed to be in the classical gravitational regime $g_s \to 0$, $l_s/L \neq 0$ fixed. This translates into the planar limit $N_c \to \infty$ at constant 't Hooft coupling

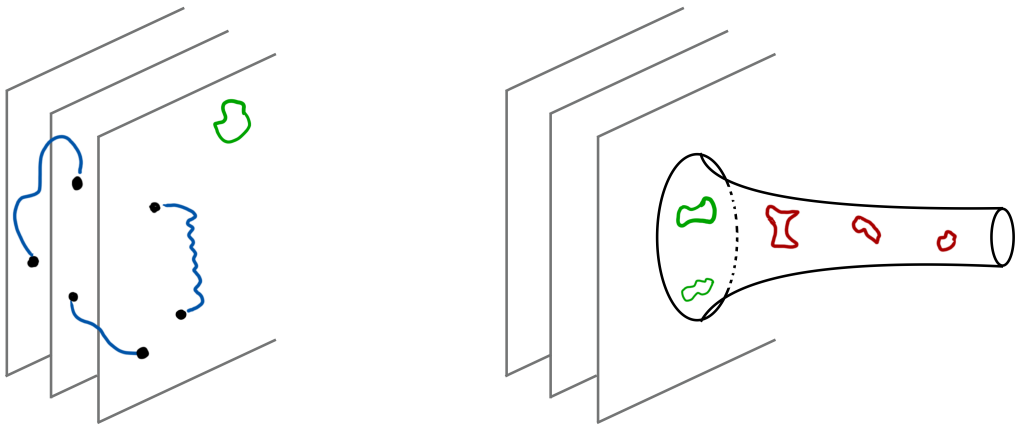

Figure 2.1: Schematic illustration of the open (left panel) and closed string perspective (right panel) on a stack of D3-branes. Open strings (in blue) can start and end on the same brane or different ones. Their parallel excitations are described by a gauge field in type IIB superstring theory, while scalar fields capture transverse fluctuations. They reduce to $\mathcal{N} = 4$ SYM theory in the small coupling, low energy limit. In both perspectives, closed strings propagate in flat Minkowski spacetime (in green, close to the stack) and in the right perspective also in a curved throat close to the BH horizon of the D3-brane (shown in red). The latter reduce to IIB supergravity theory on $\mathrm{AdS}_5 \times S_5$ in the strong coupling, low energy limit.

$\lambda \equiv g_{\mathrm{YM}}^2 N_c$. The correspondence between SYM theory at strong coupling and a classical gravitational theory at weak coupling arises if additionally the limit $\lambda \to \infty$ is taken, which maps to $l_s/L \to 0$.

2.5 Entries in the holographic dictionary

As elaborated before, apart from Maldacenas original formulation of the AdS/CFT correspondence between very specific theories, many more holographic counterparts to QFT aspects were found. We describe the most relevant ones in this short overview, motivating some of the research questions addressed in this thesis.

2.5.1 RG flow geometrization and UV/IR relation

As reviewed in [30], the AdS/CFT correspondence can be intuitively understood as a geometrization of the RG flow. Considering a D-dimensional QFT (in Minkowski spacetime) with an ultraviolet (UV) regulator ϵ, an effective field theory description at large distances $z \gg \epsilon$ is found by integrating out short-distance degrees of freedom. One can interpret the resulting set of theories, labelled by the continuous RG scale z, as a theory embedded in $(D+1)$ dimensions, where z takes the role of the additional dimension. An AdS geometry of the form (2.3) follows uniquely by demanding Poincaré and conformal symmetry. The gauge theory

energy E_{YM} is then related to its holographic counterpart E in the bulk as

$$E_{\mathrm{YM}} = \frac{L}{z} E. \tag{2.15}$$

Due to its inverse dependence on z, the UV limit ($E_{\mathrm{YM}} \to \infty$) is holographically described by bulk processes near the Minkowski boundary ($z \to 0$), while IR physics ($E_{\mathrm{YM}} \to 0$) is mapped to the region $z \to \infty$.[10] In real space, a similar geometrization of the RG flow was the basis for discrete holographic interpretations of the MERA TN, as we will describe in section 3.7.1.

2.5.2 Operator/field map

In the most general way, the gauge/gravity duality can be formulated by identifying the partition function of a conformal gauge theory with its string theory counterpart,

$$Z_O[\phi_0(x)]_{\mathrm{CFT}} = Z_\Phi[\phi_0(x)]_{\mathrm{string}}. \tag{2.16}$$

For that, we consider a bulk field Φ with a boundary value $\phi_0(x) = \lim_{z\to 0} z^{\alpha_\Phi}\Phi(x,z)$, which sources a local field operator O in the CFT partition function $Z_O[\phi_0(x)]_{\mathrm{CFT}} = \int \mathcal{D}O \exp\left(-S_{\mathrm{CFT}} + \int \mathrm{d}^d x\, O(x)\phi_0(x)\right)$.[11] The string theory partition function is typically only calculable in the classical limit as a supergravity saddle point approximation, i.e. $Z_\Phi[\phi_0(x)]_{\mathrm{string}} = \mathrm{e}^{-S_{\mathrm{SUGRA}}[\Phi[\phi_0]]}$. This procedure allows to derive correlation functions of the form $\langle O(x_1)\dots O(x_n)\rangle$ either as functional derivatives of the CFT partition function w.r.t. its sources, or, in the dual formulation, by evaluating (tree level) *Witten diagrams*. The latter can be seen as generalizations of Feynman diagrams in AdS spacetime, where the supergravity equations of motion are solved and holographically renormalized. Most prominently, for a bulk scalar field ϕ in AdS_{D+1}, one can find that its mass m is related to the scaling dimension Δ_O of a dual scalar field theory operator as $m^2L^2 = \Delta_O(\Delta_O - D)$.[12] Since this prescription relates gauge theory operators to bulk fields, it is referred to as the operator/field map. While we sketched here the prescription in Euclidean signature, the works [60,61] generalized it to Minkowski spacetimes.

2.5.3 Thermodynamic quantities

BHs and higher-dimensional black branes within an asymptotic AdS spacetime possess an event horizon as a defining property. They obey the thermodynamic laws of Hawking and

[10] As an extension, gapped theories can be can be described via a cutoff/ending at $z_0 \sim 1/m$, with m as the mass gap. Particularly interesting is the situation when z_0 is the position of a BH horizon, which allows to identify thermodynamic quantities; see below.

[11] The properties of Φ (tensor rank, spin,...) determine the specific value of the coefficient α_Φ.

[12] This relation depends on the spin and tensor type of the considered field. For a more complete overview, see, e.g., [28,59].

Bekenstein and therefore have a temperature T and entropy S. These quantities follow from the relations

$$T = \frac{\varkappa}{2\pi}, \qquad S = \frac{A_h}{4G_N^{(D+1)}}, \tag{2.17}$$

where $\varkappa$ is the surface gravity and A_h the event horizon area.[13] Based on the AdS/CFT correspondence, these are interpreted as the holographic dual of their CFT counterpart, or, more generally, of the gauge theory for more sophisticated holographic models.

2.5.4 Entanglement entropy

Throughout this thesis, entanglement entropy plays a major role to characterize quantum correlations both in QFTs and QMB systems. This quantity is defined as the von Neumann entropy

$$S(\rho_A) = -\operatorname{Tr}\left[\rho_A \log \rho_A\right] = S(\rho_B) \tag{2.18}$$

for the reduced density matrix $\rho_A = \operatorname{Tr}_B(\rho)$ of a (pure) state density operator ρ. Here, A is a connected region of the physical system and B its complement.

Ryu and Takayanagi provided in [35,36] a holographic formula for the entanglement entropy. Specifically for a subregion A on a boundary time slice of a CFT in D Minkowski dimensions, it takes the form

$$S_{\text{HEE}} = \frac{\text{Area}(\gamma_A)}{4G_N^{(D+1)}}, \tag{2.19}$$

where γ_A is the minimal bulk surface that anchors on the boundary of A, cf. Fig. 2.2 for an illustration. Since the calculation of entanglement entropy in arbitrary QFTs is very difficult, this dual formula initiated a plethora of studies, e.g. to analyze its behavior in strongly coupled QFTs, time evolution under quantum quenches or deconfinement phase transitions. These developments are partly reviewed in the lecture notes [62]. Subsequently, the work [63] found a covariant generalization, which was formally derived in [64]. Since eq. (2.19) relates a fundamental quantum measure to a geometric quantity, it was conjectured that spacetime itself could be an emergent phenomena, which is dynamically generated by the underlying entanglement degrees of freedom. Major steps in this development can be found in [65–67].

While we have briefly reviewed the holographic counterpart here, we will give a detailed discussion of entanglement entropy in the context of area laws of QMB systems and CFTs in section 3.2.

[13] We refer to the standard textbook literature on general relativity or AdS/CFT for detailed explanations of the latter quantities. Note that this framework can be extended if a charged BH with a $U(1)$ gauge field A_μ is introduced in the bulk theory. Then a chemical potential μ can be derived as $\mu = \frac{1}{L}\lim_{z\to 0} A_t$ for the temporal component A_t of the gauge field.

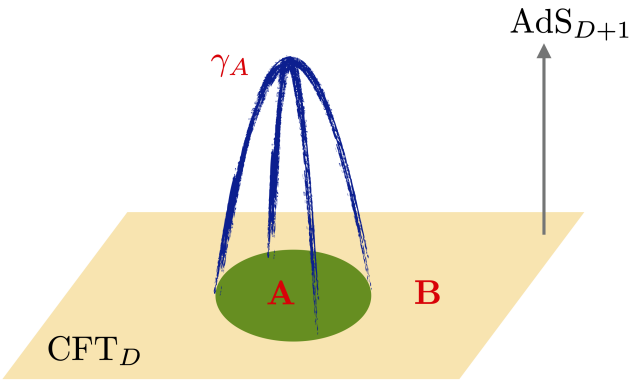

Figure 2.2: According to the Ryu–Takayanagi proposal, the entanglement entropy for a subregion A in a CFT$_D$ is calculated holographically as the area of the associated minimal surface γ_A (shown in blue) in the bulk of AdS$_{D+1}$.

2.5.5 Generalized entanglement entropies and dualities

Apart from entanglement entropy itself, also other entropy measures and interpretations have been discussed in a holographic context. For example, in [68] a more general *surface/state correspondence* was proposed in which arbitrary codimension-two space-like surfaces can be associated with a dual quantum state (independent from any boundary). Furthermore, the works [69,70] interpreted the mixed state measure *entanglement of purification* as the cross section area of the minimal surface that connects two disjoint boundary regions. In [71], a pseudo entropy was defined, which was found to generalize eq. (2.19) in time-dependent Euclidean metrics. The authors could interpret this proposal quantum information theoretically in terms of Bell pairs for specific cases. Recently, the work [72] defined a generalized entanglement measure, denoted as *entwinement*, by taking entanglement of both spatial and field degrees of freedom into account. This allowed the author to reconstruct the whole bulk geometry from a geodesic with non-zero winding number for a specific example of the AdS$_3$/CFT$_2$ correspondence. Detailed discussions on these and further entanglement measures in holography can be found in the up to date review [34].

2.5.6 Complexity

Explorations on holographic interpretations of quantum information measures through geometric quantities got fueled by Susskinds works on complexity [73]. These directly make contact to quantum gravitational aspects by describing the interior of black holes in holographic spacetimes. Based on the observation that a Einstein–Rosen bridge (ERB), which connects two copies of a CFT in the bulk of an eternal AdS BH, grows on exponentially longer time scales than present in the boundary field theory, he interpreted the additional degrees of freedom with *computational complexity*. The latter quantity describes the minimal number of gates to realize a quantum circuit. This led to the slogan "*entanglement is not enough*" [38],

which is actually referring to entanglement entropy. It was proposed that the boundary state complexity $\mathcal{C}$ can be holographically calculated either from volumes (codimension-1) [73,74] or actions (codimension-0) [39,75] as follows

$$\mathcal{C}_V(\Sigma) = \max_{\Sigma=\partial B} \left[\frac{V(B)}{l\, G_N^{(D+1)}} \right], \qquad \mathcal{C}_A(\Sigma) = \frac{S_{\mathrm{WDW}}}{\pi}. \tag{2.20}$$

In the $\mathcal{C}_V$ proposal, the maximum is taken over all bulk surfaces B whose boundary ∂B is anchored on a time slice Σ where the CFT state is considered. Here, l is a non-unique length scale and S_{WDW} denotes the gravitational action on a Wheeler–DeWitt (WDW) patch. The volume proposal is motivated by considerations of thermal entropy in the BH solution. At the same time, this represents an entanglement entropy between the two CFT copies, and hence is related to the previously discussed ideas of emergence of spacetime from entanglement. While these proposals lead to numerous studies of holographic complexity in different gravitational scenarios, they left open the question of what is the actual definition of complexity on the QFT side of the duality. While the first steps answering this question were taken in [45,46], the underlying problem motivates our research in part III of this thesis, where we will combine a geometric quantum circuit approach with a path integral optimization procedure. The latter arose as an attempt to find a microscopic understanding of the AdS/CFT duality from TN approaches (see section 3.7). We will give a more detailed introduction into these concepts in chapter 8 and 9.

3 Introduction to tensor network concepts and methods

In this chapter we describe the theoretical background of TNs in the context of quantum many-body (QMB) systems. Different types of TNs are presented as well as relevant numerical algorithms, which are used in the following parts. We also describe some holographic interpretations of discrete TN structures. The discussion primarily follows the reviews and introductions [11] and [9,12,17].

3.1 Quantum many-body systems and the Hilbert space problem

At the core of lots of physical problems is the description of QMB systems from both a theoretical and numerical viewpoint. As motivated in the previous chapter, this task is particularly important to study QFTs in the standard model, and condensed matter phenomena, such as superconductivity or topological phases and other exotic quantum matter. But also in the emerging field of quantum technologies and computing, quantum chemistry and material design, the development and progress relies on the understanding of such many-body systems. The fundamental problem associated to these systems is the exponential growth of their Hilbert space $\mathcal{H}$ of quantum states: Assuming N elementary constituents of local physical dimension d, the whole Hilbert space is represented by the tensor product of the local Hilbert spaces, i.e. $\mathcal{H} = \mathcal{H}_1 \otimes \mathcal{H}_1 \otimes \ldots \otimes \mathcal{H}_N$, with overall dimension

$$\dim(\mathcal{H}) = \mathcal{O}(d^N). \tag{3.1}$$

For any macroscopic system of the size of the Avogadro number $N \sim 10^{23}$, the resulting Hilbert space dimension, which quantifies the number of wave function coefficients, is of order $\mathcal{O}(10^{10^{23}})$, which is higher than the number of all fermions in the entire universe. More severely, also the time needed to reach the majority of the Hilbert space by starting with some initial state scales exponentially with the system size and thus easily exceeds the age of the universe for macroscopic systems [11].
The collective behavior of interacting QMB systems can exhibit complicated emergent phenom-

ena. It is therefore an overarching goal to find efficient representation methods and simulation techniques for them. While mostly an exact solution is not available, it also becomes obvious from the above estimates, that it would be inefficient and impossible to solve this system by exact diagonalization on a classical computer. This restriction to small system sizes is far away from the thermodynamic limit ($N \to \infty$) in which quantum phase transitions as an example of emergent behavior appear. Similarly, other analytical approximations and numerical approaches have their intrinsic limitations (see [11,17] and references therein for detailed discussions): For example, semiclassical and mean-field methods do not properly take quantum correlations into account and hence especially suffer in low dimensions. Perturbative and series expansion methods are restricted to small couplings. Monte Carlo methods provide a scalable way of evaluating statistical partition functions and are very successfully applied to lattice gauge theories, in particular QCD. They are however limited by the sign problem, i.e. the appearance of complex determinants or actions, which poses a NP-hard problem for real-time calculations and finite densities. Another powerful way of capturing low-energy physics of QMB systems is given by Wilson's renormalization group paradigm: By integrating out the high-energy degrees of freedom of an effective field theory model, one can extract universal information at critical phase transitions. This approach however suffers for quantitative predictions and at strong couplings. From a condensed matter perspective, White's density matrix renormalization group (DMRG) [76] is a particular example, where this procedure is further developed and allows efficient spin chain simulations in one dimension. Below, we will make use of this approach as a reformulated variational tensor network algorithm.

Tensor networks provide a new and very efficient way of tackling many QMB systems of significant physical interest, which, in contrast to the other methods, is based on entanglement considerations. As we will explain in the next section, the structure of entanglement and quantum correlations depends strongly on the dimensionality but also phase properties of the physical system. By making suitable ansätze, one can single out relevant physical corners of the huge Hilbert space. A graphical representation in form of network diagrams makes the tensor structure of the Hilbert space and its entanglement properties apparent. This is achieved by decomposing the full wave function into smaller tensors carrying the entanglement degrees of freedom and introducing an effective lattice geometry. The limitation of this method hence lies in the structure and amount of entanglement in the QMB state. This concept is very powerful, since it allows to simulate lots of relevant models in several dimensions, to include symmetries, to study systems based on a gauge principle or to work in the thermodynamic and continuum limit.

3.2 Entanglement structure and area laws

The numerical studies in part II of this thesis will be based on spin systems, which are naturally equipped with a tensor product structure on an underlying lattice geometry. These, and lots of other relevant models, typically have a local Hamiltonian. That is, one can write the Hamiltonian with finite-ranged interactions as

$$H = \sum_{i=1}^{N} h_{i,n}, \tag{3.2}$$

where the density $h_{i,n}$ acts on site i and its $n-1$ closest neighbors. As comprehensively reviewed in [77], the locality of such physical interactions in QMB systems imposes strong restrictions on the correlation and entanglement structure. The ground state, i.e. the state which minimizes $\langle\psi| H |\psi\rangle$, is of primary importance here, since quantum effects are strongest in the vacuum or low temperatures. [14] Furthermore, there are crucial differences for gapless versus gapped states, i.e. states with vanishing or finite Hamiltonian gap (from the ground state energy to the first excited state) in the thermodynamic limit. Critical systems belong to the first class with infinite correlation length ξ (described by CFTs), whereas the latter quantity is finite for gapped systems. The locality of Hamiltonian interactions is inherited to the correlation functions. In gapped models, they decay exponentially with the distance on the lattice,

$$|\langle O_A O_B\rangle - \langle O_A\rangle\langle O_B\rangle| \sim \mathrm{e}^{-\mathrm{dist}(A,B)/\xi}, \tag{3.3}$$

for operators $O_{A,B}$. This effect is sometimes denoted as *clustering of correlations* [12] and can be proven by using Lieb-Robinson bounds [78] on the speed of information spreading. In contrast, gapless models exhibit a power-law decay, represented by the normalized CFT result

$$\langle O(x_1)O(x_2)\rangle = \frac{1}{|x_1 - x_2|^{2\Delta_O}} \tag{3.4}$$

for an operator O with scaling dimension Δ_O at positions $x_{1,2}$. [15]

Beyond the decay of correlation functions, the locality of Hamiltonian interactions implies even deeper properties on the entanglement structure. This is captured by the entanglement entropy (2.18), which we consider here for the reduced density matrix $\rho_A = \mathrm{Tr}_B(\rho)$ of the (ground) state density operator $\rho = |\psi_0\rangle\langle\psi_0|$. This entanglement entropy as well as the more general Rényi entropies

$$S_\alpha(\rho_A) = \frac{1}{1-\alpha}\log(\mathrm{Tr}\,\rho_A^\alpha) \tag{3.5}$$

[14] In addition, first excited states of local Hamiltonians are typically local perturbations of the ground state, i.e. particles; see e.g. the discussion and references in [17].

[15] The *operator product expansion* (OPE) generalizes the product of two operators O_i, O_j as a sum of all possible operators O_k and coefficients c_{ij}^k, i.e. $\langle O_i(x_i)O_j(x_j)\rangle = \sum_k c_{ij}^k(x_i - x_j)\langle O_k(x_j)\rangle$.

quantify the amount of entanglement between the two subsystems. [16] In the continuum or in presence of gauge fields, the definition of reduced density matrices can lead to mathematical subtleties, which, however, will not be relevant for our subsequent spin chain calculations. An important characterization now is the scaling of the entanglement entropy with the size $|A|$ of asymptotically large subregions. For random states in the Hilbert space, there is an extensive scaling with the volume, $S(\rho_A) = \mathcal{O}(|A|)$. Ground states of local Hamiltonians behave, however, very special by satisfying an *area law*. In this case, the entanglement entropy scales with the boundary area of the region,

$$S(\rho_A) = \mathcal{O}(|\partial A|). \tag{3.6}$$

This is illustrated in Fig. 3.1 (left panel). Ground states of gapped QMB systems are believed to obey this area law generically. Specifically, this has been proven in [79] for any gapped quantum model with unique ground state in one dimension. In higher dimensions, the area law (3.6) implies $S(\rho_L) \sim L^{D-1}$ for a block of size L on a D-dimensional lattice. For specific models, such as gapped free fermionic or bosonic theories, this is explicitly proven and believed to hold for all models in any dimension. [17] MPS, which we will introduce below, are TN ansätze which satisfy this area law by construction and hence allow an accurate description of ground states in gapped models.

Critical (gapless) models show an important violation of the area law in one dimension. The entanglement entropy of critical spin systems scales as

$$S(\rho_A) = \mathcal{O}(\log(|A|)). \tag{3.7}$$

For example, at the critical point of the Ising model, which we will introduce in chapter 4, this scaling is valid for subregions of size $|A| = L \leq N/2$. Although this property violates the area law (3.6), the logarithmic correction is still mildly, i.e. exponentially smaller than the volume scaling in random states of the Hilbert space. In the CFT framework, the logarithmic divergence is given explicitly as [80]

$$S(\rho_L) = \frac{c}{3} \log\left(\frac{L}{a}\right) + \mathcal{O}(1), \tag{3.8}$$

where c is the central charge of the theory and a a UV cutoff, e.g. the lattice spacing. This scaling thus provides a way of deducing the central charge of an unknown but critical model. [18] In higher dimensions, the scaling of critical systems is not unique and known only for specific

[16] Observe that in the limit $\alpha \searrow 1$, $S_\alpha(\rho_A)$ reduces to $S(\rho_A)$.

[17] See [77] for detailed discussions and examples.

[18] For the general Rényi entropies, this formula is modified to $S_\alpha(\rho_L) = \frac{c}{6}\left(1 + \frac{1}{\alpha}\right) \log\left(\frac{L}{a}\right) + \mathcal{O}(1)$. Close to criticality, for a large but finite correlation length, the dependence is $S(\rho_L) \sim \frac{c}{6} \log\left(\frac{\xi}{a}\right)$.

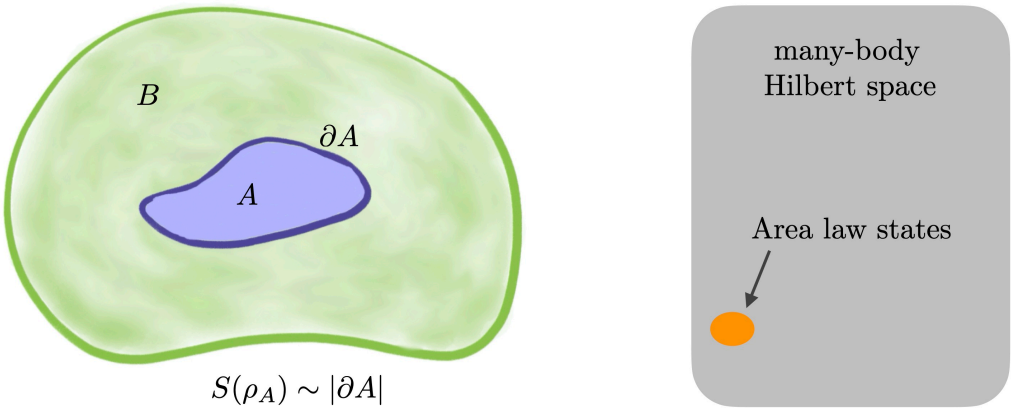

Figure 3.1: Left panel: The entanglement entropy of subregion A of a local system scales with its boundary area. Right panel: Area law states populate only an exponentially small physical corner of the entire Hilbert space.

models. [19] At finite temperature, it is known that mutual information satisfies an area law [81].

In summary, the locality of physical interactions has dramatic effects on the correlation and entanglement structure. Most of the entanglement is concentrated at the boundary of subregions. In [17], an intuitive understanding of this property is presented by observing that ground states of translationally invariant local Hamiltonians are fully determined by their extremal reduced density matrix, i.e. that one, which minimizes $E = \sum_i \mathrm{Tr}[h_{i,n}\rho_{i,n}] = \mathrm{Tr}[h_n\rho_n]$ (using the notation in (3.2)). Spins which correlate strongly with neighbors far away would destabilize the extremum and hence the entanglement should scale only with the boundary area of a bipartition. Physically relevant ground states and low excitations have much less entanglement than random states by satisfying an area law and therefore represent only an exponentially small subset of the enormous Hilbert space. This is sometimes denoted as the *physical corner of the Hilbert space* as illustrated in Fig. 3.1 (right panel). The aim and power of TNs is to define ansätze for wavefunctions of QMB states, which accurately capture the underlying entanglement structure, both for gapped and critical models.

We close this section by pointing out that area laws appeared already in other contexts in this introduction. The Bekenstein–Hawking formula (2.17) expresses the thermodynamic entropy of a BH as its event horizon area. As encapsulated in eq. (2.19), the holographic entanglement entropy formula of Ryu and Takayanagi is nothing else than a (minimal) area in the bulk of AdS spacetime. The latter is the holographic counterpart of the entanglement entropy in dual CFTs, defined in (2.18). As discussed in [82], entanglement entropy itself was found to represent a quantum correction to the BH entropy formula originating from matter fields. [20] In the limit when the boundary subsystem A in the holographic setting is chosen arbitrarily

[19] In fact, this logarithmic correction is even not always present. There are boson models satisfying an exact area law but which are critical, i.e. gapless. In other words, the converse of the expected area law for gapped states does not hold.

[20] On the other hand, it was shown in [83] that the one loop correction to holographic entanglement entropy is given by the bulk entanglement entropy between the two regions defined by the minimal surface.

large, the minimal surface tends to wrap around the BH horizon if an AdS geometry with event horizon is considered. The extensive contribution to it then represents the thermal BH entropy.

3.3 Tensor network diagrams

An arbitrary state vector $|\Psi\rangle$ in the tensor product Hilbert space $(\mathbb{C}^d)^{\otimes N}$ of a QMB system can be written as

$$|\Psi\rangle = \sum_{i_1,i_2,\ldots,i_N=1}^{d} \psi_{i_1,i_2,\ldots,i_N} |i_1\rangle \otimes |i_2\rangle \otimes \cdots \otimes |i_N\rangle , \tag{3.9}$$

where $\psi_{i_1,i_2,\ldots,i_N}$ are complex coefficients w.r.t. some basis vectors $|i_1\rangle, |i_2\rangle, \ldots, |i_N\rangle$. This exponentially large set of d^N coefficients can be interpreted as a tensor, which means a multi-dimensional array in this context. A diagrammatic notation, introduced originally by Penrose, allows to represent tensors graphically. For that purpose, the rank (or order) of the tensor denotes the dimensionality of the array. A tensor is then represented by a shape and outgoing edges stand for its indices given by the rank. Contractions (summations over all possible index values) between several tensors are represented by lines that connect the shapes. The following graph shows some elementary examples:

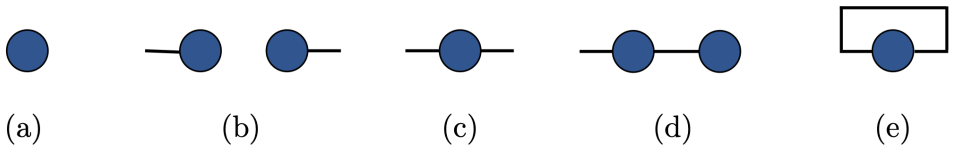

Here, (a) denotes a scalar (rank 0), (b) a vector and its dual (rank 1) and (c) visualizes a matrix (rank 2). In (d), the multiplication of a matrix with a vector is represented, while in (e) the trace of one single tensor is taken. Through this graphical notation, complicated expressions can be visualized in a very compact manner and we can refrain from explicitly writing out long tensorial equations.[21] Consequently, the wave function coefficients $\psi_{i_1,i_2,\ldots,i_N}$ are represented by a box with N edges for every physical index $i_1, i_2, \ldots, i_N$,

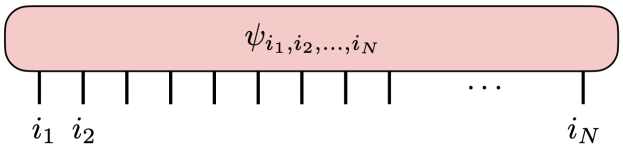

As it became apparent from the discussions in the previous chapters, the specification of all coefficients is computationally highly inefficient. Therefore, tensor networks aim for providing ansätze for the wave function that take the entanglement structure into account and reduce

[21] See, e.g., [13] for further examples and a detailed introduction to tensor operations.

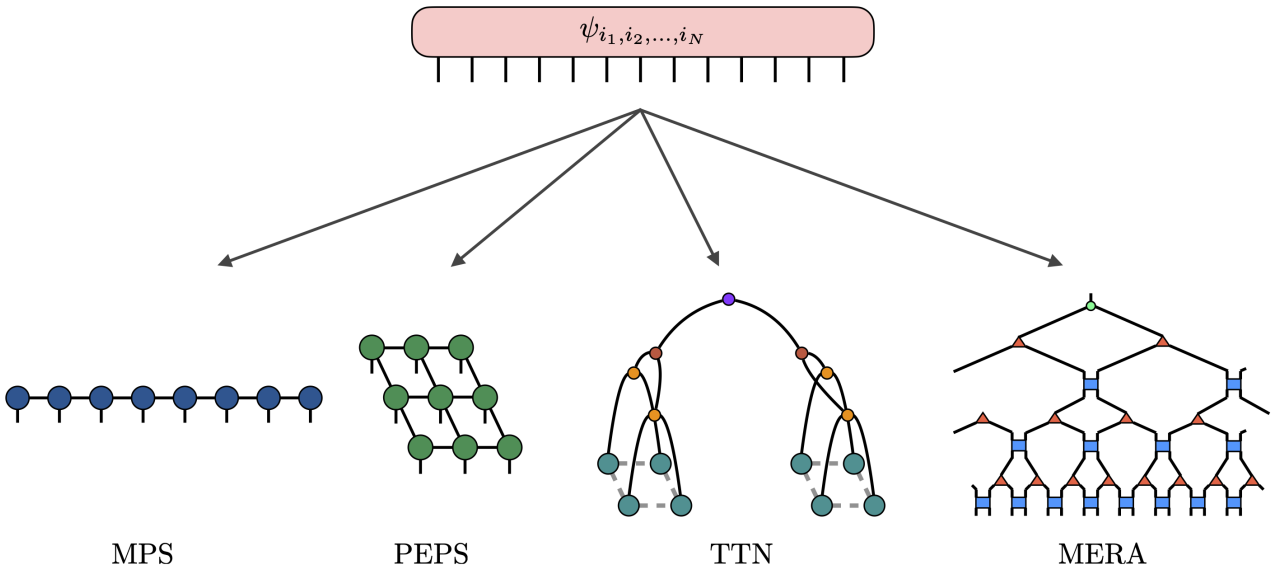

Figure 3.2: Basic idea of the tensor network ansatz and overview of tensor network diagrams: Tensor networks decompose the full wave function tensor into local tensors of lower rank. In $1D$, MPS and the MERA are examples. Projected entangled pair states (PEPS) are generalizations of MPS in $2D$. Tree tensor networks (TTN) can be extended to $2D$ (and higher).

the amount of parameters to a polynomial order. This is achieved by decomposing the full wave function tensor of rank N into a network of local tensors of lower order. *Tensor network diagrams* represent these ansätze graphically. Figure 3.2 shows some important examples in several spatial dimensions D. This procedure introduces auxiliary indices between the local tensors. Their dimension χ is called *bond dimension* and the total number of parameters is reduced to $\mathcal{O}(poly(N)poly(\chi))$ for an efficient representation. As we will demonstrate explicitly for MPS and the MERA below, both the geometric pattern of the TN and the bond dimension χ encode the entanglement structure of the QMB system and hence also parameterize the quantum correlations, ranging from product states ($\chi = 1$) up to the exact state ($\chi = d^N$). The full wave function $|\Psi\rangle$ is obtained by contracting the entire TN diagram, which gives a rank N tensor. This depends strongly on the order of the individual index summations and the optimal scheme needs to be found for every TN diagram type.

3.4 Matrix product states and operators

Matrix product states (MPS) make the following ansatz for the wave function coefficient

$$\psi_{i_1,i_2,\ldots,i_N} = A^{(1)}_{i_1} A^{(2)}_{i_2} \cdots A^{(N)}_{i_N}. \tag{3.10}$$

The full wave function (3.9) is decomposed into individual rank-3 tensors of the form $A^{(k)}_{\alpha\beta i_k}$ at every spatial position $k = 1, \ldots, N$, where the physical index i_k takes d values and α, β are

bond indices with χ entries. In (3.10), the contraction over the bond indices is implied. [22] In a TN diagram, this is represented as

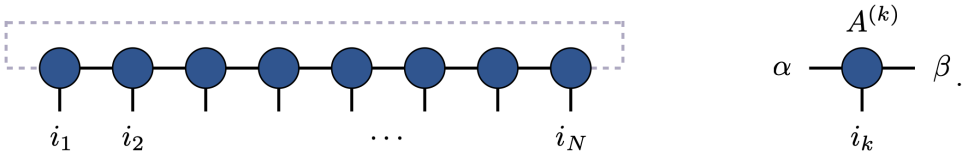

(3.11)

For a finite system with open boundary conditions, the first and last tensors are row and column vectors, respectively. If periodic boundary conditions are assumed, an overall trace is taken, which is represented by the grey dashed line in the TN diagram.

MPS play a major role for the numerical investigations in this thesis, as they are at the heart of several algorithmic approaches for TNs. From its ansatz, it becomes clear that MPS reduce the amount of variational parameters in the QMB wave function to an efficient polynomial level $\mathcal{O}(Nd\chi^2)$. For $\chi = 1$, product states are the simplest examples of MPS. [23] With (exponentially) increasing bond dimension, MPS lie dense in the full Hilbert space. From an alternative viewpoint, MPS can be introduced also as a preparation from maximally entangled pair states. In that picture one assumes two virtual systems on every lattice site, each one of it being maximally entangled with its neighbor, i.e. $|\phi_k\rangle = \sum_{i=1}^{d} |i_k i_k\rangle$. Upon acting with a projector $\mathcal{P}^{(k)} = \sum_{\alpha,\beta,i_k} A_{\alpha\beta i_k} |i_k\rangle \langle\alpha\beta|$ on every pair, one recovers the state (3.10). The same construction yields the PEPS tensor network in $2D$, c.f. Fig. 3.2.

We now describe some of the characteristic properties of the MPS ansatz. Most importantly, a one-dimensional area law is satisfied. From the representation (3.11) this becomes clear by constructing the pure state density matrix $|\Psi\rangle \langle\Psi|$. A definition of a subsystem A of length L cuts the bond indices twice and thus one has

$$S(\rho_L) \leq \log(\chi^2) = 2\log(\chi), \tag{3.12}$$

which is simply a constant, i.e. $S(\rho_L) \sim L^0$. From our previous discussion in section 3.2 we therefore conclude that MPS accurately describe ground and low excited states of gapped local Hamiltonians. More generally, any state satisfying an area law, and under the mild assumption $S_\alpha(\rho_L) \lesssim \log(N)$ for Rényi entropies with $\alpha < 1$, can be well approximated by MPS. [24] In the inverse direction, it can be shown that any arbitrary MPS of the form (3.10) is the ground state of a local gapped *parent Hamiltonian* [17].

Another important property of MPS is the exponential decay of correlation functions. For

[22] For every fixed value of the physical index i_k, this is a product of matrices, hence the name MPS.
[23] See, e.g., [13,17] for further analytical examples of MPS with finite bond dimension.
[24] This means $\chi \sim poly(N)$. See [17] for extended discussions.

this, we introduce the transfer operator

$$\mathbb{E}_O = \sum_{i,j=1}^{d} \langle i|\, O\, |j\rangle\, (A_i \otimes \bar{A}_j) \quad =$$

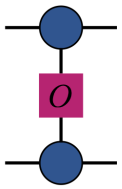

. (3.13)

If O is the identity, we denote the transfer matrix as $\mathbb{E}_I$. Assuming a translationally invariant state, powers of $\mathbb{E}_I$ are given by

$$\mathbb{E}_I^k = |r_1\rangle\langle l_1| + \sum_{j=2}^{\chi^2} \lambda_j^k\, |r_j\rangle\langle l_j|\,, \tag{3.14}$$

where λ_j are eigenvalues of $\mathbb{E}_I$ in decreasing order, $|r_j\rangle$, $\langle l_j|$ are right- and left-eigenvectors (defined by the oriented action of $\mathbb{E}_I$ onto them), and we have chosen the normalization $\lambda_1 = 1$. In the thermodynamic limit, correlation functions follow as

$$\begin{aligned}
\langle O_A O_B\rangle &= \langle l_1|\, \mathbb{E}_{O_A} \mathbb{E}_I^{\mathrm{dist}(A,B)-1} \mathbb{E}_{O_B}\, |r_1\rangle \\
&= \langle l_1|\, \mathbb{E}_{O_A}\, |r_1\rangle\, \langle l_1|\, \mathbb{E}_{O_B}\, |r_1\rangle + \sum_{j=2}^{\chi^2} \lambda_j^{\mathrm{dist}(A,B)-1}\, \langle l_1|\, \mathbb{E}_{O_A}\, |r_j\rangle\, \langle l_j|\, \mathbb{E}_{O_B}\, |r_1\rangle \\
&= \langle O_A\rangle\langle O_B\rangle + \sum_{j=2}^{\chi^2} \lambda_j^{\mathrm{dist}(A,B)-1}\, \langle l_1|\, \mathbb{E}_{O_A}\, |r_j\rangle\, \langle l_j|\, \mathbb{E}_{O_B}\, |r_1\rangle\,.
\end{aligned} \tag{3.15}$$

We therefore recover the exponential decay of correlation functions (3.3) in gapped models. The correlation length is identified as $\xi^{-1} \equiv -\log|\lambda_2|$. Algebraically decaying correlations (3.4) as in critical models cannot be captured, unless the bond dimension is large enough and only small spatial separations are considered.

A state defined by the MPS ansatz (3.10) is not uniquely specified. One can perform a gauge transformation by inserting an identity $I = XX^{-1}$ on the bond indices for any invertible matrix X. In a TN diagram, this is represented as

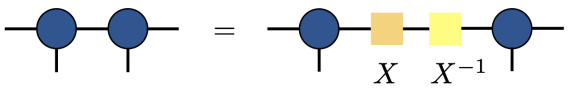

. (3.16)

This gauge freedom allows to define a convenient canonical form of the MPS. In this representation every bond index α labels the Schmidt decomposition of a state $|\Psi\rangle$ across that bond into a left and right part,

$$|\Psi\rangle = \sum_{\alpha=1}^{\chi} \lambda_\alpha\, |\Psi_\alpha^L\rangle \otimes |\Psi_\alpha^R\rangle\,, \tag{3.17}$$

where the Schmidt values $\lambda_\alpha \geq 0$ are ordered decreasingly and satisfy $\sum_\alpha \lambda_\alpha^2 = 1$ from the state

normalization. The $\{|\Psi_\alpha^{L,R}\rangle\}$ form an orthonormal basis. In this form, the MPS coefficients take the form

$$\psi_{i_1,i_2,\ldots,i_N} = \Gamma^{(1)}_{i_1}\lambda^{(1)}\Gamma^{(2)}_{i_2}\lambda^{(2)}\cdots\Gamma^{(N)}_{i_N}\lambda^{(N)}, \tag{3.18}$$

where bond indices are again suppressed. Here, the tensors $\lambda^{(k)}_{\alpha_k}$ contain the Schmidt values and the tensors $\Gamma^{(k)}_{\alpha_{k-1}\alpha_k i_k}$ realize a change between physical spin basis and Schmidt basis. If the MPS is infinite ($N = \infty$) but possesses a translational symmetry, it suffices to consider the unit cell, i.e. the minimal set of tensors that are repeating. For a 1-site translationally invariant MPS, the form (3.18) is then represented as

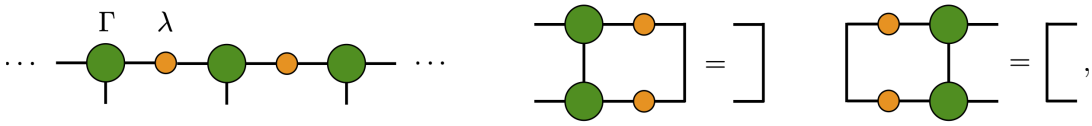

(3.19)

where the second and third diagram define the right- and left-canonical property of the tensors. In a finite size MPS, this canonical form is achieved by performing the Schmidt decomposition successively, i.e. between physical indices $\{1\}$ and $\{2,\ldots,N\}$, then between $\{2\}$ and $\{3,\ldots,N\}$ and so on, cf. the following pictorial representation

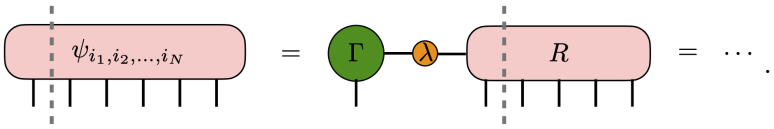

(3.20)

The Schmidt decomposition can be realized computationally by a singular value decomposition (SVD) as indicated by the grey dashed line. A SVD decomposes a matrix M as $M = USV^\dagger$, where U and V are unitary and S contains the singular values on the diagonal in decreasing order, which, upon normalization, agree with the Schmidt coefficients. Applications of SVDs are very important in TN algorithms in the next section, because a *truncation* of small singular values is known to be the best low-rank approximation of the original matrix [84]. Explicit canonicalization algorithms are also known for the unit cell of infinite MPS, see e.g. [11].

The framework presented so far can be easily extended to represent not only states but also operators. Such a matrix product operator (MPO) is defined as

$$O = \sum_{\substack{i_1,i_2,\ldots,i_N=1\\ j_1,j_2,\ldots,j_N=1}}^{d} A^{(1)}_{i_1 j_1}A^{(2)}_{i_2 j_2}\cdots A^{(N)}_{i_N j_N}\,|i_1\rangle\otimes|i_2\rangle\otimes\cdots\otimes|i_N\rangle\,\langle j_1|\otimes\langle j_2|\otimes\cdots\otimes\langle j_N|\,, \tag{3.21}$$

where summation over bond indices is implied. The tensors $A^{(k)}_{\alpha\beta i_k j_k}$ have now two physical indices corresponding to the bra and ket operation. The corresponding TN diagram is

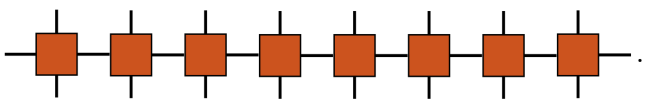

While MPS can represent pure states, MPOs allow to encode also Hamiltonians and mixed states, in particular the thermal density matrix $\rho_\beta \equiv \mathrm{e}^{-\beta H} / \operatorname{Tr}(\mathrm{e}^{-\beta H})$.

3.5 Tensor network algorithms

Apart from a correct capture of entanglement properties of QMB systems, the power of TNs is rooted in the existence of efficient algorithms to calculate ground, low excited and thermal states of local model Hamiltonians as well as performing their time evolution. We describe in this section the relevant aspects for MPS and MPO algorithms which we employ in the field theory studies in part II. We implemented these algorithms in the `Julia` language and make them available in [85].

3.5.1 DMRG

The DMRG as invented by White in [76] is a numerical RG method which allows the calculation of ground states of local lattice systems. It became later reformulated as a variational method for MPS as extensively reviewed in [10]. We describe here the latter interpretation for finite systems with open boundary conditions. [25]

In the variational ansatz, the ground state of a Hamiltonian H minimizes the energy

$$E = \frac{\langle\Psi|H|\Psi\rangle}{\langle\Psi|\Psi\rangle}. \tag{3.22}$$

Introducing a Lagrange multiplier λ, this expression is minimized by solving

$$\min_{|\Psi\rangle\in\mathrm{MPS}} \left(\langle\Psi|H|\Psi\rangle - \lambda \langle\Psi|\Psi\rangle\right), \tag{3.23}$$

where the second term ensures the normalization of the state, and one makes use of the fact that a Hamiltonian of the form (3.2) (with an implied tensor product structure) can be represented as a MPO of the form $H = M^{(1)}M^{(2)}\cdots M^{(N)}$ by defining operator-valued matrices $M^{(k)}_{\alpha\beta} = \sum_{i_k,j_k} A^{(k)}_{\alpha\beta i_k j_k} |i_k\rangle \langle j_k|$ from (3.21). [26] Due to the matrix product structure of $|\Psi\rangle$, this optimization problem is highly-nonlinear for a system of N sites. In the DMRG it is therefore tackled iteratively: The algorithm proceeds by optimizing a single MPS site $A^{(k)}_{\alpha\beta i_k}$ while keeping all others fixed. Starting from one side, the minimization is continued by sweeping site by site through the chain (back and forth) and updating the individual tensors

[25] The DMRG algorithm can also be extended to infinite translational invariant systems and to study time evolution, see the same review [10]. Periodic boundary conditions do not yield such a simple eigenvalue problem as discussed here, but can be implemented too, see e.g. [9].

[26] The individual entries can be easily constructed for a chosen (spin) Hamiltonian. Reversely, the multiplication of the operator matrices reconstructs the tensor product sum (3.2).

by solving

$$\min_{A^{(k)}} \left(\langle \Psi | H | \Psi \rangle - \lambda \langle \Psi | \Psi \rangle \right) = \min_{A^{(k)}} \left(A^{(k)\dagger} H_{eff} A^{(k)} - \lambda A^{(k)\dagger} N_{eff} A^{(k)} \right). \tag{3.24}$$

Here, the effective Hamiltonian H_{eff} and normalization N_{eff} are constructed from $\langle \Psi | H | \Psi \rangle$ and $\langle \Psi | \Psi \rangle$ by removing the tensors $A^{(k)}$ and $A^{(k)\dagger}$, respectively. Requiring that the derivative of the right side of (3.24) w.r.t. $A^{(k)\dagger}$ vanishes, the minimization is realized for the solution of the generalized eigenvalue problem [27]

$$H_{eff} A^{(k)} - \lambda N_{eff} A^{(k)} = 0. \tag{3.25}$$

In practice, one can assure $N_{eff} \equiv \mathbb{1}$ by keeping the MPS in a mixed-canonical form, i.e. left-canonical for sites $i < k$ and right-canonical for $i > k$, as defined by (3.19). In diagrammatic form, the minimization of a single site (shown in green) is hence the solution of the following equation

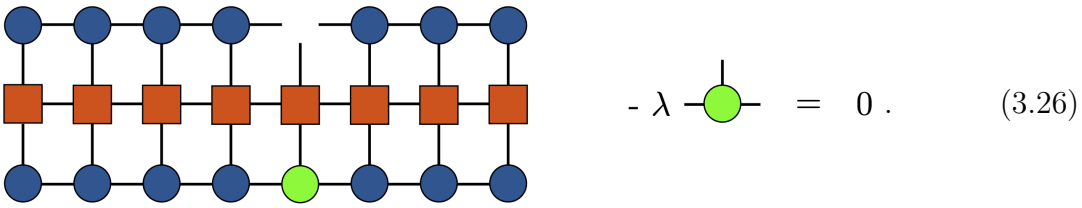

(3.26)

The eigenvalue problem is of size $(d\chi^2 \times d\chi^2)$ and the sweeping procedure is iteratively continued until convergence is reached, which can be numerically controlled by the variance $\langle \Psi | H^2 | \Psi \rangle - \langle \Psi | H | \Psi \rangle^2 \to 0$ for high enough bond dimension χ. The final minimum yields the ground state $|\Psi_0\rangle$ and its energy $E_0 \equiv \lambda_{min}$ with a very high precision, which made the DMRG to one of the leading simulation methods for strongly correlated systems in $1D$. By extension, one can also easily determine excited states by introducing further Lagrange multipliers. For example, the first excited state $|\Psi_1\rangle$ follows from solving the minimization

$$\min_{|\Psi_1\rangle \in \mathrm{MPS}} \left(\langle \Psi_1 | H | \Psi_1 \rangle - \lambda \langle \Psi_1 | \Psi_1 \rangle - \mu \langle \Psi_1 | \Psi_0 \rangle \right), \tag{3.27}$$

where the last term ensures orthogonality. Since the bond dimension limits the amount of entanglement, this allows to iteratively determine the lowest excited states.

3.5.2 TEBD

The real-time evolution of a pure state $|\Psi\rangle$ is given by the application of the unitary time evolution operator U on some initial state as

$$|\Psi(t)\rangle = \mathrm{e}^{-itH} |\Psi(t=0)\rangle \equiv U(t) |\Psi(t=0)\rangle. \tag{3.28}$$

[27] Note that H_{eff} is interpreted here as a matrix and $A^{(k)}$ as a vector through reshaping of the tensor indices.

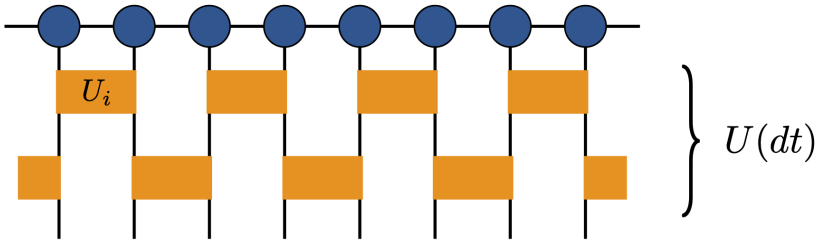

Figure 3.3: Representation of one discretized time evolution step in the TEBD algorithm [86,87]. Based on the first-order Suzuki-Trotter decomposition, the 2-site time evolution operators $U_i(dt)$ are applied on all odd sites in the first row and then on all even sites in the second row, constructing together the total evolution operator $U(dt)$.

In the language of TNs, this time evolution can be implemented based on a time discretization $t = n\,dt$ with $n \to \infty, dt \to 0$. In view of the studied models in part II, we restrict ourselves now to nearest-neighbor interactions, i.e. $H = \sum_i h_{i,i+1}$. The infinitesimal time evolution operator $U(dt)$ then can be split into a product of 2-site gates via a Suzuki-Trotter decomposition (see [88] and references therein). The first-order approximation takes the form

$$U(dt) = \mathrm{e}^{-i\,dtH} = \mathrm{e}^{-i\,dth_{1,2}}\,\mathrm{e}^{-i\,dth_{2,3}} \cdots \mathrm{e}^{-i\,dth_{N-1,N}} + \mathcal{O}(dt^2). \tag{3.29}$$

The Trotter error of order $\mathcal{O}(dt^2)$ originates from the noncummutativity of two successive terms $[h_{i,i+1}, h_{i+1,i+2}] \neq 0$. Vidal's *time-evolving block decimation* algorithm (TEBD) [86,87] exploits the fact that all terms $h_{i,i+1}$ with odd and even i are all commuting among each other, respectively. The time evolution is therefore discretized as $U(dt) = \mathrm{e}^{-i\,dtH_{odd}}\,\mathrm{e}^{-i\,dtH_{even}} + \mathcal{O}(dt^2)$. [28] Fig. 3.3 shows how this operator is applied to a finite size MPS with initial bond dimension χ. The orange blocks denote the incremental 2-site operators $U_i(dt) \equiv \mathrm{e}^{-i\,dth_{i,i+1}}$, which are applied to all odd sites in the first row and then to all even sites in the next layer. A single update consists of the following steps, yielding two new MPS tensors

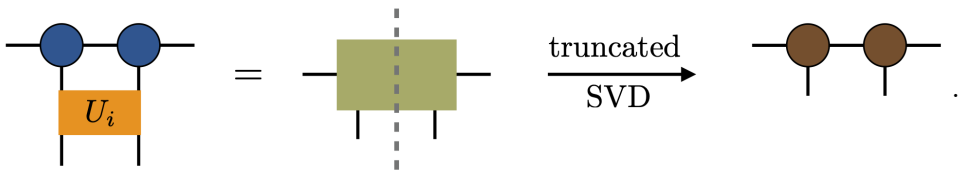

Here, the the time evolution operator $U_i(dt)$ is contracted into two MPS tensors at positions i and $i+1$. The resulting rank-4 tensor is split into the new MPS tensors via a SVD. This increases the bond dimension from χ to $d^2\chi$. To avoid the exponential growth of the tensor sizes in the overall quantum circuit with $n \gg 1$, a truncation is performed, i.e. the smallest singular values λ_α in the SVD are disregarded, giving rise to a truncation error $\epsilon = \sum_{\alpha > \chi_{max}}^{d^2\chi} \lambda_\alpha^2$ for a chosen maximal bond dimension χ_{max}.

[28] As an extension, the second-order Suzuki-Trotter decomposition reduces the error as $U(dt) = \mathrm{e}^{-i\,dtH_{odd}/2}\,\mathrm{e}^{-i\,dtH_{even}}\,\mathrm{e}^{-i\,dtH_{odd}/2} + \mathcal{O}(dt^3)$.

Interesting physical Hamiltonians introduce correlations between the constituents. Due to the resulting entanglement growth in QMB states under real-time evolution, ϵ is in general increasing for fixed χ_{max}. Alternatively, the latter can be increased dynamically to capture the entanglement content of the MPS. While the exact result is valid for $\chi_{max} \to \infty$, $\epsilon \to 0$, the achievable time scales are in practice limited for finite χ_{max} and sufficiently small ϵ. This very important property conceptually limits the predictive power of TN simulations.

The described TEBD algorithm is not restricted to real-time evolution. Analogously, one can perform imaginary time evolution, which allows to construct the (non-degenerate) ground state $|\Psi_0\rangle$ of a given Hamiltonian from any random initial state as

$$|\Psi_0\rangle = \lim_{\tau\to\infty} \mathrm{e}^{-\tau H} |\Psi(\tau = 0)\rangle \,. \tag{3.30}$$

In this case, the 2-site gates $U_i(d\tau) \equiv \mathrm{e}^{-d\tau h_{i,i+1}}$ are close to the identity operator for small enough imaginary time step $d\tau = \tau/n$, such that still a faithful truncation can be performed. From the eigenvalue decomposition $\mathrm{e}^{-\tau H} = \sum_k \mathrm{e}^{-\tau E_k} |e_k\rangle \langle e_k|$ in terms of energy eigenstates, it can be seen that the convergence is exponentially fast w.r.t. to the energy gap $\Delta E = E_1 - E_0$. In the limit $\Delta E \to 0$ of an infinite chain, the bond dimension has to grow indefinitely, $\chi_{max} \to \infty$, to represent the ground state correctly ($\epsilon \to 0$). In a gapless (critical) model, this leads to the concept of finite entanglement scaling [89] when in practice a finite χ_{max} and ϵ are chosen. This means that the entanglement entropy of a semi-infinite bipartition scales as $S(\rho_A) \sim \log(\chi_{max})$, from which the central charge of the underlying CFT can be deduced [90]. [29]

Imaginary time evolution can be also used to construct a thermal state $\rho_\beta \equiv \mathrm{e}^{-\beta H}$ of inverse temperature $\beta = 1/T$ [9,10]. This makes use of the fact that in general any mixed state ρ_X in some physical space X can be derived from a purification as $\rho_X = \mathrm{Tr}_Y |\Psi\rangle \langle\Psi|$, where the partial trace is taken over a ancillary state space Y of a pure state $|\Psi\rangle$ defined on XY. To find a MPO approximation of ρ_β, we rewrite its definition as

$$\rho_\beta \equiv \mathrm{e}^{-\beta H} = \mathrm{e}^{-\beta/2 H} \cdot \mathbb{1} \cdot \mathrm{e}^{-\beta/2 H}, \tag{3.31}$$

where the auxiliary system is just a copy of the physical state space. It therefore suffices to construct the operator $\rho_{\beta/2}$ as a MPO by performing imaginary time evolution on the identity operator, which is an exact MPO with unit bond dimension. [30] This can be implemented by the same TEBD algorithm as discussed before. For that, the identity MPO can be vectorized into MPS form with physical dimension d^2 and the imaginary time evolution can be performed

[29] Real and imaginary time evolution of MPS can also be performed as a variational method based on the DMRG algorithm. For subtle connections and differences to TEBD see [9,10].

[30] Observe that this also gives a square root computational improvement. As discussed in more detail in [9,10], the identity MPO as the infinite temperature density operator can also be seen as a maximally entangled state between the system and ancilla, written as a tensor product of maximally entangled pairs for each site in the system.

w.r.t. the Hamiltonian $H \otimes \mathbb{1}$, where the second term refers to the ancilla. The full thermal operator ρ_β then follows from its purification $\rho_{\beta/2}$ (which represents the thermofield double (TFD) state upon vectorization) as $\rho_\beta = \rho_{\beta/2}\rho_{\beta/2}^\dagger$. By keeping the state in its canonical form, the TEBD algorithm ensures the normalization $\mathrm{Tr}\,\rho_\beta = \mathrm{Tr}[\rho_{\beta/2}\rho_{\beta/2}^\dagger] = 1$. Operator expectation values follow from the purification as $\langle O\rangle_\beta = \mathrm{Tr}[\rho_\beta O] = \mathrm{Tr}[\rho_{\beta/2}\rho_{\beta/2}^\dagger O]$.

3.5.3 iTEBD

For a translational invariant Hamiltonian, one can work directly in the thermodynamic limit $N \to \infty$ by considering the elementary unit cell, which is repeating within the MPS or MPO. In the case of nearest-neighbor interactions under consideration, this simply consists of two sites. The *infinite time-evolving block decimation* algorithm (iTEBD) [91] makes use of this feature to generalize the real- or imaginary-time evolution to infinite systems. The Schmidt values of a semi-infinte bipartition of the system are properly taken into account by working in the MPS definition (3.18) using the Γ and λ tensors.

Fig. 3.4 shows how a single time evolution update is performed. In the first step (i) the 2-site gate U_i is contracted into two MPS sites, labelled by A and B, consisting of tensors Γ_A, λ_A and Γ_B, λ_B, yielding a rank-4 tensor Θ, which then is split in step (ii) by a SVD into $\Theta = X\tilde{\lambda}_A Y$. The singular values $\tilde{\lambda}_A$ are contracted up to the maximal bond dimension, representing the new Schmidt values across the link of site A. By inserting two identities $\mathbb{1} = \lambda_B\lambda_B^{-1}$ as shown in (iii), one gets the new MPS sites $\tilde{\Gamma}_A, \tilde{\Gamma}_B$, cf. (iv). This single update can be seen as the odd part of the Hamiltonian, and the full iTEBD step is completed by repeating these tensor operations for the swapped updated sites of B and A.

As described previously for the finite size case, the iTEBD algorithm can be used equally for real- and imaginary time evolution, in particular also to construct thermal MPOs. Obviously, it provides the advantage of avoiding finite size effects. As described in detail in [92], the iTEBD methods can be modified to include also non-unitary (time) evolutions, which rest upon a proper canonicalization procedure to ensure a faithful truncation of the state.

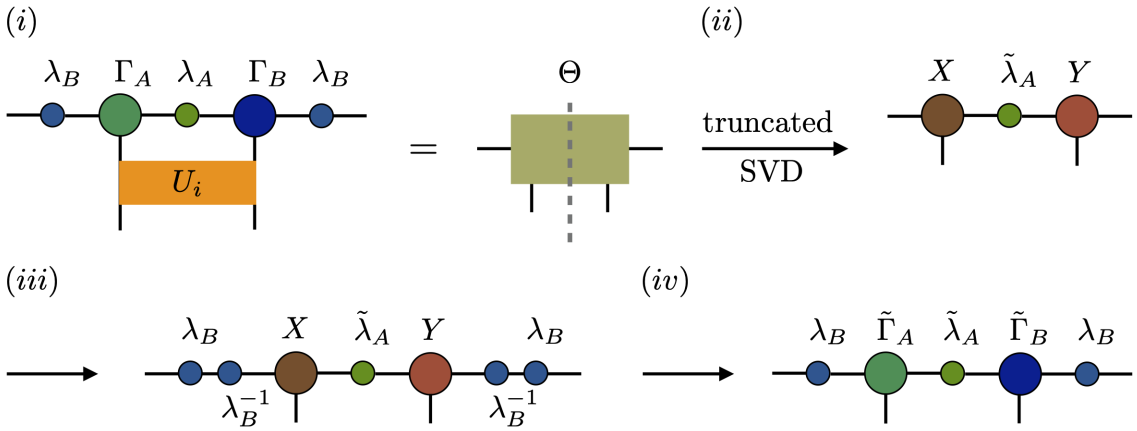

Figure 3.4: Representation of one discretized time evolution step in the iTEBD algorithm [91]. Based on the first-order Suzuki-Trotter decomposition, the 2-site time evolution operator U_i (real or imaginary) is absorbed into two MPS sites A and B, yielding two new sites by the shown steps $(i - iv)$.

3.6 The multiscale entanglement renormalization ansatz

In section 3.2 we emphasized the importance of the entanglement structure to capture the physics of QMB systems. Another major physical concept is given by the seminal work of Wilson [93], which introduced the RG paradigm. While particle physics calculations based on Feynman diagrams typically operate in momentum space, Kadanoff's block spin transformation [94] can be seen as a real-space realization of a RG transformation. It was originally applied to the classical $2D$ Ising model and unveiled that that its critical point is a fixed point of the RG transformation with correlations on all length scales, i.e. diverging correlation length. This introduced the important concept of *universality* to describe (very different) systems at macroscopic length scales and critical phenomena. The MERA, introduced by Vidal in [42], is based on the concept of entanglement renormalization [95], which combines these two principles. In summary, the MERA is a variational tensor network ansatz that combines a real-space RG approach on a lattice with a disentangling transformation to reduce the amount of entanglement in ground state wave functions of local QMB systems. We here follow the reviews and introductions [96–98] to explain the underlying ideas to make this statement precise.

The starting point of the construction is a one-dimensional lattice $\mathcal{L}_0$ with N sites, c.f. Fig. 3.5. As before, we are interested in describing pure states in the Hilbert space $\mathcal{H}_{\mathcal{L}_0} \simeq (\mathbb{C}^d)^{\otimes N}$. In a RG group picture, the MERA assembles $\tau = 1, 2, \ldots, T$ layers of a coarsegraining transformation in the vertical direction of the tensor network representation. In each layer, the number of lattice sites is exponentially decreased as $N2^{-\tau}$, defining a sequence of lattices

$$\mathcal{L}_0 \to \mathcal{L}_1 \to \mathcal{L}_2 \to \cdots \to \mathcal{L}_T. \tag{3.32}$$

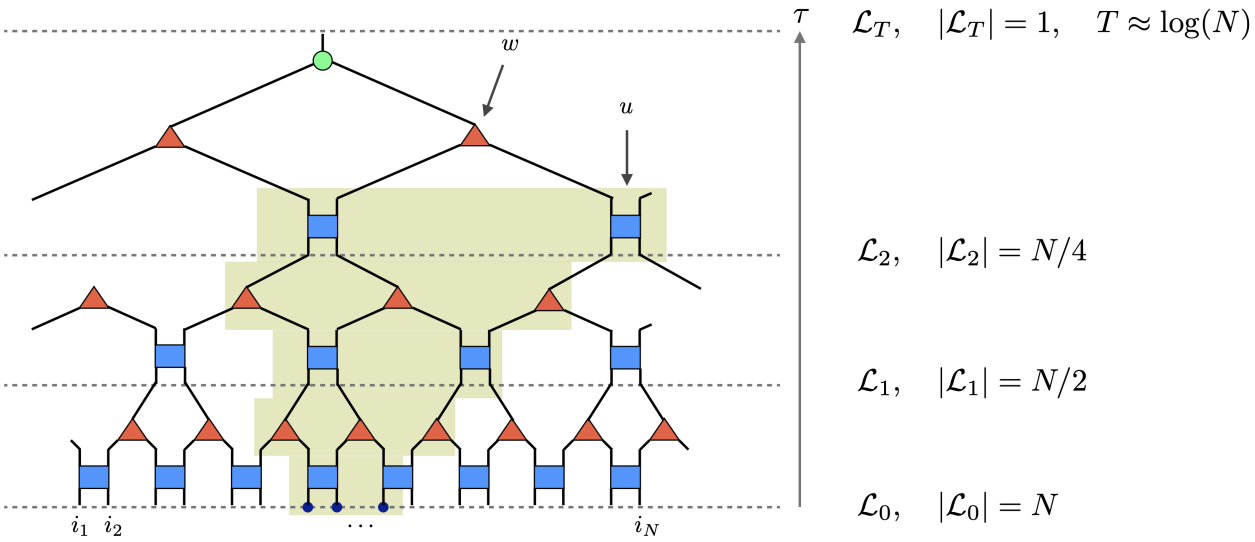

Figure 3.5: Tensor network representation of the binary MERA. The quantum circuit consists of two type of tensors, disentanglers u and isometries w, which successively implement a coarsegraining transformation, starting from an original lattice $\mathcal{L}_0$ with N sites towards the τ direction, representing the RG flow. The past causal cone of three selected sites is shown up to the second level as the shaded region.

By construction, the maximal coarsegraining is achieved after $T \approx \log_2(N)$ steps. A single coarsegraining layer is build up of two rows of different tensors, disentanglers u and isometries w. The isometries perform the actual coarsegraining transformation by blocking two sites together, while the function of disentanglers is to reduce the amount of short range entanglement in the system. The defining properties of these operators are [31]

$$w^\dagger w = \mathbb{1} \qquad \text{and} \qquad u^\dagger u = u u^\dagger = \mathbb{1}, \tag{3.33}$$

or graphically

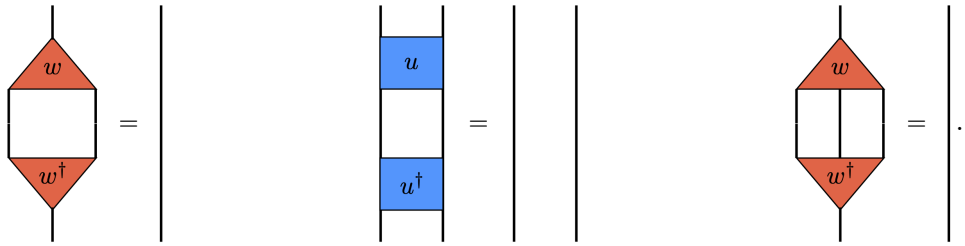

(3.34)

The entanglement renormalization step is realized by the isometric operator W_τ shown in Fig. 3.6, comprising one layer of the tensor network. It maps pure states on a lattice $\mathcal{L}_{\tau-1}$ to pure states on the succeeding coarsegrained lattice $\mathcal{L}_\tau$, that is $|\Psi_\tau\rangle = W_\tau^\dagger |\Psi_{\tau-1}\rangle$, giving rise

[31] Note that for the isometry $ww^\dagger \neq \mathbb{1}$ holds.

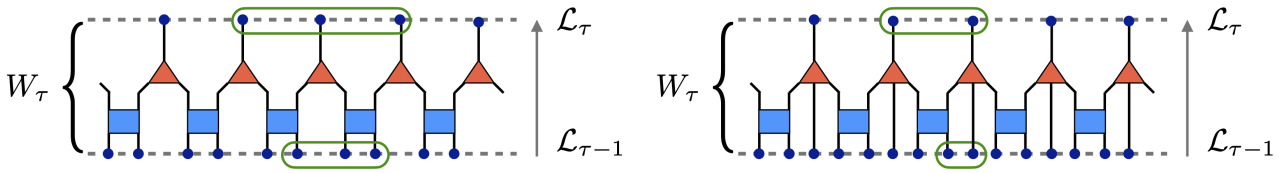

Figure 3.6: Form of the isometric operator W_τ implementing a RG transformation from the lattice $\mathcal{L}_{\tau-1}$ to $\mathcal{L}_\tau$ in the binary (left panel) and ternary (right panel) MERA. The green ovals mark the number of sites on which operators need to act to preserve locality.

to a sequence of coarsegrained states

$$|\Psi_0\rangle \to |\Psi_1\rangle \to |\Psi_2\rangle \to \cdots \to |\Psi_T\rangle \tag{3.35}$$

in the MERA tensor network. A state $|\Psi_0\rangle$ on $\mathcal{L}_0$ hence follows from the composition $|\Psi_0\rangle = W_1 W_2 \cdots W_T |\Psi_T\rangle$. By acting with the operator $W_\tau^\dagger$ on a state $|\Psi_{\tau-1}\rangle$, the function of the unitary disentanglers is in the first step the transformation into a product state as $|\Psi_{\tau-1}\rangle \mapsto |\Psi'_{\tau-1}\rangle \otimes |l\rangle$. This approach assumes that the entanglement structure is arranged in different length scales due to the locality of physical interactions, such that $|l\rangle$ contains partially decoupled local degrees of freedom. In the next step, the isometries block two sites together, yielding the lattice $\mathcal{L}_\tau$. This procedure leaves a considerable amount of freedom. In particular, we have introduced so far the *binary* MERA, in which the isometries block two sites together. As one alternative, a *ternary* MERA can be defined, in which three sites are blocked together. The right side of eq. (3.34) shows the defining property of the corresponding isometric w tensor, and the form of the coarsegraining operator is visualized in the right panel of Fig. 3.6. [32]

From the coarsegraining perspective, the MERA defines a tensor network with the fictitious time direction τ, which represents the RG flow as shown in Fig. 3.5. It is however equally valid to read this tensor network from top to bottom. In this scenario, the MERA can be seen as an implementation of a quantum circuit. The isometries are hereby seen as originating from a rank-4 unitary tensor, in which one index is in a fixed state $|0\rangle$ as follows

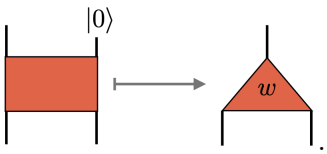

An initial product state $|\Psi_T\rangle = |0\rangle^{\otimes N}$ is then transformed into $|\Psi_0\rangle$ by the MERA circuit.

Apart from coarsegraining states, the MERA also can be used to consider the RG flow of operators. Under the action of W_τ, a local operator $o_{\tau-1}$ is transformed as $o_\tau = W_\tau^\dagger o_{\tau-1} W_\tau$.

[32] In the ternary MERA, some of the calculations considerably simplify. We therefore partially use this form of the ansatz for the following explanations. Depending on the choice, the logarithms appearing in Figs. 3.5, 3.7 and 3.8 have either base 2 or 3.

An important property of this mapping is the preservation of locality. As indicated in Fig. 3.6, the binary MERA maps 3-site operators to 3-site operators, while in the ternary case the same holds for 2-site operators, irrespective of the relative lattice position. Most relevantly, if a model with a local bare Hamiltonian H_0 of the form (3.2) is considered, then a sequence of local Hamiltonians is constructed as $H_0 \to H_1 \to \cdots \to H_T$. Similarly to the state sequence (3.35), the coarsegraining of the microscopic degrees of freedom describes the RG flow towards lower energies (or larger length scales).

The individual tensors w and u of the total tensor network $|\Psi\rangle$ are determined by minimizing the energy $\langle\Psi| H_0 |\Psi\rangle$ of the system. The reason that the individual expectation values $\langle\Psi| h_{i,n} |\Psi\rangle$ can be efficiently calculated is that past causal cones have bounded width. The past causal cone is the set of all tensors within the MERA circuit that can affect a set of chosen sites. In Fig. 3.5 an example is shown for three selected sites by the shaded region. It can be observed that the past causal cone never exceeds the size of three isometries and two disentanglers in every layer, independent of the system size N and the relative lattice position. Due to the constraint (3.34), all tensors outside the causal cone annihilate to the identity when calculating an expectation value of the form $\langle\Psi| h_{i,n} |\Psi\rangle$. As described in full detail in [96], the necessary contractions can be performed efficiently with a computational cost polynomial in the bond dimension χ. [33] The explicit entries of the isometries and disentanglers are found algorithmically by minimizing the energy iteratively. The MERA is therefore a variational TN ansatz for the ground state wave function. In contrast to Kadanoff's block spin transformation mentioned above, the RG flow in the MERA is more faithful, because short-range entanglement is removed under the action of the Hamiltonian. As an alternative to this "traditional" approach, the tensor network renormalization (TNR) algorithm of [99,100] introduced a sequential coarsegraining transformation for a uniform TN preparing the Euclidean path integral of a QMB system. The insertion of optimized disentanglers and unitaries then yields the MERA for the groundstate. [34]

For the following discussion, it is important to take symmetry considerations into account. The MERA is called *translational invariant* if the isometries and disentanglers in any chosen layer of the TN are identical. [35] Similarly, *scale invariance* is present if all layers in the circuit are identical. Considering a physical model at its quantum critical point, the Hamiltonian flow following from the variational energy minimization takes the form

$$H_0 \to H_1 \to \cdots \to H_t \to H^* \to \frac{1}{\Lambda} H^* \to \frac{1}{\Lambda^2} H^* \to \cdots . \tag{3.36}$$

[33] The tensors at the layer $\mathcal{L}_0$ have a size set by the physical dimension $\chi_0 = d$. The bond dimension χ_τ in all intermediate layers is a free parameter impacting the accuracy of the result. In the description of pure states, as we assumed so far, the top tensor has size $\chi_T = 1$.

[34] This procedure will be relevant in the context of our complexity studies for the path integral optimization program. We describe these details in section 9.2.

[35] Note that this in general does not imply that also a state defined on arbitrary sublattices is translational invariant, since lattice sites in the TN are in different relative positions w.r.t. each other.

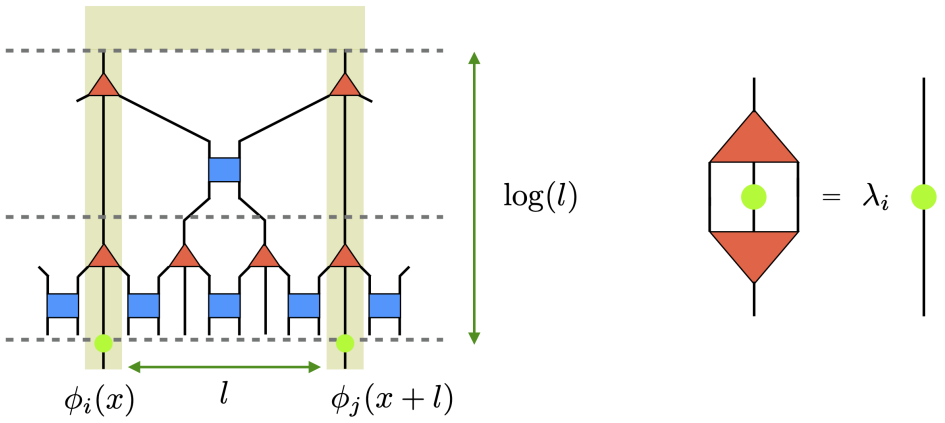

Figure 3.7: In a scale invariant MERA, scaling operators ϕ_i are given as eigenvectors of the scaling superoperator S, which is composed of two isometries in the ternary ansatz (right panel). The two-point correlation function $\langle\phi_i(x)\phi_j(x+l)\rangle$, with operator insertions at the shown specific locations with distance l in the lattice, has a very narrow past causal cone of only one site (left panel). After $\log(l)$ coarsegraining steps, these sites are neighboring, causing a polynomial decay of the correlator.

Here, the scale invariant Hamiltonian H^* represents the fixed point of the RG flow, which is (approximately) achieved after t transitional layers, in which short-distance effects are removed. The scale invariant layers then only realize the transformation $H^*_\tau = H^*_{\tau-1}/\Lambda$, where $\Lambda = \{2, 3\}$ for the binary or ternary MERA, and are fully specified by the single set of tensors $\{w^*, u^*\}$. The ground state is hence given as $|\Psi_0\rangle = W_1 W_2 \cdots W_t W^* W^* \cdots$. In such a scale invariant MERA, a local operator o transforms under the action of the entanglement renormalization operator as

$$o' = \mathcal{S}(o). \tag{3.37}$$

Here, $\mathcal{S}$ is the scaling superoperator, which is the only nontrivial part remaining inside the causal cone of o in the operator $W^{*\dagger} o W^*$. Scaling operators ϕ_i are given as eigenvectors of this superoperator,

$$\mathcal{S}(\phi_i) = \lambda_i \phi_i, \qquad \Delta_i \equiv -\log \lambda_i. \tag{3.38}$$

The scaling dimensions Δ_i are defined from the eigenvalues λ_i.[36] For a quantum critical model, this spectral decomposition includes the primary scaling operators and their scaling dimension of the underlying CFT.

In Fig. 3.7, an example of the ternary MERA is shown, in which 1-site operators are inserted at the shown specific lattice positions. The corresponding 1-site scaling superoperator consists of only one isometry (cf. right panel). From this construction, one can easily calculate the correlation function $\langle\phi_i(x)\phi_j(x+l)\rangle$ of two scaling operator insertions with distance l (cf. left panel). The operator coarsegraining transformations are performed $\log_3(l)$ times until they are nearest neighbors. Since the past causal cone consists of only one site, each layer contributes

[36] The base of the logarithm depends on the MERA type, i.e. 2 or 3 for the binary or ternary ansatz, respectively.

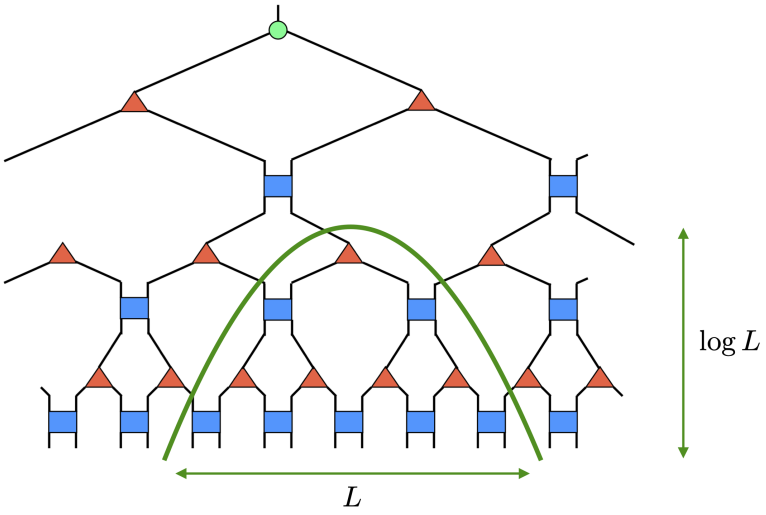

Figure 3.8: In a (binary) MERA, the minimal curve (shown in green) corresponding to a subsystem of L lattice sites has approximately $\log L$ cuts in the bulk, giving rise to a logarithmic violation of the area law for the entanglement entropy.

only an eigenvalue. One therefore has

$$\begin{aligned}\langle\phi_i(x)\phi_j(x+l)\rangle &= (\lambda_i\lambda_j)^{\log_3(l)}\langle\phi_i(x)\phi_j(x+1)\rangle \\ &= (3^{-\Delta_i}3^{-\Delta_j})^{\log_3(l)}C_{ij} \\ &= \frac{C_{ij}}{|l|^{\Delta_i+\Delta_j}},\end{aligned} \tag{3.39}$$

where C_{ij} is just a constant. The MERA is therefore capable of reproducing the algebraic decay of correlation functions as it appears in critical models and CFTs, cf. eq. (3.4). [37]

The final property of the MERA that we discuss here is the scaling of the entanglement entropy, cf. Fig. 3.8. If a subsystem of L sites is chosen, then the minimal curve inside the TN that causally connects the endpoints of the subregion, bounds the entanglement entropy. This becomes clear by observing that, if the system is cut along this curve, the contraction over it would entangle the two regions. Since there are approximately $\log L$ cuts, the entanglement entropy is estimated as

$$S(\rho_L) = -\operatorname{Tr}[\rho_L \log \rho_L] \leq \log(\chi)\cdot(\#\text{ cuts}) \sim \log(\chi)\cdot\log(L). \tag{3.40}$$

We therefore recover the logarithmic violation (3.7) in critical models. By properly calculating the actual reduced density matrix, one can extract the central charge of the underlying CFT from the result (3.8).

In summary, the discussions in this section have shown that the MERA is a TN, which is especially well suited to capture critical models. This is in contrast to the discussion of MPS,

[37] This results was derived structurally for the specific operator insertions. In any other case, it is valid for a scale invariant MERA actually encoding the ground state of a critical model, cf. e.g. [97].

which primarily recover properties of gapped models. The MERA also allows to extract (or encode) CFT data, such as scaling dimensions and the central charge. By extension, also further coefficients of the OPE can be derived. They are typically summarized as *conformal data*. Although we have focused on a $1D$ lattice, the MERA can be efficiently extended to higher dimensions, cf. e.g. the discussions in [101].

3.7 Holographic interpretations of tensor networks

The connection between holography and TNs appears in two ways in this thesis. On the one hand, the research topics presented in part II are either directly motivated by earlier holographic explorations, or physical observables calculated with TN methods have a dual holographic interpretation. On the other hand, the structure of TNs has also been associated with a discrete interpretation of the AdS/CFT correspondence. The main idea is to identify a TN diagram with a discrete geometry. If the resulting metric resembles a hyperbolic AdS spacetime, a connection between the underlying field theory content of the TN and the geometric dual can be drawn. This scenario applies to the path integral optimization program, which we consider in the context of circuit complexity in part III.
In this section, we focus on the latter connection between TNs and holography. As an introduction into the field, we concisely review some major developments. The choice of topics necessarily is very selective and we refer to [102] for a recent review of the subject focusing primarily on holographic quantum error correction in TNs.

3.7.1 AdS/MERA

The proposal of Swingle in [103,104] provided the starting point for the study of TNs encapsulating a RG flow and holographic geometry. It argues that a quantum critical state, represented by the scale invariant MERA TN, can be identified with a discrete version of AdS spacetime, hence the name AdS/MERA correspondence. Based on the MERA construction presented in the previous section 3.6, the artificial time direction τ, encoding the RG flow, is interpreted as the additional holographic dimension, such that each tensor in the network diagram is a cell lying in the *bulk* of the higher-dimensional spacetime. Since the MERA is based on the QMB entanglement structure, the geometric size of the cell is proposed to be proportional to the entanglement entropy of the corresponding site in the renormalized lattice. This makes use of the estimation (3.40), which demonstrates that discrete entanglement contributions are added along the cuts on the outside boundary of the causal cone for a subsystem. In the holographic picture, this minimal curve, which is an upper bound for the entanglement entropy in the UV, is interpreted as the minimal surface in the Ryu-Takayangi prescription for the holographic entanglement entropy. The entanglement renormalization, as generated in the discrete graph

of the MERA TN, is then associated with the metric

$$\mathrm{d}s^2 = R^2 \left(\mathrm{d}w^2 + \frac{\mathrm{e}^{-2w}}{a^2} \mathrm{d}x^2 \right), \tag{3.41}$$

where R is the entanglement entropy of local lattice sites, $w \equiv \tau$ the layer index, x the spatial lattice coordinate and a the lattice constant. By extension to finite temperature, it is further argued that also BHs are effectively described through entanglement renormalization in the higher-dimensional geometry. Apart from correlation functions (3.39) and entanglement entropy (3.40) of critical models and their underlying CFT, the MERA thus can also capture thermal BH solutions, which is another ingredient of the AdS/CFT correspondence. However, the description of critical spin chain Hamiltonians is obviously simpler than the appearance of supersymmetric CFTs in the original AdS/CFT proposal. Furthermore, the precise geometry, which can be associated to the MERA, is still under debate. For example, in [105], several consistency conditions for a proper holographic AdS identification are worked out, which are, in fact, not met by the conventional MERA. More recently, the authors of [106,107] provide an interpretation of tensor networks as path integral geometry and argue that the MERA corresponds to a null (light sheet) geometry, and only upon insertions with other tensors, can be interpreted as a dS or AdS discretization. [38] Based on these shortcomings, some of the more modern approaches, as e.g. in [108–110], try to construct holographic TNs not relying on debated MERA interpretations in holography.

3.7.2 Tree tensor network interpretation of p-adic AdS/CFT

In our earlier work [111], we constructed a discrete analog of the AdS/CFT correspondence based on p-adic numbers. The number field $\mathbb{Q}_p$ is the completion of rational numbers w.r.t. the non-Archimedean p-adic norm, which allows to write a p-adic number z as the series

$$z = p^{\nu} \sum_{m=0}^{\infty} a_m p^m; \quad \nu \in \mathbb{Z}; \quad a_m \in \{0, 1, \ldots, p-1\}; \quad a_0 \neq 0 \tag{3.42}$$

with absolute value $|z|_p = p^{-\nu}$. The value of p is typically chosen to be a prime number and by replacing $p \to p^D$, one can consider also higher-dimensional extensions. The set of all p-adic numbers can be represented as a regular tree with coordination number $p+1$, known as the Bruhat-Tits (BT) tree, cf. Fig. 3.9. In the p-adic AdS/CFT formalism, this discrete structure fills out the bulk of AdS spacetime and a p-adic CFT is living on the boundary of the tree. Holographic propagators and correlation functions of this construction resemble the expected CFT form. In [112], a concrete TTN interpretation was given for this setup. In contrast to an previous attempt [113], in which the TN comprising the BT tree was used to describe a

[38] Elements of this identification will be the starting point for our studies of path integral optimization (see below) and circuit complexity in part III.

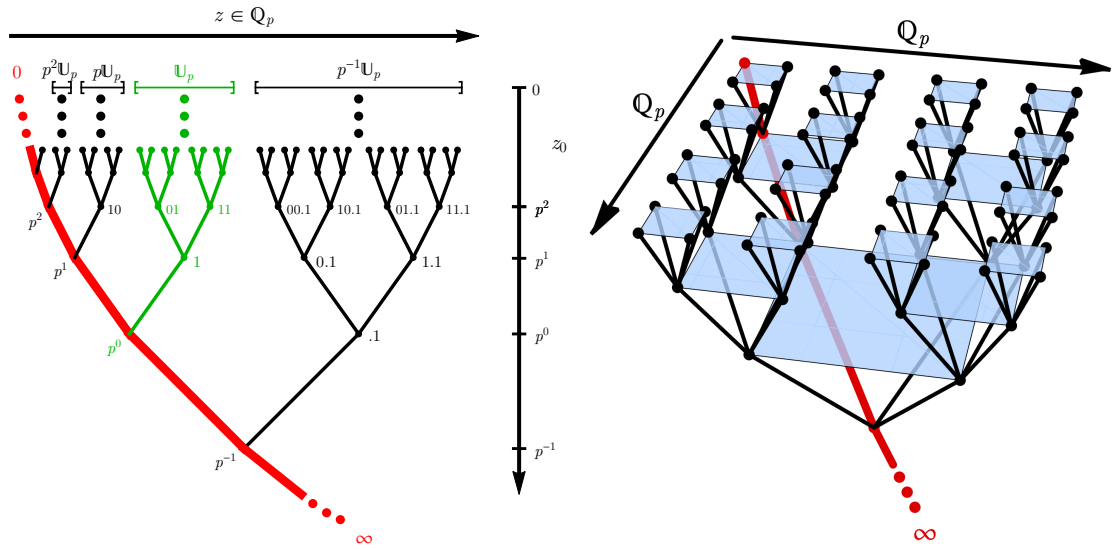

Figure 3.9: Illustration of the 2-adic Bruhat-Tits tree with a suitable coordinate system (left) and its extension to two dimensions (right). A p-adic number z of the form (3.42) corresponds to an infinite path starting from ∞ and terminating on the boundary. In the TTN interpretation of p-adic AdS/CFT, the partition function of a p-adic CFT is equivalent to a TN on the tree, representing the bulk of the higher-dimensional geometry. Figures taken from [111].

wavefunction (as e.g. in the MERA case), the authors instead propose that the TN describes a Euclidean path integral of a p-adic CFT to avoid inconsistencies. From this perspective, the TTN on the BT tree contains a tensor

$$T^{a_1 \cdots a_{p+1}} = \sum_{b_1,\ldots,b_{p-2}} C^{a_1 a_2 b_1} C^{b_1 a_3 b_2} \cdots C^{b_{p-2} a_p a_{p+1}} \tag{3.43}$$

on each vertex and all edges contain the weights $p^{-\Delta_a}$ for the contracted index. [39] Upon taking a proper regularization procedure into account, the partition function of the p-adic CFT can be calculated from the generating functional and all correlation functions are reproduced even at higher genus. By turning on sources, also RG flows and fixed points thereof can be studied. In [114,115], this framework was recently extended to show that Einstein's field equations emerge from an underlying field action on the BT tree.

An interesting lesson here is that this p-adic approach naturally allows to construct a bulk interpretation of the p-adic AdS/CFT correspondence using TTNs. In the same vein, but based on the MERA, we can interpret the path integral optimization program, which we are now discussing as an promising attempt to achieve this in the context of the standard AdS/CFT duality.

[39] Here, C^{abc} are the coefficents in the OPE of the p-adic CFT and Δ_a the primary operator scaling dimensions. In the 2-adic case as shown in Fig. 3.9, the tensors simplify to $T^{abc} = C^{abc}$.

3.7.3 Path integral optimization

The connection of TNs and holography via a path integral formulation already appeared in the previous two approaches. An independent program was presented by the authors of [116–118], who are similarly motivated by the quest for a microscopic understanding of the AdS/CFT correspondence and the emergence of spacetime via TNs. They address this question explicitly by considering Euclidean path integrals and their optimization. This allows to remain working in the continuum and to consider CFTs directly, in contrast to the other concepts, in which CFTs appear as effective descriptions of the underlying model.

We describe here the principle for $2D$ CFTs, in which the ground state wavefunction can be expressed by the discretized Euclidean path integral as

$$\Psi_0[\phi(x)] = \int \left(\prod_x \prod_{\epsilon \leq \tau < \infty} \mathcal{D}\hat{\phi}(\tau, x) \right) \mathrm{e}^{-S_{\mathrm{CFT}}[\hat{\phi}]} \cdot \prod_x \delta(\hat{\phi}(\epsilon, x) - \phi(x)). \tag{3.44}$$

Here, $\hat{\phi}$ are the fields of the theory specified by the action S_{CFT} and ϵ is a UV cutoff, i.e. lattice spacing, w.r.t. the flat space metric $\mathrm{d}s_0^2 = \epsilon^{-2}(\mathrm{d}\tau^2 + \mathrm{d}x^2)$. The initial discretization hence can be seen as a square lattice as depicted in the left panel of Fig. 3.10. The optimization process means a change of the structure of the lattice discretization without changing the correct ground state functional up to a normalization factor, i.e. finding a relation $\Psi_{opt} \sim \Psi_0$. In the first work [116], this was done by introducing a position dependent cutoff: Considering the path integral in Fourier space, only modes with wavelength above the lattice spacing, i.e. $k \ll 1/\tau$, contribute. In the lattice discretization, this means, that at each temporal step τ, $\mathcal{O}(\tau/\epsilon)$ lattice sites can be combined. This coarsegraining procedure introduces a factor $1/\tau^2$ in the metric and the modified geometry is hence identified with a hyperbolic space, in particular with a time slice of AdS_3. It is further argued that the wavefunction resembles the continuous generalization of the MERA (cMERA) [120], which allows a holographic interpretation of the TN. From a different viewpoint [117,118], the optimization procedure can be realized as a modification of the background metric itself, cf. the middle panel in Fig. 3.10. This procedure can be seen as a continuous generalization of TNR, in which a uniform TN approximation of the path integral is transformed into the MERA. The maximal optimization is achieved by minimizing a functional $I_\Psi[g(\tau, x)]$, which is associated to each quantum state. For Weyl rescaled geometries of $2D$ CFTs, it is argued in [117,118] that this functional is given by the Liouville action and its minimization is identified with the computational complexity of the state.

In part III we provide a more detailed introduction into the path integral optimization program and its conjectured connection to complexity. By employing a specific path integral discretization provided in [106,107], we rigorously connect it to the concept of circuit complexity and show its connection to variants of the MERA with tensor insertions following from

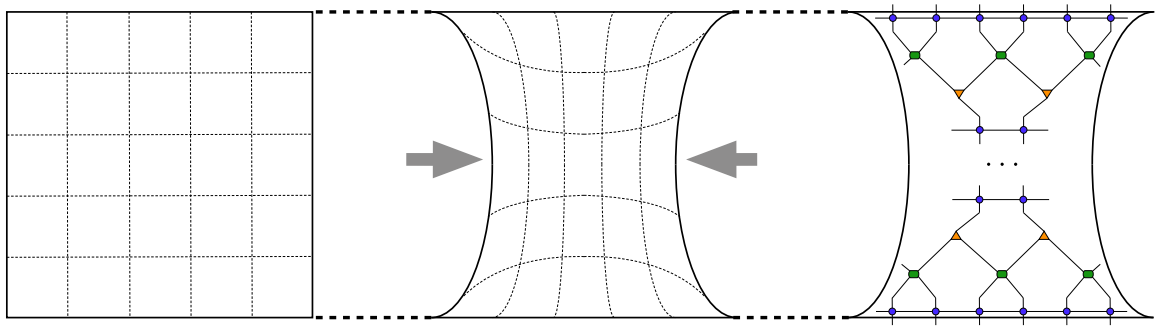

Figure 3.10: Schematic illustration of the path integral optimization procedure and its relation to tensor networks. The ground state wave function of a $2D$ CFT can be calculated from the Euclidean path integral on a strip of flat (left) or deformed geometry (middle). (Dashed lines indicate lines of constant time (horizontal) and spatial position (vertical).) Its optimization is related to a specific form of the MERA tensor network (right). See text for further explanations. Figure taken from our discussion in [119].

TNR (cf. right panel in Fig. 3.10). Since it was argued in [121], that Einstein's equation can be derived from this complexity functional, this framework also directly provides access to quantum gravity aspects.

Part II

From spin chains to thermal field theory

4 Real-time thermal field theory

Understanding properties of QCD is one major motivation behind several research directions in contemporary physics. As motivated in chapter 1, HICs are the most relevant experimental tool to probe phases of QCD. Their theoretical description needs to take the dynamical behavior of collective QFT states into account. In particular, the QGP, which is created in a far-from-equilibrium initial state, is strongly correlated and relaxes, according to our current phenomenological understanding, to a long hydrodynamic regime. The precise process of its formation in the initial stage after the collision and its subsequent in-medium thermalization is not yet understood. Over the past decade, progress in a microscopic understanding was made primarily with interdisciplinary approaches based on kinetic theory (as an approximation to weakly-coupled QFTs), relativistic hydrodynamics, weakly-coupled QFTs or holography (for a description of strongly-interacting QFTs). For an overview of these developments, we refer to the reviews [30,32,33,122].

Real-time thermalization and relaxation dynamics are also an interdisciplinary and timely field of research in QMB systems, which has been fueled by the enormous recent progress in experimental and numerical techniques. The term thermalization hereby means that expectation values of observables assume at late times after an initial perturbation values indistinguishable from those in thermal equilibrium (despite unitarity of time evolutions). Comprehensive discussions on that topic and its underlying mechanisms can be found, e.g., in the reviews [123–128]. One important aspect of these developments for our work is integrability in the context of equilibration dynamics. In particular, while integrable theories are usually believed to be too constrained to thermalize in the standard sense, it is known that the magnetization of the critical Ising model at non-zero temperature is decaying, i.e. thermalizing at late times [126,129,130] although the model is integrable in terms of free fermions. (See e.g. reference [131], where this phenomenon was recently analyzed in the context of an operator thermalization hypothesis.)

While holographic approaches or kinetic theory approximations are respectively suitable for strongly or weakly-interacting regimes, the knowledge about collective QFT dynamics in the most relevant regime of intermediate coupling is very limited. TN methods allow to study exactly this parameter range in an efficient ab initio way. An overview of these developments is given in [132–134]. Their applicability is based on the absence of the sign problem, which allows to study real-time phenomena and finite-density problems and therefore goes beyond the

power of conventional Monte Carlo (i.e. LGT) methods. For completeness, let us mention that also related TNR techniques [135,136] and quantum link models [137,138] were successfully employed to study properties of such QFTs.
In this chapter, we study questions motivated by the formation and relaxation of the QGP in HICs using MPO simulations. We consider linear response theory as a natural starting point to study real-time dynamics of QFTs. In particular, this allows us to calculate retarded correlation functions at non-zero temperature fully ab initio. We consider a class of (1+1)-dimensional QFTs, which emerge in the IR limit of the quantum Ising model. By developing a signal analysis method based on the Prony method, we can extract the analytic structure of retarded correlators in the complex frequency plane, which gives access to relaxation properties of the underlying QFT from the numerically simulated real-time signal. The IR description covers both the parameter case of a massive free fermion QFT, which we use to compare the numerical data with analytical results, as well as nonintegrable interacting QFTs with mesonic bound states. As motivated already in the overview chapter 1, the latter are particularly important in the context of QCD phenomenology. Although the structure of the spin chain Hamiltonian is rather simple, we therefore can make highly nontrivial predictions about the thermal response of QFTs to local perturbations. Moreover, this setup allows us to solve and study integrable interacting QFTs such as the E_8 regime discussed below.
Before explaining linear response theory and the quantum Ising model as the underlying frameworks for our numerical studies in section 4.2 and 4.5, we at first provide a short discussion of QCD and HICs in the next section. Section 4.3 then summarizes some holographic results, which motivate our studies about transient effects in correlation functions in section 4.9. In section 4.4 we gain insights into $2D$ models from a kinetic theory approach. Sections 4.7 and 4.8 then outline the computational setup of MPO simulations and signal analysis, respectively. In sections 4.9 and 4.10 we study separately transients and mesons as two major types of poles.

4.1 Aspects of QCD and heavy-ion collisions

The strong force in nature is described by QCD as a non-Abelian QFT with gauge group $SU(N_c)$. (For an introduction see e.g. [139].) On a classical level, the defining Lagrangian

$$\mathcal{L}_{\mathrm{QCD},cl} = -\frac{1}{4}F^a_{\mu\nu}F_a^{\mu\nu} + \sum_f^{N_f} \bar{q}_f(i\gamma^\mu D_\mu - m_f)q_f \tag{4.1}$$

contains $N_f = 6$ quark flavors, which are described by Dirac spinors $q^c_{f\alpha}$. Here, $c = 1, \ldots, N_c$ is the color index and $\alpha = 1, \ldots, 4$ the spinor index. Gluons A^a_μ ($a = 1, \ldots, N_c^2 - 1$; $\mu = 1, \ldots, 4$) enter the field strength tensor $F^a_{\mu\nu} \equiv \partial_\mu A^a_\nu - \partial_\nu A^a_\mu + g f^{abc} A^b_\mu A^c_\nu$ as gauge bosons with g being the gauge coupling and f^{abc} the structure constants of the associated Lie algebra. This form of the field strength tensor allows not only quark-gluon interactions but also multiple gluon self-

interactions. While quarks are defined in the fundamental representation, gluons appear in the adjoint representation. The covariant derivative $D_\mu = \partial_\mu - igA^a_\mu t_a$ contains the representation matrices t_a of the group $SU(N_c)$. The quark masses m_f as the only free parameters are experimentally measured (see e.g. [140]). Within QCD, mesons appear as non-perturbative bound states of a quark-antiquark pair. They are described as currents, e.g. the singlet current $\bar{q}_f \gamma^\mu q_f$, which are constructed from left and right-handed components of the quark fields. [40]
To quantize the classical theory, canonical schemes for a perturbative treatment are applicable as well as path integral methods, which are relevant for numerical Monte Carlo techniques. The β function (2.5) at one-loop order then takes the form

$$\beta(g) = -\left(11N_c - 2N_f\right)\frac{g^3}{48\pi^2} + \mathcal{O}(g^5). \tag{4.2}$$

The important minus sign of this negative expression implies a decreasing of the coupling at high energies or momentum. This property is known as *asymptotic freedom*. Conversely, it causes the *confinement* of quarks into color-neutral hadrons at large distances (or low energies). A complete theoretical understanding of this phenomenon is currently not at hand. The finite values of m_f at the physical point break classical scale invariance explicitly. In the quantized theory, the trace anomaly of the energy-momentum tensor also breaks this symmetry and introduces a scale $\Lambda_{\mathrm{QCD}} \simeq 200\,\mathrm{MeV}$ by dimensional transmutation.
Together, these quantum properties of QCD cause the rich set of emergent phenomena but also demand the necessity for numerical or non-perturbative methods to explore the strongly-coupled regime. In particular, asymptotic freedom suggests a phase transition from the confined hadronic phase to a deconfined QGP of individual quarks and gluons. LGT methods provide a way to evaluate the grand partition function of QCD in the path integral formalism on a discretized spacetime lattice and extrapolate the results to the continuum limit. They unveiled [141] that this phase transition is at zero chemical potential a continuous crossover in the temperature range $150 - 170\,\mathrm{MeV}$ [142,143]. [41]
The QGP created in HICs provides the primary experimental way of studying conditions similar to the first few microseconds after the big bang in the early universe. As comprehensively reviewed in [30,32,33,122], highly Lorentz-contracted nuclei or nucleons collide and form a droplet of extremely high temperature (primarily in central collisions) and density (primarily in fixed-target setups). The time evolution of a HIC is typically modelled in three different stages, which we summarize here following [32,122] and using Fig. 4.1.

1) The initial stage takes place from the moment of the collision up to a characteristic proper time scale of order $\tau_0 \sim 1\,\mathrm{fm/c}$. The lump of primordial matter is in a state far

[40] For example, the π^+ and π^0 mesons as prominent pseudoscalar examples consist of an *up* and *anti-down* quark in different combinations.
[41] As pointed out in [122], this absence of a first-order phase transition is the reason why there are no observable cosmological imprints visible in the present universe.

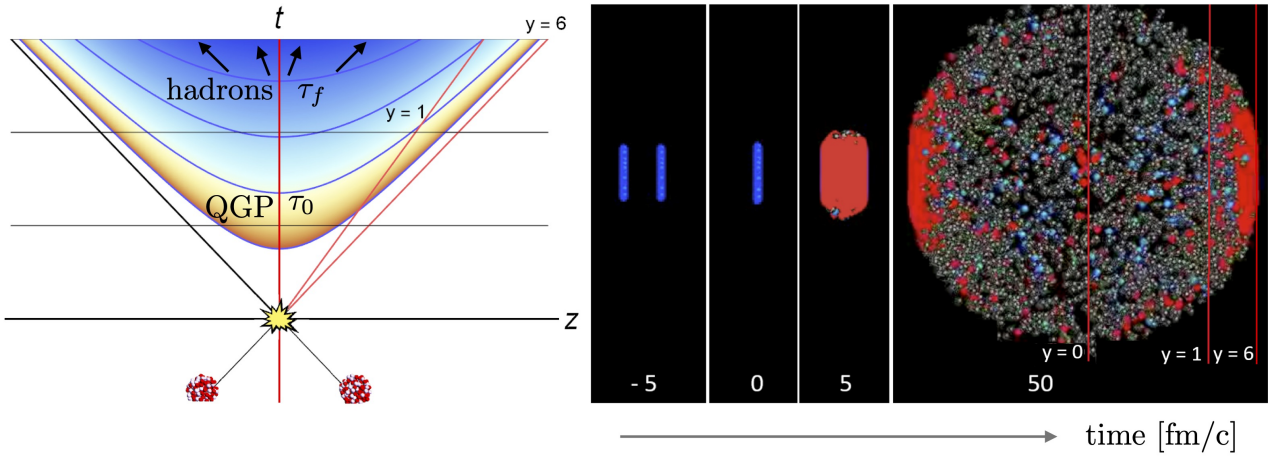

Figure 4.1: Illustration of the different phases in a HIC. The left panel shows a space-time diagram with lines of constant proper time as hyperbolas assuming a collision at the origin. The color is a proxy for the temperature. The right panel shows a numerical simulation of a lead-lead collision at different times. Blue and grey spheres indicate hadrons, red ones represent the QGP. In both figures, red lines denote constant rapidities y. The figures visualize the freezeout of hadrons from an initial far-from equilibrium stage in the HIC. Figure taken and adapted from the arXiv version of [122]. The right panel was originally adapted from [144].

from equilibrium with many nuclear constituents interacting in a very complex manner. During this process, a QGP with deconfined but strongly-interacting quarks and gluons is created. Microscopic approaches, which aim for a theoretical description of this stage, assume some initial condition of the colliding matter when using an effective QCD modelling (such as a color glass condensate). Alternatively, holographic approaches allow an ab initio study of the collision but are based on phenomenological models in some class of QFTs. The prospect of TNs is precisely to overcome this difficulty, since they allow an ab initio study of the underlying QFT, which can address both equilibrium and non-equilibrium physics in the time, temperature (or more generally energy density) and (charge) density domain. As a first step in this direction, this motivates us to study retarded thermal correlators in this chapter, since such correlation functions give access to the fundamental relaxation and thermalization behavior of a QMB system. Although established TN methods limit us to (1+1)-dimensional systems, we can still explore a nontrivial class of interacting QFTs, which shares important confinement features with QCD. TN methods also provide the advantage of giving access to entanglement properties and thus allow to study the process of (entanglement) entropy production in this violent first stage of a HIC. This topic was recently addressed in [145] in a QED context.

2) The second stage is characterized by the evolution of the QGP at a very low shear viscosity to entropy density ratio. Assuming local thermalization, relativistic viscous hydrodynamics provided a successful framework to explain particle momentum anisotropies as a phenomenological consequence of spatial anisotropy. Holographic studies came to

the competing conclusion that the hydrodynamic regime is applicable even when spatial anisotropies are still present (i.e. in absence of thermal equilibrium) [146–150].

3) When the expanding matter has cooled down enough, hadronic, i.e. confined particles decouple and freeze out at times later than a scale $\tau_f > \tau_0$. This process takes place sequentially and causes detectable particle signatures.

In summary, TN methods have the prospect of giving new insights particularly for the most difficult far-from-equilibrium initial stage of a HIC. This is not only relevant for a theoretical understanding of this dynamical process itself, but also due to the fact that HICs provide a way of exploring rich structures in the QCD phase diagram. The latter is standardly studied as a function of temperature and baryon density and is a topic of intense research from both the QCD side (see e.g. [151–154]) and holography (see e.g. [155,156]).

4.2 Linear response theory

Linear response theory provides a framework to study the near-equilibrium properties of perturbed thermal systems. We motivate here the calculation of retarded correlation functions to characterize the relaxation behavior of QMB systems and QFTs following the discussion in [32] and the general introduction in the corresponding chapter of [157]. [42]
The basic assumption is that the equilibrium Hamiltonian H_0 of a physical system is perturbed by a small source $\mathcal{J}(t,x)$ coupled to some operator O,

$$H = H_0 + \mathcal{J}O. \tag{4.3}$$

We are interested in the change in the thermal expectation value $\delta\langle O\rangle$ w.r.t. an initial thermal equilibrium state $\rho_\beta = \mathrm{e}^{-\beta H_0}$ at inverse temperature $\beta = 1/T$, which is given in real space as

$$\delta\langle O\rangle(t,x) = \int_{-\infty}^{t} \mathrm{d}t' \int \mathrm{d}x'\, G_R^O(t-t', x-x')\, \mathcal{J}(t',x'). \tag{4.4}$$

The differential change $\delta\langle O\rangle$ is proportional to the source, which is chosen to satisfy $\mathcal{J}(t \to -\infty, x) \to 0$. The two-point function $G_R^O(t-t', x-x')$ of the operator O depends only on the retarded arguments, ensuring causality of independent perturbations at different spacetime points. It can be calculated explicitly with *Kubo's formula* as a thermal expectation value of the operator commutator, given by

$$G_R^O(t,x) = i\,\theta(t)\ \mathrm{Tr}\left\{\rho_\beta[O(t,x), O(0,0)]\right\}, \tag{4.5}$$

[42] The notation here is adjusted to (1+1)-dimensional systems with coordinates t,x but the conclusions hold generally.

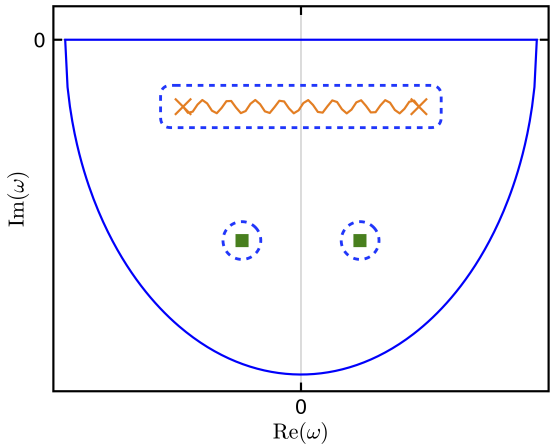

Figure 4.2: Nonanalytic structures in the lower complex frequency plane of the contour integral (4.6). The integration along the blue curve can encompass pole singularities (green squares) and branch cuts (orange curve) between branch points (orange crosses). Every individual frequency contribution is a *mode* of the retarded thermal correlation function. Figure reproduced from [32].

where we have chosen without restriction $t' = x' = 0$.[43] Causality is represented in this equation by the Heaviside theta function $\theta(t - t')$. In Fourier space, eq. (4.4) reads

$$\delta\langle O\rangle(t,p) = \int \mathrm{d}\omega \; \mathrm{e}^{-i\,\omega\,t} \; G_R^O(\omega,p)\,\mathcal{J}(-\omega,-p). \tag{4.6}$$

Here, p is the momentum of the system and arguments specify the transformed functions. This expression is now evaluated as a contour integral. As a consequence of causality, the retarded correlation function is analytic in the upper half plane of the complex frequency ω, while nonanalytic features in the lower half plane provide important insights into the response. These are inevitable to characterize the thermalization or, more generally, relaxation behavior of the perturbed system. As illustrated in Fig. 4.2, they encompass (arbitrarily many) pole singularities and branch cuts stretching between branch points. Time reversal symmetry demands that all structures are symmetric w.r.t. the imaginary axis. A single pole singularity at a value $\omega = \omega_{pole}(p)$ gives rise to a term

$$\delta\langle O\rangle(t,p) = \mathrm{e}^{-i\,\omega_{pole}(p)\,t}\,. \tag{4.7}$$

The real part of $\omega_{pole}(p)$ causes persistent oscillations in time, while the imaginary part describes an exponential decay. On the other hand, branch cut singularities generate time dependencies in the form of power-laws on top of the branch point pole singularities. A singularity in the Fourier-transformed retarded two-point function at some value of the frequency ω (i.e. on the right hand side of eq. (4.6)) is therefore identified with its corresponding time-dependent

[43] We focus here on a single operator O, but the formula generalizes trivially for two distinct operators in the commutator.

feature of the response $\delta\langle O\rangle(t,p)$ (i.e. on the left hand side of eq. (4.6)), which is constrained by the fundamental equations of motion of the system. Any such contribution is called a *mode*. The specific pattern and structure of modes is a property of the microscopic model or QFT under consideration. Of particular importance is a potential mode $\omega_1(p)$ with the smallest imaginary part. Its inverse provides the relaxation time scale $\tau_R = 1/\operatorname{Im}(\omega_1(p))$ of the system. Such a mode is called *hydrodynamic*, because it is arbitrarily long-lived in the limit $\operatorname{Im}(\omega_1(p)) \to 0$. Further modes (and branch cut singularities) with a larger imaginary part are faster decaying, hence short-lived. They are denoted as *transient* or *nonhydrodynamic* modes or features. Equilibrium excitations with a real part of a mode much bigger than the imaginary part can be interpreted as quasiparticles.

4.3 Elements of holographic descriptions

The study of the structure of retarded correlators as a probe of a system's thermal response to perturbations is explicitly motivated by similar holographic explorations, for which we give a short summary in this section. Our discussion is based on [32,158]; other useful overviews on the subject are given, e.g., in [159–161].

In a gravitational theory, *quasinormal modes* (QNMs) are eigenfrequencies of a linearly perturbed fixed background. For this we consider a system described by the Einstein–Hilbert action (2.1) plus some matter fields, represented by the Lagrangian $\mathcal{L}_m$,

$$S = S_{\mathrm{EH}} + \int \mathrm{d}^{D+1}x\sqrt{-g}\mathcal{L}_m. \tag{4.8}$$

The underlying equations of motion are then given by the gravitational field equations, $R_{ab} - \frac{1}{2}Rg_{ab} + \Lambda g_{ab} = 8\pi G_N^{(D+1)} T_{ab}$, with T_{ab} as the gravitational energy momentum tensor, in combination with the equations of motion for the matter fields. [44] By considering the linearization of the system around background fields, defined by $g_{ab} = g_{ab}^{\mathrm{bg}} + h_{ab}$ for the metric and $\Phi = \Phi^{\mathrm{bg}} + \phi$ for a bulk field (of any type), one gets a simplified set of linear differential equations for the perturbations. QNMs are complex frequencies, which appear in solutions of these equations in Fourier space for physically motivated initial and boundary conditions (at spatial infinity and the BH horizon).

The operator/field map, introduced in section 2.5.2, allows to identify the QNMs of the gravity fluctuation ϕ in asymptotically AdS_{D+1} spacetimes (with a BH solution) with the poles of the retarded thermal correlation function of the dual operator O in a D-dimensional QFT. In particular, the boundary value of the metric h_{ab} itself sources the energy-momentum tensor $T_{\mu\nu}$ of the dual gauge theory. Its expectation value can be extracted from the near-boundary behavior of the bulk metric perturbation: For a bulk metric ansatz $\mathrm{d}s^2 = g_{ab}(x,z)\,\mathrm{d}x^a\,\mathrm{d}x^b =$

[44] Here, we use Latin indices for the $(D{+}1)$-dimensional spacetime and Greek indices for the QFT in D spacetime dimensions.

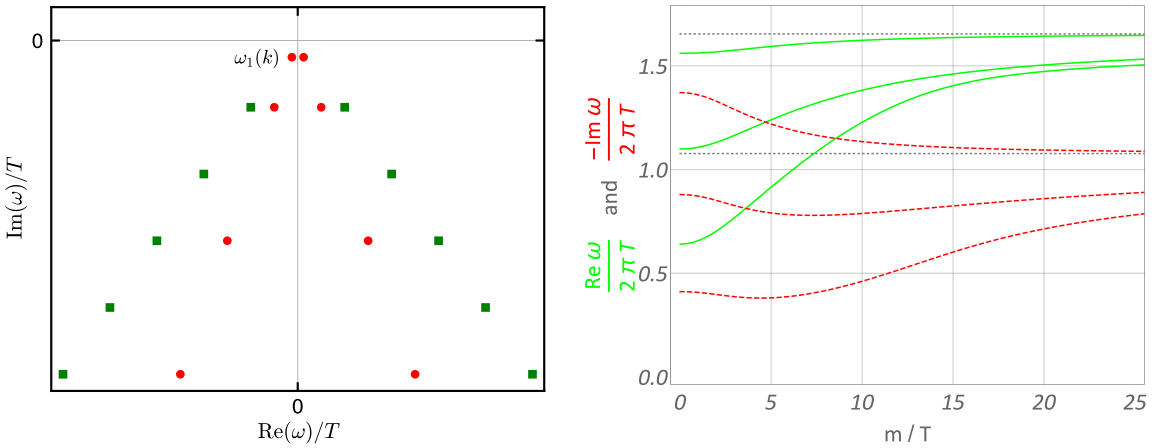

Figure 4.3: Left: Schematic illustration of the pattern of the lowest QNMs in (3+1)-dimensional holographic CFTs, which can be interpreted as poles of the retarded thermal correlator. Green squares represent a large spatial momentum k, red circles a small momentum value. Only the first mode ω_1 is hydrodynamic. The frequencies are measured in units of T, which provides the only scale in the CFT.
Right: Dependence of the real (green) and imaginary (red) part of the lowest QNM ω_1 in a nonconformal $\mathcal{N} = 2^*$ gauge theory in dependence on the mass perturbation. The curves correspond to scalar operators of dimension $\Delta = 2, 3, 4$ (from bottom to top). Figure taken from the arXiv version of [162].

$\frac{L^2}{z^2}(g_{\mu\nu}(x,z)\,\mathrm{d}x^\mu\,\mathrm{d}x^\nu + \mathrm{d}z^2)$, one finds the following behavior for $z \to 0$

$$g_{\mu\nu} = \eta_{\mu\nu} + \frac{\pi^2}{2c}\langle T_{\mu\nu}\rangle(x) z^4 + \mathcal{O}(z^6). \tag{4.9}$$

Here, $\eta_{\mu\nu}$ is chosen as the flat Minkowski metric. Holography therefore provides a framework to analyze the pole structure of the retarded two-point function of the gauge theory stress tensor, which characterizes the near-equilibrium behavior of the system, via the QNM spectrum of the perturbed background. This setup is typically considered in (3+1) dimensions, where the the linear response specializes to the form

$$\delta\langle T^{\mu\nu}\rangle(x) = -\frac{1}{(2\pi)^4}\int \mathrm{d}^3k \int \mathrm{d}\omega\, \mathrm{e}^{-i\omega x^0 + i\vec{k}\cdot\vec{x}}\, G_R^{\mu\nu,\alpha\beta}(\omega,\vec{k})\delta g_{\alpha\beta}(\omega,\vec{k}), \tag{4.10}$$

with $\vec{k}$ as the three-momentum vector. It can be shown that the components decompose into a scalar, shear and sound channel. For all these components, and more generally also for other operators, as well as for different holographic CFTs under consideration, a rather universal picture arises as visualized in the left panel of Fig. 4.3. The QNMs consist of infinitely many single poles at frequencies $\omega_n(k)$, symmetrically to the imaginary axis in the lower half plane and depending continuously on $k = |\vec{k}|$. Their position is aligned on a linear axis, whereby only the first mode ω_1 with the smallest imaginary part is (arbitrarily) long-lived ($\omega_1 \to 0$ for $k \to 0$), i.e. hydrodynamic, as identified in the previous section. Note that these hydrodynamic

modes exist only for conserved quantities, such as the stress tensor under discussion. The real and imaginary part of all other modes are of the same order of magnitude and therefore fast decaying in absence of quasiparticle excitations.

While these findings are formally valid for CFTs and their holographic counterpart, the work [162] initiated the study of QNMs also for massive theories, i.e. with broken conformal symmetry, which are a starting point for realistic models of the QGP. As demonstrated in the right panel of Fig. 4.3, the authors found for a particular nonconformal gauge theory that the position of lowest QNM is altered mildly by the mass deformation and the overall equilibration time scale is dominated by the temperature scale.

This motivates us to perform similar considerations also for (1+1)-dimensional systems, where TN methods are applicable. In fact, the study of 2-dimensional holographic CFTs provided the starting point of explorations on the QNM structure in thermal correlators [163]. We describe these results in section 4.6 and compare our extracted singularity structure from the MPO simulations to them. However, beyond the conformal case (and more generally massive free fermion regime), nothing is known when massive perturbations additionally also break the integrability of the system. We use our TN simulations to make fully ab initio predictions in exactly this most complicate regime. Furthermore, we are interested in the role of branch cuts, which are absent in all higher-dimensional holographic calculations. To get a more complete picture on these analytic structures in (1+1) dimensions, we at first consider a kinetic theory model in the next section. We finally point out that the importance of these QNM analyses stems from the fact that, beyond thermalization time scales, they also provide access to dispersion relations and further transport coefficients, which lead to the famous holographic result $\eta/s = 1/4\pi$ [31]. [45]

4.4 Insights from kinetic theory

In this chapter we are primarily interested in the analytical structure of retarded correlators of (1+1)-dimensional systems. To gain further insights about the physical properties of such systems, in particular for massive theories with broken conformal symmetry, we consider in this section a kinetic theory model to develop some intuition about the structure of correlators. As discussed in [32,33], kinetic theory effectively describes a system in terms of phase space distributions of particles and represents a weakly-interacting approximation to QFTs at high temperatures and densities, in which particles acquire effective masses and widths. It assumes that the de Broglie wavelength of quasiparticles is smaller than the mean free path between collisions, and that quantum interference effects are are negligible. In [165], this was for the first time worked out for QCD using effective action techniques. Whereas similar and

[45] Note that this value holds for two-derivative gravity duals. More general cases can yield smaller values as discussed in [164].

more recent considerations as e.g. in [166–168] focus on (3+1) dimensions to describe the QGP thermalization towards the hydrodynamic regime, the present lower-dimensional case is typically not considered in the literature. To the best of our knowledge, the results presented here have not been worked out in the literature before. We do not intend to give an introduction into the topic kinetic theory itself. For this purpose we refer instead to the literature, for example the lecture notes [169].

We consider the Boltzmann equation in the relaxation time approximation

$$p^\mu \partial_\mu f = \frac{p^\alpha u_\alpha}{\tau_R} \left(f - f_{eq}\right), \tag{4.11}$$

which describes the time evolution of the one-particle distribution function $f(x,p)$. The latter quantity represents the number of states per phase-space volume. Here, f_{eq} is the local equilibrium distribution function, p^μ is the particle's four-momentum, u^μ is a collective four-velocity vector and τ_R the relaxation time scale (which is proportional to the mean free path). For notational convenience, we suppress arguments. Small perturbations δf and δf_{eq} obey the relation

$$p^\mu \partial_\mu \delta f = \frac{p^\alpha u_\alpha}{\tau_R} \left(\delta f - \delta f_{eq}\right). \tag{4.12}$$

Assuming $u^\alpha(t,\vec{x}) = (1,\vec{0}) + \delta u^\alpha(t,\vec{x})$, this equation reads in Fourier space

$$-ip^\mu k_\mu \widetilde{\delta f} = -\frac{p^0}{\tau_R}\left(\widetilde{\delta f} - \widetilde{\delta f_{eq}}\right), \tag{4.13}$$

from which one can deduce

$$\widetilde{\delta f} = \frac{p^0 \widetilde{\delta f_{eq}}}{-i\tau_R p^\mu k_\mu + p^0} = \frac{p^0 \widetilde{\delta f_{eq}}}{-i\tau_R p^0 \omega + i\tau_R \vec{p}\vec{k} + p^0}. \tag{4.14}$$

We assume the local equilibrium function to have the Boltzmann type form

$$f_{eq} = \mathrm{e}^{\beta p^\alpha u_\alpha}, \tag{4.15}$$

which depends on the inverse temperature $\beta = 1/T$ and the velocity u_α as macroscopic quantities. Using this ansatz, perturbations of the local equilibrium are given as

$$\delta f_{eq} = \frac{f_{eq,0}}{T_0}\left(p^\alpha \delta u_\alpha - \frac{\delta T}{T_0} p^\alpha u_\alpha\right) = \frac{f_{eq,0}\, p^0}{T_0}\left(\frac{p^\alpha}{p^0}\delta u_\alpha + \frac{\delta T}{T_0}\right). \tag{4.16}$$

The global equilibrium distribution is $f_{eq,0} = \mathrm{e}^{-p^0/T_0}$.[46] Perturbations of the energy-momentum tensor, which is defined as the second moment w.r.t. the distribution function f, i.e. as

[46] In the following, a subscript "0" denotes quantities in global thermal equilibrium.

$T^{\mu\nu} = \langle p^\mu p^\nu f \rangle$, are given in Fourier space as

$$\widetilde{\delta T^{\mu\nu}} = \int \frac{\mathrm{d}^d p}{(2\pi)^d} \frac{p^\mu p^\nu}{p^0} \widetilde{\delta f} = \int \frac{\mathrm{d}^d p}{(2\pi)^d} \frac{p^\mu p^\nu}{p^0} \frac{f_{eq,0}}{T_0} \frac{(p^0)^2 \left(\frac{p^\alpha}{p^0} \widetilde{\delta u_\alpha} + \frac{\widetilde{\delta T}}{T_0} \right)}{-i\tau_R p^0 \omega + i\tau_R \vec{p}\vec{k} + p^0}, \tag{4.17}$$

where we used (4.14) and (4.16).

The aim of this section is to analyze the structure of the retarded correlation function $G_R^{\mu\nu,\alpha\beta}$, which describes the response of the energy-momentum tensor to metric perturbations:

$$\langle T^{\mu\nu} \rangle = \frac{\partial T^{\mu\nu}_{eq}}{\partial h_{\alpha\beta}}\bigg|_{h=0} h_{\alpha\beta} - \frac{1}{2} G_R^{\mu\nu,\alpha\beta} h_{\alpha\beta} \quad \Longleftrightarrow \quad G_R^{\mu\nu,\alpha\beta} = \frac{\delta T^{\mu\nu}}{\delta h_{\alpha\beta}}. \tag{4.18}$$

We are particularly interested in breaking conformal invariance in 1+1 dimensions by introducing a finite mass m, where the energy component of the momentum vector takes the form $p^0 = \sqrt{m^2 + p^2}$. Instead of finding explicit expressions for the correlator as in [166,167] for massless particles in higher dimensions, we analyze its structure by identifying (non)hydrodynamic poles (modes) or branch cuts in the complex frequency plane.

As discussed in [167], an intuitive picture of generic properties of the retarded correlator in kinetic theory can be obtained by considering the following situation: Assuming alternating overdense and underdense regions with wavelength $2\pi/k$, sound channel perturbations of an equilibrium state can be mimicked by studying the response of an initial overdense sheet at the spacetime point $(\vec{x}, t = 0)$. For massless interacting particles, the contribution to the retarded correlator is given by integrating the following expression over a sphere of radius 1, representing particles at the speed of light: [47]

$$\int_{|\vec{v}|=1} \mathrm{d}^d v \frac{1}{1 - i\tau_R \omega + i\tau_R \vec{k}\vec{v}} = \int_{-1}^{1} \frac{\mathrm{d}\cos\theta\, \Omega_{d-2}}{1 - i\tau_R \omega + i\tau_R |\vec{k}| \cos\theta}. \tag{4.19}$$

In dimensions greater than $1+1$, this gives rise to a term

$$\ln \left[\frac{1 - i\tau_R(\omega - |\vec{k}|)}{1 - i\tau_R(\omega + |\vec{k}|)} \right], \tag{4.20}$$

resulting in a logarithmic branch cut between the two poles $\omega = -i/\tau_R \pm |\vec{k}|$ in the complex ω plane. In $1+1$ dimensions, we only get a term

$$1 - i\tau_R \omega \pm i\tau_R |\vec{k}|, \tag{4.21}$$

i.e. there are only two poles located at $\omega = -i/\tau_R \pm |\vec{k}|$, which we identify as nonhydrodynamic ones. How does this behavior change for broken conformal invariance with massive particles

[47] Here, we are use the notation $v^\mu \equiv p^\mu/p^0 = (1, \vec{v})$.

in $1+1$ dimensions? In this case, the expression contributing to the retarded correlator takes the form [48]

$$\int \mathrm{d}^d p \frac{1}{p^0(1-i\tau_R\omega) - i\tau_R \vec{k}\vec{p}} = \int_{-\infty}^{\infty} \mathrm{d}p \frac{1}{\sqrt{p^2+m^2}(1-i\tau_R\omega) - i\tau_R kp}. \tag{4.22}$$

In the limiting case $p = 0$, the denominator in the integrand takes the form $m(1 - i\tau_R\omega)$, implying a singularity at $\omega = -i/\tau_R$. For $p \to \pm\infty$, the denominator reads $p(1 - i\tau_R(\omega \pm k))$, implying poles at $\omega = -\frac{i}{\tau_R} \pm k$. We therefore conclude that the entire correlator exhibits a nonhydrodynamic branch cut stretching between the two poles at $\omega = -\frac{i}{\tau_R} \pm k$. This property is similar to the structure in higher dimensions discussed above. Breaking conformal invariance explicitly by finite particle masses thus has an effect similar to higher dimensions in the massless case.

To identify also hydrodynamic poles in the complex ω plane, we need to solve the kinetic model (4.11) self-consistently by imposing the following Landau matching conditions:

$$T_0^{\mu\nu} = \langle p^\mu p^\nu f_{eq}^0 \rangle, \tag{4.23}$$

$$T^\mu{}_\nu u^\nu = -\epsilon u^\mu. \tag{4.24}$$

Using $u^\alpha u_\alpha = -1$ (from which follows $\delta u^\alpha u_\alpha = 0$ and hence $\delta u^0 = 0$), the second condition (4.24) implies

$$\delta T^{00} = \delta\epsilon \quad \text{and} \quad \delta T^{i0} = (\epsilon_0 + P_0)\delta u^i \tag{4.25}$$

(from the timelike and spatial components respectively). In 1+1 dimensions, the first condition (4.23) can be solved analytically: Writing the energy-momentum tensor in global equilibrium as $T_0^{\mu\nu} = \mathrm{diag}(\epsilon_0, P_0, P_0, P_0)$, the temporal and spatial components of the integral can be expresses in terms of modified Bessel functions as

$$\epsilon_0 = \frac{m}{\pi}\left[mK_0(m/T_0) + T_0 K_1(m/T_0)\right] \quad \text{and} \quad P_0 = \frac{mT_0}{\pi} K_1(m/T_0). \tag{4.26}$$

Denoting the two integrals in the sum (4.17) as $I_u^{\mu\nu}$ and $I_T^{\mu\nu}$ (w.r.t. the perturbations $\widetilde{\delta u_\alpha}$ and $\widetilde{\delta T}$ respectively), the Landau matching conditions (4.25) imply

$$\widetilde{\delta T^{00}} = I_u^{00}\widetilde{\delta u_1} + I_T^{00}\widetilde{\delta T} = \frac{\partial\epsilon}{\partial T}\widetilde{\delta T} \tag{4.27}$$

$$\widetilde{\delta T^{01}} = I_u^{01}\widetilde{\delta u_1} + I_T^{01}\widetilde{\delta T} = (\epsilon_0 + P_0)\widetilde{\delta u_1}. \tag{4.28}$$

[48] The components are denoted as $k^\mu = (\omega, k)$ and $p^\mu = (p^0, p)$ with $p^0 = \sqrt{p^2+m^2}$.

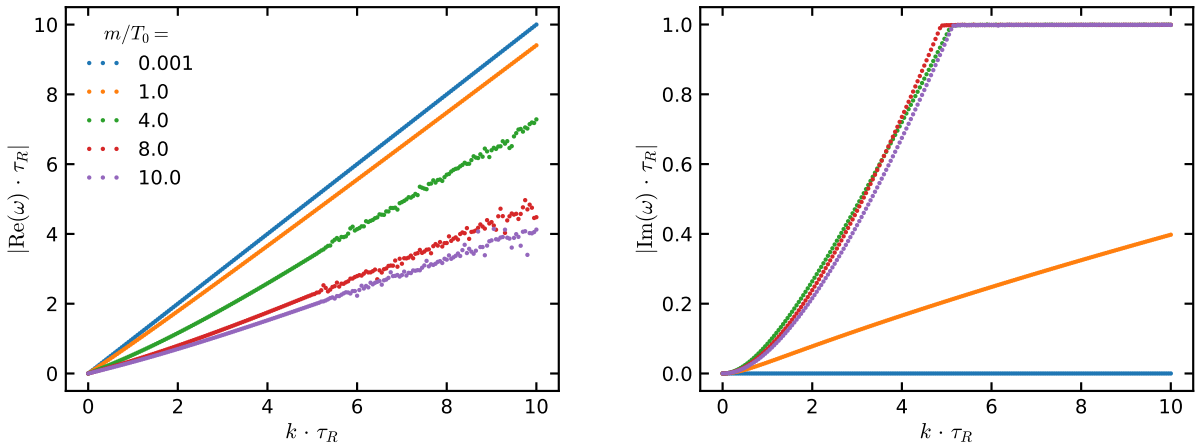

Figure 4.4: Hydrodynamic modes for a $(1+1)$-dimensional kinetic model in the relaxation time approximation. The dispersion relation is shown as $\mathrm{Re}(\omega)$ (left panel) and $\mathrm{Im}(\omega)$ (right panel) in dependence of the momentum k.

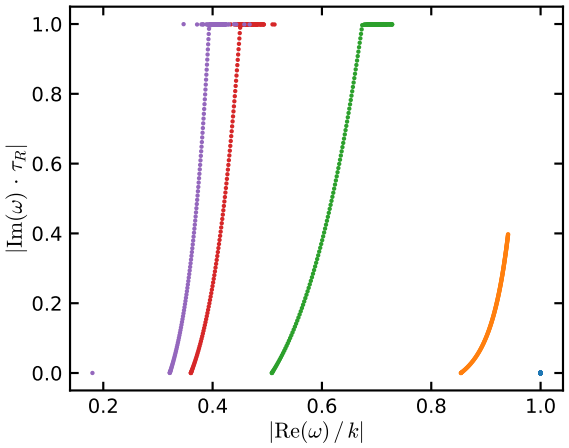

Figure 4.5: Pole locations for hydrodynamic modes in the kinetic model in the scaled complex ω-plane.

In matrix form, this system can be rewritten as

$$\mathcal{F} \begin{pmatrix} \widetilde{\delta T} \\ \widetilde{\delta u_1} \end{pmatrix} \equiv \begin{pmatrix} I_T^{00} - \frac{\partial \epsilon}{\partial T} & I_u^{00} \\ I_T^{01} & I_u^{11} - (\epsilon_0 + P_0) \end{pmatrix} \begin{pmatrix} \widetilde{\delta T} \\ \widetilde{\delta u_1} \end{pmatrix} = 0, \tag{4.29}$$

where we call $\mathcal{F}$ the fluctuation matrix. For given values of m and k, one can identify hydrodynamic poles as solutions to the equation

$$\det \mathcal{F} = 0 \tag{4.30}$$

in the complex ω plane.

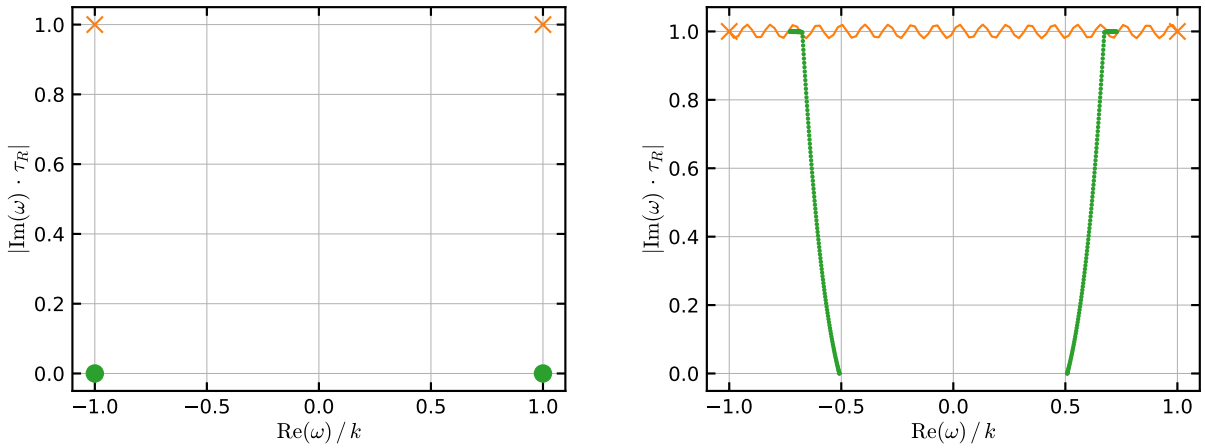

Figure 4.6: Overview of the results for poles in the complex ω-plane in the (1+1)-dimensional kinetic theory model with relaxation time approximation: The left panel illustrates the conformal case ($m = 0$), which exhibits two nonhydrodynamic poles (orange) and two hydrodynamic poles (green). For broken conformal invariance ($m > 0$, right panel), a nonhydrodynamic branch cut stretches between the the branch points of the confromal case (orange). Hydrodynamic poles lie, depending on their mass and momentum, inside of the complex plane.

For massless particles, $m = 0$, the integrals can be easily solved analytically and one gets

$$\omega = \pm k \tag{4.31}$$

as the hydrodynamic poles. For finite m, we solve the condition (4.30) numerically by setting $\tau_R = T_0 = 1$ (which defines the units $m[T_0]$, $\omega[\tau_R]$ and $k[\tau_R]$). Figure 4.4 shows the resulting dispersion relations (left and right panel) and Fig. 4.5 the location of poles in the complex ω plane for several values of m. The real part $\mathrm{Re}(\omega)$ shows a linear dependence with k and the slope can be interpreted as the speed of sound. For small values of k, the imaginary part $\mathrm{Im}(\omega)$ is quadratic in k. With increasing mass, the locations of the poles are shifted towards smaller real frequencies. Note that the blue curve in Fig. 4.5 corresponds to a very small mass. It exhibits a pole at $\omega/k \approx 1$ on the real frequency axis as already found analytically above. The horizontal lines at $|\,\mathrm{Im}(\omega)\tau_R| \approx 1$ indicate that we numerically hit the branch cut between $\omega = -i/\tau_R \pm k$. Since we numerically do not have access to the next sheet, we cannot determine the pole locations for large values of k.

The results from this kinetic theory analysis are summarized in Figure 4.6. It can be concluded that beyond hydrodynamic poles also nonhydrodynamic structures play a significant role in the relaxation behavior of (1+1)-dimensional systems. Breaking conformal invariance can have significant effects, since branch cuts can arise and pole locations are significantly altered.

4.5 The quantum Ising model and IR QFTs

4.5.1 Phase diagram

The Ising model, originally developed by Ernst Ising in [170] as a model for ferromagnetism, represents even a century after its introduction still a cornerstone in present-day quantum and condensed matter physics. We follow here the modern discussion in [129]. Another useful reference is [171]. The nearest-neighbor quantum Ising model in one spatial dimension is defined by the Hamiltonian

$$H_{\mathrm{NN}} = -J \left(\sum_{j=1}^{N-1} \sigma_j^z \sigma_{j+1}^z + h \sum_{j=1}^{N} \sigma_j^x + g \sum_{j=1}^{N} \sigma_j^z \right). \tag{4.32}$$

This local Hamiltonian is of the form (3.2) and therefore possesses all previously discussed properties on the entanglement and correlation structure. Here, quantum spins are described by Pauli matrices $\sigma_j^{x,z}$ at lattice positions j in a chain of N sites. The energy scale is set by the unit $J > 0$ and the parameters $h > 0$ and g quantify transverse and longitudinal perturbations w.r.t. the first interaction term. [49] In fact, the form (4.32) of the Hamiltonian is a short-hand notation for tensor products of the Pauli matrices, which commute with each other on different sites, and identity matrices at all remaining lattice sites. It is common to work in the σ_j^z basis with eigenvalues ± 1, such that the two possible spin orientations can be interpreted as "up" $|\uparrow\rangle_j$ and "down" $|\downarrow\rangle_j$ states. At $h = 0$ the model is classical (through its diagonal form) but at any finite $h > 0$, entanglement is present in the system that can induce spin flips via tunneling. From this basic definition, the phase diagram shown in Fig. 4.7 follows for the $1D$ quantum Ising model. [50] We consider at first the case $g = 0$. At large field values $h \gg 1$, the transverse term is dominating, such that the ground state is given by $|0\rangle = \prod_j |{\rightarrow}\rangle_j$ with $|{\rightarrow}\rangle_j = (|\uparrow\rangle_j + |\downarrow\rangle_j)/\sqrt{2}$ as the eigenstate of σ_j^x with eigenvalue $+1$. This is the disordered *paramagnetic* phase. On the other hand, at $h = 0$, the ground state consists of all spins pointed upwards or downwards, i.e. $|0\rangle = \prod_j |\uparrow\rangle_j$ or $|0\rangle = \prod_j |\downarrow\rangle_j$, which is denoted as *ferromagnetic* ordering. The Ising Hamiltonian (4.32) admits invariance under a global $\mathbb{Z}_2$ symmetry, generated by $\prod_j \sigma_j^x$, which maps $\sigma_j^z \mapsto -\sigma_j^z$ and $\sigma_j^x \mapsto -\sigma_j^x$. In combination with a vanishing tunneling matrix element between these two degeneracies, this is the reason why in an infinite system the ferromagnetic ordering persists also for small values of h, since only a small number of spins will be flipped. As a consequence, there must be a phase transition at some critical value h_{crit}. It is a *quantum phase transition*, since it exist at zero temperature and is entirely induced by quantum fluctuations (in contrast to thermal fluctuations).

[49] We set $J \equiv 1$ for all our numerical studies.

[50] Note that the classical Ising model in arbitrary D dimensions is identical to the quantum Ising model with a transverse field in $D-1$ dimensions. By this duality, the quantum phase transition in $1D$ corresponds to the thermal critical point of the classical $2D$ Ising model. For details of the mapping see [129].

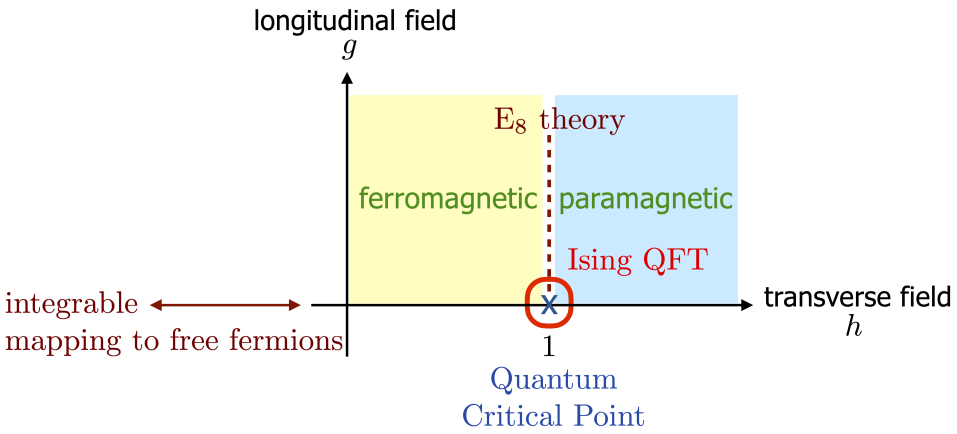

Figure 4.7: Phase diagram of the one-dimensional quantum Ising model (4.32).

4.5.2 Free fermion mapping

The precise value of the critical transverse field can be determined via a mapping to free fermions. This is possible for vanishing longitudinal field ($g = 0$), in which case the system is integrable, i.e. it can be solved analytically.[51] The well-known procedure outlined here is described for example in [129]. Detailed calculations are available in the documents [171,174]. The starting point is the Jordan–Wigner transformation [175], which allows to rewrite a spin-$\frac{1}{2}$ system as spinless fermions with the definitions

$$\sigma_j^x = 1 - 2\, b_j^\dagger\, b_j \quad \text{and} \quad \sigma_j^z = \left(\prod_{l<j}(1 - 2\, b_l^\dagger\, b_l)\right)(b_j + b_j^\dagger). \tag{4.33}$$

Here, $b_j^\dagger$ and b_j are respectively fermionic creation and annihilation operators that satisfy the anticommutation relations $\{b_i, b_j^\dagger\} = \delta_{ij}$ and $\{b_j, b_j\} = \{b_j^\dagger, b_j^\dagger\} = 0$. The form (4.33) ensures at the same time the commutation rules $[\sigma_i^+, \sigma_j^-] = \delta_{ij}\sigma_i^z$ and $[\sigma_i^z, \sigma_j^\pm] = \pm 2\delta_{ij}\sigma_i^\pm$ of the Pauli spin flip operators $\sigma_j^\pm \equiv (\sigma_j^x \pm i\sigma_j^y)/2$ through the inserted string of operators. Using these definitions, the Hamiltonian (4.32) is transformed into

$$H_{ff} = -J\sum_j \left(b_j^\dagger b_{j+1} + b_{j+1}^\dagger b_j + b_j^\dagger b_{j+1}^\dagger + b_{j+1} b_j - 2h b_j^\dagger b_j + h\right). \tag{4.34}$$

The apparent violation of the fermion number conservation can be circumvented via a Bogoliubov transformation. For that, we work with Fourier space operators[52]

$$b_k = \frac{1}{\sqrt{N}}\sum_j b_j\, \mathrm{e}^{-ikx_j} \tag{4.35}$$

[51] As remarked before, the resulting solution is transformable to the classical $2D$ Ising model, which was first solved by Onsager in [172]. The solution in the form presented in this section was found by Pfeuty [173].
[52] Here, the position $x_j = ja$ contains the lattice spacing a.

with wave number $k = \frac{2\pi}{Na} n$ $(n = 0, \ldots, N-1)$, and introduce fermionic operators [53]

$$\gamma_k \equiv u_k b_k - i v_k b_{-k}^\dagger. \tag{4.36}$$

For the parametrizations [54] $u_k \equiv \cos(\theta_k/2)$ and $v_k \equiv \sin(\theta_k/2)$ and the choice

$$\tan\theta_k = \frac{\sin(ka)}{h - cos(ka)} \tag{4.37}$$

the resulting free fermion Hamiltonian reads

$$H_{ff} = \sum_k \epsilon_k \left(\gamma_k^\dagger \gamma_k - \frac{1}{2} \right), \tag{4.38}$$

which obeys the fermion number conservation principle. The single-particle energy $\epsilon_k \geq 0$ follows the dispersion relation

$$\epsilon_k = 2J\sqrt{1 + h^2 - 2h\cos(ka)} \tag{4.39}$$

and takes its minimal value $M_h \equiv \epsilon_{k=0} = 2J|1-h|$ for vanishing momentum. The vanishing mass gap at $h = 1$ marks the critical point of the Ising model, where the quantum phase transition between the ferromagnetic $(h < 1)$ and paramagnetic $(h > 1)$ phase takes place.

4.5.3 Continuum limit and IR QFTs

The existence of a critical point in the transverse Ising model suggests that in the continuum the IR physics is effectively captured by a CFT. The QFT limit for the most general form (4.32) of the Hamiltonian is nicely discussed in [176]. This description follows from the introduction of two independent Majorana fermion fields as $\psi(x = ja) = \sqrt{\pi/a}(b_j^\dagger + b_j)$ and $\bar\psi(x = ja) = -i\sqrt{\pi/a}(b_j^\dagger - b_j)$. The lattice spacing is set to $a = 2/J$, from which the speed of light follows as 1. In the continuum limit $a \to 0$, the fields anti-commute with each other and satisfy $\{\psi(x), \psi(y)\} = \{\bar\psi(x), \bar\psi(y)\} = 2\pi\,\delta(x-y)$, ensuring that two-point correlation functions decay in the vacuum as $\frac{1}{x-y}$ at long distances, which is demanded by the CFT result. In the thermodynamic limit $N \to \infty$, combined with the scaling limit, which encompasses $a \to 0$ and $M_h/J \to 0$, while the ratio M_h/M_g is kept fixed, the IR, i.e. long distances compared to the lattice spacing, is described by the following Majorana fermion QFT [176]

$$H_{\mathrm{IR}} = \int_{-\infty}^{\infty} \mathrm{d}x \left\{ \frac{i}{4\pi} \left(\psi\partial_x\psi - \bar\psi\partial_x\bar\psi \right) - \frac{iM_h}{2\pi}\bar\psi\psi + \mathcal{C} M_g^{15/8}\,\sigma \right\}. \tag{4.40}$$

[53] The anticommutation relations translate into $\{\gamma_k, \gamma_{k'}^\dagger\} = \delta_{k,k'}$ and $\{\gamma_k, \gamma_{k'}\} = \{\gamma_k^\dagger, \gamma_{k'}^\dagger\} = 0$.
[54] The functions in the Bogoliubov transformation obey the properties $u_k^2 + v_k^2 = 1$ and $u_k = u_{-k}$, $-v_k = v_{-k}$.

Apart from the previously defined free fermion mass $M_h \equiv 2J|1-h|$, the longitudinal mass scale M_g is given as $M_g \equiv \mathcal{D}J\,|g|^{8/15}$. Here, $\mathcal{C} \approx 0.062$ and $\mathcal{D} \approx 5.416$ are numerical constants [176, 177]. For non-zero temperatures, IR degrees of freedom are excited in the limit $\beta J \to \infty$. From the scaling limit, it becomes apparent that the Ising model, defined by the lattice Hamiltonian (4.32) is described in the vicinity of the critical point by the class of QFTs captured by the Hamiltonian (4.40). As visualized in Fig. 4.7, there are several distinct parameter regimes, which we now discuss in detail.

- $M_h = M_g = 0$: The parameters translate into the lattice fields $\{h = 1, g = 0\}$ at the quantum critical point of the Ising model. The Hamiltonian (4.40) represents the Ising CFT, which is a free Majorana fermion CFT with central charge $c = \frac{1}{2}$. There are two scalar primary Hermitian operators: $\epsilon \equiv i\bar{\psi}\psi$ with scaling dimension $\Delta_\epsilon = 1$ and σ with $\Delta_\sigma = \frac{1}{8}$. In the lattice discretization (4.32), they are given in terms of transverse and longitudinal Pauli matrices as $\epsilon(ja) = -\frac{a}{\pi}\sigma_j^x$ and $\sigma(ja) = a\sigma_j^z$.

- $M_h \neq 0$, $M_g = 0$: This massive free fermion QFT, characterized by the fermion mass M_h, is integrable. It corresponds to the continuum limit of the transverse Ising model in the phase diagram (cf. Fig. 4.7), in which the free fermion mapping allows to find analytical expressions in both the ferromagnetic and paramagnetic phase.

- $M_h = 0$, $M_g \neq 0$: This regime describes the integrable and interacting E_8 QFT of Zamolodchikov [178], which is mathematically captured by the exceptional simple Lie algebra of rank 8. It contains 8 stable mesons as nonperturbative fermionic bound states in the spectrum. Their masses M_n are known and can be expressed as analytical ratios in terms of the lightest mass $M_1 = M_g$ as given in Tab. 4.1.

- $M_h \neq 0$, $M_g \neq 0$: This parameter range with both ϵ and σ perturbations turned on represents an interacting nonintegrable QFT with stable and unstable bound states [178–181].

Table 4.1: Analytical ratios of meson masses for the integrable interacting E_8 QFT [178] in comparison to the numerically extracted value from the TN+Prony method outlined in sections 4.7 and 4.8.

	M_2/M_1	M_3/M_1	M_4/M_1	M_5/M_1
analytical	$2\cos\frac{\pi}{5}$	$2\cos\frac{\pi}{30}$	$4\cos\frac{7\pi}{30}\cos\frac{\pi}{5}$	$4\cos\frac{2\pi}{15}\cos\frac{\pi}{5}$
numerical	1.6180	1.9890	2.4049	2.9563
TN+Prony	1.6147(7)	1.962(1)	2.413(2)	2.936(3)

M_6/M_1	M_7/M_1	M_8/M_1
$4\cos\frac{\pi}{30}\cos\frac{\pi}{5}$	$8\cos^2\frac{\pi}{5}\cos\frac{7\pi}{30}$	$8\cos^2\frac{\pi}{5}\cos\frac{2\pi}{15}$
3.2183	3.8912	4.7834
3.165(6)	3.52(3)	-

While the massive free fermion regime allows us to benchmark our TN simulations, we are primarily interested to study the nonintegrable regime at non-zero temperature, where the combination of TN simulations and subsequent signal analysis methods, which we develop below, have the most predictive power. Despite the simplicity of the Ising lattice Hamiltonian, we therefore can study highly nontrivial QFTs. We denote the entire class of QFTs described by the Hamiltonian (4.40) as Ising QFT. As pointed out in [176], this Hamiltonian makes no distinction between the ferromagnetic and paramagnetic phase. Only at the level of the Hilbert space, the difference becomes visible. In the ferromagnetic phase at $g = 0$, elementary excitations can be interpreted as domain walls. As soon as a longitudinal field is turned on ($g \neq 0$), these are non-perturbatively confined into mesons [182]. In the paramagnetic phase, excitations are interpreted as spin waves and a longitudinal field instead introduces perturbative corrections. Due to the relativistic nature of the Ising QFT, any excitation with mass M_n follows the dispersion relation $\omega(p) = \sqrt{M_n^2 + p^2}$, where p is the spatial momentum.

4.6 Retarded thermal correlators in solvable cases

As emphasized before, we are interested in this chapter in the frequency structure of retarded thermal correlators. The free fermion mapping allows us to derive an explicit expression for this quantity in the integrable free case at $g = 0$. In particular, for zero momentum ($p = 0$), the retarded correlator $G_R^{-\frac{\pi}{a}\,\sigma^x}$ of the transverse magnetization can be derived as follows. From the Jordan–Wigner transformation (4.33), the relevant term is given by

$$G_R^{-\frac{\pi}{a}\,\sigma^x}(t > 0, j - l) = 4i \operatorname{Tr}\left([b_j^\dagger(t) b_j(t), b_l^\dagger(0) b_l(0)]\right). \tag{4.41}$$

Using the inverse of the Fourier modes (4.35) and working in an energy eigenbasis with modes (4.39), the correlator can be evaluated as

$$G_R^{-\frac{\pi}{a}\,\sigma^x}(t > 0, p = 0) = \frac{4}{N^2} \operatorname{Tr}\left(\sum_k \frac{\mathrm{e}^{-\beta\epsilon_k}}{Z_\beta} [\mathrm{e}^{i\epsilon_k t}\, b_k^\dagger b_k\, \mathrm{e}^{-i\epsilon_k t}, b_k^\dagger b_k]\right), \tag{4.42}$$

where Z_β is the finite temperature partition function. Upon insertion of the Bogoliubov-transformed fermion operators (4.36) in their inverted form (given as $b_k = u_k \gamma_k + i v_k \gamma_{-k}^\dagger$), only terms with an equal amount of creation and annihilation operators in the commutator contribute to the trace. In the thermodynamic limit, $N \to \infty$, the sum over k is replaced by $\sum_k \to \frac{N}{2\pi} \int \mathrm{d}k$. Terms of the form $\gamma_k^\dagger \gamma_k$ yield the Fermi–Dirac distribution $n_k = (1 + e^{\beta\,\epsilon_k})^{-1} = n_{-k}$ in the canonical ensemble average. Using $u_k^2 v_k^2 = \frac{\sin^2\theta_k}{4}$ (as defined in (4.37)), one arrives at

$$G_R^{-\frac{\pi}{a}\,\sigma^x}(t > 0, p = 0) = 2J \int_{-\pi}^{\pi} \mathrm{d}k\, (2n_k - 1)\, \sin^2\theta_k\, \sin(2\,\epsilon_k\, t). \tag{4.43}$$

A similar calculation for finite momentum p generalizes this result to

$$G_R^{-\frac{\pi}{a}\sigma^x}(t>0,p) = 2J\int_{-\pi}^{\pi} \mathrm{d}k\big[\sin\left(t(\epsilon_k+\epsilon_q)\right)(n_k+n_q-1)(u_kv_q+u_qv_k)^2 + \sin\left(t(\epsilon_k-\epsilon_q)\right)(n_k-n_q)(u_ku_q-v_kv_q)^2\big], \tag{4.44}$$

where $k-q\equiv p \pmod{2\pi}$.

We are primarily interested in the case of vanishing momentum. The integral formula (4.43) then can be understood via two-particle exchanges: The operator σ_j^x excites a continuum of states consisting of fermions with zero net momentum but distinct relative momentum. The corresponding analytic structure in the complex frequency plane can be derived by simple observations: The integral contains terms that oscillate in the time domain with frequencies ranging from $2\epsilon_0 = 2M_h$ (i.e. twice the fermion mass) to $2\epsilon_\pi = 8J-2M_h$ (containing the lattice spacing $a=2/J$). This results in a branch cut stretching between the IR and UV scale, set by these two limits. Fig. 4.8 shows this representation in the scaled complex ω plane in blue. From a mathematical viewpoint, it is well known that the location of branch cuts between two branch points is ambiguous. That is, one can alternatively represent the structure as shown in red in Fig. 4.8. Here, a branch cut stretches between the points $\pm 2M_h$, originating from the creation of fermion pairs with relative momenta $\pm p$ and hence zero net momentum. Additionally, there is a second branch cut connecting the UV scale with infinity and extra poles originating from zeros of the Fermi–Dirac function. They are known as *Matsubara frequencies* $\tilde{\omega}_n = -i\frac{\pi}{\beta}(2n+1)$ $(n\in\mathbb{N})$ [183]. As a consequence of he factor 2 in the sinus function in (4.43), the poles lie at $\omega_n \equiv 2\tilde{\omega}_n$. From the general remarks about correlators in section 4.2, we can identify their contribution as a transient effect. Due to this separation of IR and UV scales, this representation is inherent to a QFT viewpoint.

The result (4.43) is valid for an infinite chain but not yet in the continuum (arising in the limit $\beta J\to\infty$ at constant βM_h). The described features, in particular decaying poles, are therefore present also in the discrete spin chain system. In the conformal case ($M_h = M_g = 0$), we expect the continuum result to be given by CFT techniques. In fact, conformal symmetry entirely fixes in (1+1) dimensions the retarded two-point function on a line at non-zero temperature to the form [131,163]

$$D_R^{O_{\Delta=h_L+h_R}}(t>0,x) = i\theta(t)\left\{\frac{(\pi T_R)^{2h_R}}{\sinh^{2h_R}[\pi T_R(x-t+i\varepsilon)]}\frac{(\pi T_L)^{2h_L}}{\sinh^{2h_L}[\pi T_L(x+t-i\varepsilon)]} - (\varepsilon\mapsto-\varepsilon)\right\}, \tag{4.45}$$

where the subscripts L and R refer to left- and right-moving sectors. From the Fourier transformation of this function, assuming $T_L = T_R \equiv T = 1/\beta$, it follows that an operator of conformal dimension $\Delta = h_L + h_R$ has single poles at frequencies

$$\omega_n = \pm p - i\,2\pi\,T\,(\Delta+2\,n) \quad \text{for} \quad n\in\mathbb{N}_0. \tag{4.46}$$

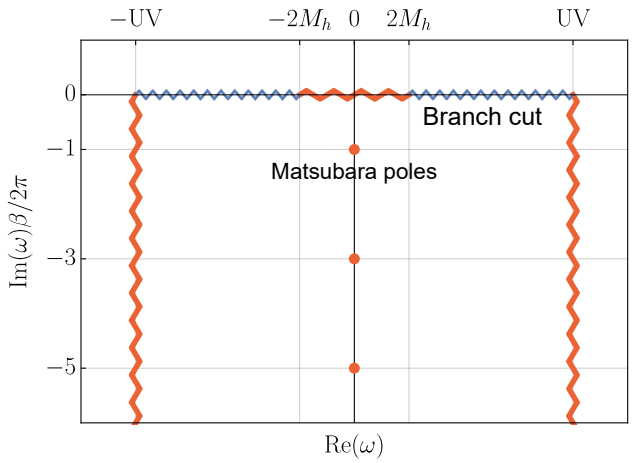

Figure 4.8: Analytic structure of the retarded thermal correlator (4.43). The freedom to deform branch cuts leads to two valid choices as illustrated in blue and red. The latter one decouples the UV scale from the IR which makes it more natural for QFT considerations. In this case, single poles related to Matsubara frequencies arise. Figure taken from [1].

These values are in agreement with the frequencies originating from the Matsubara poles for the $\Delta = 1$ operator considered above. The simplified Fourier transformation of (4.45) at $p = 0$, yields the following explicit result for the correlator (neglecting contact terms)

$$G_R^{\mathcal{O}_{\Delta=1}}(t > 0, p = 0) = -\frac{4\pi}{\beta} \mathrm{e}^{-\frac{2\pi}{\beta}t} \left(1 - \mathrm{e}^{-\frac{4\pi}{\beta}t}\right)^{-1}, \tag{4.47}$$

which has a sequence of poles at the values (4.46). Additionally, we can now read off that the residues are given by $-\frac{4\pi}{\beta}$. This value agrees with the prediction following from (4.43) in the scaling limit ($\beta J \to \infty$ at $M_h = 0$). The value of the residue of a transient pole therefore provides strong indications for us to correctly identify the QFT regime. We numerically extract these data by combining MPO simulations with a Prony based signal analysis method, which gives access to residues as normalization coefficients of complex exponentials. It will be demonstrated below that the CFT regime is reached even for moderate values of βJ in the order of 5 to 10.

Finally, we want to stress the dual holographic interpretation of the sequence of frequency values (4.46). In the important work [163], the authors identify these CFT modes as QNMs of the BTZ black hole solution. [55] This allowed, for the first time, the identification of thermalization time scales in a CFT from the inverse of the lowest transient mode in the decay of BH perturbations and initiated all further explorations of higher-dimensional QNMs as motivated in section 4.3 above. Interestingly, this in turn means that our spin chain setup allows us directly to address questions and problems, which have a dual gravitational interpretation, although we are not considering explicitly a holographic CFT.

[55] The BTZ metric, named after Bañados, Teitelboim and Zanelli, is a particular BH solution in AdS_3 [184].

4.7 Tensor network setup

Real and imaginary time evolution can be combined in TN simulations in order to obtain thermal response functions [185–188]. We are interested here to numerically calculate retarded thermal correlation functions of the form

$$G_R(t) = i\theta(t)\,\mathrm{Tr}(\rho_\beta[O_1(t), O_2(0)]) \tag{4.48}$$

for local operators defined in terms of Pauli matrices as

$$O_1(0) = \sum_j \sigma_j^{x,z} \quad \text{and} \quad O_2(0) = \sigma_{N/2}^{x,z}. \tag{4.49}$$

This amounts to the calculation of individual expectation values of the form

$$\langle O_1(t)O_2(0)\rangle_\beta = \mathrm{Tr}\left\{\rho_\beta U^\dagger(t)O_1(0)U(t)O_2(0)\right\}. \tag{4.50}$$

As discussed in detail in [188], the real and imaginary time steps can be grouped in different ways, the optimal configuration being dependent on the concrete setup. Here, we can evaluate the expectation value as

$$\langle O_1(t)O_2(0)\rangle_\beta = \mathrm{Tr}\left\{[U^\dagger(t/2)\rho_{\beta/2}O_1(0)U(t/2)]\,[U(t/2)O_2(0)\rho_{\beta/2}U^\dagger(t/2)]\right\}, \tag{4.51}$$

which allows us to gain a factor of two in the real-time evolution. We use the TEBD algorithm (cf. section 3.5.2) to efficiently represent the purified thermal state $\rho_{\beta/2}$ as a MPO approximation [189–192] through imaginary time evolution for a finite system with open boundary conditions. In the second group of operators in (4.51) (indicated by the brackets), the operator O_2 acts at time $t = 0$ onto this thermal state $\rho_{\beta/2}$ (at the mid chain position). Since it is a local operator, this step does not change the bond dimension of the MPO. The resulting new MPO is then evolved for time $t/2$. In the first group of operators in (4.51), the operator product of the thermal state with O_1 is evolved backwards in time. We use again the TEBD algorithm to implement the real-time evolution of the individual MPOs. The growth of entanglement during real time evolution is reflected by the increasing truncation error in the numerical simulation. The convergence of the results can be checked by comparing data for different values of the maximal bond dimension χ, or by comparing to the exact result when available. Evolving each term for only half the time hence allows us to reach longer total times with the same resources. Finally, the desired expectation value is obtained from the contraction of the two time evolved MPOs, which can be computed exactly in an efficient manner.

In general, the retarded correlator can be calculated w.r.t. the transverse or longitudinal Pauli matrix. Based on the general principles of the linear response framework (cf. section 4.2), the convolution of the correlator with a time-dependent profile of the fields h or g then either

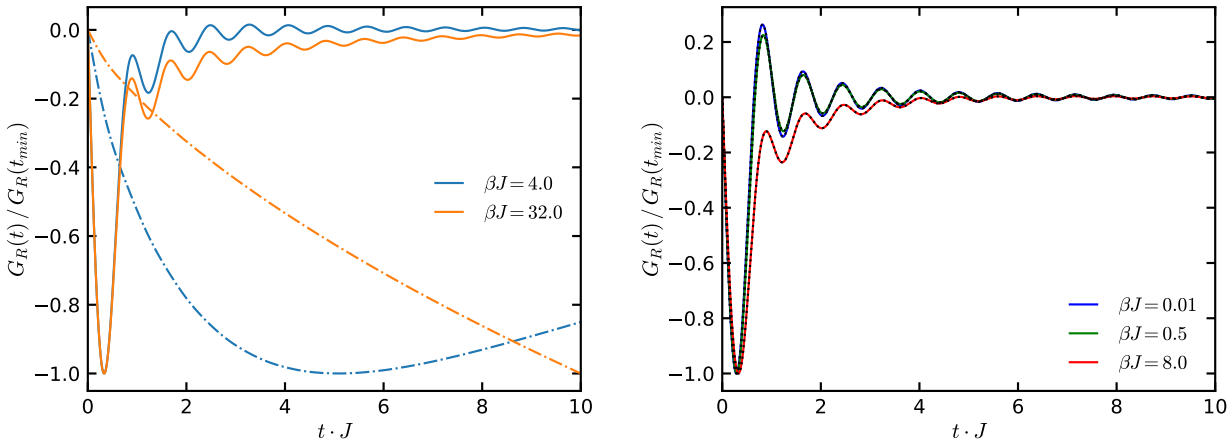

Figure 4.9: Left: Results of MPO simulations for the transverse (solid curves) and longitudinal (dash-dotted curves) response function (at $\beta M_h = 0.2$, $\beta M_g = 0$ in the ferromagnetic phase and two lattice spacing values corresponding to $\beta J = 4$ and $\beta J = 32$). Observe that the longitudinal response is oscillating on a much longer time scale.
Right: Results of MPO simulations (solid curves) and exact results from free fermions (black dotted curves) for the transverse response function at criticality ($\beta M_h = \beta M_g = 0$). One can observe an excellent agreement for all lattice spacing values βJ.
Numerical parameters: $N = 100$, $\chi = 200$, $J\delta t = 0.005$, $Jt_{\max} = 10$, 2^{nd} order Trotter decomposition. Both plots are scaled w.r.t. the minimum of the correlation function for graphical purposes. Figures taken from [1].

yields the transverse or longitudinal magnetization, which the system follows under small perturbations. From the discussions around the Ising QFT Hamiltonian (4.40), we know that the two corresponding CFT operators ϵ and σ differ by a factor of 8 in their scaling dimensions. Within coverable simulation time scales, the longitudinal response therefore decays too slowly to be seen and analyzed efficiently. The left panel in Fig. 4.9 demonstrates this for a particular parameter value in the massive free fermion regime. Here, the σ^z-correlator is calculated by the outlined method using MPO simulations.

From now on, we focus entirely on the transverse correlation function. The right panel in Fig. 4.9 shows the time dependence of this quantity for several temperatures (or lattice spacings) at criticality. One can observe damped oscillations, which qualitatively differ only at the lowest temperature $\beta J = 8$ near the ground state. Note that the visible signal is dominated by the UV, which causes fast oscillations at high frequencies. The aim to study IR physics therefore demands us to extract frequencies with small real parts. On top of the numerical data obtained by MPO simulations (shown as colored solid curves), the results of the free fermion solution (4.43) are superimposed (shown as dash-dotted curves). The two curves agree respectively very well in the whole time period.

4.8 Prony signal analysis

To analyze the analytic structure of the retarded response function, we need to exploit a method that is able to extract complex frequencies from the numerical real-time signal. The standard Fourier transformation is limited to real frequency values in this regard: Real frequencies (describing oscillations) appear as peaks in the spectrum. The imaginary frequency part (describing their decay) is, however, hidden in an indefinite way in the width of the peak. Complicating matters further, the frequency resolution depends on the total time interval available and therefore obscures the actual peak width. A way out is offered by the Prony method, which was invented in its original form already a long time ago [193]. The basic concept of this method is to represent a function (i.e. the retarded correlator) as a sum of complex exponentials,

$$G(t) = \sum_{k=1}^{M} c_k \, \mathrm{e}^{-i\,\omega_k\,t} \,. \tag{4.52}$$

Here, the coefficients c_k and frequencies ω_k are chosen complex valued and M is the (variable) total number of modes. The mathematical background of the Prony method and its generalization in terms of eigenfunctions of linear operators are explained in detail in [194], including numerical codes for their implementation. In its original form, Prony's method makes use of the fact that the ansatz (4.52) satisfies a finite difference equation for sparse input data $G_R(0), G_R(1), \ldots, G_R(2M-1)$. It consists of the following steps [194].

i) Construct the Hankel matrix $\mathbf{H} := (G_R(n+l))_{n,l=0}^{M-1}$ and the vector $\mathbf{g} := (G_R(M+n))_{n=0}^{M-1}$ and solve the system $\mathbf{Hp} = -\mathbf{g}$ for the coefficients $\mathbf{p} = (p_n)_{n=0}^{M-1}$.

ii) Set $p_M = 1$ and determine all roots $z_k \equiv \mathrm{e}^{-i\,\omega_k}$ of the characteristic polynomial $P(z) = \sum_{n=0}^{M} p_n z^n$.

iii) Construct the Vandermonde matrix $\mathbf{V} := (\mathrm{e}^{-i\,\omega_k n})_{n=0,k=1}^{M-1,M}$ and the vector $\mathbf{f}_1 := (G_R(n))_{n=0}^{M-1}$ and solve the system $\mathbf{Vc} = \mathbf{f_1}$ for the coefficients $\mathbf{c} = (c_k)_{k=1}^{M}$.

Due to the linearity of this system of equations, the algorithm is able to determine the frequencies ω_k independently from the coefficients c_k. For our numerics, we use a version of this Prony method known as `ESPRIT` (estimation of signal parameters via rotational invariance techniques) [195]. As a modification, this algorithm performs a SVD on the Hankel matrix and takes only singular values into account that are larger than some chosen threshold ε. The number of modes M represents then an upper bound. Some related methods, known as *linear prediction*, have also been used in the context of TN simulations [185,196–200].

Based on the functional ansatz (4.52), one can expect to faithfully recover single poles in the frequency space of the retarded correlator. However, the identification of branch cuts, which play a major role in the analytical solution discussed above and as visualized in Fig. 4.8, is not directly possible by this ansatz. The key novelty of our method here is to identify also the

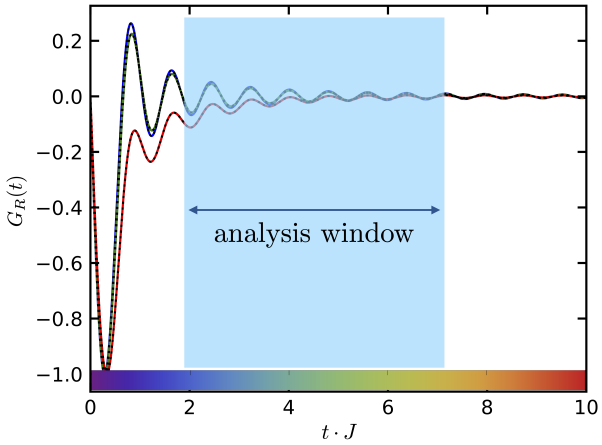

Figure 4.10: Schematic illustration of our Prony signal analysis procedure: The Prony method is applied only in the finite analysis window, which is sequentially shifted towards later times. For each analysis window, defined by its starting and end time, a unique color (shown in the colorbar) is associated to all identified complex frequency values.

latter as a sequence of single poles inherent to the Prony method we employ. This is achieved by applying the Prony algorithm to a sequence of time-shifted data analysis windows. See Fig. 4.10 for an illustration of this procedure. Identified complex frequencies are then visualized in different colors for each time window. Poles of the correlator will appear as frequencies that are stable across different time windows, while branch cuts are visible as streaks. The uncertainty of any such structure is related to its "fuzziness" in the complex ω plane. (In the next section we will develop a quantitative estimate of it based on a rigorous procedure.)

We test our signal analysis method in the free case for the transverse correlator (4.43), for which we have sketched the derived analytical structure in Fig. 4.8. The left panel in Fig. 4.11 shows the Prony result for that case at criticality, which allows to identify both the UV branch cuts and Matsubara poles: One can clearly see the first two transient poles on the imaginary axis. On the other side, the Prony method seems to favor a vertical representation of the UV branch cuts in the lower half plane, which are visible as the colorful bands of poles, which are concatenated from different time windows. The precise identification of these decaying structures is a clear advantage over the conventional Fourier transform, which was employed in a real-time context e.g. in [201], but allows a reliable identification of frequencies only on the real axis. The right panel in Fig. 4.8 shows the same situation but for finite momentum. In this case, only the first CFT transient is visible, which now attains a finite real part as given in (4.46). (Additional poles on the real axis arise from the lattice result (4.44).)

The ambiguity in the location of branch cuts is visible in Fig. 4.12. [56] Here, the retarded correlator is analyzed with the Prony method for two masses. For a small mass (left panel) the red representation of the analytic structure in Fig. 4.8 is obtained, while the blue representation is assumed for a larger mass (right panel). The Prony method seems to make implicitly a

[56] Such a non-uniqueness played in a similar context also a role in a kinetic theory model of [167].

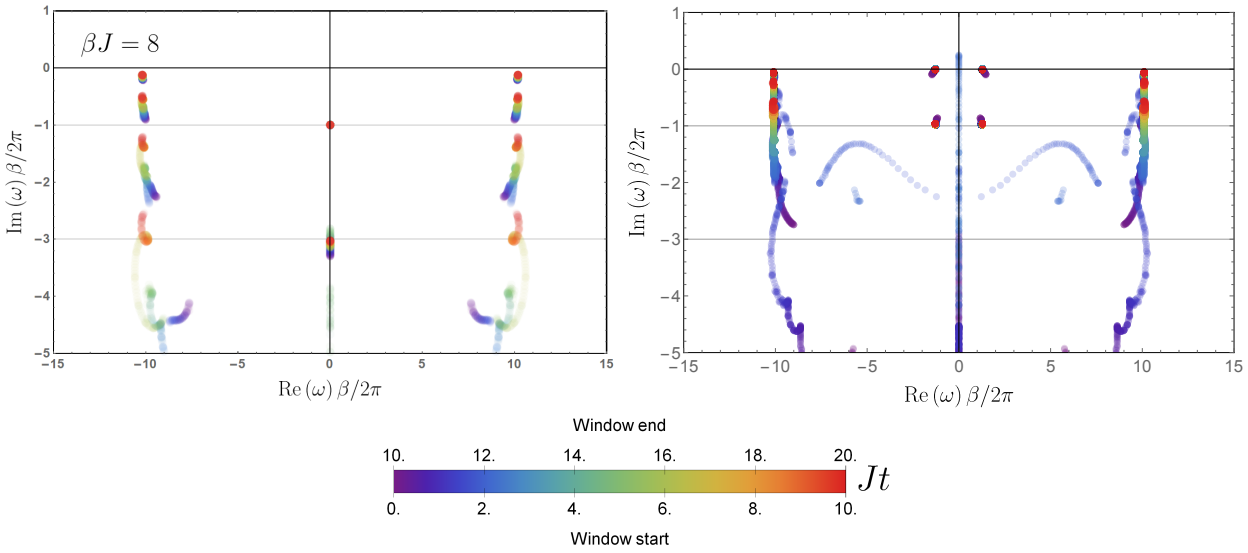

Figure 4.11: Result of the Prony method applied to the retarded transverse correlator (4.44) at criticality ($M_h = 0$) for zero momentum ($p = 0$, left) and finite momentum ($p = 1$, right). The shifted time windows in the signal analysis are visualized according to the shown colorbar. The identified complex frequency structure on the left has to be compared to the analytical expectation shown in red in Fig. 4.8 (for $M_h = 0$). At finite momentum, the Matsubara poles are shifted away from the imaginary axis according to (4.46). Left figure taken from [1].

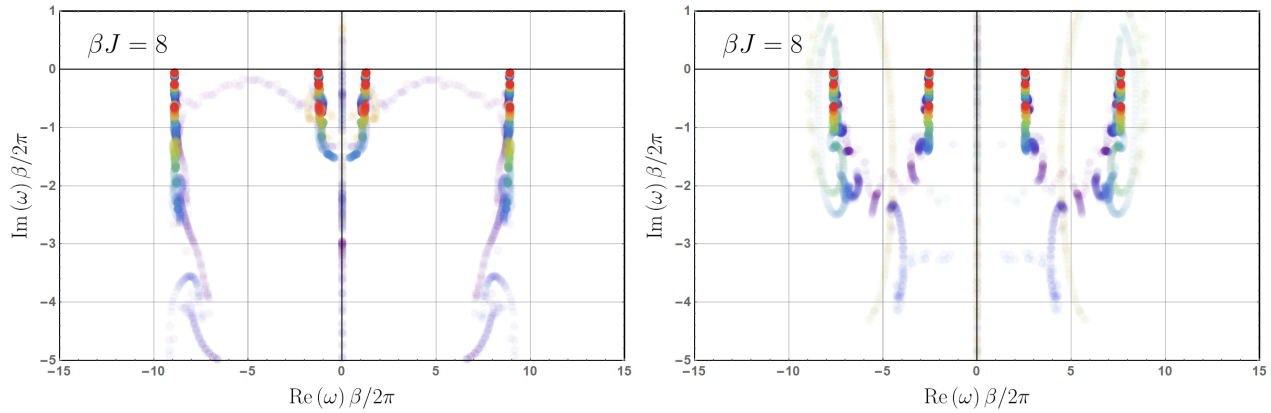

Figure 4.12: Result of the Prony method applied to the retarded zero momentum transverse correlator (4.43) at small mass ($M_h/J = 0.5$, left) and large mass ($M_h/J = 1$, right). The identified complex frequency structures have to be compared to the analytical expectation shown in red and blue in Fig. 4.8. The colorbar is as in Fig. 4.11.

choice, which favors a vertical alignment within the lower half plane. At an intuitive level, such a representation is favored at late times since poles with larger imaginary part will decay fast. However, this alignment then potentially obscures transient poles on the imaginary axis. As it becomes apparent from the left panel, the first transient is not visible anymore, since it is overlaid by the IR branch cut. Only the second transient is faintly identifiable. When putting the focus on the identification of transient features, the transverse mass hence should be small enough to not obfuscate Matsubara poles by branch cut locations.
In the following sections we want to use the MPO simulations in combination with the presented Prony signal analysis technique to analyse properties of the retarded thermal correlator in the Ising QFT.

4.9 Transient singularities of the retarded thermal correlator

4.9.1 The free fermion QFT limit

The preceding discussions have shown exemplarily that the Prony method allows us to identify the lowest transient poles when applied directly to the analytical integral formula (4.43) for the ϵ correlator. In the CFT case they are given by (4.46), which exemplifies them as intrinsically thermal features that cause exponential decays in time. We now want to study systematically the QFT limit $\beta J \to \infty$ by applying the Prony analysis to integrable massive free fermion results (at $M_h \neq 0$, $M_g = 0$) in comparison to the numerical MPO simulations. Based on the findings about branch cut locations, we choose a small transverse perturbation $\beta M_h = 0.2 \equiv \text{const}$. The continuum is approached for $\beta J = \{2, 4, 8, 12, 16, 32\}$, which translates into transverse field values $h = \{0.95, 0.975, 0.9875, 0.991667, 0.99375, 0.996875\}$ in the ferromagnetic phase. Since the transverse mass M_h/J is decreasing as the critical point at $h = 1$ is approached, the IR length scale of the free fermion $l \sim 1/M_h$ is increasing. We therefore have to keep in mind that finite size effects might play a role for a considered chain of $N = 100$ sites. Under the assumption of a prefactor of order $l \sim \mathcal{O}(1)/M_h$, this should set in only at the largest chosen value of $\beta J = 32$.
Fig. 4.13 shows the resulting Prony diagrams for the free fermion results in an infinite system (left) and the MPO simulation of the finite spin chain (right) at two selected lattice spacing values $\beta J = 8, 32$ (top and bottom). As observed previously, the UV branch cut is approximated as a vertical line of poles in the lower half plane. The IR branch cut between the branch points $\pm 2M_h$ is visible at $\beta J = 8$ only as a pole at the origin. It cannot be clearly resolved since only the time interval up to $Jt_{max} = 10$ is analyzed, while such small real frequencies would require longer time intervals to see their oscillation periods. In contrast to the left plot in Fig. 4.12 (which is for a larger transverse mass), it does, however, not obscure the transient

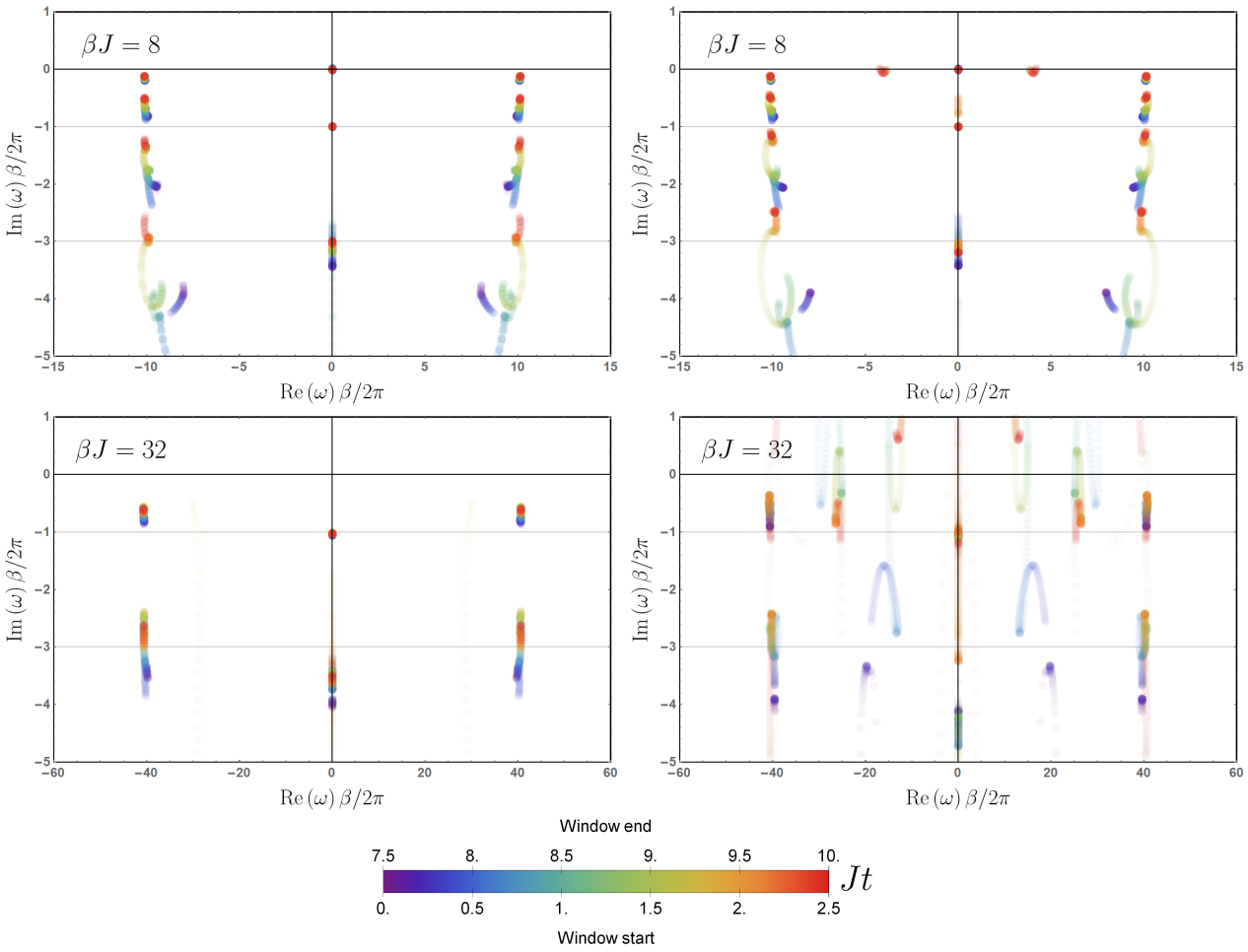

Figure 4.13: Results of the Prony frequency analysis for the transverse retarded correlator in the free (integrable) continuum limit at $\beta M_h = 0.2$. Identified poles are shown in the scaled complex $\omega\beta/2\pi$ plane based on the analytical result (left column) and MPO simulations (right column) for two temperatures (first and second row). Horizontal lines denote the analytical locations for the transients.
Numerical parameters: $N = 100$, $\chi = 200$, $J\delta t = 0.005$, $Jt_{\max} = 10$, 2^{nd} order Trotter decomposition. Figures taken from [1].

poles, which are our main focus here. On the rescaled imaginary axis, these decaying poles (4.46) are located at $-1, -3, \ldots$. In all examples, the first transient pole is clearly visible. For both the analytical result and the MPO simulation at $\beta J = 8$ also the second transient is visible, whereas at $\beta J = 32$ only the Prony method applied to the analytical result allows an identification of the latter. The previously anticipated finite size effects are visible in the lower right panel of Fig. 4.13. Here, the MPO simulation of the finite spin chain causes spurious and erratic poles in the complex ω plane.

From the Prony analyses we want to extract the position of the first two transients in a quantitative manner. Using our signal analysis technique, we chose an analysis window that encompasses 75% of all discrete data points of the retarded correlator, which is then shifted towards later times. In each time window, there are potentially frequencies which respectively

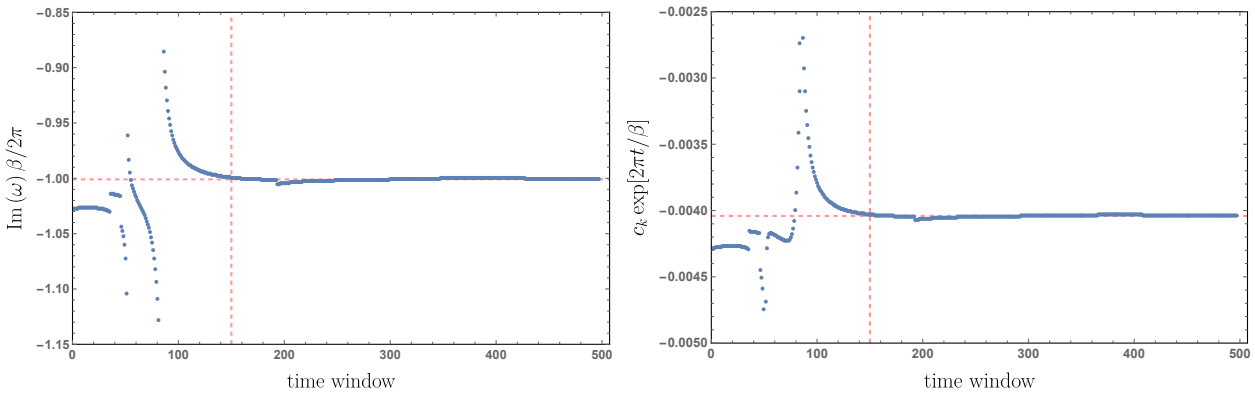

Figure 4.14: Example of a Prony analysis applied to the MPO simulation of the retarded transverse correlator at $\beta J = 8$. Left: (Scaled) position of the first transient on the imaginary axis for each time window (with time increment step $\delta t = 0.005$). Right: The corresponding coefficient multiplied with the inverse time dependence $\exp[2\pi t/\beta]$ for each time window. Horizontal red lines indicate respectively the average value which is assumed for time windows later than the vertical red lines indicate. Figures taken from [1].

can be identified as the transient poles. A sufficiently large number of time windows therefore allows us to obtain statistically significant information on the position and stability of decaying poles. The left panel in Fig. 4.14 demonstrates this procedure for the first transient in a selected example. The identified position on the imaginary axis is plotted for all time windows. The numerical values are unstable at early times, which is presumably caused by the overlapping of several transient frequencies. At later times, when higher-order transients are decayed enough and thus do not overlap the signal anymore, the imaginary frequency stabilizes. In each simulation, we identify this stable branch, from which we calculate its mean value and standard deviation.

The resulting uncertainties of the first two transient positions, which we determine from this analysis, are shown as error bars in Fig. 4.15. The left panel is based on the free fermion calculation, the right on the MPO simulation. The plots demonstrate that the numerical continuum limit for increasing values of βJ is consistent with the analytical expectations $-\frac{1}{2\pi}\,\mathrm{Im}(\beta\omega_1) = 1$ and $-\frac{1}{2\pi}\,\mathrm{Im}(\beta\omega_2) = 3$. In particular, the first transient position can be identified for all temperatures (or lattice spacings) in the free fermion and MPO case. The uncertainty increases from less than than 1% ($\beta J \leq 8$) up to 5% (free fermions) or 18% (MPO simulations) at $\beta J = 32$. The second transient can be extracted with less accuracy in the temperature range $8 \leq \beta J \leq 32$ for free fermions and $8 \leq \beta J \leq 16$ for the MPO simulations. The fact that this second mode is not visible at low βJ is that the UV branch cut is bending towards the imaginary axis and therefore obscures the decaying poles. At large βJ, on the other side, it is an interplay of finite time and finite size effects that hamper the visibility of the pole. The latter becomes relevant for the MPO simulations, where the increasing fermion (or correlation) length scales close to criticality can exceed the system size. Since the uncertainty increases also in the free fermion case (for an infinite system), it is also the limited Prony time

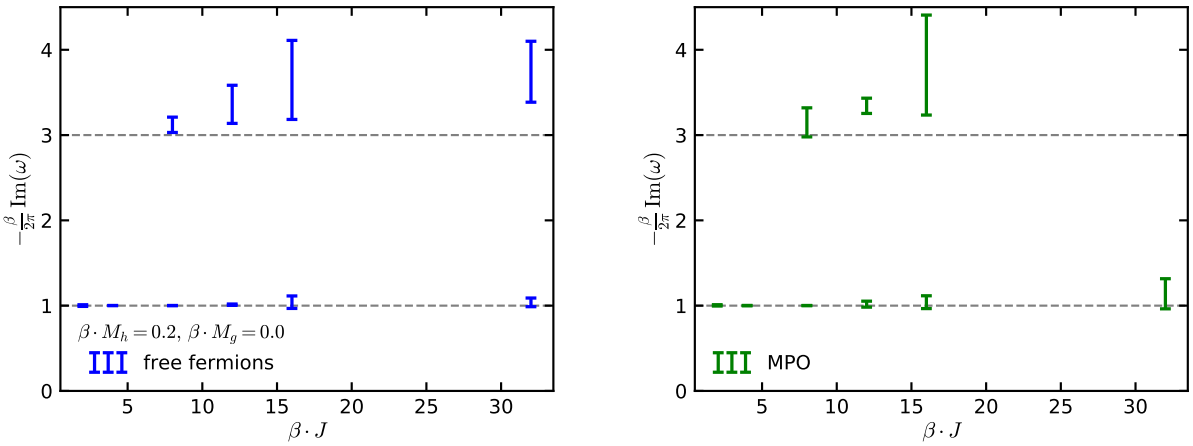

Figure 4.15: Results of the extracted position of the first two transient poles in the free (integrable) ferromagnetic phase at $\beta M_h = 0.2$ based on the Prony analysis applied to the analytical result (left) and MPO simulation (right). Error bars denote the uncertainty of the calculated pole locations, grey lines represent the analytical values. The continuum limit is approached for increasing values βJ. Figures taken from [1].

window that causes deviations from the analytical frequency value.

The piece of information, which was left out until now are the coefficients c_k in the Prony ansatz (4.52). The right panel in Fig. 4.14 shows their extracted values in all time windows for the same parameter example as before. They are multiplied with the inverse time dependence of the first decaying mode. As in the case for the imaginary frequency value on the left side, a stable branch forms at late times. Using the same methodology as for the pole location, we calculate the residue r_1 of the transient as its mean value. The corresponding uncertainties are shown in the right panel of Fig. 4.16. For a comparison, we perform the same analysis also in the CFT regime (i.e. at criticality) as shown in the left panel. For both cases, one can see that the residues approach for increasing values βJ the analytical continuum value (shown as grey dashed lines), which is calculated from (4.43). Despite a non-optimal numerical resolution, one can clearly find a shift in the extracted residue data between the critical point (describing the CFT) and the ferromagnetic phase (describing a massive free fermion QFT). The best agreement is visible at intermediate values $\beta J = 5 \ldots 15$ for both the data based on free fermion results (shown in blue) and MPO simulations (shown in green). The deviation of the MPO based result at the largest inverse temperature $\beta J = 32$ indicates again the impact of finite size effects. As explained in section 4.6, the residue is important to identify the QFT regime. From these findings we hence conclude that our Prony signal analysis method is indeed capable of identifying the proper QFT regime at large enough βJ. Moreover, the results suggest that the method is sensitive enough to see the effect of massive transverse perturbations. This applies to both the analyses based on analytic free fermion results as well as to our MPO simulations, which, upon marginal finite size effects, agree very well with each other in all our studied quantities.

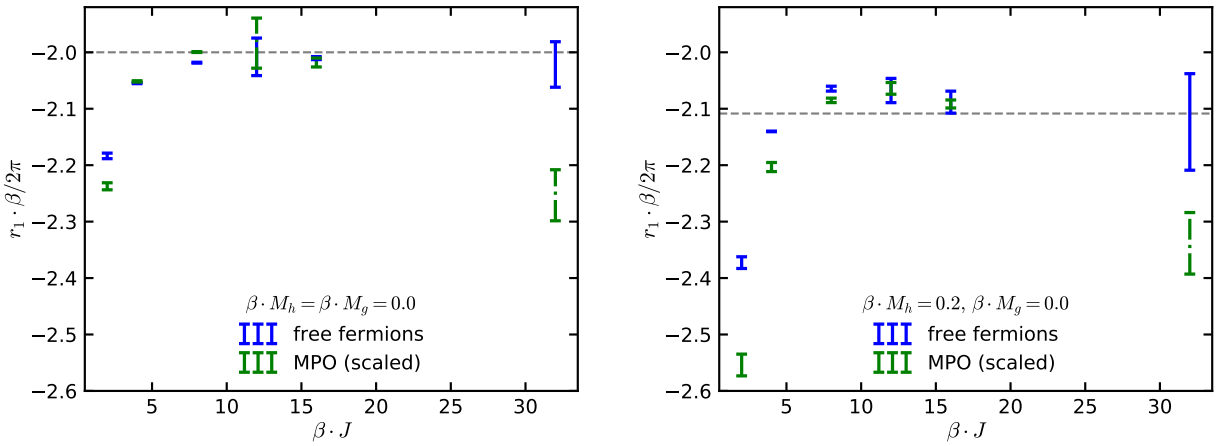

Figure 4.16: Results of the extracted residue of the first transient in the continuum limit at criticality (left) and for finite transverse mass in the ferromagnetic phase (right). Blue error bars are based on analytical results, green error bars on MPO simulations. Grey lines represent the analytical values. The MPO simulations are rescaled to take the finite chain normalization from the free fermion mapping into account. Figures taken from [1].

4.9.2 The nonintegrable QFT limit

Having established our TN based simulations in combination with the signal analysis technique as a reliable tool to extract thermal QFT information in the free and integrable regime of the $2D$ Ising QFT, we now turn to interacting nonintegrable parameter ranges, where our analyses allow us to make predictions. In particular, we want to systematically analyze the question whether the locations (4.46) of the transients are modified for finite longitudinal perturbations ($M_g \neq 0$). This investigation is directly motivated by holographic results (cf. section 4.3), where it was found that integrability breaking perturbations can lead to changes in the QNM structure (cf. Fig. 4.3). Here, we choose $\beta M_h = 0.5$ and $\beta M_g \approx \{0.27, 0.54, 1.08, 1.62\}$. From our previous explorations we expect that it will be possible to describe continuum physics for the parameter range $\beta J = \{6, 8, 10\}$. We again use MPO simulations for a spin chain with $N = 100$ sites to calculate the transverse retarded correlator up to the maximal time $J\, t_{max} = 10$.

Fig. 4.17 shows the resulting Prony diagrams for two selected values of βM_g (first and second row) in the ferromagnetic ($h < 1$, left column) and paramagnetic phase ($h > 1$, right column) at $\beta J = 10$. A first transient mode is visible at $\frac{\beta}{2\pi}\,\mathrm{Im}(\omega) \approx -1$ in all plots. The blurred set of poles in the lower left panel (for the largest integrability breaking $\beta M_g \approx 1.62$) around this frequency value indicates that the corresponding uncertainty is larger in the ferromagnetic phase than in the paramagnetic phase (in which a clearer pole is visible in the lower right panel). This implies that the continuum limit is not identical in the two phases, which can be explained with the nonsymmetric existence of meson versus quasiparticle states in these two phases. In addition, also the second transient mode is identifiable on the imaginary axis in all parameter examples of Fig. 4.17. However, its uncertainty is naturally larger (visible

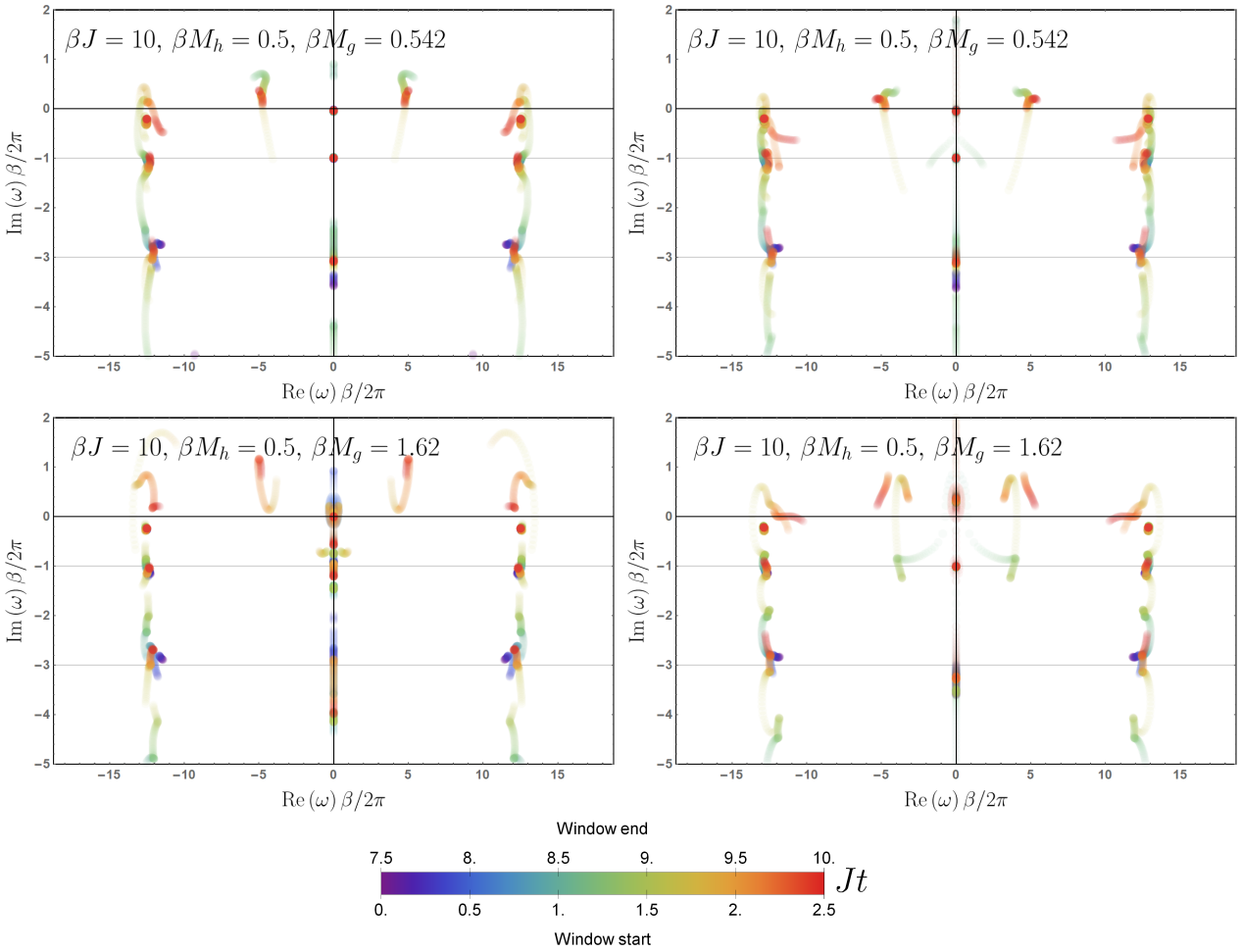

Figure 4.17: Results of the Prony frequency analysis for the transverse retarded correlator in the nonintegrable continuum limit for two integrability breaking parameters βM_g (first and second row). Identified poles are shown in the scaled complex $\omega\beta/2\pi$ plane in the ferromagnetic (left column) and paramagnetic (right column) phase. Horizontal lines denote the analytical locations for the transients in the free (integrable) case for a comparison. Numerical parameters: $N = 100$, $\chi = 200$, $J\delta t = 0.005$, $Jt_{\max} = 10$, 2^{nd} order Trotter decomposition. Figures taken from [1].

as a fuzzier pole structure), since it is a sub-leading contribution that can be less accurately determined by the Prony analysis. We therefore focus entirely on the first transient mode in the following quantitative discussions of this section.

Using the same analysis technique as in the integrable massive free fermion case, we determine the position (i.e. frequency value) of the the first transient on the imaginary axis and its residue. To further strengthen the robustness of this analysis, we vary the Prony cutoff value in the range $10^{-6} \leq \varepsilon \leq 10^{-4}$ and the length of the time analysis window in the range $75-85\%$ of the total discrete simulation data. We estimate the resulting uncertainty as the mean value from several parameter combinations in the Prony method. Fig. 4.18 shows the so obtained frequency values in both phases. For increasing perturbations βM_g and increasing βJ the uncertainty grows up to 13 % in the ferromagnetic phase while it does not exceed 5% in the

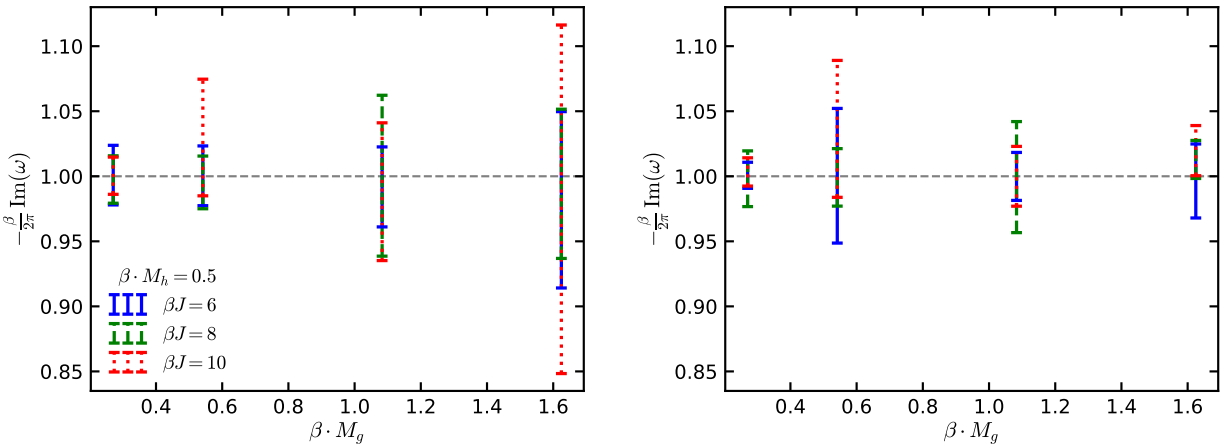

Figure 4.18: Results of the extracted position of the first transient pole in the ferromagnetic (left) and paramagnetic (right) phase using TN+Prony. The continuum limit is approached for increasing values βJ at fixed $\beta M_h = 0.5$ and different values of βM_g. Figures taken from [1].

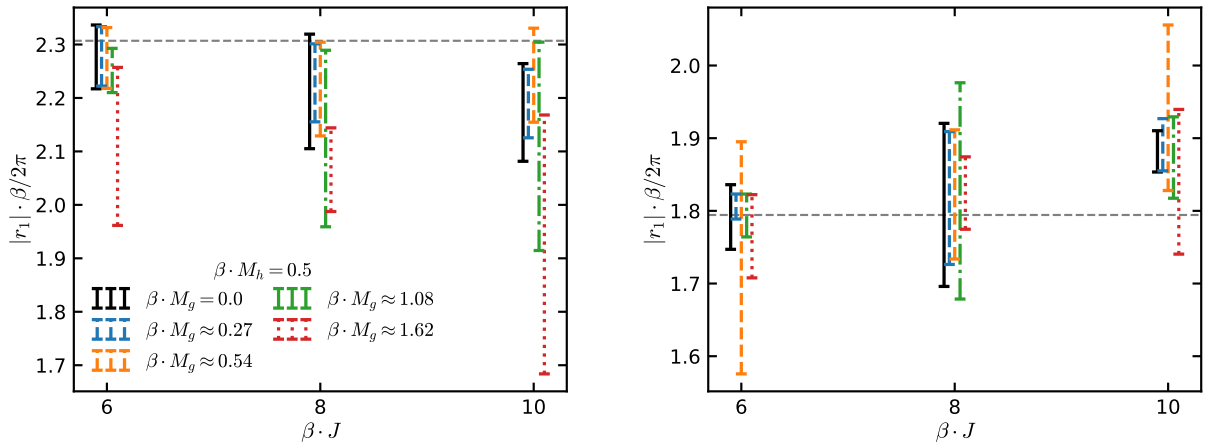

Figure 4.19: Results of the extracted residue of the first transient pole in the ferromagnetic (left) and paramagnetic (right) phase using TN+Prony. The continuum limit is approached for increasing values βJ at fixed $\beta M_h = 0.5$ and different values of βM_g. For a comparison the free (integrable) case ($\beta M_g = 0$), with analytical result given by the grey dashed line, is shown by the black error bars. The error bars are shown slightly displaced for graphical purposes. Figures taken from [1].

paramagnetic phase. This discrepancy is again a signature of differences in the continuum limit between the two phases. Importantly, all obtained values are consistent with the CFT value $\frac{\beta}{2\pi}\,\mathrm{Im}(\omega_1) = -1$ (indicated by the grey dashed line). Under the influence of longitudinal perturbations, the position of the leading transient does not seem to undergo considerable changes within the achieved numerical resolutions.

Further information on the leading transient is provided by the corresponding residues r_1, which are shown in Fig. 4.19. The extracted uncertainties of the scaled values $|r_1|\beta/2\pi$ are plotted in dependence of the inverse temperature βJ for all ferromagnetic (left) and paramag-

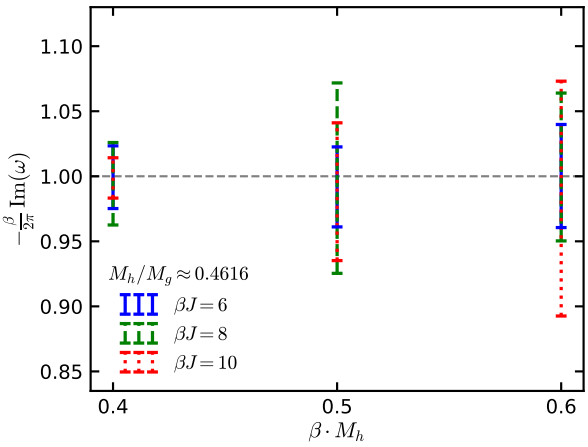

Figure 4.20: Results of the extracted position of the first transient pole in the ferromagnetic phase using TN+Prony. The continuum limit is approached for increasing values βJ at fixed $M_h/M_g \approx 0.4616 \equiv$ const and different values of βM_h and βM_g. Figure taken from [1].

netic (right) perturbations. For a comparison, black error bars denote the result of the same analysis for the free case ($\beta M_g = 0$) with an analytical result represented by the grey dashed line. As for the pole locations, the uncertainties grow for increasing values of βJ and βM_g. There seems to be the tendency that residues decrease in the ferromagnetic phase and increase in the paramagnetic phase as the continuum is approached for growing values βJ. Observe in particular the situation represented by the orange error bars, when the transverse ($\beta M_h = 0.5$) and longitudinal perturbation ($\beta M_g \approx 0.54$) are comparable. In this case the data seem to be consistent with the analytical value of the integrable free result. That is, the nonintegrable longitudinal perturbation does not seem to modify the residue value.

To further confirm the independence of the transient position on the perturbation, we additionally perform independent simulations of the transverse retarded correlator with different values of βM_h and βM_g, but keeping their ratio $M_h/M_g \approx 0.4616$ constant. The continuum is approached for $\beta J = \{6, 8, 10\}$ in the ferromagnetic phase with results presented in Fig. 4.20. Here, the data points at $\beta M_h = 0.5$ (corresponding to $\beta M_g \approx 1.08$) are identical to the third set of poles in the left panel of Fig. 4.18. The varying perturbations probe different instances of the Ising QFT. Also in this scenario, all data points are consistent with the CFT result for the pole position (shown as grey dashed line).

In summary, we have shown that the first transient mode, as the single-pole singularity governing the leading exponential decay of the retarded thermal correlator, exists also in the case of integrability breaking longitudinal perturbations of the Ising QFT. Within the uncertainties originating from the MPO simulations and subsequent signal analysis with the Prony method, we make the surprising prediction that its position on the lower imaginary frequency axis does not experience significant systematic deviations from the free fermion QFT result $\frac{\beta}{2\pi}\,\mathrm{Im}(\omega_1) = -1$. This conclusion is valid for both the ferromagnetic and paramagnetic phase of the Ising QFT.

4.10 Meson singularities of the retarded thermal correlator

4.10.1 Finite temperature effects

As soon as a longitudinal field g is turned on in the ferromagnetic phase of the Ising model, free fermions get confined and form nonperturbative meson bound states. In the paramagnetic phase the (perturbative) counterpart can be interpreted as magnons (spin waves). In this section, we use the combination of MPO simulations and Prony signal analysis in the longitudinal parameter regime to study the retarded ϵ correlator at non-zero temperature $T = /\beta$ and vanishing spatial momentum $p = 0$. In essence, the discussions in this section show that the branch cut along the real axis between $\pm 2M_h$ (cf. Fig. 4.8), which originated for a free fermion CFT from the exchange of zero net momentum fermion pairs, is transformed into a set of single poles at frequencies corresponding to meson masses.

In the integrable E_8 theory there are 8 stable mesons whose mass ratios are analytically known as tabulated in Tab. 4.1. Similar to the extraction of transient frequencies, we benchmark the accuracy of our mass predictions at a very low temperature by determining their frequency ratios on the real axis. The numerical results for seven out of eight mesons are listed in the last row in Tab. 4.1. Except the heaviest detected meson, all mass ratios are in accordance with the analytical value within 1.5% and in three cases even within a fraction of a percent.

We now consider the interacting nonintegrable regime of the Ising QFT in detail. We choose $M_h/J = 0.125$ and $M_g/J \approx 1.354$, keeping the ratio $M_h/M_g \approx 0.09$ constant. For these theory parameters, meson or particle masses have been calculated previously using numerical truncated Hamiltonian methods [180,181]. From these results the mass gaps, i.e. the the masses of the first excited states, follow as $M_1/J \approx 1.5$ in the ferromagnetic and $M_1/J \approx 1.2$ in the paramagnetic phase. Fig. 4.21 shows the mesonic part of the Prony reconstructed correlator from the MPO simulations in both phases at low temperature ($\beta M_1 \approx 24.5$ and $\beta M_1 \approx 19.5$). Identified frequency poles agree very well with the known meson/particle masses. In particular, we can identify 7 mesons in the ferromagnetic phase and 2 particles in the paramagnetic phase (indicated respectively as solid vertical lines). In fact, in the latter also an additional pole at $\mathrm{Re}(\omega)\beta/2\pi \approx 8$ is visible, which was previously not predicted as a particle in the literature.

Slightly above M_3 in the ferromagnetic phase or M_2 in the paramagnetic phase, there is a fuzzy structure of poles appearing. It is lying at $2M_1$, which marks the two-particle continuum threshold (indicated respectively as dashed vertical lines). This feature should be associated with a branch cut, which is identified as a set of poles that are the actual source of this fuzziness. In both phases, there is a further fuzzy structure appearing slightly below M_1 (indicated respectively as dashed vertical lines). This value, in fact, is an effect of open boundary conditions that enable the existence of excitations close to the edges of the chain. It is consistent with a finite size result found with the DMRG algorithm.

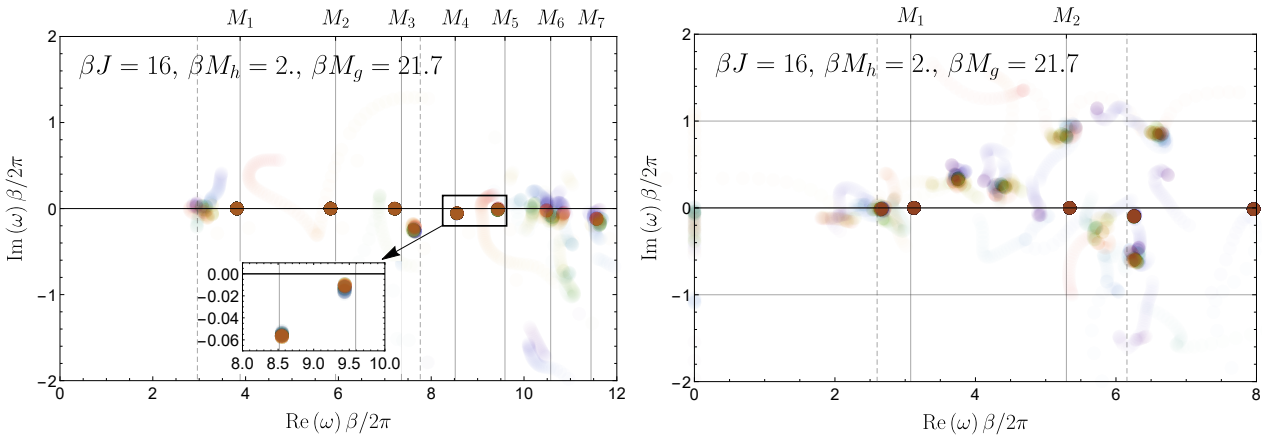

Figure 4.21: Results of the Prony analysis of the retarded transverse correlator of $\epsilon = i\,\bar{\psi}\psi$ near the vacuum in the nonintegrable ferromagnetic (left) and paramagnetic (right) phase. Solid vertical lines represent meson masses from ref. [180]. Dashed lines mark the continuum threshold of $2M_1$ and a boundary state calculated with DMRG. The inset zooms in on the 4^{th} and the 5^{th} meson to emphasize their imaginary parts.
Simulation parameters: $N = 200$, $\chi = 170$, $J\,\delta t = 0.02$, $J\,t_{\max} = 50$, 2^{nd} order Trotter decomposition.

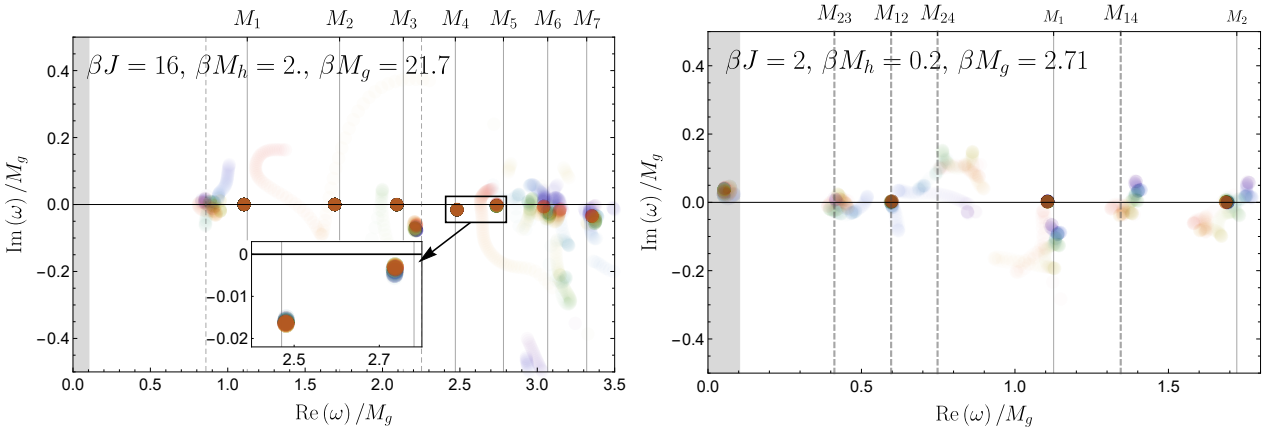

Figure 4.22: Results of the Prony analysis of the retarded transverse correlator of $\epsilon = i\,\bar{\psi}\psi$ near the vacuum (left) and for the highest achieved temperature (right) in the nonintegrable ferromagnetic phase. The shaded regions indicate frequencies with wavelengths not fitting in the time window. Solid vertical lines represent meson masses from ref. [180].
Left: The dashed lines mark the continuum threshold of $2M_1$ and a boundary state calculated with DMRG. The inset zooms in on the 4^{th} and the 5^{th} meson to emphasize their imaginary parts. Right: The dashed lines indicate mass differences appearing as a result of heating the system.
Simulation parameters: $N = 200$, $\chi = 170$, $J\,\delta t = 0.02$, $J\,t_{\max} = 50$, 2^{nd} order Trotter decomposition. Figures taken from [1].

As a consequence of integrability breaking, meson poles above the continuum threshold can develop an imaginary part, indicating their instability. In particular, this appears for the fourth and fifth meson in the ferromagnetic phase. The ratio between their imaginary parts (see inset in the left panel of Fig. 4.21) can be deduced from the Prony result as 0.22 ± 0.04, which is in surprisingly good agreement with the value 0.233 obtained in ref. [179].

The effect of increasing the temperature is studied in Fig. 4.22 for the ferromagnetic phase. For a comparison, the left panel is the same as in Fig. 4.21, but the data are now shown in units of M_g, which allows some further interesting observations. In particular, the deviation of the of the first meson mass ratio $M_1/M_g \approx 1.1$ from 1.0 indicates the effect of the transverse perturbation on top of the E_8 regime, in which $M_1 = M_g$ holds. This effect is at the same order as the chosen parameter values $M_h/M_g \approx 0.09$ suggest. Simulations at high temperature $\beta M_1 = \mathcal{O}(1)$ are numerically more demanding, since the entanglement growth is larger. The right panel in Fig. 4.21 shows the highest achieved temperature with $\beta M_1 \approx 3$. A clear thermal effect, which is not present in the low temperature result on the left, is the appearance of poles at locations corresponding to mass differences $M_{ij} \equiv M_i - M_j$. In particular, M_{12} is visible as a clean pole. Additional fuzzier pole structures are also visible for M_{23}, M_{24} and M_{14}. The existence of such mass differences can be understood from a semi-analytic treatment of the retarded thermal correlation function. In Fourier space (such that $\int \mathrm{d}x \, \exp(ipx) = \int \mathrm{d}x \, 1$ for $p = 0$) and in an energy eigenbasis in which the Fermi–Dirac distribution $n(E)$ enters, the correlator can be expressed as

$$
\begin{aligned}
&G_R^O(t > 0, p = 0) = i\,\theta(t)\,\mathrm{Tr}(\rho_\beta[O_1(t,x), O_2(0,0)]) \\
&= i \int \mathrm{d}x \int \mathrm{d}E'\, n(E') \frac{\mathrm{e}^{-\beta E'}}{Z_\beta} \langle E'| \, [O_1(t,x), O_2(0,0)] \, |E'\rangle \\
&= i \int \mathrm{d}x \int \mathrm{d}E' \mathrm{d}E''\, n(E') n(E'') \frac{\mathrm{e}^{-\beta E'}}{Z_\beta} \big\{ \langle E'| \, O_1(t,x) \, |E''\rangle \, \langle E''| \, O_2(0,0) \, |E'\rangle - \\
&\qquad\qquad \langle E'| \, O_2(0,0) \, |E''\rangle \, \langle E''| \, O_1(t,x) \, |E'\rangle \big\} \\
&= i \int \mathrm{d}x \int \mathrm{d}E' \mathrm{d}E''\, n(E') n(E'') \frac{\mathrm{e}^{-\beta E'}}{Z_\beta} \big\{ \mathrm{e}^{i(E'-E'')t} \langle E'| \, O_1(0,x) \, |E''\rangle \, \langle E''| \, O_2(0,0) \, |E'\rangle - \\
&\qquad\qquad \mathrm{e}^{-i(E'-E'')t} \langle E'| \, O_2(0,0) \, |E''\rangle \, \langle E''| \, O_1(0,x) \, |E'\rangle \big\} \\
&= i \int \mathrm{d}x \int \mathrm{d}E' \mathrm{d}E''\, n(E') n(E'') \frac{\mathrm{e}^{-\beta E'}}{Z_\beta} 2i\,\mathrm{Im} \Big\{ \mathrm{e}^{i(E'-E'')t} \langle E'| \, O_1(0,x) \, |E''\rangle \, \langle E''| \, O_2(0,0) \, |E'\rangle \Big\} .
\end{aligned}
$$

Here, we made use of the operator time evolution for O_1 and the observation that the two summands in the bracket on the second last line are complex conjugate of each other, and therefore $z - z^* = 2i\,\mathrm{Im(z)}$ where z symbolizes the first summand. Exponentials of the form $\mathrm{e}^{i(E'-E'')t}$ do not remain in the zero temperature limit $\beta \to \infty$ and correspond to our observed mass differences at high temperatures.

Within our uncertainties, we do not observe that meson masses (i.e. the real frequency part of

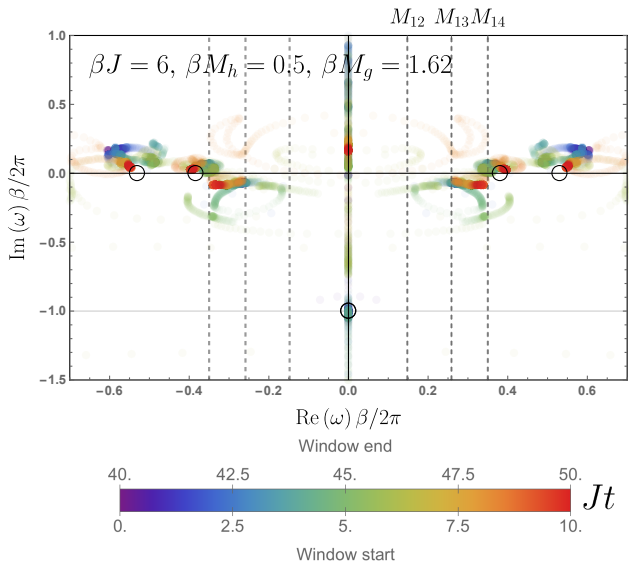

Figure 4.23: Results of the Prony reconstruction of the retarded transverse correlator of $\epsilon = i\bar{\psi}\psi$ in the nonintegrable ferromagnetic phase in the continuum limit. The circles represent vacuum meson masses [180] and the leading transient for the free fermion QFT case, respectively. Dashed lines indicate meson mass differences.
Simulation parameters: $N = 200$, $\chi = 250$, $J\,\delta t = 0.005$, $J\,t_{\max} = 50$, 2^{nd} order Trotter decomposition. Figure taken from [1].

poles) or decay rates (imaginary frequency part) change as the temperature is increased. Such a feature would be a rough analogy to the QCD deconfinement phase transition. In this high-temperature regime, one can expect that the natural degrees of freedom become fermions. We analyze this numerically challenging problem in the context of meson melting in section 6.3.1, where we can observe a decrease of the residues associated to the meson poles.

While we have so far discussed transient effects and meson states separately, we finally demonstrate that both features can be detected simultaneously in the Prony reconstructed correlator signal. Fig. 4.23 shows such a nonintegrable example in the ferromagnetic phase. The first decaying pole is naturally most visible in light blue colors at early time windows (when the transient contribution is not yet decayed too much), while meson states at large real frequencies are best identified at late times (in red colors). The numerical results are in reasonable agreement with the analytical data for the meson masses and what in a CFT would be the transient's position. Also in this case, features at meson mass differences are visible. Poles on the positive imaginary axis are attributed to numerical artefacts. This analysis demonstrates that nonperturbative bound state features, including thermal effects on such meson states, and purely thermal poles causing decaying (transient) signals can be jointly identified in the QFT regime.

4.10.2 Ground state simulations

The main motivation for the research project under discussion are thermal effects in $2D$ QFTs, which are exemplarily studied using the Ising model. But of course the same methodology of TN simulations and Prony signal analysis can also be used to explore ground state properties. In this final section we demonstrate that by analyzing meson features in the retarded two-point function in the vacuum. We consider the nonintegrable ferromagnetic phase with the same transverse and longitudinal mass as in Fig. 4.22 in the previous section.

In the fist approach, we calculate the ground state $|0\rangle$ using the DMRG algorithm for some chosen bond dimension $\sqrt{\chi}$. The ground state projector $|0\rangle\langle 0|$ is then represented as a MPO with bond dimension χ. The subsequent real-time evolution of the retarded response function is performed performed with the same TN setup as in the thermal case. The left panel in Fig. 4.24 shows the result of the Prony reconstruction. Similarly to the very low temperature result in Fig. 4.22 (left panel), the first three stable mesons can be identified very accurately. While the continuum threshold $2M_1$ is again visible as a branch cut stretching vertically in the complex frequency plane, the boundary state below M_1 is not seen here. The ratio of the imaginary parts of the fifth to the fourth meson agrees equally well with the prediction in ref. [179] as in the small temperature simulation. Structures at higher frequency values become more fuzzy in the Prony reconstruction but still are identifiable at positions matching known meson masses. Overall, these results clearly confirm that the previously found appearance of mass differences in the correlator is indeed induced by thermal effects and that the Prony method is sensitive enough to resolve them. These findings unsurprisingly demonstrate that the vacuum density matrix approximated from the imaginary TEBD algorithm as $\lim_{\beta\to\infty} e^{-\beta H}$ for large enough β yields an equally well Prony reconstruction as the ground state projector $|0\rangle\langle 0|$ constructed from DMRG.

In a second approach, instead of the projector MPO $|0\rangle\langle 0|$, the the ground state $|0\rangle$ can be used itself as a MPS to calculate the time dependence of the retarded two-point function. In this case, the bond dimension does not enter the simulation squared and hence the correlator can be evolved for longer times more accurately. The right panel in Fig. 4.24 shows the corresponding result of the Prony reconstruction. Here, higher meson poles become sharper. Apart from the continuum threshold $2M_1$, one now can also identify the mass sum $M_1 + M_2$ as a branch cut (indicated by dashed vertical lines). Further mass sums lie very close to single meson states and thus cannot be clearly distinguished.

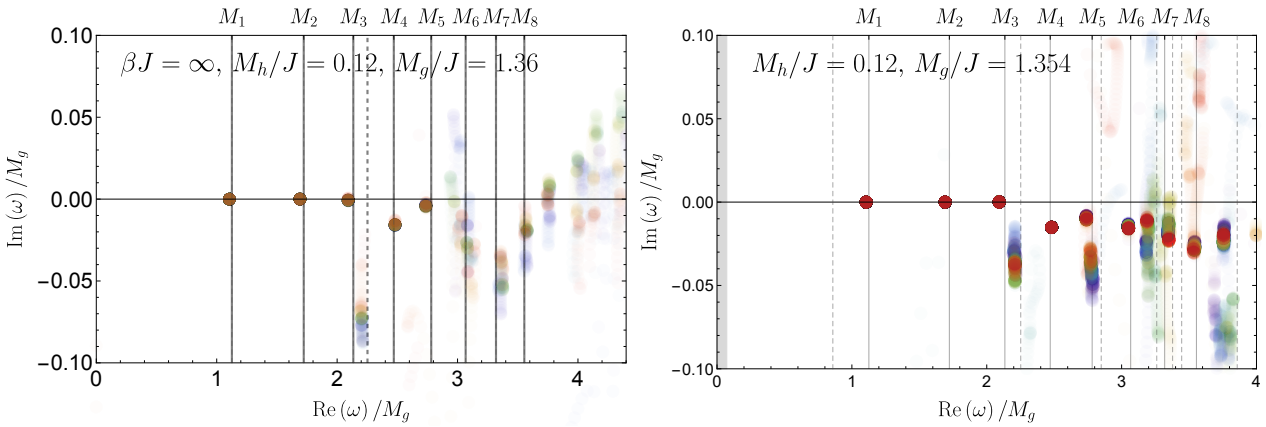

Figure 4.24: Results of the Prony analysis of the retarded transverse correlator of $\epsilon = i\,\bar{\psi}\psi$ in the vacuum (i.e. for the ground state) in the nonintegrable ferromagnetic phase. Solid vertical lines represent meson masses from ref. [180].
Left: The result is based on a MPO simulation. The dashed line marks the continuum threshold of $2M_1$. Simulation parameters: $N = 200, \chi = 170, J\,\delta t = 0.02, J\,t_{\max} = 50$, 2^{nd} order Trotter decomposition.
Right: The result is based on a MPS simulation. Dashed lines mark the continuum threshold and further mass sums. Simulation parameters: $N = 200, \chi = 150, J\,\delta t = 0.02, J\,t_{\max} = 80, 4^{\text{th}}$ order Trotter decomposition. Figures taken from [1].

4.11 Discussion and outlook

In this chapter we have initiated an in-depth study of real-time thermal field theory properties. Motivated primarily by holographic models, we studied retarded correlation functions at non-zero temperature and analyzed their analytic structure in the complex frequency plane, which gives invaluable insights into dynamical and thermalization properties of the physical system. By solving a kinetic theory model, we learned that integrability breaking mass deformations can alter this structure (also) in $2D$ systems which are not free. Using a combination of MPO simulations and a signal analysis procedure based on the Prony method, we extracted the structure within different classes of the Ising QFT (4.40). Although real-time simulations with TNs are in general reliable only for a finite time window, we have demonstrated here that this technique is reliable to extract the singularity and pole structure from the available data. Notice that we were not interested to predict the full details of correlators at late times (i.e. beyond the reliable time simulation window), but instead to utilize the available numerical data at intermediate times to reconstruct relevant features of the model by identifying the structure of complex modes in Fourier space.

We could benchmark the accuracy of this method in the integrable massive free fermion regime as well as in the integrable interacting E_8 QFT. In the case of nonintegrable QFTs we reproduced both the real and imaginary parts of several meson and quasiparticle frequencies that were earlier found in [178–181]. As the system is heated up we observe the appearance of frequency poles corresponding to mass differences. Apart from meson poles we also analyzed

transient poles, which describe decaying contributions to the retarded correlator that are intrinsically triggered by non-zero temperatures. In the free fermion case they are related to Matsubara frequencies [167] and for holographic CFTs correspond to QNMs of AdS_3 BH solutions [60,159]. Within the numerical accuracy of our simulations that allow us to study such frequencies we predict that these modes are not affected by interactions or integrability breaking. We confirmed that our conclusions are stable w.r.t. numerical variations in the system size, bond dimension and other parameters. Overall, our study provides important insights into thermalization properties of $2D$ QFTs, a timely subject, which was recently addressed e.g. in [202] from a hydrodynamic perspective.

This analysis framework and physical setting opens up several research directions that we address in the following chapters. In particular, we have focused so far on MPS and more generally MPO as the underlying type of TNs. It is, however, a intriguing question whether other TN classes allow a better discretization of the underlying QFT or the extraction of relevant data. We will address this point of view using the MERA in the following chapter. Furthermore, the existence of mesons even in rather simple toy models such as the Ising QFT allows us to investigate physical effects that are in rough analogy to QCD. In chapter 6 we will follow this exciting research direction to study the phenomenon of meson melting within a TN approach. Finally, we want to find out how much of information on meson physics can be deduced from relatively small systems that are experimentally realizable on quantum simulators. In chapter 7 we analyze that for a model relevant to ion traps.

5 Entanglement renormalization

The line of research in the present part of this thesis is characterized by the description of a QFT from an underlying lattice discretization. This approach can be seen in general from two sides: On the one hand, one can ask what is the best discretization scheme for a given QFT, which then can be solved computationally in interesting regimes. On the other side, one can explore how much and exactly QFT information can be extracted from a given lattice model. TN ansätze provide a natural framework to pursue the latter path. Up to now, we employed MPOs (and MPS) to implement a Hamiltonian formulation of a spin model with a continuum (Ising) QFT emerging in the IR limit close to criticality. In this form, the Ising model was defined on a linear line. As we introduced in detail in section 3.6, the MERA instead represents a TN with a $2D$ circuit geometry. By organizing physical degrees of freedom in different length scales and removing short-range entanglement, a faithful RG flow is realized. While MPS reproduce by construction properties of gapped systems, the MERA encodes critical systems more faithfully and therefore allows to extract precise CFT data. In line with our previous studies, interesting theories can arise from relevant deformations of CFTs. Hence, having better control over CFT data might result in a better ability to deal with such theories. Based on these preconditions, we want to analyze in this chapter if scaling operators originating from the MERA allow a more accurate description of the continuum theory w.r.t. dynamical quantities. In particular, we will refer to the original nearest-neighbor Ising Hamiltonian (4.32) as the *bare* model, and study in comparison an analytic wavelet solution [43] for the MERA. The latter represents a scale invariant, i.e. infinitely *coarsegrained* system at criticality, which reproduces some operator scaling dimensions exactly. We are interested to make use of the scaling operators, which follow from these analytic MERA tensors, to calculate from them retarded thermal correlation functions using MPO simulations. In contrast to the previous chapter, where the lattice operators were given in terms of one-site Pauli matrices as in (4.49), the MERA operators follow as more complicate numerical combinations of Pauli matrices, defined on three lattice sites. Both descriptions give rise to the Ising QFT (4.40) in the continuum. Since the MERA based primary operators partially encode CFT data exactly, it is a intriguing possibility that the resulting correlation functions allow a better lattice discretization. In this section, we test this hypothesis for relatively small system sizes. The motivation for that comes from the fact that the underlying MERA is defining a scale invariant system, which potentially allows to extract QFT information already

on small lattices. Such small systems could be realized in experiments, which would open the avenue for their quantum simulation.

5.1 The wavelet MERA tensor network

In section 3.6 we introduced the MERA as a variational class of TN states, which rests on numerical simulations by minimizing the energy. In view of holographic interpretations of TNs as well as for encodings of CFT data, it would be highly desirable to have instead analytic forms of the MERA tensors available. Evenbly and White provided the first such solution in [43]. [57] This result was obtained by employing concepts of wavelets and wavelet transforms [204]. These are methods originating from the field of signal analysis, which became very important for data and image compression. In contrast to the standard Fourier transform, which is fully localized in momentum space and completely delocalized in real space, wavelets are compact in both spaces. They allow to construct a basis of wavelet functions, which can be used to represent arbitrary functions. When combined with a scaling transformation, their recursive (i.e. repeated) application on a lattice valued function resolves information on different length scales. This similarity with a real space coarsegraining procedure was used in [43] to find a unitary representation of this discrete wavelet transformation, which resembles exactly the structure of the MERA when seen as a quantum circuit. In the case of $1D$ free spinless fermions, a MERA circuit built from so-called Daubechies D4 wavelets was found to prepare an accurate approximation of the ground state of the critical quantum Ising model. For this solution, the isometry w and the disentangler u take in the lowest order the form

$$w \quad = \quad \quad = \quad \frac{\sqrt{3}+\sqrt{2}}{4} II + \frac{\sqrt{3}-\sqrt{2}}{4} ZZ + \frac{i(1+\sqrt{2})}{4} XY + \frac{i(1-\sqrt{2})}{4} YX$$

$$u \quad = \quad \quad = \quad \frac{\sqrt{3}+2}{4} II + \frac{\sqrt{3}-2}{4} ZZ + \frac{i}{4} XY + \frac{i}{4} YX \tag{5.1}$$

for the binary MERA. Here, XY and others are short notations for tensor products of Pauli matrices X, Y, Z and the identity I, e.g., $XY \equiv \sigma^x \otimes \sigma^y$ etc. The definition for w is understood in the sense of (3.36). The analytic forms (5.1) are valid for the smallest possible bond dimension $\chi = 2$. In [43], it is also outlined how higher order tensors can be constructed from multiple contractions, the second lowest being of dimension $\chi = 2^3 = 8$. The importance of this analytic result stems from the fact that this solution allows for a precise encoding of some conformal data. From the following discussion, this will become apparent even for the smallest nontrivial bond dimension $\chi = 2$, which is much lower than for numerically optimized tensors. Furthermore, this MERA generates a Hamiltonian RG flow to a gapless fixed point in the sense

[57] An excellent overview and discussion of it and related new results is presented in [203] by one of the authors.

of (3.36), which was previously thought to be impossible from variational considerations, in which relevant RG perturbations are numerically introduced.
As described in the general discussion in section 3.6, primary scaling operators follow as eigenvectors of the superoperator. Here, the averaged 3-site scaling superoperator for the binary MERA is defined as

$\mathcal{S}_3 \;=\; \frac{1}{2}$ 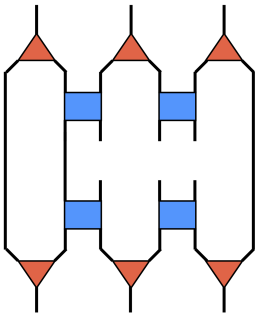 $+\; \frac{1}{2}$ 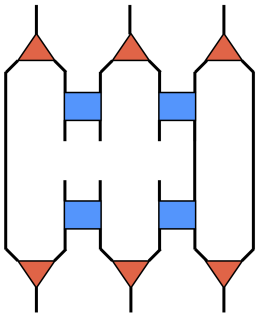 . (5.2)

Its diagonalization yields uniquely the identity operator I with scaling dimension $\Delta_I = 0$, $\epsilon = i\bar{\psi}\psi$ with $\Delta_\epsilon = 1$ and the spin field σ with $\Delta_\sigma = 0.1402\ldots \approx 1/8 = 0.125$ as one of the eigenvectors, respectively. Amazingly, the first two scaling dimensions are obtained numerically exactly, i.e. this part of the CFT data is encoded exactly even for the lowest order combination of Pauli matrices (5.1), while the scaling dimension for the σ operator can be improved as $\Delta_\sigma = 0.1233$ at the next analytical order for $\chi = 8$. Furthermore, the diagonalization of $\mathcal{S}_3$ yields four degenerate Hermitian eigenvectors with scaling dimension $\Delta = 2$ (numerically exact). Physical operators with these properties include T, $\bar{T}$, $\partial_t\epsilon$ and $\partial_x\epsilon$. They differ in their conformal spin as $s = \pm 2$ for the first two and $s = \pm 1$ for the latter. While it is in principle possible to devise a scheme to construct the Hamiltonian fixed point density $h^* \sim T + \bar{T}$ from a priori unknown linear combinations of these eigenvectors, it was already observed in the original work [43], that h^* can be obtained alternatively by projecting the bare Hamiltonian onto the subspace of operators with scaling dimension $\Delta = 2$. Altogether, we hence have the operators ϵ and σ at our disposal as well as the Hamiltonian density h^*, which generates the dynamics.

5.2 Real-time correlator simulations

5.2.1 The CFT case

Based on the operators h^* and ϵ or σ, we can construct thermal states and perform the real-time evolution of retarded two-point functions using MPO simulations. We consider here the case of the lowest order wavelet MERA tensors with bond dimension $\chi = 2$. When we refer to these fixed point tensors, we denote them as the coarsegrained system. In contrast to the bare system, in which the operators are one-site tensors, all scaling operators now act on three sites. To make use of the TEBD algorithm in the form described in section 3.5.2, we symmetrize the

3-site gates as follows

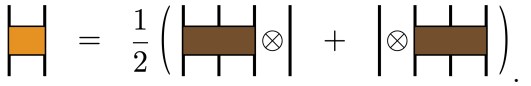

(5.3)

This implicit blocking procedure increases the bond or, equivalently, physical dimension from $d = 2$ (rhs of (5.3)) to $d = 4$ (lhs of (5.3)). Thermal expectation values of the retarded two-point function (4.48) are then calculated as

$$\langle O_1(t)O_2(0)\rangle_\beta = \mathrm{Tr}\left\{O_1(0)[U(t)O_2(0)\sqrt{\rho_\beta}U^\dagger(t)]\sqrt{\rho_\beta}^\dagger\right\} \tag{5.4}$$

for operators

$$O_1(0) = \sum_j \epsilon_{j,j+1} \quad \text{and} \quad O_2(0) = \epsilon_{N/2,N/2+1}. \tag{5.5}$$

We consider N spins with physical dimension $d = 2$, which are treated as a finite chain of length $N/2$ with dimension $d = 4$ and open boundary conditions. The perturbation $O_2(0)\sqrt{\rho_\beta}$ acts locally on the mid chain position of the thermal state and is subsequently evolved in time as indicated by the term in brackets. Individual traces w.r.t. the first operator in (5.5) are then summed up. To faithfully compare the bare and coarsegrained system, we need need to ensure a proper normalization of the latter. This is achieved by diagonalizing the total Hamiltonian $H = J\sum_j h^*_{j,j+1}$ on small lattices and normalizing the first excitation, such that it assumes the value $1/8$ as required by the smallest scaling dimension of all possible Ising CFT primaries. [58] Considering several small system sizes up to $N = 12$, we find the following fit function

$$J = (0.134 + 3.33/N^{2.58})^{-1}. \tag{5.6}$$

From this setup, we calculate the retarded thermal correlation function for the ϵ operator at criticality. We choose $\beta J = 8$, which we know from our previous studies to lie in the IR QFT regime. Fig. 5.1 compares the resulting curves for the coarsegrained system (right panel) to the bare model (left panel, calculated as discussed in detail in chapter 4) for small up to moderate chain lengths $N = 10$, 20 and 40. In both scenarios, the fast decay after the first peak at early times represents the effect of transient poles. After the initial appearance of damped oscillations, large revival effects are visible, indicating the effect of the finite chain length. As N is increasing, the onset of these revivals is accordingly pushed towards later times. The curves of the bare and coarsegrained model exhibit structural differences, i.e. the decay and oscillation pattern is not identical. Note for example that the magnitude of the first peak is strongly modified by finite size changes in the bare model but not in the coarsegrained case. Overall, however, there do not seem to be fundamental differences between the two cases. By that we mean that systems of the same size exhibit a similar time onset of revivals for both the

[58] In [43] it was observed that the resulting numerical energy spectrum resembles already for 10 sites closely the low-lying Ising CFT spectrum, which is determined by the scaling dimensions of the primary operators.

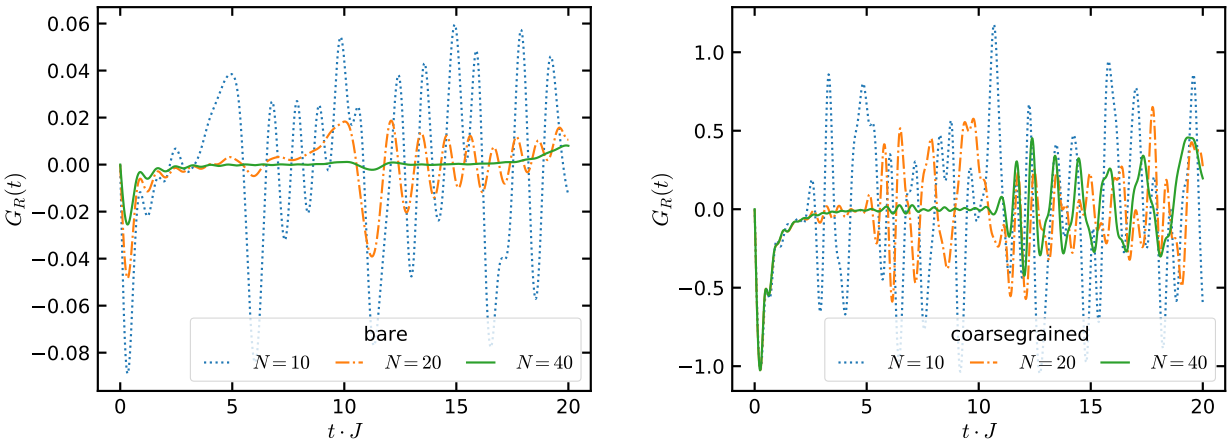

Figure 5.1: Comparison of the time-dependent transverse retarded thermal correlation functions of the ϵ operator in the bare model (left panel) and coarsegrained system (right panel). Simulations are performed for chains of different sizes N at the critical point of the quantum Ising model ($\beta M_h = \beta M_g = 0$).
Numerical parameters: $\beta J = 8$, $\chi = 150$, $J\delta t = 0.02, Jt_{\max} = 20$, 2^{nd} order Trotter decomposition.

bare and coarsegrained simulation. Although the latter one is based on a Hamiltonian, which follows through an infinite number of RG steps from the bare one, that property does not seem to translate directly into different finite size dependencies when discretized on a linear lattice.

From these results it becomes apparent that we need a sufficiently large chain also in the coarsegrained system to reliably identify the QFT part of the correlator signal. We therefore analyze the signal for $N = 40$ in more detail. In Fig. 5.2, the results of the Prony signal analysis are compared for the bare model (in the left panel) and coarsegrained system (in the right panel). In contrast to our previous studies in chapter 4 for large systems, we here analyze only the time window up to $tJ = 5$ to avoid finite size imprints in the signal (cf. the color bar). While the bare simulation exhibits the usual vertical UV branch cut at $\omega/J \approx 8$, the UV behavior of the coarsegrained simulation is altered. The latter one shows additional double branch cut structures at larger frequency values. Due to the indefinite relation between the UV scale in the bare and coarsegrained system, we are not able to provide an analytical expectation for this analytical structure. Instead, our simulations here have predictive character for this particular aspect. In contrast to the bare model, the IR and UV are separated even more here, which necessarily is an outcome of the RG flow of the MERA. Apart from the branch cut, both simulations show the first transient at the expected analytical position $\beta/2\pi\,\mathrm{Im}(\omega) = -1$. Although the coarsegrained simulation is able to capture this thermal feature, the corresponding pole is more fuzzy. From a detailed analysis using the methodology introduced in section 4.9.1, we find the values -0.998 ± 0.004 in the bare model and -1.020 ± 0.040 in the coarsegrained system for the position $\beta/2\pi\,\mathrm{Im}(\omega_1)$ of the first transient pole. As we emphasized previously, apart from this frequency value, its associated residue value is important to compare with the

CFT prediction. Since the relatively small size limits the available time window, a reliable extraction of this value is, however, not possible in this case. Contrary to the bare simulation, there is no indication for the second transient pole visible in the coarsegrained simulation.

5.2.2 The interacting E_8 regime

In section 4.9.1 we came to the conclusion that the position of the first transient pole in the complex frequency plane does not change for perturbations away from criticality, independent from phase properties. Here, we check this prediction for a perturbation of the critical fixed point Hamiltonian with σ into the interacting E_8 QFT regime to confirm the stability. In other words, we construct a thermal state at $\beta J = 8$ w.r.t. the Hamiltonian density $h := Jh^* + \sigma$. To have longer time windows available, we choose a chain of $N = 60$ sites. Fig. 5.3 shows the corresponding result of the Prony analysis. It should be noted at this point, that the simulations of the coarsegrained system are computationally much more demanding and costly. One reason is that due to the symmetrization in eq. (5.3), contractions with physical indices enter squared in their dimension as compared to the bare calculation. Furthermore, the truncation error, as defined in section 3.5.2, is growing larger for wavelet based simulations. This is visible from Fig. 5.4, which shows the time dependence of this quantity. For the previously considered critical case at $N = 40$, the coarsegrained system (blue solid curve) is growing larger than the bare system (orange solid curve) at early times, but reaches a comparable magnitude at the latest times. In the present case in the E_8 regime (blue dashed curve), the truncation error at late times is several orders of magnitudes larger instead. We therefore choose only the the time interval up to $tJ = 7$ for the Prony analysis, in which finite size effects are not yet present and the truncation error is sufficiently low. In the corresponding Prony result, several spurious poles appear in the frequency plane. The first transient pole is visible as a fuzzier structure than at criticality. We can extract the value $\beta/2\pi \operatorname{Im}(\omega_1) = -1.02 \pm 0.04$ for its location, which is again consistent with what constitutes the CFT result, i.e. our original claim.

5.2.3 Discussion and outlook

In this chapter we explored the capabilities of wavelet based MERA tensors to encode thermal QFT information from a dynamical viewpoint. Focusing on the lowest order solution with physical dimension $d = 2$ and its corresponding scaling operators, the outcome is that MPO simulations of retarded correlators allow at most an equally good resolution of the first transient pole as an intrinsic finite temperature effect when compared to the bare system. This comes as a surprise to us, since from the underlying RG flow in the MERA, which generates the fixed point tensors with their exact scaling dimensions, we expected that the encoding of thermal QFT data could have been better. Instead, the bare and coarsegrained system show a

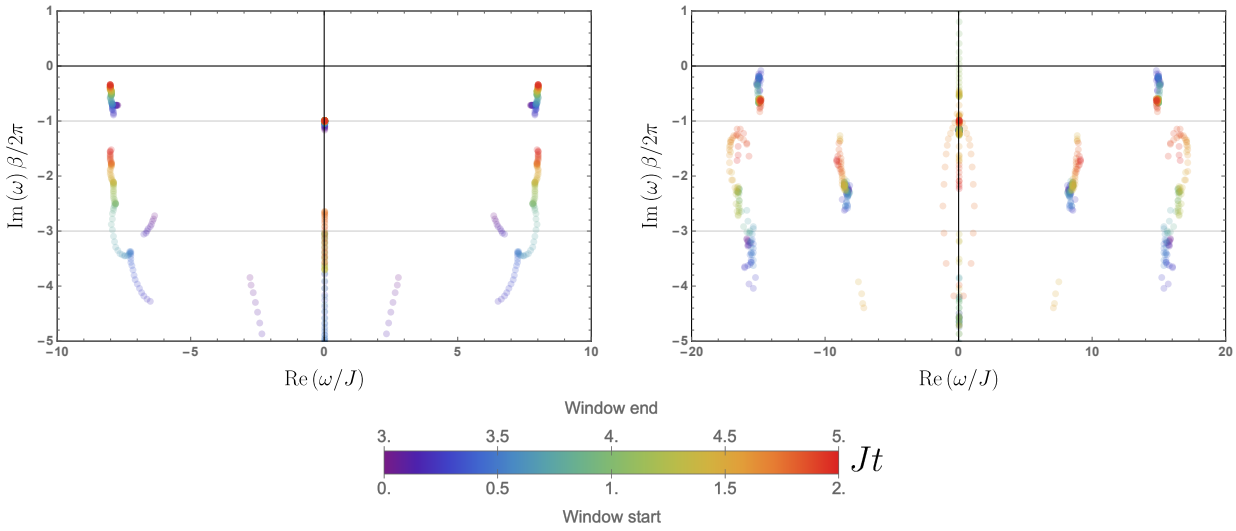

Figure 5.2: Results of the Prony frequency analysis for the transverse retarded correlator of the ϵ operator at criticality in the bare (left) and coarsegrained (right) system. In both cases, a chain of $N = 40$ sites is considered, corresponding to the green curves in Fig. 5.1.

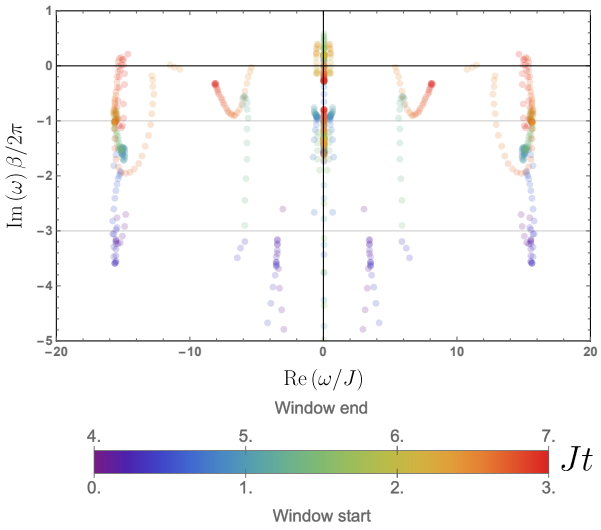

Figure 5.3: Results of the Prony frequency analysis for the transverse retarded correlator of the ϵ operator in the E_8 regime. The results are obtained in the coarsegrained system. Numerical parameters: $\beta J = 8$, $N = 60$, $\chi = 200$, $J\delta t = 0.02$, $Jt_{\max} = 20$, 2^{nd} order Trotter decomposition.

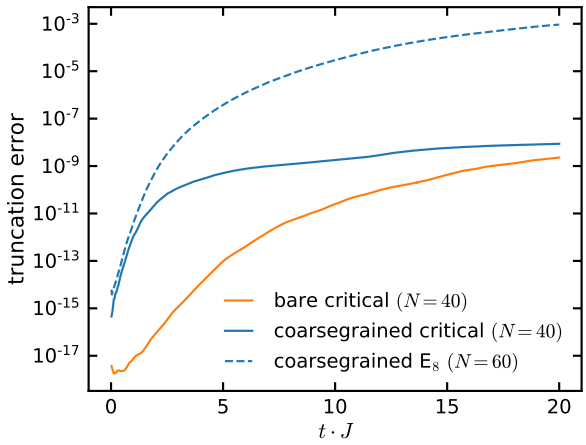

Figure 5.4: Time dependence of the truncation error in the finite size TEBD algorithm for several systems.

similar finite size dependence of the correlation function for the same number of spins-1/2 on a chain. Therefore, a reliable extraction of QFT data from the wavelet tensors is not possible for smaller system sizes than for the bare case. Naively, this might be understood from the fact that in both scenarios the physical dimension $d = 2$ is identical and simply no better encoding of the Ising CFT is possible at this matrix size. Indeed, in preliminary studies we see indications that the next higher order wavelet solution with $d = 8$ allows a better encoding of spectral properties. This seems to support the picture, that an exact encoding of the CFT data might be formally available in the limit of $d \to \infty$. However, similar calculations of dynamical quantities with such tensors would be computationally very costly, and it is not yet clear if they are feasible at all. From a broader perspective, it would be desirable to explore in a similar vein also other quantities of interest, including static ones. In transition to our next chapter, this could encompass in particular entanglement measures and entropies, which provide invaluable insights into QMB systems and QFTs.

6 Meson melting

6.1 Motivation from QCD

Emergent phenomena of QFTs under extreme conditions can pose significant challenges for their theoretical treatment. Our motivation here is again driven by QCD at finite temperature, where the melting process of mesons, as one such example, is of major interest in the theoretical and experimental community. Building up on our general introduction to QCD and HICs in section 4.1, we provide here an introduction into the topic based on the recent and comprehensive review [205]. Apart from a conceptual understanding of quarkonium in conditions similar to the first microsecond after the big bang in the early universe, the significance of the meson melting mechanism and its inverse, the recombination of individual quarks into bound states, stems from the fact that it causes observable effects in the experimental detection of a HIC. This is the reason why historically the suppression and melting of meson are studied and discussed often together.

The key task at hand is the development of theoretical tools to characterize the physics of a meson as a nonperturbative bound state immersed in a thermal environment consisting of the QGP and nuclear matter. Over the last decades, the understanding of this setup shifted from a static to a dynamical paradigm to explain meson melting as a sequential process. The precise nature of the strong interactions between meson states and the deconfined environment, and more generally the hadronization and thermalization process itself, are currently not understood from a detailed microscopic theory or at least model.

In this chapter, we want to introduce a new paradigm in the understanding of meson melting by studying entanglement measures. We see this as an important new concept for a comprehensive understanding of the melting phenomenon. The simple reason is that beyond QCD as the underlying QFT, in which particles are mathematically described as field excitations, the system under consideration is additionally also a QMB problem. In the latter viewpoint, entanglement is the key property, which mediates correlations among the constituents. Its study therefore can unveil new features which are not accessible by other approaches. In the present work, we focus on nonintegrable parameter regimes of the $2D$ Ising QFT with mesons in the spectrum. Inspired by the two different viewpoints, we study both static and time-dependent thermal states in the thermodynamic limit of the quantum Ising model near its critical point. The entanglement content in the QMB system is probed by analyzing (generalized) entangle-

ment entropies, which, in contrast to QFT methods, are easily available with TN simulations. The dynamical setup is generated by a quantum quench - a common method, which creates an out-of-equilibrium state through an (instantaneous) parameter change in the underlying Hamiltonian. This protocol can be seen as a theoretical method by itself, since it can induce entirely new dynamical features to the system. We use it to mimic a a dynamical situation as in the modern QCD viewpoint on meson melting. The next two subsections deepen the background on meson melting from the QCD side to provide a more complete overview.

6.1.1 Theoretical methods

Spectral functions are the main quantity studied within thermal field theory to describe mesons in a medium. To derive them, let $M(\vec{x},t) \equiv \bar{q}_f(\vec{x},t)\,\Gamma\, q_f(\vec{x},t)$ be the *meson operator* constructed from the Dirac spinor q_f of a quark with flavor f and Γ is the vertex operator - a combination of gamma matrices, which selects the spin and angular momentum. [59] Real-time properties such as strength and form of field fluctuations are captured by the time-ordered two-point function

$$D(\vec{x},t,\vec{x}_0,t_0) = \langle \mathcal{T} M(\vec{x},t) M^\dagger(\vec{x}_0,t_0)\rangle_\beta = \mathrm{Tr}\{\rho_\beta \mathcal{T} M(\vec{x},t) M^\dagger(\vec{x}_0,t_0)\} \tag{6.1}$$

$$= \int \mathrm{d}[A^+,q_f^+,\bar{q}_f^+]\mathrm{d}[A^-,q_f^-,\bar{q}_f^-]\,\langle A^+,q_f^+,\bar{q}_f^+|\rho_\beta|A^-,q_f^-,\bar{q}_f^-\rangle\cdot$$

$$\cdot \int_{A^+,q_f^+,\bar{q}_f^+}^{A^-,q_f^-,\bar{q}_f^-} \mathcal{D}[A,q_f,\bar{q}_f]\mathcal{T} M(\vec{x},t) M^\dagger(\vec{x}_0,t_0)\,\mathrm{e}^{iS_{\mathrm{QCD},cl}}\,. \tag{6.2}$$

Here, $\mathcal{T}$ is the the time-ordering operator, $S_{\mathrm{QCD},cl}$ is the QCD action following from the classical Lagrangian (4.1), A is the short-hand notation for the gluon fields and the superscripts $\pm$ denote the forward and backward branch of the Schwinger–Keldysh contour, over which the path integral in (6.2) is taken in the complex time plane. The first part in the path integral on the second line contains the thermal density matrix elements and represents the initial conditions, while the remaining term on the third line describes the quantum dynamics. Similar to our considerations in chapter 4, the related definition of the retarded correlator,

$$D_R(\vec{x},t,\vec{x}_0,t_0) = \theta(t-t_0)\langle [M(\vec{x},t), M^\dagger(\vec{x}_0,t_0)]\rangle_\beta, \tag{6.3}$$

[59] See [205] for a detailed selection of possible choices. In the simplest cases, the identity $\mathbb{1}$ or gamma matrix γ^μ can be chosen.

is of particular relevance here since it appears in the following decomposition of the time-ordered two-point function

$$D(\vec{x},\vec{x}_0,t,t_0) = \frac{1}{2}\langle\{M(\vec{x},t),M^\dagger(\vec{x}_0,t_0)\}\rangle_\beta + \frac{1}{2}\,\mathrm{sign}(t-t_0)\langle[M(\vec{x},t),M^\dagger(\vec{x}_0,t_0)]\rangle_\beta \tag{6.4}$$

$$\equiv F(\vec{x},t,\vec{x}_0,t_0) - \frac{i}{2}\,\mathrm{sign}(t-t_0)\rho(\vec{x},t,\vec{x}_0,t_0). \tag{6.5}$$

Here, we defined the *statistical function* F, which measures the population of states, and the *spectral function* ρ. In a QCD context, the latter quantity is typically considered in Fourier space via a Wigner transformation, in which relative frequency and momentum coordinates $(\vec{p},\omega)$ are used. It is then given in thermal equilibrium as the negative imaginary part of the retarded correlator,

$$\rho(\vec{p},\omega) = -\,\mathrm{Im}[D_R(\vec{p},\omega)]. \tag{6.6}$$

The spectral function in this form probes the particle content of the physical system. Fig. 6.1 shows some example calculations for QCD. Meson bound states show up as peaks at frequency values given by their masses. They depend on the momentum $\vec{p}$, following the (relativistic) dispersion relation of the QFT. Above the *continuum threshold*, given by twice the mass of the lightest particle, unbound particle pair peaks can appear within a continuous background structure. The *thermal width* of any such peak is proportional to the inverse lifetime of the corresponding (quasi)particle. Another important quantity is the *binding energy* of a bound state, which is given by the difference of its mass peak to the continuum threshold. In the special case of a regularized theory with a discrete spectrum, the spectral function can be written in terms of energy eigenstates $|n\rangle$ and $|m\rangle$ as

$$\rho(\omega) = \frac{1}{Z_\beta}\sum_{n,m}\mathrm{e}^{-\beta E_n}\left\{\delta[\omega+E_n-E_m]-\delta[\omega+E_m-E_n]\right\}|\langle n|M(t_0)|m\rangle|^2, \tag{6.7}$$

where all described features translate into single and densely spaced delta peaks.

Within QCD, there are several methods established to calculate spectral functions. Each of it has intrinsic limitations as reviewed in detail in [205]. First, effective field theory approaches make use of the fact that meson flavors of large mass can be integrated out to get a nonrelativistic approximation of QCD. The resulting expansion in energy scales is, however, truncated, limiting the physical content of the description. Furthermore, lattice QCD allows a nonperturbative treatment on a discretized spacetime lattice based on Monte Carlo sampling. However, the computations in taking the continuum limit are numerically extremely expensive. Both these methods give access to the Euclidean correlator

$$D_E(\vec{x},\tau) = \langle M(\vec{x},-i\tau)M^\dagger(\vec{0},0)\rangle_\beta, \tag{6.8}$$

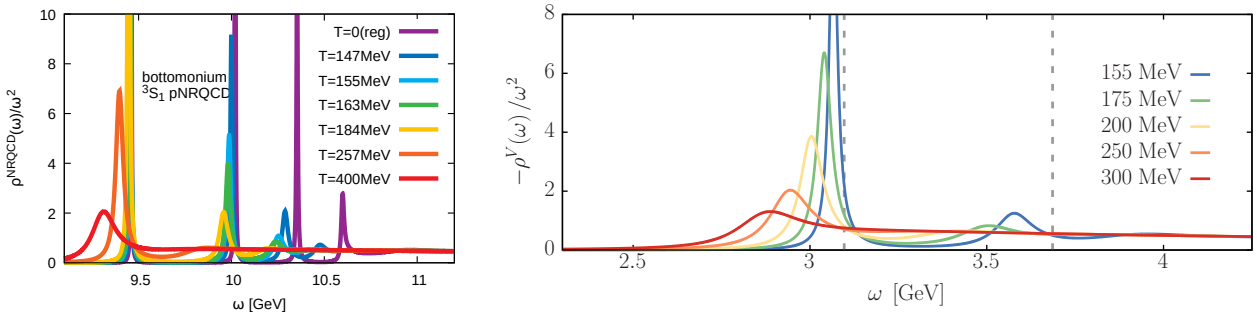

Figure 6.1: Left: Frequency dependence of the Euclidean in-medium bottonium spectral function based on an effective nonrelativistic QCD description on the lattice [206].
Right: The same for the charmonium flavor, based on a lattice vetted potential method [207].
Figures taken from the arXiv version of [205]. (See this reference and citations therein for details.)

which is related in Fourier space to the spectral function via the integral transformation

$$D_E(\vec{p},\tau) = \frac{1}{\pi}\int_{-\infty}^{\infty} \mathrm{d}\omega \frac{\mathrm{e}^{-\tau\omega}}{1-\mathrm{e}^{-\beta\omega}}\rho(\vec{p},\omega). \tag{6.9}$$

The extraction of $\rho(\vec{p},\omega)$ from this relation for only a limited number of discrete, uncertainty-prone lattice data points limits the quantitative robustness of the results. An alternative approach is based on a potential method. To define it, consider the real-time Wilson loop

$$W_\square(r,t) = \mathcal{P}\exp\left[ig\oint_{r\times t} A^\mu \mathrm{d}z_\mu\right] \tag{6.10}$$

along a rectangular path of size r times t in the spatial and time direction. The static interquark potential V_s is then defined as

$$V_s(r) = \lim_{t\to\infty}\frac{i\partial_t W_\square(r,t)}{W_\square(r,t)}. \tag{6.11}$$

This potential together with a mass and kinetic term defines a Hamiltonian, which governs the time evolution of the two-point meson correlator via the Schrödinger equation. The imaginary part of its solution in Fourier space yields the spectral function. The accuracy of this method is limited through the omittance of finite velocity corrections.
Overall, the presented methods of determining in-medium spectral functions for quark bound states at finite temperature provide the basis for our current understanding of the meson melting process, which we summarize now in the next subsection.

6.1.2 Phenomenology of the melting process

The influential work [208] initiated studies on suppression and melting of mesons. Starting from an analogy with Debye screening in an electromagnetic plasma, the authors argue that

the QGP created in a HIC weakens the binding energies of meson bound states in the thermal environment, causing a suppression of meson detection rates. Building up on that, the work [209] put forward the picture of a sequential process. In this static scenario, a in-medium Hamiltonian describes mesons as its eigenstates. The potential term in the Hamiltonian gets weaker for increasing temperatures, such that bound states transform into scattering states at a unique *melting temperature*. Weakly bounded mesons states melt first, while strongly bounded ones survive longer in the thermal medium. The work [210] opened a new way of thinking about this process by showing that the quark potential (6.11) is complex. This implies that a meson bound state is a dynamical system, which interacts constantly with its thermal environment by scattering processes. In this modern picture, the melting process is best understood from the behavior of spectral functions in dependence of the temperature, which can be calculated by one the methods described above. Fig. 6.1 shows an example for two different flavors. With increasing temperature (from blue to red curves), the meson peaks move towards smaller frequency values. Their magnitude is decreasing while their thermal width is increasing. Peaks at larger frequencies, i.e. lower binding energies, melt first and their peak structure dissolves completely into a continuum. The combination of thermal broadening and decreasing of the binding between the quarks means that mesons transition into other (unknown) states. The dynamical origin of this process is not known from this description. As a consequence, the definition of a melting temperature in this time-dependent, sequential scenario is not uniquely determinable any more and a less important concept. The overall intuitive picture drawn in [205] is that the thermal environment acts as a sieve that filters out weakly bounded meson states, which are exposed to intensifying scattering events as the temperature is raised.

From these elaborations, it becomes obvious that only a fully real-time treatment can describe all dynamical processes contributing to the melting of meson bound states. The open quantum systems approach provided new insights in this direction (see, e.g., references in [205]). It treats the interactions between a system (quark-antiquark pair) and its environment (thermal medium) in a real-time Schrödinger formalism. Because of the sign problem, a fully nonperturbative QCD calculation is not available on the lattice in this framework. Interestingly, it could link the melting process to the quantum mechanical effect of decoherence (see e.g. [211,212] and references in [205]). In this line of research, we would like to integrate the real-time quench studies, which we will present in this chapter. The ab initio setting gives us access to entanglement entropies as fundamentally quantum mechanical properties, which we expect to drive the melting phenomenon. In contrast to the usual QCD frameworks, these entropies are directly available in the spin-chain language, which we employ as models to study mesons in $2D$ QFTs.

6.2 Insights from holographic models

Also in the context of meson melting, holographic approaches provide a framework to study high-temperature properties of quarkonium. We briefly want to point out some major lessons from these explorations, based on the recent series of papers [213–220], which are jointly discussed in [221]. The basic ingredient is the description of meson states as test particles in a fixed asymptotic AdS spacetime. [60] The underlying action

$$S = \int \mathrm{d}^4x\mathrm{d}z\, \sqrt{-g}\, \mathrm{e}^{-\phi}\, G(\phi) F_{mn}F^{mn} \tag{6.12}$$

contains a dilaton field ϕ, a flavor coupling function $G(\phi)$, and a $U(1)$ gauge field V_m in the definition $F_{mn} = \partial_m V_n - \partial_n V_m$ of the field strength tensor. The dilaton breaks conformal symmetry and models the running coupling in QCD. Upon a field redefinition ψ in Fourier space, the equation of motion of the gauge field takes in tortoise coordinates [61] the Schrödinger form

$$\left(\partial_\xi^2 - [U_T - m^2]\right)\psi = 0 \tag{6.13}$$

with a temperature-dependent potential U_T. Normalizable solutions of this equation yield a discrete mass spectrum m_n^2 ($n \in \mathbb{N}$). The original *soft-wall model* of [222] uses a quadratic ansatz (w.r.t. z) for the dilaton field and the simplest choice $G \equiv 1$ to enforce a linear spectrum of the form $m_n^2 = c_0 + c_1 n$, which matches experimental data of radial meson excitation spectra at $T = 0$. At finite temperature, the potential well in $U_T(z)$ is decreasing, implying the existence of lesser bound states. In other words, the model is capable of reproducing the sequential melting of meson states. A typical example for such a scenario is shown in the left panel of Fig. 6.2. Further studies in [223–230] on refinements of this model found, however, unrealistic melting temperatures much below the QCD deconfinement scale $\mathcal{O}(150\,\mathrm{MeV})$. The authors of [213–220] resolved that problem by finding one-parameter extensions of the metric and dilaton as well a construction principle for the blackening function that result in consistent melting temperatures, and, at the same time, exhibit thermodynamic properties consistent with the equation of state from lattice QCD. While this approach is based on ad-hoc ansätze for the background, the latter can be determined also self-consistently, for example, in a Einstein–dilaton model, defined by the action

$$S = \frac{1}{16\pi G_{\mathrm{N}}^{(5)}} \int \mathrm{d}^4x\mathrm{d}z\, \left(R - \frac{1}{2}(\partial\phi)^2 - V(\phi)\right), \tag{6.14}$$

[60] As test particles, different meson flavors do not react back between themselves nor with the metric and the dilaton.

[61] The tortoise coordinate ξ follows from the blackening function f and the holographic coordinate z as $\mathrm{d}\xi = \mathrm{d}z/f$. The mass m is the zero component p_0 of the four-momentum.

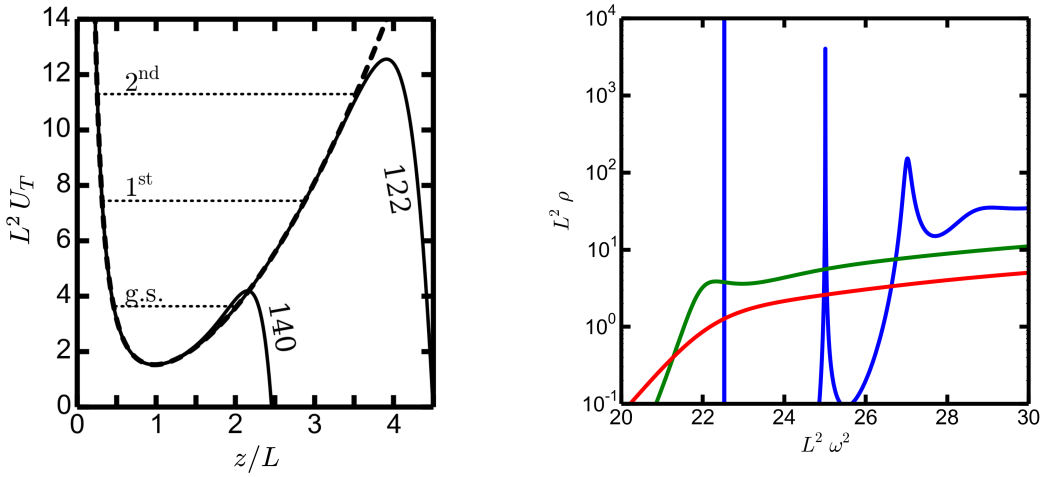

Figure 6.2: Left: Temperature dependence of the Schrödinger potential U_T in the soft-wall holographic model of [213] for a specific set of parameters. The dashed curve is for $T = 0$, solid curves are for temperatures indicated by the labels (in units of MeV). The first three meson bound states are marked. Figure taken and adapted from the arXiv version of [213]. Right: Spectral function of the Υ-meson for a specific parameter set in the holographic model of [220]. The colors correspond to the different temperatures 100 MeV (blue), 150 MeV (green) and 200 MeV (red). Figure taken from the arXiv version of [220].

where the dilaton potential $V(\phi)$ governs the thermodynamic system properties. It was found, that then only non-trivial flavor functions $G(\phi)$ allow a consistent description of both meson trajectories (governed by U_T) and thermodynamic functions (as a crossover deconfinement transition). Based on the linear response framework for holographic settings (cf. section 4.3), one can calculate the spectral function $\rho(\omega) = -\operatorname{Im} G_R(\omega)$ from the boundary asymptotics of the bulk field. The right panel in Fig. 6.2 shows a result for a selected meson species. In [220], this lead to the observation that the temperature, at which a peak forms in the spectrum might be much larger than the melting temperature following from the Schrödinger potential. Overall, we can fairly conclude that holographic methods do not yet reach the level to provide robust quantitative predictions of all QCD relevant features (meson trajectories, thermodynamic quantities, spectral functions). As noted also in [205], some of the holographic models, e.g. in the recent work [231], predict the melting of spectral functions towards larger frequencies at high temperatures, which is in direct contradiction to the QCD results shown in Fig. 6.1.

In contrast to QCD based methods, holographic approaches provide the advantage of giving access to entanglement measures. Starting with the work [232], it was observed that holographic entanglement entropy can serve as a probe (i.e. order parameter) of the confinement-deconfinement transition. [62] However, no studies so far analyzed this phenomenon explicitly related to meson states or their melting process. Our TN simulations in the next sections therefore provide the genuinely first study of entanglement in this physical context.

[62] See also our earlier work [233] and references therein, where we studied this quantity in a Einstein–Maxwell–dilaton model to characterize different structures in the QCD phase diagram.

6.3 Results from tensor network simulations

6.3.1 Thermal correlator studies

The previous two sections have shown clearly that in a QCD context meson melting is indicated by a thermal broadening and movement of peaks in the in-medium spectral function. In the Ising spin chain model introduced in chapter 4, we have studied in detail retarded thermal correlation functions. In this setup, in which the IR is governed by the $2D$ Ising QFT, we do not have an explicit meson operator available. However, due to the sensitivity of the ϵ operator with scaling dimension $\Delta_\epsilon = 1$ as a real-time probe of meson frequencies, as demonstrated in section 4.10, and the intimate relation of the spectral function with the retarded correlator, it is justified to expect that the melting of meson bound states could show up at high temperatures as the emergence of an imaginary part in the frequency of a meson pole or a change of its real part. In the Fourier spectrum along the real frequency axis, this would correspond to a broadening of the thermal peak. However, in none of our previous simulations, such features were visible. Since we considered the retarded correlator in chapter 4 at the nonintegrable point $M_h/M_g \approx 0.09$ near the E_8 theory, it is a viable possibility that this potential change in the signal is suppressed due to proximity to the integrable E_8 regime.

To examine if this hypothesis holds, we compute here retarded thermal correlators via MPO simulations at the nonintegrable point $M_h/M_g \approx 0.91$ in the ferromagnetic Ising phase, i.e. at about an order of magnitude larger transverse mass perturbations than before. We choose $\beta J = \{0.5, 1, 2, 4, 16\}$ and $\beta M_h = \{0.25, 0.5, 1, 2, 8\}$. Measuring the temperature in units of the first physical meson mass $M_1/J \approx 1.4$, which we extract from the results of [180], the parameters result in $\beta M_1 \approx \{0.7, 1.4, 2.8, 5.6, 22.3\}$. Fig. 6.3 shows the time dependence of the retarded correlator for three selected temperatures. Transient effects, which we studied in section 4.9, correspond to the rapidly decaying peak at early times while mesons show up as persisting oscillations at late times. With increasing temperatures (blue towards red curve), these oscillations are seemingly suppressed. Using the quantitative method outlined in section 4.9, we extract in Fig. 6.4 the residue of the first meson pole as the mean normalization coefficient corresponding to its frequency in the Prony analysis. At low temperatures, $\beta M_1 \gtrsim 5$, the residue is nearly identical, i.e. not changing. On the other hand, it is decreasing by two orders of magnitude at high temperatures ($\beta M_1 \lesssim 3$), which quantifies the visual suppression of meson oscillations in Fig. 6.3. Despite this decreasing of meson residues with increasing temperatures, this effect is not accompanied by any movement of the first meson pole in the complex frequency plane. That is, no thermal broadening via an imaginary part of the complex frequency can be associated to the first meson peak. Based on our previous observations, this conclusion seems to be robust against different parameter regimes of the underlying QFT.

In summary, a direct analogous analysis inspired by QCD approaches does not provide an identical phenomenological picture regarding meson melting. While we can observe a decaying

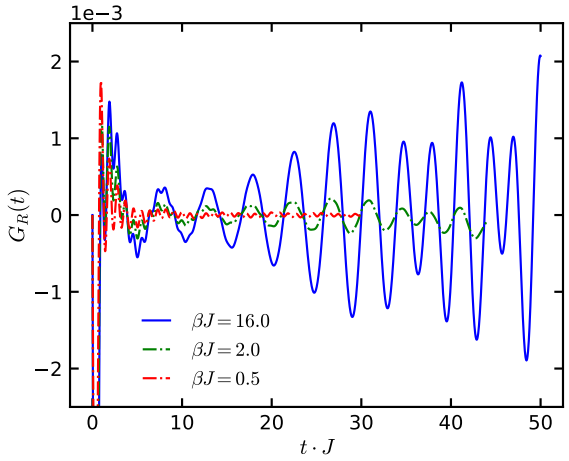

Figure 6.3: Time dependence of the (transverse) retarded thermal correlator in the non-integrable ferromagnetic phase of the Ising model at $M_h/M_g \approx 0.91$. Late-time frequencies are dominated by meson masses and mass differences. Simulation parameters: $L = 200$, $\chi = 200$, $J\,\delta t = 0.006$ (at $\beta J = 0.5$), $J\,\delta t = 0.01$ (otherwise), 2^{nd} order Trotter decomposition.

meson residue, this effect does not correspond to thermal broadening and frequency shift. We therefore cannot assess with certainty, if this process is induced by the melting of individual meson states. This might be not surprising, since we do not have an accurate meson operator at out disposal. On the other hand, it cannot be excluded that the observed properties are specific for the special $2D$ Ising QFT under consideration. To get a better phenomenological understanding, we therefore start now considering entanglement measures. The motivation for this approach comes from the fact that entanglement entropies are sensitive to several correlations existing in the system and therefore could provide a better probe of meson features at high temperatures.

6.3.2 Thermal Rényi entropy scaling

In this section we study entanglement properties of thermal states, i.e. in a static (equilibrium) setting. Entanglement entropy, as defined in eq. (2.18), is a rigorous entanglement measure for pure states. For mixed states, it receives contributions both from classical (here thermal) and quantum correlations. In absence of quantum correlations, it is in thermal systems even identical to the statistical entropy. Such an entwinement is also existing for Rényi entropies, but it is less pronounced due to their higher-order powers in the reduced density matrix. We therefore now consider the second Rényi entropy density as a quantity which can characterize to large extent entanglement properties also in thermal states, defined by

$$s_2 = -\frac{1}{N} \log \frac{\operatorname{Tr} \rho_\beta^2}{(\operatorname{Tr} \rho_\beta)^2}. \tag{6.15}$$

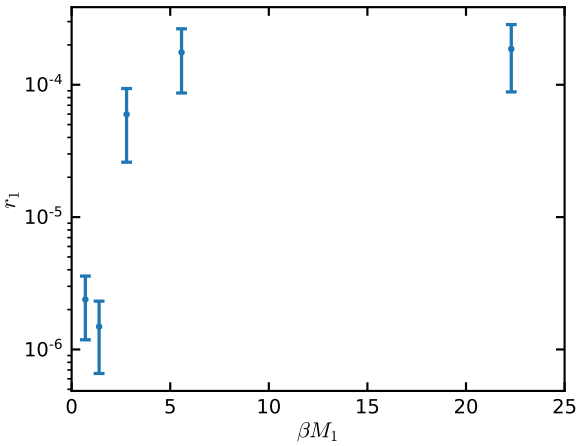

Figure 6.4: Temperature dependence of the residue r_1 of the first meson pole. The residue is extracted from the Prony method applied to the real-time correlator signal from MPO simulations. Temperatures are measured in units of the first physical meson mass M_1.

Here, we analyze the global thermal state $\rho_\beta = \exp[-\beta H]$ for the Ising system in the thermodynamic limit. That is, the iTEBD algorithm (see section 3.5.3) is used to represent the purification $\sqrt{\rho_\beta} \equiv \exp[-(\beta/2)H]$ as a 2-site MPO for the unit cell. Since the normalization condition $\operatorname{Tr} \rho_\beta = 1$ is naturally obeyed in the canonical form, the second Rényi entropy density then follows directly from the dominant eigenvalue η of the transfer operator $\mathbb{E}_{\rho_\beta^2}$ as

$$s_2 = -\log \eta. \tag{6.16}$$

For the thermal system under consideration, the transfer operator $\mathbb{E}_{\rho_\beta^2}$ takes the form

$\mathbb{E}_{\rho_\beta^2}$ =

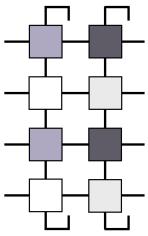

, (6.17)

where a trace over the physical indices is implied. [63] The value of η can be determined efficiently by considering the action of $\mathbb{E}_{\rho_\beta^2}$ on an eigenvector and using iterative eigensolvers.
We are again interested in the nonintegrable ferromagnetic phase, where our TN simulations have the most predictive power. We choose the same Ising QFT parameter point as in section 4.10, specified by $M_h/M_g \approx 0.09$. Additionally, we vary the individual masses M_h and M_g according to the parametrization

$$M_{h,g}^{(n)} = \frac{M_{h,g}^{(0)}}{2^n}, \tag{6.18}$$

[63] In (6.17), the two columns represent the two repeating sites in the 2-site unit cell of the translational invariant chain. Light boxes symbolize $\sqrt{\rho_\beta}$ and darker boxes respectively the adjoint $\sqrt{\rho_\beta}^\dagger$.

keeping their ratio constant. The values $M_h^{(0)}/J = 0.125$, $M_g^{(0)}/J \approx 1.356$ are identical to the parameters of section 4.10. For increasing values of n, the masses are decreasing, i.e. we approach the critical point in the phase diagram.[64] The resulting masses M_1/J of the first meson, which we read out from [180], are hence also decreasing. For a fixed range of lattice spacing values, $\beta J \in [1, 16]$, we therefore can probe different physical temperatures, measured in units βM_1.

Before discussing the results of these simulations, let us consider the expected scaling behavior in the transverse Ising model, i.e. without longitudinal field perturbations causing confinement. From the free fermion mapping (cf. section 4.5), the partition function follows as

$$Z_\beta = \mathrm{Tr}\left[\mathrm{e}^{-\beta H}\right] = \prod_k 2\cosh\left(\frac{\beta\epsilon_k}{2}\right), \tag{6.19}$$

where the single-particle energies are given in (4.39). The definition (6.15) implies immediately that the second Rényi entropy density can be calculated as $s_2 = 2\beta[f(2\beta) - f(\beta)]$, where the free energy density is given as

$$f(\beta) = -\frac{1}{N\beta}\log Z_\beta = -\frac{1}{\beta}\log 2 - \frac{1}{N\beta}\sum_k \log\left[2\cosh\left(\frac{\beta\epsilon_k}{2}\right)\right]. \tag{6.20}$$

This results in

$$s_2(\beta) = \log 2 - \frac{1}{N}\sum_k \log\left[\frac{\cosh(\beta\epsilon_k)}{\cosh^2(\frac{\beta\epsilon_k}{2})}\right]. \tag{6.21}$$

In the thermodynamic limit ($N \to \infty$), the discrete sum is replaced by the integral expression

$$s_2(\beta) = \log 2 - \frac{1}{\pi}\int_0^\pi \mathrm{d}k \log\left[\frac{\cosh(\beta\epsilon_k)}{\cosh^2(\frac{\beta\epsilon_k}{2})}\right]. \tag{6.22}$$

At low temperatures, i.e. in the limit $\beta \to \infty$, one can assume that the dominant contribution to s_2 originates from $k = \pi$, which gives

$$s_2 \sim \frac{\mathrm{e}^{-2\beta J|h-1|}}{\sqrt{\frac{\pi\beta Jh}{|h-1|}}}. \tag{6.23}$$

Note that the term $|h-1|$ is proportional to the free fermion mass $M_h = 2J|1-h|$. On the other hand, at the critical point ($h = 1$), the integral can be evaluated to give a power-law decay with the inverse temperature,

$$s_2 \sim \frac{\pi}{16}\left(\frac{1}{\beta} + \frac{1}{16\beta^3} + \ldots\right). \tag{6.24}$$

[64] This means nothing else than taking the scaling limit described in section 4.5.3.

The exponential scaling at low temperatures in the massive free fermion regime is clearly distinct from the power-law decay at high temperatures at criticality. While we do not have a prediction for the scaling in the nonintegrable ferromagnetic regime, it is tempting to assume that the temperature dependence could be equally determined by the existence of a mass gap in the spectrum. To test this hypothesis, we need to analyze both the low-temperature regime, given for $\beta M_1 \gg 1$, and the high-temperature regime, given by $\beta M_1 \lesssim 1$. In the latter case, we additionally need to ensure that the result is not dominated by lattice excitations, i.e. $\beta/a \gtrsim 1$.

Fig. 6.5 (left panel) shows the behavior of s_2 in dependence on the temperature βM_1. In all parameter examples, a linear behavior in the logarithmic axis scaling is visible at low temperatures. In the right panel, we analyze this regime quantitatively (exemplarily for $n = 1$) by applying the Prony analysis on the signal as a function of βJ and decomposing it into harmonic contributions with complex parameters. Assuming βJ to be artificially complex valued, two clear poles on the imaginary axis are visible. They quantify the exponential decay at low temperatures. The values agree with the masses of the first two meson states (shown as black circles). Based on these findings, we postulate the following low-temperature scaling of the Rényi entropy density

$$s_2 \sim \sum_i c_i \, \mathrm{e}^{-\beta M_i} \tag{6.25}$$

for some coefficients c_i and meson masses M_i, whereby M_1 is obviously dominating. This form of the asymptotic scaling is the natural generalization of the massive free fermion result $s_2 \sim \mathrm{e}^{-\beta M_h}$ in (6.23).

Fig. 6.6 (left panel) shows again s_2 in dependence on βM_1 but emphasizing the high-temperature regime in a double-logarithmic plot. To the left of the grey line the high temperature regime $\beta M_1 \lesssim 1$ starts, while the dashed lines denote the estimated lattice scale for each curve. As n is increasing, i.e. the individual masses $M_{h,g}$ are decreasing, one can observe the emergence of a linear scaling in between these two curves, indicating a power-law behavior. Assuming the general functional dependence

$$f(\beta) \sim \beta^{-p}, \tag{6.26}$$

we extract in Tab. 6.1 the values of the power-law exponents p from a linear fit to the numerical data in between these two scales. For $f = s_2$, the value $p = 1$ is obtained with a very good accuracy of only a few percent. This implies that the high-temperature scaling behavior matches the CFT expectation from (6.24). Based on the clear observation of meson states in the entropy scaling at low temperatures and their absence at high temperatures, we interpret this signature as strong evidence for meson melting. In this regime, which is not yet influenced by the lattice scale, melted meson states do not leave an imprint on the entropy scaling any more, which is why the scaling is identical to a critical system. To further corroborate this finding, we additionally analyse also the scaling behavior of the thermal entropy (right panel

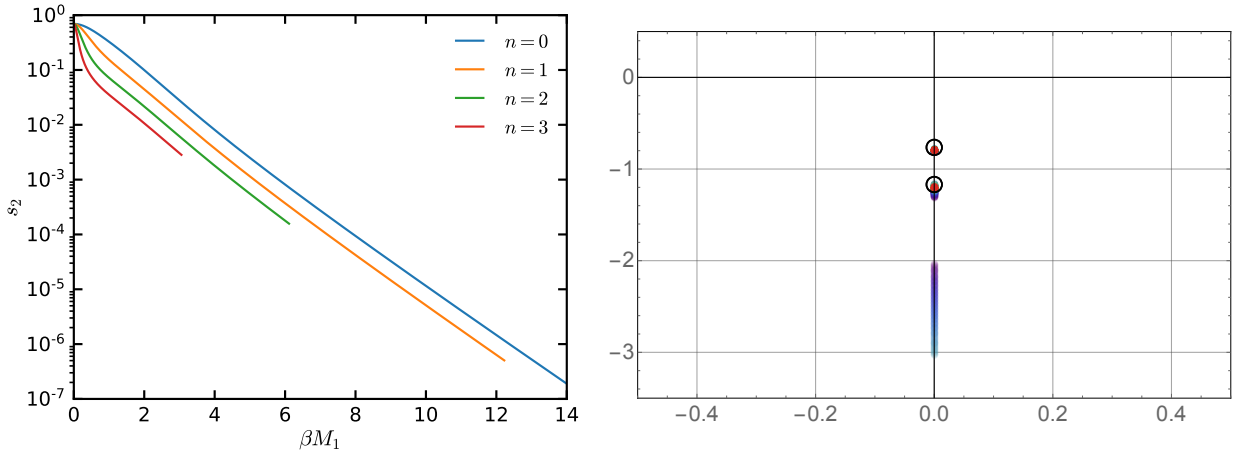

Figure 6.5: Left: Temperature dependence of the Rényi entropy density s_2. The curves are calculated using iMPO simulation at constant ratio $M_h/M_g \approx 0.09$ in the nonintegrable ferromagnetic phase using the parametrization (6.18).
Right: Prony result of the $n = 1$ curve of $s_2(\beta J)$ in the complex βJ plane. The low temperature decay is dominated by frequencies matching the meson masses M_1/J and M_2/J, shown as black circles.

Table 6.1: High-temperature scaling exponents p in the functional power-law ansatz (6.26) for several quantities f.

f	$n=0$	$n=1$	$n=2$	$n=3$	exact
s_2	0.926	1.073	1.106	1.078	1
E	1.171	1.645	1.933	2.022	2
$\partial E/\partial\beta$	1.176	2.027	2.709	2.955	3

in Fig. 6.6) and its derivative. Both these thermodynamic quantities show a similar power-law scaling at high temperatures. The corresponding exponents are tabulated in Tab. 6.1. At $n = 3$ they agree well with the analytical expectation, which is set by the scaling dimension $\Delta = 2$ of the CFT operator. Interestingly, the Rényi entropy s_2 seems to allow an even better estimation of the scaling exponent for all values of n, indicating that entanglement measures can provide a cleaner identification of the meson melting process.

In summary, we have shown that the scaling behavior of the second Rényi entropy density, as the selected entanglement measure for thermal states, provides a clear signature of the asymptotic high and low-temperature regime in a nonintegrable QFT with meson bound states. At low temperatures, we found that the behavior is dominated by the exponential damping of the form (6.25). At high temperatures, the power-law dependence (6.26) matches the CFT behavior. We interpret the latter scaling with the fact that the meson states have been melted. In fact, a similar analysis for the E_8 regime yields the same qualitative picture, providing evidence that the results are independent from integrability properties of the underlying system. Naively, it might look trivial that a massive QFT matches at high temperatures the CFT behavior due to the fact that the temperature then provides effectively the only scale

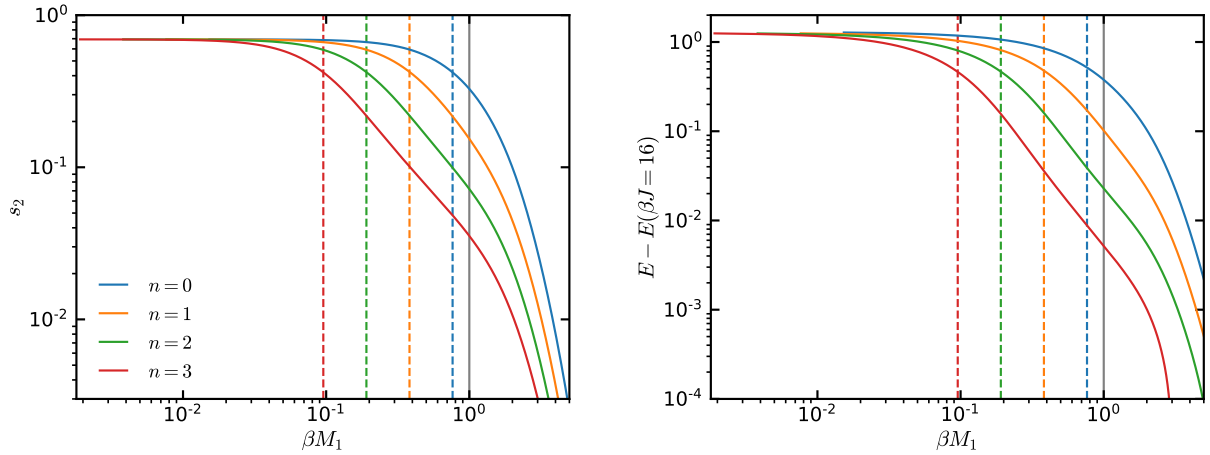

Figure 6.6: High-temperature scaling of the second Rényi entropy density s_2 (left) and thermal energy density E (right) in the nonintegrable ferromagnetic phase at $M_h/M_g \approx 0.09$ for the parametrization (6.18). The grey line at $\beta M_1 = 1$ indicates the high-temperature threshold. Dashed lines indicate the lattice scale for each curve.

in the system. (A similar situation for the massive free fermion regime in the Ising model is discussed for example in [129].) However, in our present studies we do have nonperturbative meson bound states in the spectrum, which are "visible" at low temperatures, and we observe a smooth transition to the high-temperature regime, which we can disentangle from the UV lattice scale. We therefore see the scaling properties of the second Rényi entropy as a clear witness of the meson melting process in a static situation. While we have focused on the second order definition, it is possible that this conclusion holds also to higher-order Rényi entropies.

6.3.3 Thermal quantum quenches

Quantum quench as a paradigm

We now turn to the concept of quantum quenches to study a dynamical situation in the context of meson melting. A quantum quench means a rapid change of a Hamiltonian parameter governing the time evolution of a physical system. Initiated primarily by the the works [234,235], quantum quenches became a theoretical paradigm to probe and characterize dynamical properties of QMB systems. In contrast to all previous situations considered in this thesis, the modification of the underlying Hamiltonian during time evolution kicks the system out of equilibrium. This drastic change can induce new processes and effects through dynamical interactions. An overview of thermalization and relaxation phenomena of such perturbed systems can be found in [124,125].

The powerful quench approach plays a major role in all areas of physics. For example, in our own work [6], we study quenches in a cosmological context in curved spacetime. Further works analyze quench properties in (other) QFTs [236–238] and holography [239,240]. A characteristic feature of some systems' response to quenches are universal scaling behaviors.

This can be observed not only for operator expectation values (see [238] and references therein) but also for complexity [241] as a quantum information quantity. If a quench is performed across a quantum critical point, dynamical quantum phase transitions [242] occur, which are signalled by a nonanalytic kink of a time-dependent rate function, and can carry universal CFT information in the entanglement spectrum [243]. Moreover, quantum quenches can cause the scrambling of quantum information [244]. Besides this theoretical perspective, quantum quenches became realizable via quantum simulations [245,246], which opens the intriguing possibility to analyze out of equilibrium dynamics experimentally.

The following studies are motivated by the important work [201]. Therein, the authors analyze the entanglement growth for quantum quenches in the Ising model. In more detail, iTEBD methods are used to prepare the ground state $|\psi_0\rangle$ of some Hamiltonian H_0, which then is time evolved with a Hamiltonian H_1 in the ferromagnetic phase in presence of meson states, i.e. at finite longitudinal field values. It was observed that the existence of mesons causes oscillations in the entanglement entropy at frequencies given by their masses and mass differences. If the initial state is in the paramagnetic phase (i.e. a quench across the phase boundary), the associated entanglement growth persists mostly forever, whereas it is always bounded if $|\psi_0\rangle$ is located in the ferromagnetic phase. While the original work [201] considered a semi-classical parameter regime away from the quantum critical point, the recent paper [247] observed such *entanglement oscillations* also in the E_8 QFT regime of the Ising model. Similar observations were made for gauge theories in [248–250] as well as for quasiparticles in paramagnetic quenches [251,252].

Many properties of the entanglement production and spreading after quantum quenches can be understood with a *quasiparticle model* (QPM). Originally developed in [253] for the Ising model, it was later found to hold also for generic integrable systems (in absence of mesons) [254–256] and TFD states [257]. A generalization of the model was provided in [258]. See also [259] for a pedagogical review on the topic. In essence, the model describes the initial state as a source of independent entangled quasiparticle pairs, which are created at any given point and move after the quench with opposite momentum and velocity through the QMB system and therefore spread quantum correlations. In lattice systems, the maximum speed of propagation is limited by the Lieb–Robinson bound [78]. As a consequence, the entanglement entropy is increasing linearly as long as only one partner of the particle pair leaves a considered subregion of finite size. When also the second partner leaves the interval, the entanglement entropy saturates.[65] This picture is consistent with general entanglement scaling laws in the time evolution found in [260]. For the special case of a semi-infinite spatial bipartition this implies an indefinite entanglement growth. However, also the boundedness of entanglement production for the meson case can be explained within the quasiparticle picture [201]. Namely, the existence of a confining potential, due to the presence of meson states, induces that quasi-

[65] Note that it does not decrease since also new quasiparticle pairs are created.

particles bounce back as they get separated from their partners, causing the oscillatory and bounded behavior.

Apart from influencing the entanglement evolution in QMB systems and QFTs, mesons impact also the thermalization behavior of thermodynamic quantities after quantum quenches [261, 262]. In fact, as it is studied in the latter two references, thermalization can be avoided due to the existence of rare and non-thermal states in the spectrum. The same conclusion holds also for (1+1)-dimensional QCD as shown in [263]. The authors of [176,177] employed Hamiltonian truncation methods to study quenches in the Ising QFT. In contrast to TN simulations, they, however, do not provide access to entanglement measures. Further relaxation and thermalization aspects in spin chains are discussed, e.g., in [264,265] for global quenches and in [266,267] for broken translational invariance.

In the following, we are interested to apply the above quench protocol to thermal states. Instead of ground state quenches, finite temperature quenches are much less explored, see [268–273] for selected results. In this scenario, we analyze the time evolution of generalized entanglement entropies to detect the melting of mesons at high temperatures. Some of these Rényi entropies became recently measurable in quantum simulation experiments [274]. This opens the opportunity to study similar physical systems and test our predictions beyond the classical realm.

Setup

In our analysis, we prepare a pre-quench purified thermal state $\sqrt{\rho_0} = \exp[-\beta H_0/2]$ using the iTEBD algorithm, and in the subsequent real-time evolution we consider the purification $\sqrt{\rho_1}(t) = U(t)\sqrt{\rho_0}$ where $U(t) = \exp[-iH_1 t]$, i.e. an instantaneous global quench is applied at $t = 0$. The post-quench Hamiltonian H_1 is kept fixed to study the same physical point in the phase diagram. For the latter, we choose again the parameters $M_h^{(0)}/J = 0.125$ and $M_g^{(0)}/J \approx 1.356$ from the parametrization (6.18), which possess the smallest time period $2\pi J/M_1 \approx 4.2$ (for $M_1/J \approx 1.5$) of the first meson in comparison to the other parametrized masses. As we know from the equilibrium studies in section 4.10.1, MPO simulations and Prony signal analysis allowed a reliable identification of the QFT meson masses from available time windows in this regime.

The previously considered global Rényi entropy density s_2 in eq. (6.16) would be constant under time evolution for this setup, while its corresponding value for a finite subsystem is computationally too demanding to calculate for large bond dimensions. We therefore consider a semi-infinite spatial bipartition and calculate the *reflected (Rényi) entropies* $\tilde{s}_{1,2}$ from the

singular values λ_i of the purified thermal state $\sqrt{\rho_1}(t)$ as

$$\tilde{s}_1 = -\sum_i \lambda_i^2 \log(\lambda_i^2), \tag{6.27}$$

$$\tilde{s}_2 = -\log\left(\sum_i \lambda_i^4\right). \tag{6.28}$$

These reflected entropies can be interpreted as upper bounds for the corresponding Rényi entropies, which would follow from minimal purifications. We will monitor their growth and behavior of entanglement oscillations during the time evolution after the quench. The reflected entropy was originally introduced in [275] in a holographic setting as a proposed dual to the area of the entanglement wedge cross section. While we employ it here primarily for computational reasons, reflected entropies found recently a considerable amount of attention in the context of the AdS/CFT correspondence, see e.g. [276–280] for relevant explorations. In particular, the works [281–283] discussed it also for CFT quenches, whereas [284] analyzed a variety of related mixed state entanglement measures as a holographic probe of confinement.

Any such quench will perturb the initial state by increasing the energy density of the thermal state. To quantify the quench magnitude, we introduce the important concept of the *effective (inverse) temperature* β^*. This quantity is defined by equating the (bare) energy density of the pre-quench thermal state, measured w.r.t. H_1, with the (bare) energy density of an equilibrium state in the post-quench Hamiltonian, i.e. [66]

$$\mathrm{Tr}\left[H_1\, \mathrm{e}^{-\beta H_0}\right] = \mathrm{Tr}\left[H_1\, \mathrm{e}^{-\beta^* H_1}\right]. \tag{6.29}$$

Since we keep the final Hamiltonian H_1 fixed, the effective temperature can be increased either by varying the initial temperature β w.r.t. a fixed pre-quench Hamiltonian H_0 or by modifying the parameters of H_0 for fixed β. We will employ both methods in our studies. In the latter scenario, we choose the initial points in the phase diagram as shown in Fig. 6.7. The different quench protocols, labelled by the numbers in Fig. 6.7, result in the effective temperatures $\beta^* J$ (measured w.r.t. H_1) summarized in Tab. 6.2 (determined up to two digits) for several initial temperatures βJ (measured w.r.t. H_0). The final quench point is realized for $h = 0.9375$ and $g \approx 0.0746$. In the quench protocol ①, we have $h = 0.93$, and for ⑥ $h = 0.8732$. In type ⑦, the longitudinal field is chosen asymptotically large as $g = 100$. The remaining initial parameters are identifiable from Fig. 6.7. Note in particular that protocol ④ and ⑤ start in the classical regime, whereas ② is in the E_8 phase and ③ at the critical point. The different quench types encompass pure transverse quenches (①,②,④,⑥) and longitudinal quenches ⑦. Otherwise, both fields are quenched. We consider the case of an initial low temperature (i.e. close to the ground state) at $\beta J = 16$ as well as higher initial temperatures, cf. Tab. 6.2. Note

[66] Note that we always consider densities here since we work with the unit cell in the iMPO formalism. For our global quench setup, the relation (6.29) is then identically also valid for the whole system.

Table 6.2: Comparison of the initial pre-quench temperatures βJ of the thermal state (w.r.t. H_0) and the resulting post-quench effective temperatures $\beta^* J$ (w.r.t. H_1) for the different quench types shown in Fig. 6.7.

initial temperature $(\beta J)_{H_0}$	effective temperature $(\beta^* J)_{H_1}$						
	①	②	③	④	⑤	⑥	⑦
16	6.10	3.55	1.55	0.91	0.66	3.55	0.93
2	2.00	1.92	1.34	-	-	-	-
0.97	-	-	0.91	-	-	-	-
0.5	0.50	-	-	-	-	-	-

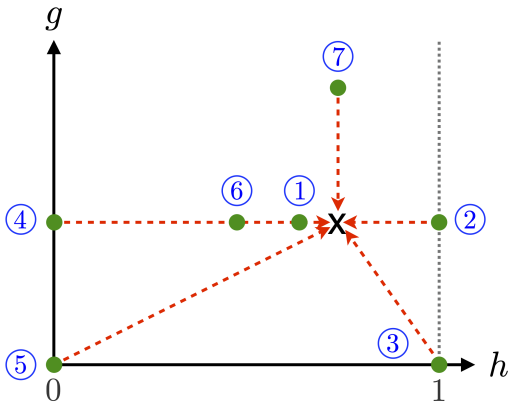

Figure 6.7: Overview of the different quench protocols in the transverse (h) vs. longitudinal (g) field plane. Thermal initial states are prepared at inverse temperature β for the parameter locations marked by green dots. By quenching to the final nonintegrable ferromagnetic point, denoted by red arrows towards the black cross, an effective temperature β^* as listed in Tab. 6.2 is induced by the thermal quench. The E_8 regime is marked by the grey dotted line.

that protocol ⑥ is tuned such that is has the same effective temperature as ② for $\beta J = 16$. Similarly, type ④ and ⑦ at $\beta J = 16$ and ③ at $\beta J = 0.97$ result in (nearly) the same effective temperature. Overall, we have adjusted our setup to achieve both low physical temperatures $\beta^* M_1 \gg 1$ as well as high temperatures $\beta^* M_1 \lesssim 1$, while avoiding the lattice regime $\beta^* J \ll 1$.

Results

We start out considerations for quenches from an initial low-temperature thermal state at $\beta J = 16$. Fig. 6.8 shows the results for $\tilde{s}_1$ (top row) and $\tilde{s}_2$ (bottom row) for the quench protocols ①-④. As listed in Tab. 6.2, the effective temperatures are in increasing order from $\beta^* J \approx 6.10$ to $\beta^* J \approx 0.91$. As a consequence, it is visible from Fig. 6.8, that the entanglement is growing larger as the effective temperature is raised, or, in other words, quantum correlations are building up. In the quench types ① and ②, which are shown in detail in the right column, $\tilde{s}_1$ and $\tilde{s}_2$ exhibit an oscillatory behavior, similar to the ground state case as first discussed in [201]. As we will analyze in detail below, these entanglement oscillations are caused by the meson states at characteristic frequencies of their masses. Type ② (orange curves) shows

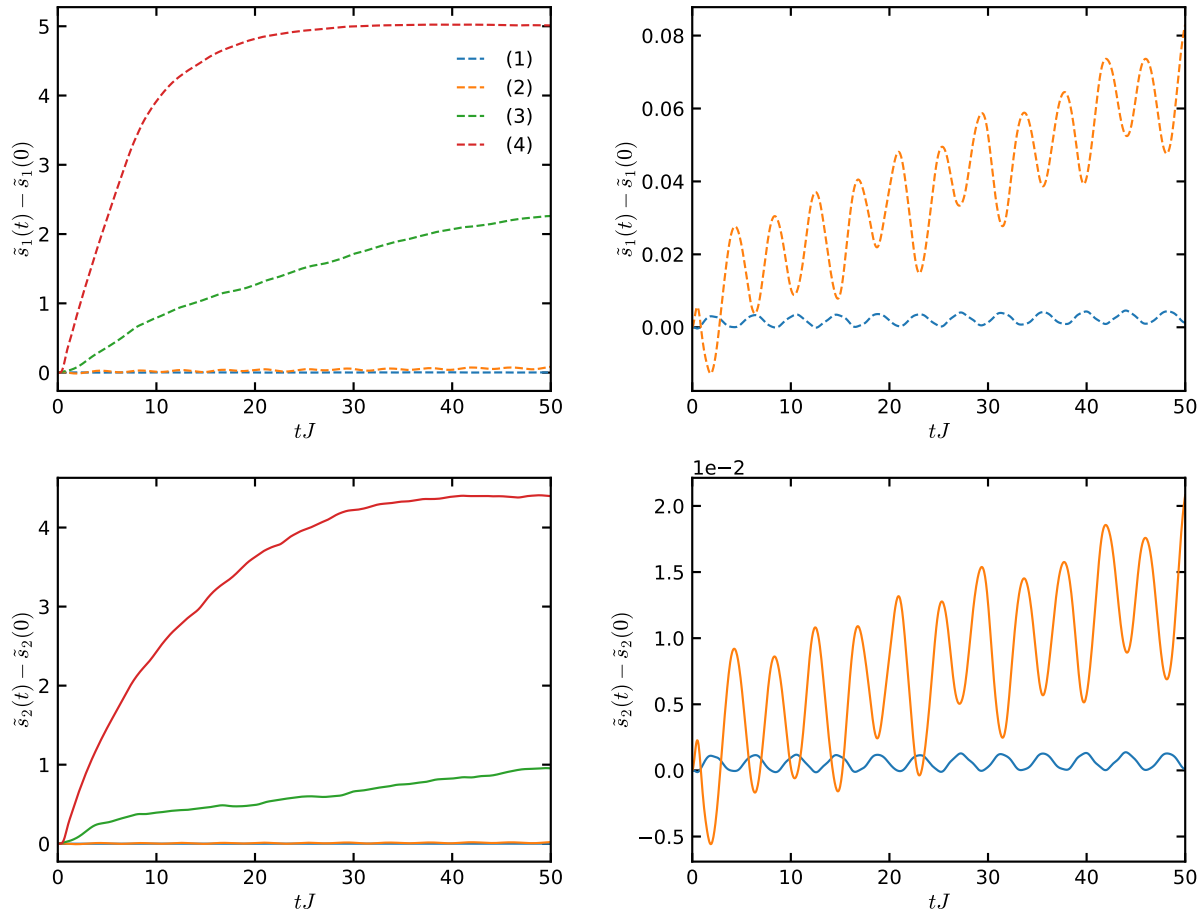

Figure 6.8: Time dependence of the first (top) and second (bottom) reflected entropies for the quench protocols ①-④ with an initial temperature $\beta J = 16$. The right column zooms into the first two quench types. With increasing effective temperature (in order of the quench labels) the entanglement growth is getting enhanced and suppresses the entanglement oscillations.

on top of these entanglement oscillations an overall increase, which does not yet seem to be bounded as expected from the predictions in [201]. However, we have to keep in mind that we have chosen a parameter point in the QFT regime of the Ising model close to its critical point. The meson masses, e.g. in absolute units of J, are smaller as compared to a semi-classical regime and hence the arising envelope frequencies (that bound the entanglement growth) would require (much) longer time scales. These are not in our focus here and partially also not easily numerically achievable. We therefore concentrate our discussion on the entanglement behavior at early and intermediate time scales after the thermal quantum quench. From Fig. 6.8 it then becomes apparent that the entanglement oscillations become heavily suppressed as the effective temperature is raised from type ① to ④. By that we mean that the meson states do not dominate the entanglement growth at their characteristic mass frequencies anymore. In particular, the first reflected entropy of quench protocol ④ (red dashed curve in top left panel) seems to grow very strongly at early times, which superficially seems to resemble a

linear behavior. Note that the plateau existing for this curve at times $tJ \gtrsim 20$ is, in fact, not physical but an effect of the finite bond dimension. Below, we will study these effects in detail separately.

These findings are in general valid for both $\tilde{s}_1$ and $\tilde{s}_2$ as plotted in the two rows in Fig. 6.8. Observe, however, that the growth of $\tilde{s}_2$ is suppressed as compared to $\tilde{s}_1$. For this reason, it turns out that the second reflected entropy allows for a more precise identification of meson masses from the entanglement oscillations. That is why we now consider $\tilde{s}_2$ for a detailed analysis using both the Prony signal analysis method as well as the Fourier spectra. The results are presented in Fig. 6.9 for the first 3 quench protocols (from left to right). At the lowest effective temperature $\beta^* M_1 \approx 9.3$ for quench type ① (left column), the Prony analysis allows a clear identification of the first 5 meson poles, which are in good agreement with their QFT mass values when compared to the predictions in [180] (solid vertical lines). Additional features are visible also at M_6 to M_8, which, however, become fuzzier and hence more uncertain. In addition, the continuum threshold at $2M_1$ is identifiable as a vertical line of poles, indicating a branch cut (shown as the dashed vertical line). In the corresponding Fourier spectra, the meson poles translate into peaks at their frequency values. The peak of the first meson is largely dominating over the other ones. Overall, the Fourier spectrum is decreasing over several orders of magnitude towards larger frequencies. The green dash-dotted lines in the Fourier spectra mark all 6 possible mass differences between the first 4 meson states. At their respective values, kinks appear in the spectrum, corresponding to additional poles in the Prony plot. They lie at frequencies smaller than the first meson mass as well as between M_1 and M_2.

As the effective temperature is raised to $\beta^* M_1 \approx 5.4$ in protocol ② (middle column) and $\beta^* M_1 \approx 2.4$ in protocol ③ (right column), the meson pole identifications become fuzzier in the Prony analysis. Notably, the absolute values of the corresponding Fourier spectra are raised by 3 and 6 orders of magnitude, respectively. For protocol ③, the Fourier spectrum is flattening out. Since in all cases the post-quench nonintegrable QFT regime is identical, it can be concluded that this effect is induced by raising the effective temperature. When comparing the meson peak heights to the overall magnitude of the Fourier spectrum, the impact of the meson mass frequencies seems to get suppressed at high temperatures. We see this thermal suppression effect on the entanglement spectrum as a first hint how the melting of meson states at even higher temperatures can be detected. The available data in Fig. 6.9 are, however, inconclusive whether this process is consistent with a sequential process as existing in a QCD context (cf. the discussion in section 6.1).

To analyze the influence of the initial state in more detail, the time evolution of the reflected entropies and resulting Fourier spectra of quench protocols ② and ⑥ are compared in Fig. 6.10. Starting from a pre-quench thermal state at $\beta J = 16$, they both have the same effective temperature $\beta^* J \approx 3.55$ or $\beta^* M_1 \approx 5.4$ but are initially prepared in the E_8 regime versus the ferromagnetic phase. Both $\tilde{s}_1$ (dashed curves) and $\tilde{s}_2$ (solid curves) differ only marginally in

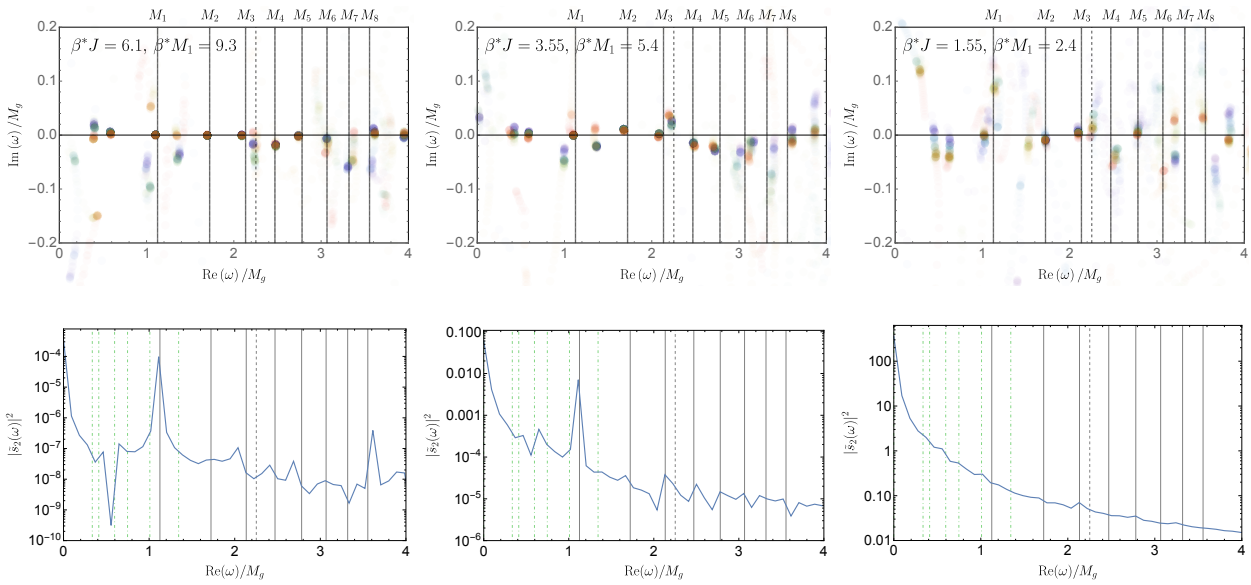

Figure 6.9: Results of the Prony signal analysis (top) and Fourier spectra (bottom) of $\tilde{s}_2$ for the quench protocols ①-③ (from left to right) with an initial temperature $\beta J = 16$ and effective temperatures $\beta^* J$ as shown. Solid vertical lines represent meson masses from ref. [180] and dashed lines mark the continuum threshold of $2M_1$. Green dash-dotted lines mark all possible mass differences of the first 4 mesons.

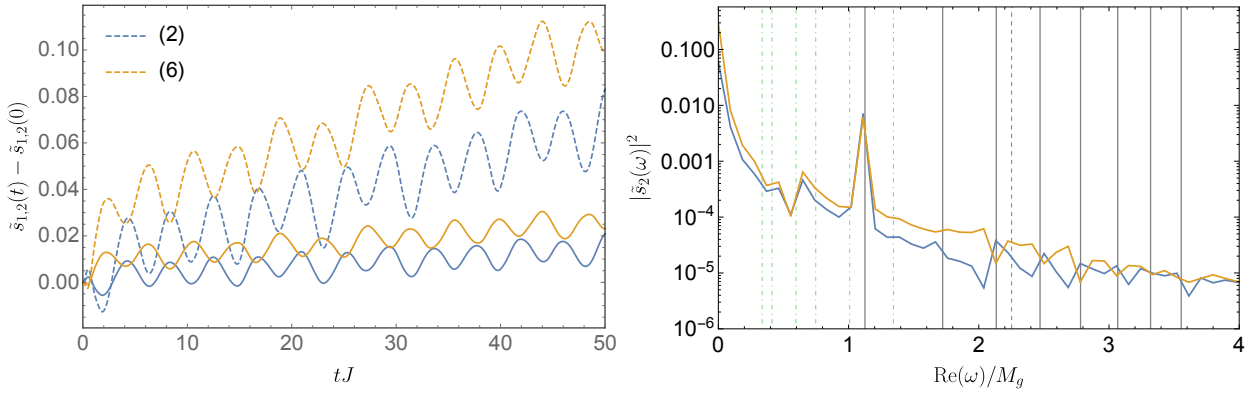

Figure 6.10: Comparison of the quench protocols ② [in blue] and ⑥ [in yellow] for an initial temperature $\beta J = 16$ and the same effective temperature $\beta^* J \approx 3.55$ or $\beta^* M_1 \approx 5.4$. Left: Time dependence of the first (dashed) and second (solid) reflected entropy in both models. Right: Corresponding Fourier spectra of the second reflected entropy.

the two quench protocols and exhibit a slight phase shift. The first meson peak dominates the Fourier spectrum equally in both models. For the available frequency resolution and range, both Fourier spectra are in close correspondence with each other. These results indicate that the described effects, for this particular case, are primarily driven by thermal effects, set by the effective temperature. Below, we will find a similar situation also for other models at even higher temperatures, providing evidence for the robustness of the physical interpretation about thermal effects from our findings.

We now study the situation of raised effective temperature by starting from an initial thermal state at a higher temperature $\beta J = 2$. In this case, the entanglement growth is larger and it becomes important to monitor carefully the behavior of the truncation error in the iTEBD simulation. The obtained reflected entropies are shown in the upper row of Fig. 6.11 for two bond dimensions, and the corresponding truncation error is plotted in the lower row for the quench protocols ①-③ (from left to right). The effective temperatures for protocol ① and ② are very close, $\beta^* M_1 \approx 3.1$ and $\beta^* M_1 \approx 2.9$, resulting in very similar curves for the reflected entropies. For quench type ③, the effective temperature $\beta^* M_1 \approx 2.0$ causes an entanglement growth about twice as large. The results for the reflected entropies deviate at late times for the different bond dimensions (blue vs. orange curves), demonstrating that the results have not yet fully converged in the simulated time interval. Due to the slower entanglement growth, this effect is milder for $\tilde{s}_2$. Once the maximal bond dimension is reached during the time evolution, the truncation error is continuously growing as visible in the bottom row of Fig. 6.11. In contrast to simulations at even higher temperature, which will be discussed below (cf. Fig. 6.13), this simulation is, however, still faithful. That means that the truncation error is not decreasing or saturating, which would be a sign that the obtained MPO does not contain physical information anymore. Being aware of these limitations, we compare in Fig. 6.12 the Prony results and Fourier spectra of $\tilde{s}_2$ for the different quench protocols (for the highest bond dimension). In all examples, features in the complex frequency become fuzzier in the Prony analysis when compared to the quench results in Fig. 6.9 at lower temperatures. Some of the meson poles fully disappear, in particular for type ③ (top right panel). The corresponding Fourier spectra are increased by several orders of magnitude and now flattened out in all cases.

The overall phenomenological picture that arises from these analyses is that an increase of the effective temperature leads to an enhancement of the entanglement growth, which suppresses the entanglement oscillations caused by meson states in the thermal bath. In absence of mesons, the QPM predicts a fully linear growth of entanglement entropies. We therefore aim in the following discussion to identify a linear growth of the reflected entropies as a signature of meson melting at the highest attainable temperatures. For this line of reasoning, we consider in Fig. 6.13 the time evolution of reflected entropies for the quench protocol ④ with an effective temperature $\beta^* M_1 \approx 1.4$ at different bond dimensions (left panel) and their corresponding truncation error (right panel). Due to the large entanglement growth, convergence is realized

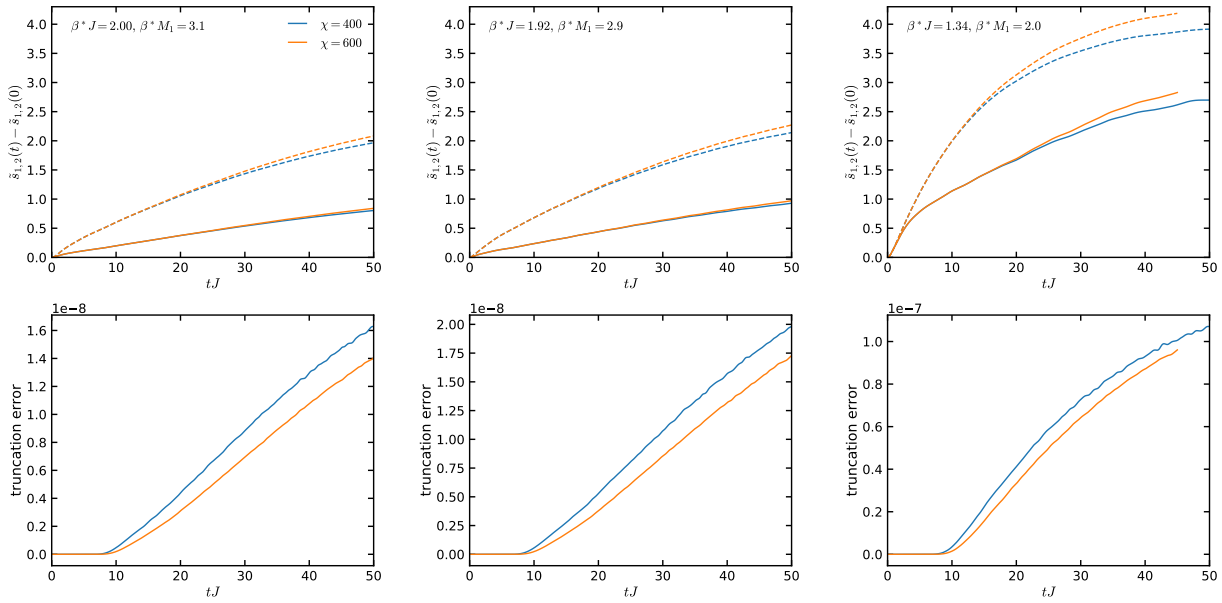

Figure 6.11: Time dependence of the reflected entropies (top) and truncation error (bottom) for the quench protocols ①-③ (from left to right) with an initial temperature $\beta J = 2$ and effective temperatures $\beta^* J$ as shown. The first (dashed) and second (solid) reflected entropy are shown for several bond dimensions, indicating the time interval of convergence.

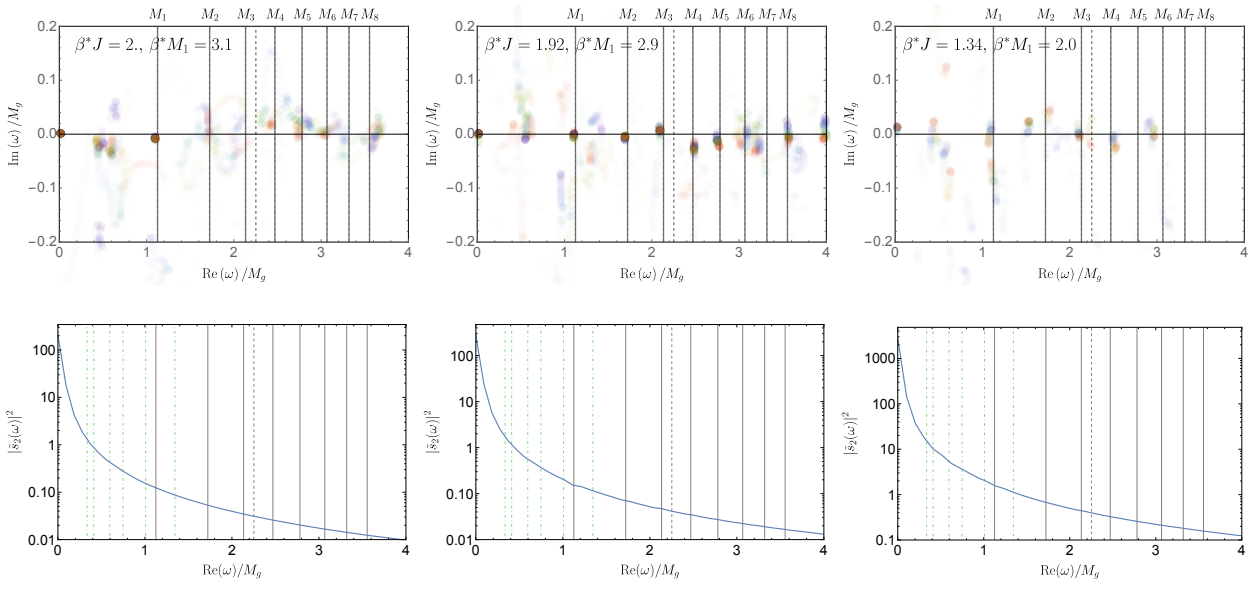

Figure 6.12: Results of the Prony signal analysis (top) and Fourier spectra (bottom) of $\tilde{s}_2$ for the quench protocols ①-③ (from left to right) with an initial temperature $\beta J = 2$ and effective temperatures $\beta^* J$ as shown. Solid vertical lines represent meson masses from ref. [180] and dashed lines mark the continuum threshold of $2M_1$. Green dash-dotted lines mark all possible mass differences of the first 4 mesons.

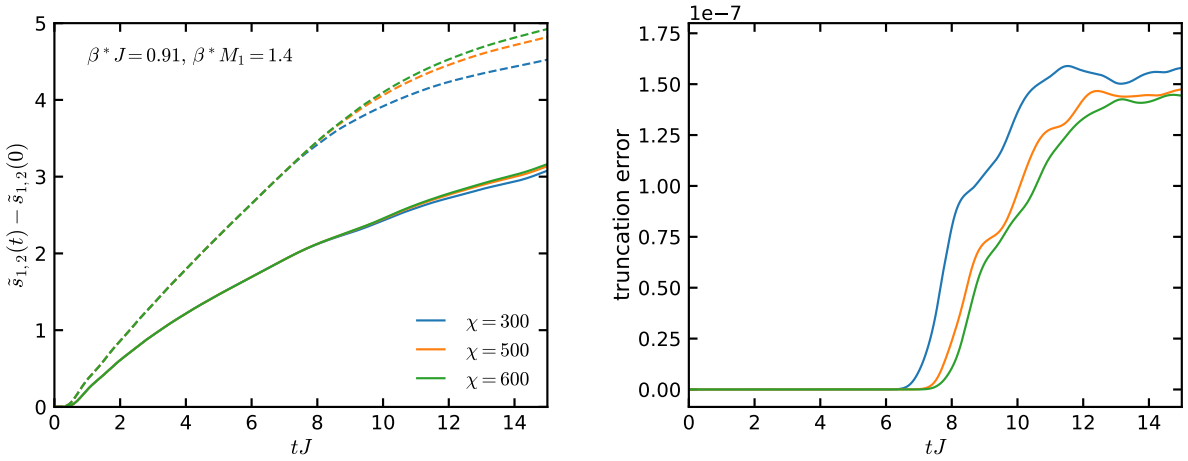

Figure 6.13: Time dependence of the reflected entropies (left) and truncation error (right) for the quench protocols ④ with an initial temperature $\beta J = 16$ and effective temperature $\beta^* J$ as shown. The first (dashed) and second (solid) reflected entropy are shown for several bond dimensions χ.

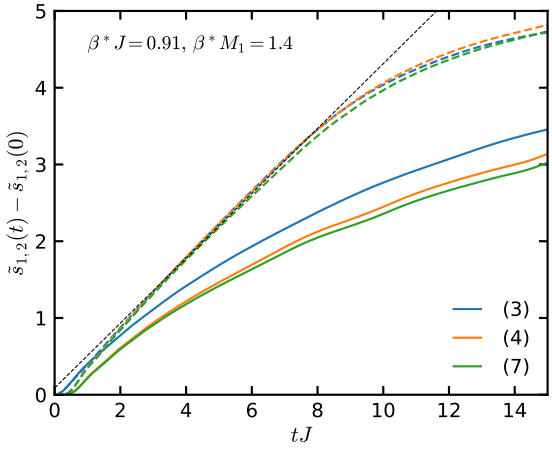

Figure 6.14: Time dependence of the first (dashed) and second (solid) reflected entropy for the quench protocols ③, ④ and ⑦ with the same effective temperature $\beta^* J \approx 0.91$. The data are based on the $\chi = 500$ simulations. The black dashed line marks a linear fit function for $\tilde{s}_1$ at early times.

only up to times $tJ \lesssim 9$. At later times the entropies bend and saturate (cf. also the red curves in Fig. 6.8 for $\chi = 500$). This effect is coinciding with an irregular behavior of the truncation error, which partially decreases and then saturates at even later times. As argued before, we can interpret this unphysical feature as a signature of the breakdown of the MPO simulation. In Fig. 6.14 the same data are compared to quench type ③ and ④ at (nearly) the same effective temperature (cf. Tab. 6.2). There are only marginal differences for $\tilde{s}_1$ between all quench protocols and a small scaling difference for $\tilde{s}_2$ in type ③ (blue solid curve) compared to the others. Since the initial states are in very different regimes (classical, ferromagnetic and critical) and even at different initial temperatures, the overall agreement confirms that the discussed effects on the entanglement growth are indeed thermally induced. Since the

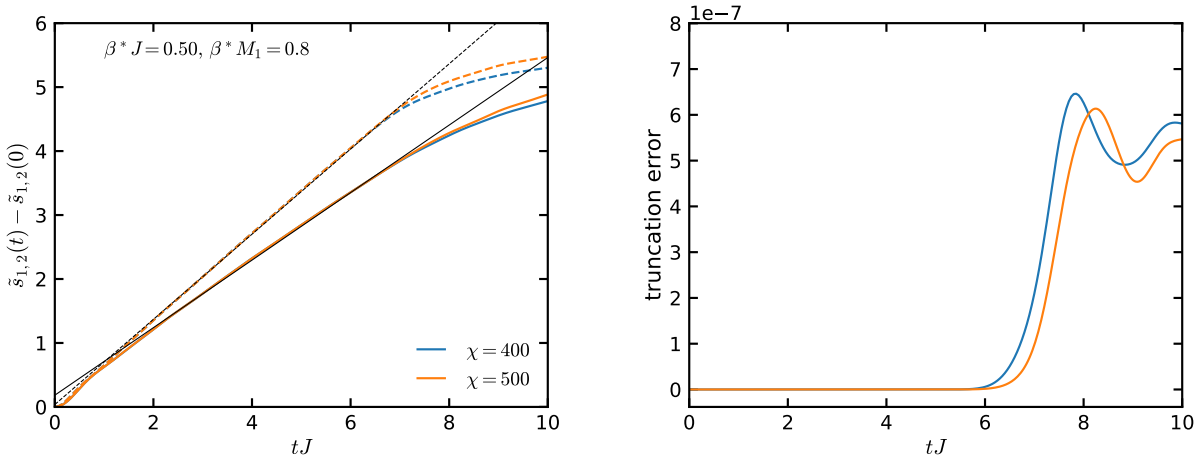

Figure 6.15: Time dependence of the reflected entropies (left) and truncation error (right) for the quench protocol ① with an initial temperature $\beta J = 0.5$ and effective temperature $\beta^* J$ as shown. The first (dashed) and second (solid) reflected entropy are shown for several bond dimensions χ. The black dashed and solid lines mark a linear fit function for $\tilde{s}_1$ and $\tilde{s}_2$ at early times, respectively.

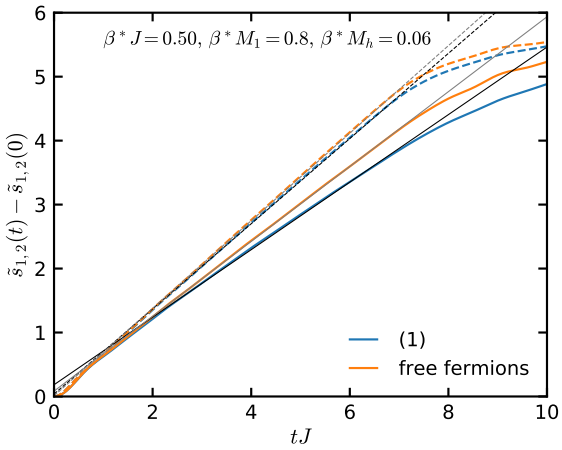

Figure 6.16: Time dependence of the first (dashed) and second (solid) reflected entropy for the quench protocol ① (blue) and the corresponding free fermion regime (orange) with an initial temperature $\beta J = 0.5$ and effective temperature $\beta^* J$ as shown. The data are based on the $\chi = 500$ simulations. Linear fit functions for $\tilde{s}_1$ and $\tilde{s}_2$ at early times are marked respectively in black for type ① and in grey for the free fermion case.

trustable time ranges are now very limited, a Prony signal analysis or Fourier transformation is not applicable. Fig. 6.14 therefore exhibits directly also a linear function, which is obtained by fitting $\tilde{s}_1$ in the time interval $2 \leq tJ \leq 9$ as $0.09 + 0.42(tJ)$. The data for $\tilde{s}_1$ seem to be bounded by such a linear growth, but, upon careful inspection, do not (yet) follow exactly this scaling behavior. On the other hand, the curves for $\tilde{s}_2$ grow less strongly in a nonlinear fashion.

The data for the highest achieved effective temperature $\beta^* M_1 \approx 0.8$ are displayed in Fig. 6.15. The entropy curves (left panel) are obtained for quench protocol ① at two bond dimensions,

indicating convergence up to $tJ \approx 7.5$. At later times, the truncation error (right panel) is again irregular and hence signalling the limitations of the simulation. One can observe a strong growth of both reflected entropies. In the time interval $1.5 \leq tJ \leq 7.5$, we can fit the functions $0.04 + 0.67(tJ)$ and $0.18 + 0.53(tJ)$ to $\tilde{s}_1$ and $\tilde{s}_2$, respectively. In contrast to the simulations at intermediate temperatures, both reflected entropies now seem to follow this linear growth behavior after a brief initial time period with irregular growth induced through the quench itself. As alluded before, this linear increase can be only understood within the QPM if there are no meson states existent. Since in the present case we have $\beta^* M_1 < 1$ in the physical high-temperature regime, we explain this qualitative behavior through the fact that the mesons are melted, i.e. do not contribute entanglement oscillations to the overall growth of entanglement entropies anymore.

This interpretation is corroborated through a quench study in the (massive) free fermion regime. For that case, we set the longitudinal field value to $g = 0$ in quench type ① and choose again the highest initial temperature $\beta J = 0.5$. This integrable transverse quench results analogously in the effective temperature $\beta^* J \approx 0.50$. In Fig. 6.16 the resulting reflected entropies (shown in orange) are compared to the previous nonintegrable counterpart (blue curves). The differences in the entanglement growth between these two quench types are relatively small. In particular, the free fermion data confirm the linear growth of the reflected entropies after the initial quench period. We can respectively fit the functions $0.01 + 0.68(tJ)$ and $0.08 + 0.59(tJ)$ to $\tilde{s}_1$ and $\tilde{s}_2$, which are shown as grey curves and can be compared to the black ones for the previous nonintegrable regime. These results confirm that a linear growth of reflected entropies is a property of the free fermion regime, which is in accordance with the QPM description. It therefore strengthens our interpretation on meson melting for the nonintegrable ferromagnetic case, since this qualitative behavior can be only explained when meson states are not present in the physical system.

6.4 Discussion and outlook

In this chapter we provided an in depth study of the meson melting phenomenon from a quantum information perspective. Modern QCD approaches treat this mechanism as a sequential process that strictly requires a dynamical treatment. While both QCD and holographic approaches indicate the melting of individual meson states through a thermal broadening of their corresponding peaks in the spectral function, we could not observe a related feature in the complex frequency structure of retarded thermal equilibrium correlators in nonintegrable ferromagnetic parameter regimes of the $2D$ Ising QFT (cf. the analyses in section 6.3.1). It should be emphasized that the absence of this feature for this particular observable does not mean that the melting process does not take place or exist. Instead, one can interpret this property through numerical challenges in its detection and the unavailability of an explicit

meson operator in analogy to QCD.
We therefore motivated a new paradigm to capture and describe meson melting properties in this theory via entanglement properties. In particular, for a thermal equilibrium setting, we showed that the scaling of the second Rényi entropy density is determined at low temperatures through an exponential damping (as a function of the inverse temperature β) set by the meson masses. In contrast, at high temperatures, the behavior is identical to that one expected in a CFT (power-law dependence), meaning that meson states have been melted, i.e. the temperature sets the only scale in the physical system.
Independent from these findings, we could observe similar scaling differences also in a truly out of equilibrium setting by studying real-time properties of reflected entropies and entanglement production in the time evolution after thermal quantum quenches. For that, we prepared initial thermal states in the ferromagnetic phase of the Ising model and implemented a quantum quench by simulating their evolution under a fixed post-quench Hamiltonian in the nonintegrable ferromagnetic phase. We could vary the effective temperature of this setup either through different parameter regimes in the pre-quench state or by modifying its initial temperature. While at low effective temperatures mesons give rise to entanglement oscillations, we observed a linear entanglement growth at the highest achieved temperatures, meaning that the imprint of mesons is (fully) suppressed. The latter observation is consistent with a QPM interpretation that excludes the presence of meson states, and MPO simulations in the massive free fermion regime. We similarly infer from these dynamical properties that the meson melting process took place.
Our analyses comprehensively show that basic entanglement measures such as Rényi or reflected entropies can serve as witnesses of the meson melting process both in static and dynamical settings at finite temperature. For the particular theory under consideration, the $2D$ Ising QFT, we do not see conclusive indications to decide whether this process is consistent with a sequential picture. In future studies, it therefore would be very interesting to address the latter problem in more detail. While we focused on a relativistic QFT emerging in the IR limit of a spin chain model, it would be of course highly desirable to analyse a similar setting also in more complicated gauge theories. In particular, we want to export our viewpoint, namely the study of entanglement measures as intrinsic properties of QMB systems, also directly into the QCD community, where we are convinced that this new perspective can shine light on many open questions related to meson properties.

7 Prospects for quantum simulations

The previous chapters in this part of the thesis exemplified how TN simulations help us in understanding emergent phenomena of QMB systems, which are important across different fields in physics [285–287]. Many of these developments are closely connected to the field of quantum computation and simulation, in which qubits as fundamental degrees of freedom are used to carry out computational tasks or simulate physical systems. The first viewpoint is referring to *digital* QS, in which quantum gates are sequentially applied to a quantum state, and the second one is realizing an *analog* simulation by implementing a QMB Hamiltonian. TN methods allow similar algorithmic procedures by either contracting individual gates onto a quantum state (like in the TEBD algorithm) or representing (Hamiltonian) operators as MPOs. Over the last decade, QS technologies [288–290] advanced rapidly in controllable platforms like optical lattices [291–293] or ion traps [294–297]. In contrast to TN approaches, they promise to study physical systems and fundamental effects beyond the capability of classical computers. For example, previous experiments already analyzed static and dynamical properties of quantum matter [246,274,298–308] and LGTs [309–311]. Many proposals make concrete suggestions on the observation of physical effects and theories on near-future devices [290,312–320].

Concretely, we are interested in this chapter to explore the capabilities of analog ion trap simulations to identify and analyze relativistic meson physics on current devices. Similarly to chapter 4 and 6, we are motivated by QCD, where the phenomenology of mesons is important for a dynamical understanding of HICs, which in turn gives insights into early universe physics by studying the QGP [151]. As the previous research chapters have already shown, meson states have also in a condensed matter context severe implications for entanglement, correlations, and thermalization in QMB system at zero and finite temperature [247,250,261,262,321–325]. Ion trap quantum simulators can implement 1-dimensional (Ising) spin chain Hamiltonians with long-range (LR) interactions. Previously we employed parameter regimes of the nearest-neighbor (NN) Ising model with a longitudinal field, which confines domain walls into bound states, i.e. mesons [182]. The relatively new results [326,327] show that experimentally realizable LR interactions have, in fact, the same effect. We want to make use of this feature to study meson physics in interesting physical parameter ranges. Under such conditions, it is already known that the existence of meson states has also profound phenomenological consequences. For example, they lead to the emergence of anomalous cusps in dynamical quantum phase transitions [320,328,329].

The first experimental observation of mesons in LR spin chains was provided in [330] via trapped-ion QS of correlation spreading in quenched systems. From a theoretical perspective, the recent works [331–333] analyzed the capabilities of quantum simulators to detect string breaking and meson scattering as interesting fundamental processes. In all these examples, a semiclassical regime was considered or very small transverse field values were assumed, allowing for a reformulation as simple gauge theory. Here, we instead focus on Zamolodchikov's relativistic E_8 regime of the Ising QFT [178], see our earlier discussion in section 4.5.3 for an introduction. The integrability properties of this theory can be seen as a prediction, which were first experimentally confirmed by measuring its meson spectrum in [334]. The recent papers [335–337] expanded these neutron scattering based measurements and spectroscopic methods to better precision and new materials in solid-state crystals.
In the present chapter, we want to systematically study if experimentally realizable small spin chain models allow for an identification of the E_8 meson regime. Exact diagonalization techniques are employed to calculate the energy absorption spectrum within the linear response framework. We will show that for sufficiently strong LR suppression, the low-lying E_8 meson states can be identified, and that the spectra are in accordance with analytical expectations of the E_8 QFT. We then propose an experimental protocol to realize this setup via absorption spectroscopy [301,303] on ion trap quantum simulators. Fueled by the promising experimental [309,310] and theoretical [338–344] progress in implementing and studying LGTs on QS devices, we foresee the potential to probe meson physics also in relativistic gauge theories, which are relevant on the route to develop theoretical ideas for the QS of the standard model in particle physics on near-future devices.

7.1 The long-range Ising model

In section 4.5 we have introduced the NN Ising model, defined by the Hamiltonian (4.32), which gives rise to the Ising QFT (4.40) in the IR regime of the continuum limit. This model now serves as an ideal prototype, which we compare to the LR Ising model, which can be experimentally implemented on ion trap quantum simulators. It is defined by the Hamiltonian [299,300,302,345]

$$H_{\mathrm{LR}} = -J \left(\sum_{i<j}^{N} \frac{1}{|i-j|^{\alpha}} \sigma_i^z \sigma_j^z + h \sum_{j=1}^{N} \sigma_j^x + g \sum_{j=1}^{N} \sigma_j^z \right). \tag{7.1}$$

The algebraic LR interaction between two spins at spatial index positions i and j is quantified by the coefficient α. It now becomes important to consider differences in systems with open boundary conditions (obc) versus periodic boundary conditions (pbc), defined by $\sigma_{N+1} = \sigma_1$. In the NN model, this amounts to the addition of the interaction term $-J\sigma_N^z \sigma_1^z$, while for LR interactions on a circle we assume that two spins interact along their minimal distance

between i and j. Observe that the NN model is formally recovered in the limit $\alpha \to \infty$. In contrast, only the range $0 \leq \alpha \leq 3$ is accessible in experimental setups [346,347]. However, it was previously observed [348] that already LR systems with $\alpha \approx 3$ resemble very closely the physics of the NN Ising model.

7.2 Energy and absorption spectra

In the following analyses, we use numerical diagonalization techniques to characterize the the LR model in the the E_8 regime, i.e. for longitudinal perturbations along the critical point ($h = 1$, $g > 0$). The NN and LR Ising model are compared with each other to investigate whether the E_8 meson spectrum (with analytical mass ratios given in Tab. 4.1) is surviving and identifiable also in presence of power-law interactions. The relatively small system sizes, to which the numerical diagonalization methods are limited, are within the scope of a few dozens of trapped ions on current quantum simulators [296,297]. The basic logic for the observability of meson states in such small systems is that the associated length scale of the first meson, $l \sim 1/M_1 \sim |g|^{-8/15}$, is sufficiently small to be captured by the finite size chain. This is achieved when the longitudinal field value g is chosen large enough. While it might look contradictory to observe QFT information further away from the critical point, it was, however, observed in [349] that even relatively large values of g are able to reproduce the E_8 spectrum. The latter reference was for a realistic model of a solid state crystal, which indicates the strong impact of the QFT regime on the physics of the model.
We consider two main quantities in this section. The first are the energy levels (also denoted as energy spectrum), expressed via the normalized mass gaps m_n/m_1 for the lowest $n = 1, 2, \ldots$ excited eigenstates. Here, the mass gap m_n of level n is given as the as the energy difference to the groundstate, i.e. $m_n = E_n - E_0$. Furthermore, we calculate the absorption spectrum within the linear response framework. The latter is of primary interest, since spectroscopic methods have been developed in recent years which allow to measure spectra on ion traps [301,303] akin to neutron-scattering experiments in solid states. For that, following [157], we assume that a constant operator A is perturbing the system Hamiltonian in the time domain as follows

$$H = H_0 + H_1, \qquad \text{where} \qquad H_1 = -A\, f(t), \tag{7.2}$$

and let O be an (a priori different) operator whose response to the system is considered. We may A assume to be Hermitian, $A = A^\dagger$, such that a real external perturbation of the form $f(t) = \cos(\omega t)$ can be chosen. The field induced energy absorption rate is then given as

$$Q \equiv \frac{\mathrm{d}}{\mathrm{d}t} \langle H \rangle = \left\langle \frac{\partial H}{\partial t} \right\rangle = - \langle A(t) \rangle \frac{\partial f}{\partial t}, \tag{7.3}$$

where we consider the (now time-dependent) operator A in the Heisenberg picture. It can be

shown that the *mean energy absorption rate* follows as

$$\overline{Q} = \overline{\left\langle \frac{\partial H}{\partial t} \right\rangle} = \frac{1}{2}\omega\, \chi''_{AA}(\omega), \tag{7.4}$$

where $\chi''(\omega) \equiv \chi''_{AA}(\omega)$ is the imaginary (dissipative) part of the susceptibility (for $A = O = A^\dagger$). For in general distinct operators A and O, it is given in the Lehmann representation as

$$\chi''_{OA}(\omega) = \pi \sum_{n,m=0}^{2^N-1} \langle n|A|m\rangle \langle m|O|n\rangle \,(p_n - p_m)\, \delta[\omega - (E_m - E_n)], \tag{7.5}$$

where the double sum is taken over all eigenstates $|n\rangle$ and $|m\rangle$ of the system. The delta function in eq. (7.5) ensures a contribution to the susceptibility iff the probe frequency ω equals the energy differences $E_m - E_n$. We are interested in the zero temperature case, in which the finite temperature population factors $p_n = \mathrm{e}^{-\beta E_n}/Z_\beta$, with $Z_\beta = \sum_n \mathrm{e}^{-\beta E_n}$ as the partition function, simplify to $p_n = 0, 1$. In particular, we consider the situation of all absorption energies measured w.r.t. the ground state $|0\rangle$ with energy E_0, and $p_0 = 1$ and $p_n = 0$ for $n > 0$. (Either $m = 0$ or $n = 0$ is set in the double sum (7.5).) It will turn out that salient meson features are accessible with the measurable operator

$$O = A = \sum_{i=1}^{N} \sigma_i^z \cos(k r_i). \tag{7.6}$$

Here, $k \in [-\pi, \pi]$ is the quasi-momentum and $r_i = ai$ the lattice position. We restrict our studies to the zero momentum case of $k = 0$. Upon relabelling, the expression for the imaginary part susceptibility then takes the form

$$\chi''(\omega, k = 0) = \pi \sum_{n=0}^{2^N-1} \sum_{i=1}^{N} |\langle 0|\sigma_i^z|n\rangle|^2 \left\{\delta[\omega - (E_n - E_0)] - \delta[\omega + (E_n - E_0)]\right\}. \tag{7.7}$$

To mimic a realistic experimental situation, we have to keep in mind that the energy resolution is restricted by the reachable observation time t_{obs}. The delta function can then be approximated by a Lorentzian

$$\delta[\omega - (E_n - E_0)] \approx \frac{\Gamma}{[\omega - (E_n - E_0)]^2 + \Gamma^2} \tag{7.8}$$

according to the Wiener–Khintchine theorem [350,351], where the width is related as

$$\Gamma = \frac{1}{t_{\mathrm{obs}}}. \tag{7.9}$$

Based on this framework, we carefully analyze in the following subsections the dependence on the system size, LR parameter and longitudinal field value to assess the prospects of identifying the E_8 regime in spin chain models amenable to ion trap QS.

7.2.1 Finite size effects

We consider system sizes in the range $12 \leq N \leq 18$, which are solvable either by exact numerical diagonalization, or iterative eigensolvers for sparse matrices while ensuring to keep a large portion of the spectrum. Fig. 7.1 shows the resulting mass gaps m_n/m_1 for the lowest $n = 1, \ldots, 400$ ($N = 12$, top row) and $n = 1, \ldots, 600$ ($N = 18$, bottom row) excited eigenstates. [67] We choose an exemplary longitudinal field $g = 3$ in the NN (left column) and LR (right column) Ising model with the largest experimentally possible decay parameter $\alpha = 3$. As in any finite size system, the spectrum is discrete and energy levels show up as as band structures. The systems with obc (blue data) match some of the higher analytical E_8 mass ratios (shown as grey dashed background lines) but deviate from the lowest ones. In contrast, for pbc (orange data) at least 5 lowest meson levels can be cleanly identified (6 levels for $N = 12$). Only the fourth meson level is slightly underestimated, otherwise the gap ratios agree well with the analytical expectations. In this case, the first $n = 1, \ldots, N$ eigenvalues are determined by the momentum dispersion relation in the first Brillouin zone and comprise the the first meson level. The effect of the finite size difference on the energy spectrum (top vs. bottom row) is very mild for both obc and pbc. For the former, it can be observed that higher bands in the LR model seem to resemble a semi-continuous branch.

In the E_8 theory, multiparticle states exist above the continuum threshold at $2M_1$ and form a continuum. Although the spectrum is discrete in the finite size system under consideration, one still can identify the mass sum $M_1 + M_2$ (shown as the lowest grey dotted line). Higher order mass sums are obscured since they are very close to some of the analytical mass ratios. These results are overall valid for both NN and LR interactions. The latter resemble nearly identically the NN profiles for pbc and are only slightly smeared-out for obc. In both cases, pbc reproduce well the low-lying analytical meson spectrum. We therefore focus in the following analyses on finite systems on a ring, but compare the results to the E_8 theory on an infinite line (as represented in Tab. 4.1), i.e. we neglect finite volume corrections according to Lüscher's formula [352].

From the characteristic eigenstates of the models, the absorption spectra, shown in Fig. 7.2 as a function of the frequency, are following from eqs. (7.7) and (7.8). We have chosen the experimentally realistic value $\Gamma/J = 0.1$ in both the NN (left panel) and LR model (right panel). Peaks exist at or very close to the analytical E_8 mass ratios (marked by the grey

[67] The two system sizes differ exponentially in the number of their eigenstates. However, for this choice of range for n, which is bounded by the computational resources at $N = 18$, we can keep a comparable excerpt of the total spectrum.

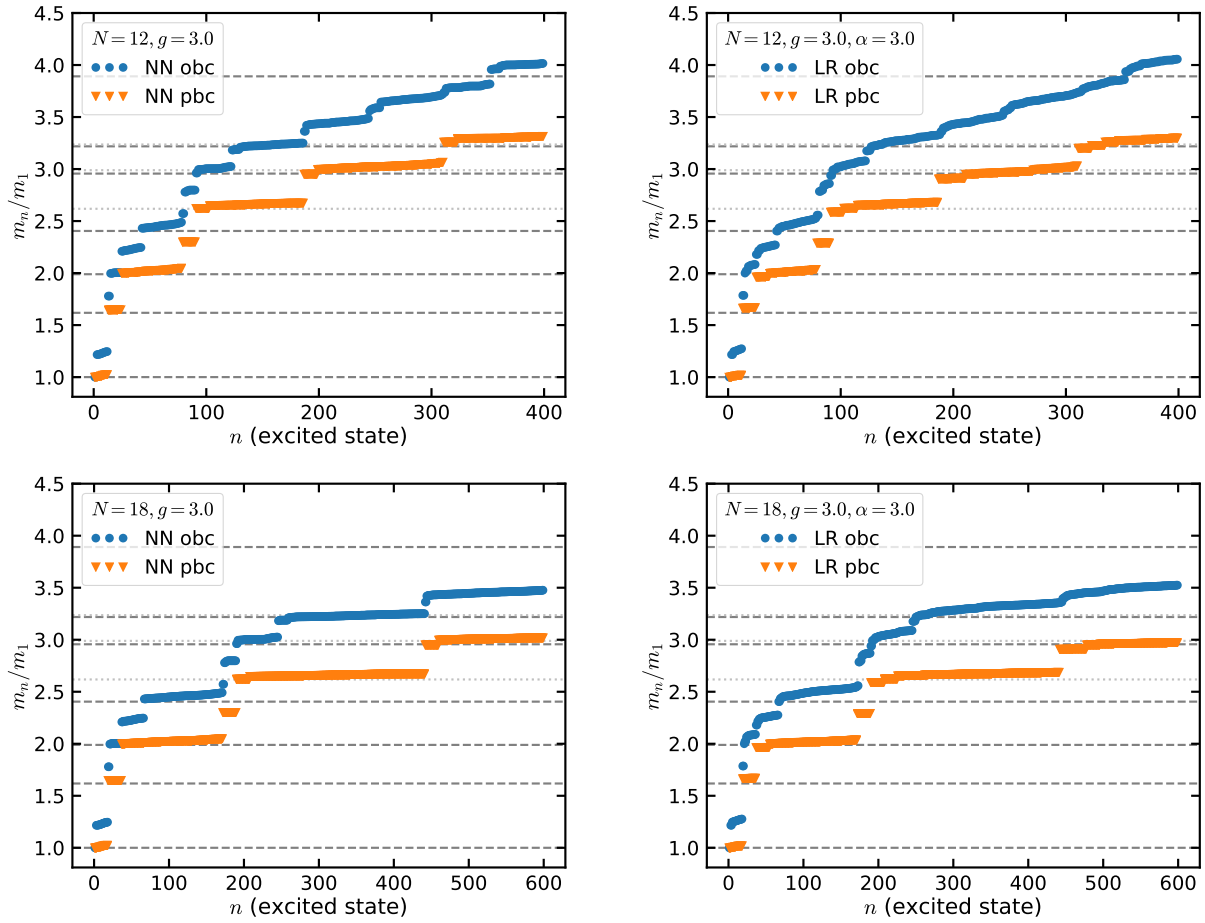

Figure 7.1: Comparison of the numerical energy spectra (normalized mass gaps of excited states) in the NN (left) and LR (right) Ising model with obc (blue data) and pbc (orange data) for chains of size $N = 12$ (top) and $N = 18$ (bottom). Grey dashed lines represent the the analytical E_8 meson mass ratios (cf. table 4.1). Grey dotted lines correspond to multiparticle states with masses $M_1 + M_2$, $M_1 + M_3$ and $2M_2$ (in ascending order).

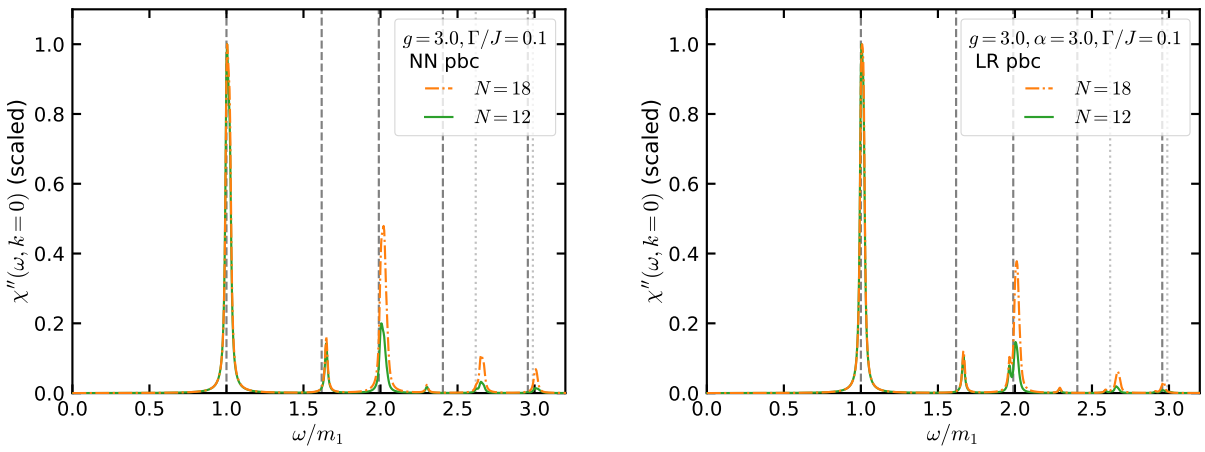

Figure 7.2: Comparison of the energy absorption spectrum in the NN (left) and LR Ising model (right) for different chain sizes N. The data are scaled to the maximum of the spectrum. Grey dashed lines represent the the analytical E_8 meson mass ratios (cf. table 4.1). Grey dotted lines correspond to multiparticle states with masses $M_1 + M_2$ and $M_1 + M_3$.

dashed lines), indicating the existence of mesons. The first two meson peaks are very sharp and there are nearly no differences visible between the results for $N = 12$ and $N = 18$. Differences occur only in multiparticle states above the the continuum threshold at $2M_1$. In particular, the third and fifth peak structure are overlapping with the continuum threshold and the mass sum $M_1 + M_3$, respectively. The mass sum $M_1 + M_2$ is independently visible as a separate peak. Similar to the energy levels, these peak features appear almost equivalently in the NN and LR model, i.e. experimentally measurable algebraic interactions allow an equally good identification of the E_8 meson spectrum.

7.2.2 Long-range dependence

We now analyze the dependence on the LR coefficient by considering the range from $\alpha = 0$ (all-to-all LR interactions) up to $\alpha = 3$ (strong LR suppression) in detail. To minimize finite size effects as much as possible, we set $N = 18$ and choose $g = 3$. In Fig. 7.3 the resulting energy spectra are shown for all integer values of α. At $\alpha = 0$, three completely degenerate and identical branches exist for obc and pbc. As α is increasing for obc, semi-continuous branches become more and more gapped. For pbc, the branches split into discrete bands, resembling the E_8 theory ratios already for $\alpha \gtrsim 2$.

The resulting absorption spectra are displayed for a quantitative comparison on an absolute scale in the right panel of Fig. 7.4, and for a better visual perception also in relative units in the left panel of Fig. 7.5. The left panel in Fig. 7.4 compares the spectra to the results of the NN Ising model. As α is increasing, peaks form at the analytical E_8 meson mass ratios and the previously identified and described mass sums. Their absolute height is enlarging and already at $\alpha = 3$ there is only a very small difference in the spectral intensity of the first meson peak in the LR vs. NN model. In fact, the first meson peak always retains the largest density and, at $\alpha = 0$, is the only one which can be clearly identified.

In the right panel of Fig. 7.5, the absorption spectrum of the LR model at the largest suppression $\alpha = 3$ (green curve) is compared explicitly to the NN model (orange curve). In addition, the *dynamical structure function* as the analogon in the E_8 QFT is shown (blue curve). The latter was very recently calculated in [353] for a comparable frequency broadening of $0.05M_1$. It is formally defined as the Fourier transformation of the two-point correlation function,

$$D^{\Phi\Phi}(\omega, k) = \int \mathrm{d}t \sum_{r_i} \mathrm{e}^{i\omega t - ikx} \langle 0| \Phi(x,t)\Phi(0,0) |0\rangle \,. \tag{7.10}$$

Using the relation $\langle 0| \Phi(x,t)\Phi(0,0) |0\rangle = \langle 0| \mathrm{e}^{-iPx} \mathrm{e}^{iHt} \Phi(0,0) \mathrm{e}^{-iHt} \mathrm{e}^{iPx} \Phi(0,0) |0\rangle$, the zero net

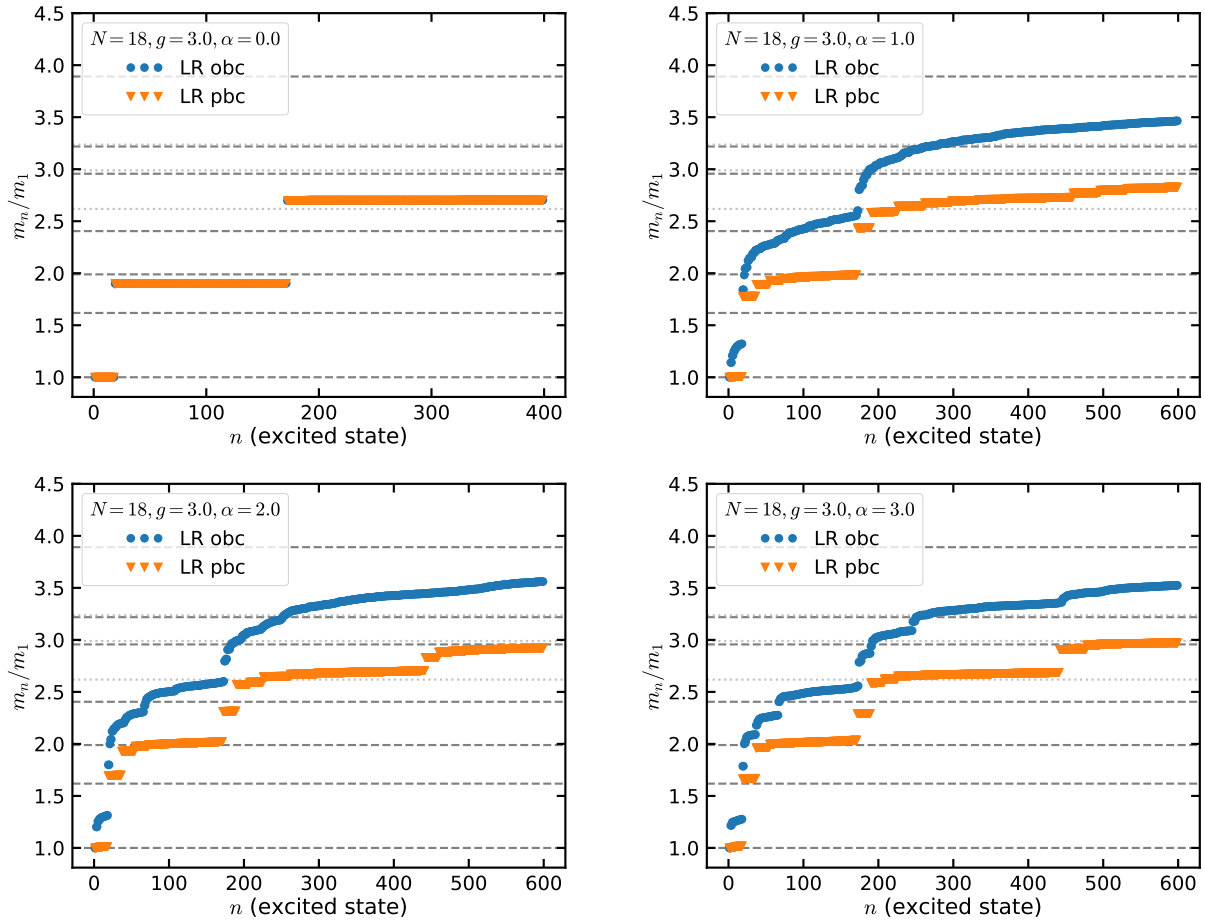

Figure 7.3: Effect of the LR coefficient α on the numerical energy spectrum (normalized mass gaps of excited states). Background lines are as in Fig. 7.1. Figures taken from [2].

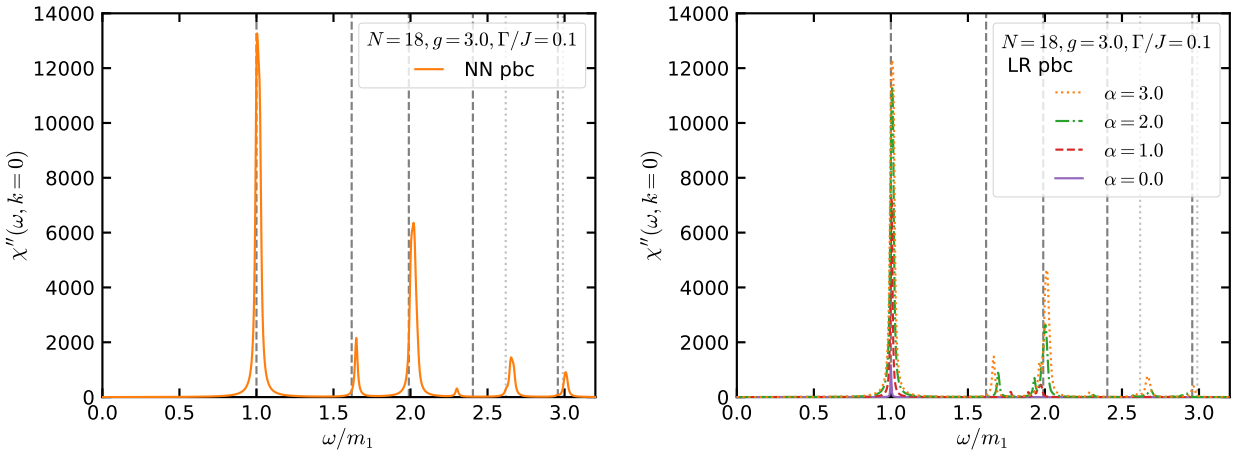

Figure 7.4: Comparison of the absorption spectrum in the NN (left) and LR Ising model (right). In the LR model, the coefficient α is varied over the whole experimentally accessible range of values. Background lines are as in Fig. 7.2. Figures taken from [2].

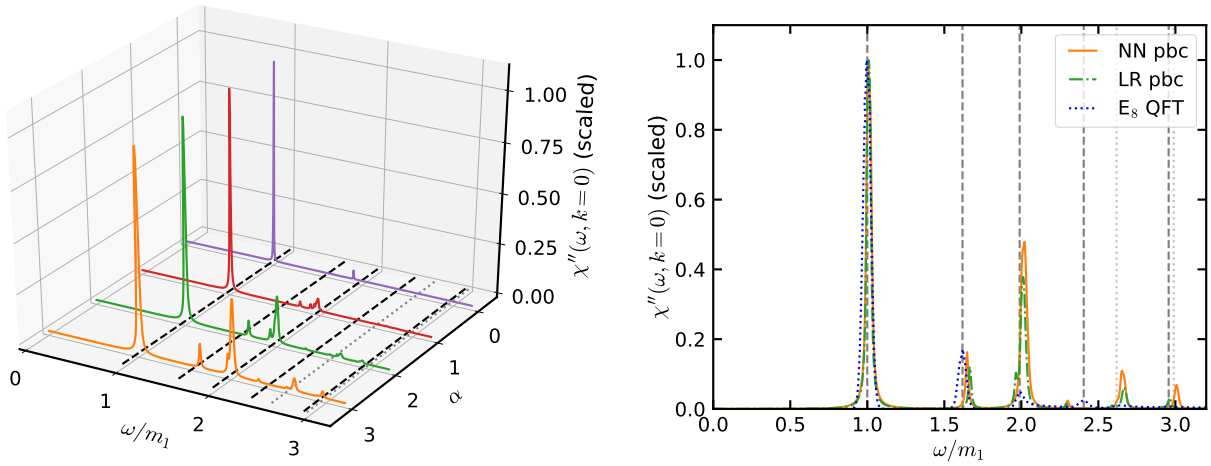

Figure 7.5: Left: Energy absorption spectrum of the LR model with pbc in dependence on the power-law coefficient α. The data are scaled to the maximum of the spectrum. Black dashed lines represent the analytical E_8 meson mass ratios (cf. table 4.1). Grey dotted lines correspond to multiparticle states with masses $M_1 + M_2$ and $M_1 + M_3$.
Right: Comparison of the scaled energy absorption spectrum in the NN and LR model (at the largest suppression $\alpha = 3$) with the analytical E_8 dynamical structure function from [353]. Background lines are as in Fig. 7.2.
Numerical parameters: $N = 18$ (pbc), $\Gamma/J = 0.1$, $g = 3$. Figures taken from [2].

momentum result can be expressed for QFT states as follows [353]

$$D^{\Phi\Phi}(\omega, k=0) = \sum_{n=0}^{\infty} \sum_{\{a_i\}} \left(\prod_{a_i=1}^{8} \frac{1}{n_{a_i}!} \right) \frac{1}{(2\pi)^{n-2}} \int_{-\infty}^{\infty} \mathrm{d}\theta_1 \cdots \mathrm{d}\theta_n \, |\langle 0| \, \Phi \, |A_{a_1}(\theta_1), \ldots, A_{a_n}(\theta_n)\rangle|^2 \times \quad \delta\left[\omega - \sum_{i=1}^{n} E_i\right] \delta\left[\sum_{i=1}^{n} p_i\right] . \tag{7.11}$$

Here, $|0\rangle$ is the vacuum in the E_8 QFT, Φ is one of the Pauli operators $\sigma^{x,y,z}$ and $|A_{a_1}(\theta_1), \ldots, A_{a_n}(\theta_n)\rangle$ are asymptotic momentum and energy eigenstates, which form an orthonormal basis. Any of the $a_1, \ldots, a_n$ assumes the values $a_i = 1, \ldots, 8$, labelling the 8 different mesons.[68] The relativistic rapidity is related to the energy and momentum via $E_i = M_{a_i} \cosh\theta_i$ and $p_i = M_{a_i} \sinh\theta_i$. From the data in Fig. 7.5 (right panel), it becomes discernible that both the LR and NN model allow for an identification of the first 5 meson states as well as the mass sum $M_1 + M_2$, as signalled by their peak structure. With exclusion of the fourth meson, their frequency position is very close to the analytical meson mass ratios and there are only marginal differences between the two models. In contrast to the numerical data for the finite size systems, peak heights in the exact E_8 spectrum are continuously decreasing. Nevertheless, one can observe that the ratio of the first to the second meson peak height is also quantitatively in good agreement with the QFT prediction. Since we observed in the previous section no

[68] The relation (7.11) follows by inserting an identity from a complete set of E_8 basis states, i.e. $\mathbb{1} = \sum_{n=0}^{\infty} \sum_{\{a_i\}} \left(\prod_{a_i=1}^{8} \frac{1}{n_{a_i}!} \right) \frac{1}{(2\pi)^{n-2}} \int_{-\infty}^{\infty} \mathrm{d}\theta_1 \cdots \mathrm{d}\theta_n \, |A_{a_1}(\theta_1), \ldots, A_{a_n}(\theta_n)\rangle \langle A_{a_1}(\theta_1), \ldots, A_{a_n}(\theta_n)|$.

significant finite size differences for the first two meson peaks below the continuum threshold, we conclude that this agreement is a stable feature in the NN and LR model.

7.2.3 Longitudinal field dependence

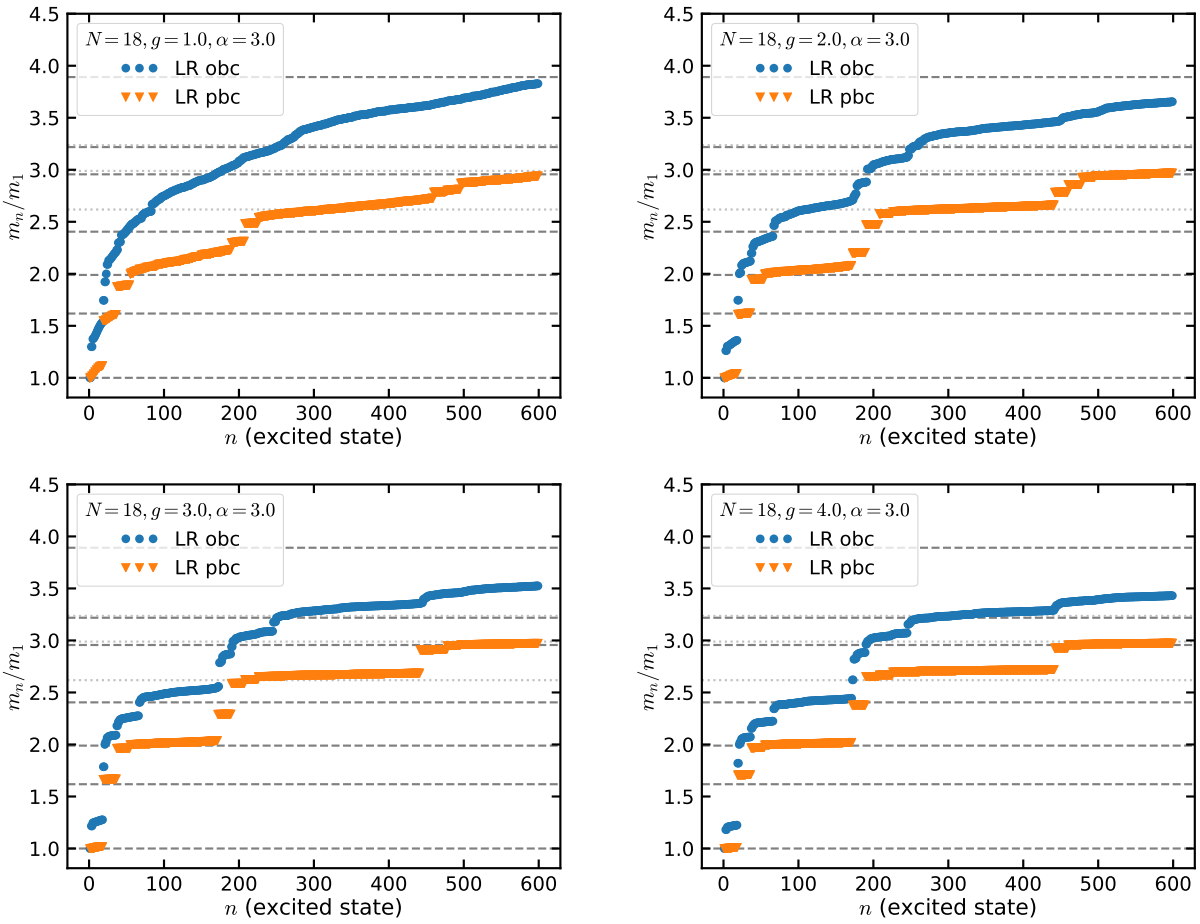

Figure 7.6: Effect of the longitudinal field value g on the numerical energy spectrum (normalized mass gaps of excited states) in the LR model. Background lines are as in Fig. 7.1. Figures taken from [2].

In the former discussions, we had chosen one exemplarily longitudinal field value $g = 3$. We now analyze meson properties in the LR and NN model assuming g to be a free parameter. The energy spectra in the LR model (at the largest experimentally accessible suppression $\alpha = 3$) are displayed in Fig. 7.6 for several integer values of g. As the field strength is increasing, large semi-continuous branches break apart into several discrete and gapped bands. For pbc, they flatten out at the expected analytical E_8 mass ratios.

The eigenstates give rise to the absorption spectra shown in Fig. 7.7. For a suitable visual perception, we compare the LR model to NN interactions for both the scaled spectra (top row) and on an absolute scale for a quantitative comparison (bottom row). The splitting of the energy levels translates into peaks that get narrower and sharper as the longitudinal field

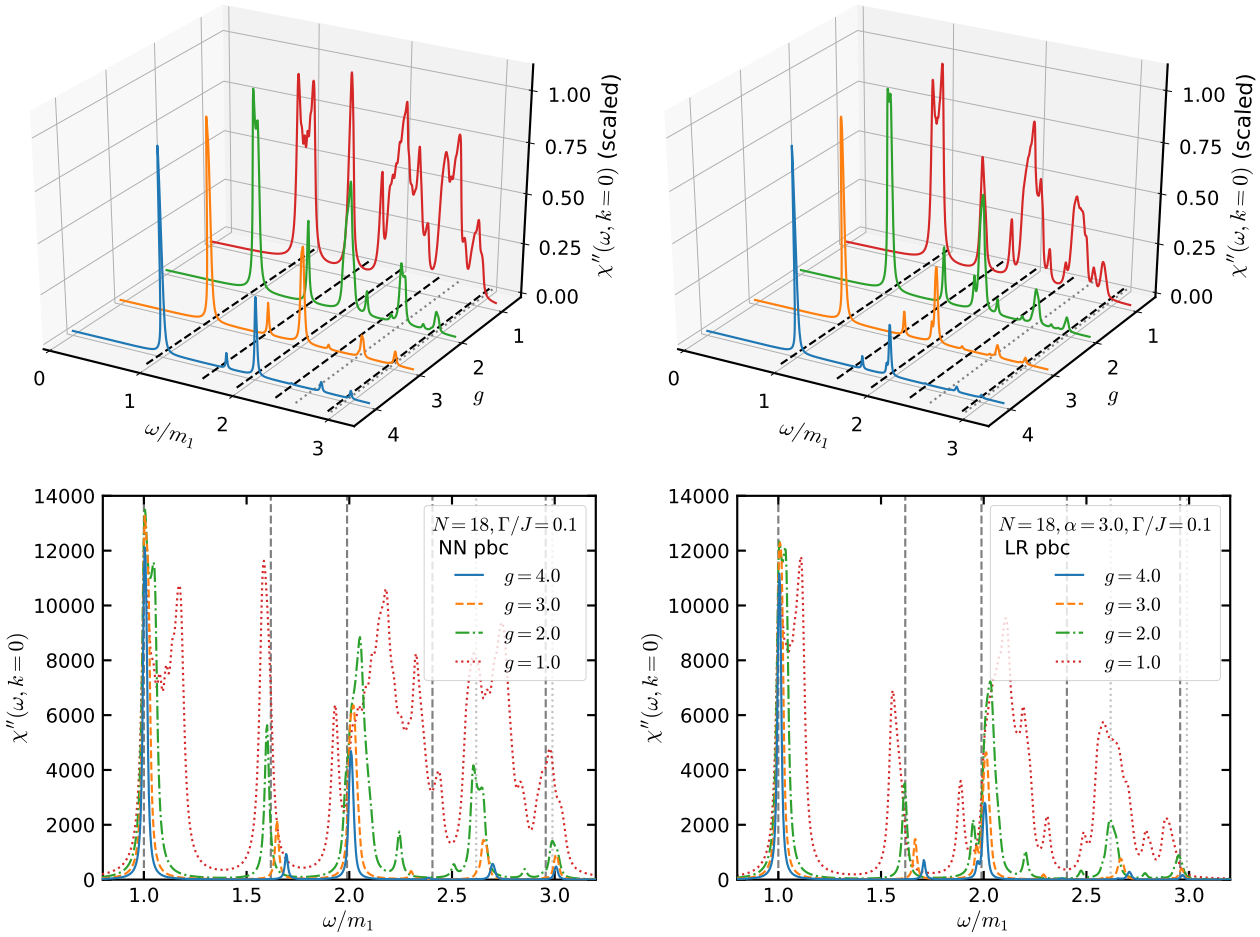

Figure 7.7: Comparison of the scaled (top) and absolute (bottom) absorption spectra in the NN (left) and LR Ising model (right) with pbc in dependence on the longitudinal field value g. Background lines are as in the left panel of Fig. 7.5 or Fig. 7.2, respectively. Figures taken from [2].

is increasing. For such a small analyzed system of $N = 18$ sites, we can conclude that for longitudinal field values $g \gtrsim 2$ all meson length scales are captured in the finite chain, since they allow for the identification of meson states and mass sums through their peak structures. Observe in particular that only at the smallest field value $g = 1$ (red curves), the NN and LR model differ qualitatively in the form of the spectrum. For all larger values, only marginal differences appear in the absolute scale of the absorption spectra.

7.3 Meson mass identifications

We now quantify how precise the meson mass ratios can be extracted from the absorption spectra in comparison to the analytical E_8 theory ratios (cf. Tab. 4.1). We obtain individual meson masses $\widetilde{M}_n$ from a Gaussian fit to each peak in units of the mass gap m_1 of the first excited state and estimate the corresponding uncertainty as its full width at half maximum. The resulting data are shown in the left panel of Fig. 7.8 for the first 5 meson levels (encoded

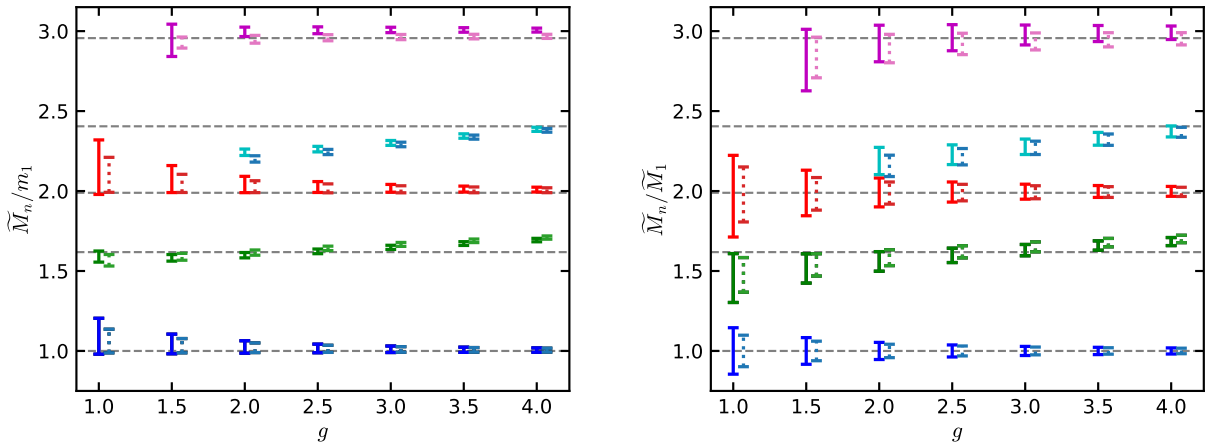

Figure 7.8: Extracted meson mass ratios from the absorption spectra in dependence of the longitudinal field g. The left panel expresses the results in units of the first mass gap m_1, the right panel in units of the first extracted meson mass M_1. Solid errorbars are for the NN model, dotted ones for the LR model (shown slightly displaced for graphical purposes). Grey dashed lines represent the the analytical E_8 meson mass ratios (cf. table 4.1). Numerical parameters: $N = 18$ (pbc), $\Gamma/J = 0.1$, $\alpha = 3$. Figures taken from [2].

by the different colors) in dependence on the longitudinal field value g. Experimentally, the mass gap m_1 (or of any other individual eigenstate) is not accessible. We therefore express in the right panel of the same figure the results in units of the first extracted meson mass $\widetilde{M}_1$ by propagating its uncertainty.

As g is increasing, the uncertainty of the mass ratios is decreasing, allowing for a reliable identification of the analytical E_8 mass ratios M_n/M_1 (shown as grey dashed background lines) up to the fifth level in both the NN (solid errorbars) and the LR model (dotted errorbars). Only the fourth meson, which is identifiable as a separable peak for $g \gtrsim 2$, is always underestimated except for the largest considered longitudinal field strength $g = 4$. At $g = 1$, only remnants of the first three meson peaks can be extracted with a large uncertainty. Overall, the numerical data of the finite size system are in best agreement with the E_8 QFT in the range $3 \leq g \leq 4$, justifying in retrospect our previous choice $g = 3$ for our detailed analyses. In fact, the measurable ratio $\widetilde{M}_n/\widetilde{M}_1$ in the right panel even allows for a slightly better consistency with the analytical data. The uncertainty in the LR model is even smaller than in the NN case, which is caused by a narrower peak structure in the absorption spectra. Note that these results for the uncertainties are following as properties of the spectrum and eigenstates, but also in combination with the chosen inverse observation time $\Gamma/J = 0.1$.

7.4 Fidelity analysis

The previous analyses have shown that there is a clear band structure in the energy spectrum as well as meson peaks in the absorption spectrum of the LR Ising model. Since we observed

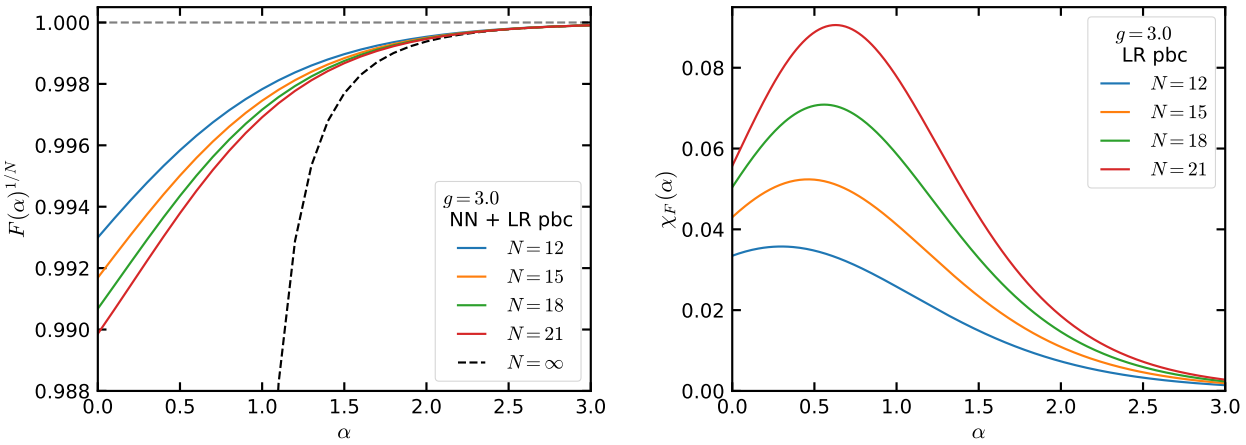

Figure 7.9: Dependence of the fidelity (left) and fidelity susceptibility (right) on the LR coefficient α. Coloured solid curves are for finite size systems, while the black dashed curve represents and extrapolation to the thermodynamic limit. Figures taken from [2].

these features for sufficiently large longitudinal field values but still relatively small values of α and N, the question is raised whether whether the underlying quantum states still can be interpreted as mesons resembling the E_8 regime of the NN Ising model (corresponding to $\alpha = \infty$). In this section, we want to address this problem on a conceptual deeper level of quantum information measures. In fact, this question is twofold. First, the previously cited works [326,327] show that LR interactions indeed confine domain walls into mesons in the Ising model. Discrete band structures therefore can be interpreted as meson states of the underlying Hamiltonian. Second, we also have a longitudinal field acting in the physical system, which also enables the existence of meson states. In the present case, we use the *fidelity* $F(\alpha)$ and *fidelity susceptibility* $\chi_F(\alpha)$ to quantify the agreement with the E_8 parameter range of the NN Ising model. Both quantities have been used previously for ground [354,355] and excited states [345,356] as a theoretical framework to identify and characterize quantum phase transitions. Here, we study these quantities to analyze if there is a fundamental change in the meson structure as the LR coefficient α is varied.

In systems with pbc the first meson band is comprised of the first $n = 1, \ldots, N$ excited eigenstates of the Hamiltonian. In fact, these states have different degeneracies in the LR and NN model, such that the overlap of some of these states is not well-defined and hence numerically not unique. Only the first excited state ($n = 1$) is nondegenerate in all cases and allows us to calculate the following well-defined fidelity

$$F(\alpha) = |\langle \phi_1(\alpha) | \phi_1(\alpha = \infty) \rangle|, \tag{7.12}$$

where ϕ_1 denotes the first excited state in the LR and NN model, respectively. Following [354,

355] we calculate the fidelity susceptibility as

$$\chi_F(\alpha) = -\frac{\partial^2 F(\alpha, \delta\alpha)}{\partial(\delta\alpha)^2}\bigg|_{\delta\alpha=0} = \lim_{\delta\alpha\to 0} \frac{-2\ln F(\alpha, \delta\alpha)}{(\delta\alpha)^2}, \tag{7.13}$$

where $F(\alpha, \delta\alpha) = |\langle\phi_1(\alpha)|\phi_1(\alpha+\delta\alpha)\rangle|$ is the overlap between two states in the LR model with infinitesimally varied decay parameter. In our numerics, we use the second relation with the numerical increment $\delta\alpha = 0.01$ and probe the experimentally realizable range $0 \leq \alpha \leq 3$ at the longitudinal field value $g = 3$.

Fig. 7.9 displays the results for the fidelity per site $f(\alpha) \equiv F(\alpha)^{1/N}$ (left panel) and the fidelity susceptibility $\chi_F(\alpha)$ (right panel) for several chain lengths. The former is a monotonically increasing function of α. In all considered finite system sizes (colored solid curves), $f(\alpha)$ lies close to the maximal value of 1 for $\alpha \gtrsim 2$, i.e. the first meson retains a large overlap with the "ideal" counterpart in the E_8 regime of the NN model. However, even at all-to-all LR interactions ($\alpha = 0$) the fidelity per site deviates at most by 1% from this value, indicating that the quantum nature of the first excited state in the LR model resembles very closely its counterpart in the NN case, as long as finite system sizes are regarded.

This behavior seems to be modified in the thermodynamic limit $N \to \infty$. To extrapolate the data, we use the scaling ansatz $f(\alpha) = f_\infty(\alpha) + c(\alpha)N^{-b(\alpha)}$, in which we leave $c(\alpha)$ and $f_\infty(\alpha)$, but also the exponent $b(\alpha)$ as free fit parameters, since we do not have an a priori theoretical expectation for the latter. The additive constant $f_\infty(\alpha)$ then represents the prediction for the thermodynamic limit and is shown as the black dashed curve. While it shows similarly fast convergence for large α, the curve indicates a transition in the nature of the first meson state for large system sizes through the rapid decrease around $\alpha \lesssim 1.5$.

On the other side, the fidelity susceptibility is characterized by a peak at small values of α and a fast decrease towards 0 for strong LR suppression. The appearance of a peak in $\chi_F(\alpha)$ suggests a transition in the first excited meson state occurring at some intermediate value of α. As the system size is increasing, the peak becomes sharper and its position $\alpha_{\max}$ moves towards larger values of α. Assuming a scaling with N^{-1} to extrapolate the data towards $N \to \infty$, we can extract the value $\alpha_{\max} \approx 1.07 \pm 0.02$ for the thermodynamic limit. This finding is in agreement with the range of the rapid decrease of the fidelity.

In summary, the first excited state as a proxy for the first meson seems to retain the same physics across the entire range of α in the finite size LR model. The scaling analysis suggests for the thermodynamic limit the appearance of interesting new physics in the LR versus NN model.

7.5 Quantum simulation with trapped ions

Ions, which are trapped by a confining potential in electromagnetic fields, can be used to constitute an analog quantum simulator. The modern standard of technology allows to routinely encode the basis states $|\uparrow\rangle$ and $|\downarrow\rangle$ of spin-1/2 systems in two long-lived hyperfine states to realize effective magnetic models. Their effective spin–spin interactions $\sim J$ as well as effective magnetic fields $\sim h, g$ can be induced through additional laser beams. [69]
To identify the E_8 meson spectrum via absorption spectroscopy, we propose the following protocol.

1. The effective spins are prepared in the fully polarized electronic groundstate $|\uparrow, .., \uparrow\rangle$ at $g = \infty$. Any parameter values can be adjusted by decreasing g and turning on J and h, which adiabatically transfers the system to the ground state. For the considered scenario, we saw that a relatively large longitudinal field value g is necessary, implying a large mass gap $M_g \equiv M_1 = \mathcal{D} J\,|g|^{8/15}$. In particular, for $g = 3$, one has $M_1 \approx 9.7J$ and and thus the initial state preparation can occur adiabatically in times much shorter than $\hbar/J$, which in turn are much shorter than typical coherence times. As an alternative to this procedure, variational algorithms [310] can be employed to prepare ground states of the desired parameters in trapped-ion quantum simulators.

2. After initialization, a periodically modulated laser beam can be used to perturb the system with a time-dependent magnetic field, realizing an operator of the form (7.6).

3. The imaginary part susceptibility (7.7) can be extracted via two possible spectroscopy methods: Either, an instantaneously turned on perturbation $A = O$ is tracked in the subsequent time evolution by standard fluorescence measurements [297,316,357]. Its Fourier transform then yields $\chi''(\omega)$ [157]. Alternatively, the absorbed energy per unit time, related to $\chi''(\omega)$ through eq. (7.4), follows from a temporally modulated perturbation of the form $f(t) = \cos(\omega t)$, and can be accessed indirectly by measuring few-body correlators as demonstrated in [310].

The implementation of this protocol on ion trap quantum simulators for a many-body spin system typically generates LR interactions [299–303]. The spatial power-law decay, as encapsulated by the studied Ising Hamiltonian in eq. (7.1), is realized in linear chains with obc to good precision [347,358]. A crucial result from our analyses, however, is that pbc are necessary to reliably identify QFT information in the E_8 regime even for small systems. Such preparations of trapped-ions on ring configurations are already possible [359–361]. In principle, the experimentally possible range of power-law decay exponents is $0 \leq \alpha \leq 3$ [346]. While all-to-all LR interactions ($\alpha = 0$) are most favorable to implement, our studies on the LR dependence for

[69] In this thesis, we are only interested in the theoretical concepts of our proposal. For more detailed comments regarding experimental implementations, we refer to our own paper [2] and references therein.

both the absorption spectra and fidelity have shown, that strong meson features resembling the E_8 theory, can be expected already for $\alpha \gtrsim 2$.

7.6 Discussion and outlook

In this chapter we have demonstrated that current ion trap QS technologies allow for the identification of the relativistic E_8 QFT. When implementing the LR Ising model at sufficiently strong spatial power-law suppression with pbc, the system is closely resembling the NN model, enabling the detection of E_8 meson states even for relatively large longitudinal field values and surprisingly small systems with 12 to 18 sites. We have discussed an experimental protocol to access the energy absorption spectrum within the linear response framework. Based on exact numerical diagonalization techniques, we calculated the latter for large parameter ranges and showed that it shares qualitative and quantitative properties with its QFT equivalent. From the peak structure, mesons and multiparticle states show up at frequencies very close to their masses and mass sums, allowing for a precise extraction of the analytically predicted E_8 meson mass ratios. In future studies, it would be appealing to extend these analyses also to the finite momentum case from which relativistic dispersion relations can be deduced.
The first meson always retains the strongest spectral density, even when higher-order mesons are significantly altered through longer-ranged interactions. From a detailed fidelity analysis, we conclude that in finite size systems this first meson state changes only insignificantly its quantum nature across all experimentally accessible values of α. There are, however, strong indications from a scaling extrapolation that this behavior is modified in the thermodynamic limit at a critical value around $\alpha_c \approx 1$, i.e. at a spatial power-law interaction $\sim 1/r$.
The relativistic E_8 theory, which we considered previously in this chapter also in our TN simulations, emerges from longitudinal perturbations along the critical point of the simple Ising model. Although its existence has been experimentally confirmed already earlier from spectroscopic measurements in solid state crystals, ion trap QS additionally enable the analysis of meson states induced through LR interactions as well as the implementation and analysis of (lattice) gauge theories [40]. The latter opens the new realm of studying meson physics also in theories of the standard model beyond classical resources. Furthermore, recent advances [362, 363] lay out a framework to implement also finite-temperature systems with trapped-ions, which would allow us to address our previous topics about thermal correlators and meson melting also from a QS perspective.

Part III

Complexity

8 A holographic primer

The AdS/CFT correspondence and holographic concepts from the gauge/gravity duality initiated a plethora of studies on connections between quantum information, the emergence of spacetime and their (quantum) gravitational encodings. Over the last years, this discussion became very stimulated through explorations on *complexity* as a quantum information measure. From the very beginning, these ideas were motivated or closely connected to TNs. In this chapter, we want to introduce the concept of holographic and computational complexity, which provides the background for our research on their corresponding QFT interpretation.
The starting point of these analyses were the works [38,73,74] of Susskind and collaborators on the eternal AdS BH as the holographic dual of the TFD state [364]. The latter entangles two copies of a CFT, labelled by L and R, and evolves in time as follows

$$|\mathrm{TFD}(t_L, t_R)\rangle = \frac{1}{\sqrt{Z_\beta}} \sum_n \mathrm{e}^{-\beta E_n/2}\, \mathrm{e}^{-iE_n(t_L+t_R)}\, |E_n\rangle_L\, |E_n\rangle_R\,. \tag{8.1}$$

Here, Z_β is the canonical partition function and $|E_n\rangle_{L,R}$ are energy eigenstates in either copy of the CFT, such that a partial trace over one subsystem yields the thermal density matrix of the other at inverse temperature $\beta = 1/T$. In other words, the TFD state is the canonical purification of the thermal density matrix. As such, it is a similar quantity as in our thermal quench studies in section 6.3.3, from which we defined reflected entropies. In the corresponding Penrose diagram of the holographic dual (cf. Fig. 8.2), the asymptotic boundaries are connected by a wormhole, i.e. a ERB. According to the "ER=EPR" principle [365], such a ERB is created only iff two systems are entangled. [70] This setup therefore provides an invaluable laboratory for quantum gravitational studies on the BH interior beyond the event horizon. The puzzle emerging from this system is as follows: Susskind and collaborators observed that the ERB is a dynamical object and grows in time. In particular, the rate of the volume increase is given by the constant value [38,73,74]

$$\frac{\mathrm{d}V}{\mathrm{d}t} = \frac{L}{D-1} A_h \varkappa, \tag{8.2}$$

where we use the same notation as for the BH thermodynamics in eq. (2.17). Classically, the resulting linear growth persists forever, while quantum mechanically recurrences potentially

[70] In more detail, the lhs of this principle stands for the ERB connecting two distant BHs, which are interpreted as maximally entangled BH states forming a complex EPR pair, named after Einstein, Podolsky and Rosen on the rhs.

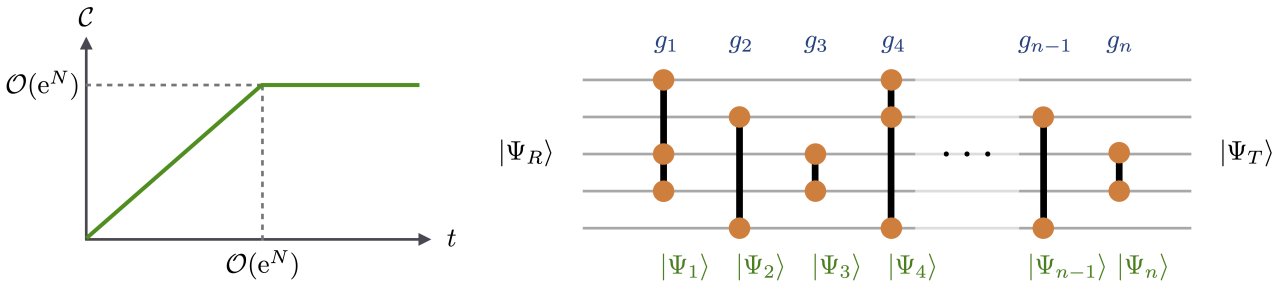

Figure 8.1: Properties of holographic and computational complexity.
Left: The graph visualizes Susskind's conjecture [38,73] that the complexity of a QMB system with N qubits increases linearly to an exponentially large value $\mathcal{O}(e^N)$ up to a time scale $t \sim e^N$ and then saturates.
Right: The figure illustrates a quantum circuit for a $N = 5$ qubit system. The sequential application of gates g_i transform a reference state $|\Psi_R\rangle$ over intermediate states $|\Psi_i\rangle$ into the target state $|\Psi_n\rangle = |\Psi_T\rangle$. The minimal number of gates is defined as the complexity.

occur only on exponentially large time scales. On the boundary QFT side, in contrast, thermal equilibrium is reached very fast, at order of $\beta \log S$, as estimated by the scrambling time scale. Apparently, "*entanglement (entropy) is not enough*" [38] to explain this mismatch, since spatial entanglement entropy saturates for finite subsystems while the volume keeps growing [366]. It was therefore conjectured that the *quantum computational complexity* of the TFD state is the relevant quantity capturing this feature.

Complexity is a quantity originating from the field of computer science and quantum computation, for a broad review see, e.g., [367]. In the context of QMB systems, the problem at hand is to create a *target state* $|\Psi_T\rangle$ from a *reference state* $|\Psi_R\rangle$ by sequentially applying *gates* $g_1, g_2, \ldots, g_n$, i.e.

$$|\Psi_T\rangle = U\,|\Psi_R\rangle = g_n g_{n-1} \cdots g_1\,|\Psi_R\rangle\,. \tag{8.3}$$

While the resulting *quantum circuit* U is typically built from unitary gates in a quantum mechanical context, we impose no restrictions here to keep the context as general as it will be relevant for our studies on path integral optimization in chapter 10. The right panel in Fig. 8.1 shows an example of such a circuit for a $N = 5$ qubit system. The application of the gates onto $|\Psi_R\rangle$ results in a sequence of states $|\Psi_1\rangle, |\Psi_2\rangle, \ldots, |\Psi_n\rangle = |\Psi_T\rangle$. The minimal number of gates to obtain the target from the reference state is defined as the *state complexity*. When the circuit U is viewed as an object itself, we preferably denote the gate number as *circuit complexity*. Clearly, the complexity $\mathcal{C}$ depends on the choice of allowed gates g_i. For example, in Fig. 8.1, we have two types of gates, acting either on two or three sites. A discrete circuit like this can be implemented experimentally on a quantum computer. It then makes sense to calculate the complexity w.r.t. some a small precision ε to take into account that the circuit cannot realize the identity (8.3) exactly, i.e.

$$\| \, |\Psi_T\rangle - U\,|\Psi_R\rangle \, \|^2 \leq \varepsilon \tag{8.4}$$

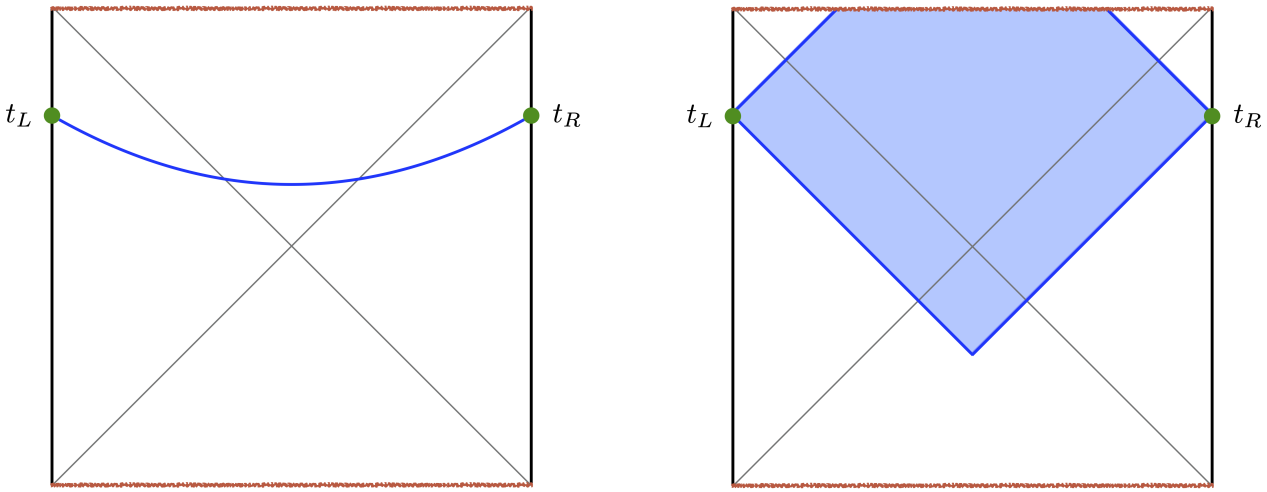

Figure 8.2: Setups for the volume (left) and action (right) conjecture as the holographic dual to complexity. The panels show the Penrose diagram of an eternal AdS BH describing the TFD state. The singularities are marked by the red lines. Left: A maximal spacelike surface (blue curve) connects two boundary time slices $t_{L,R}$. Right: The marked region represents the corresponding WDW patch. Figure adapted from [45].

for some operator norm. In a QMB system consisting of N qubits, important properties of complexity can be derived from basic estimates and considerations [38]. First, due to the exponential size of the Hilbert space, the maximal complexity for arbitrary state configurations is of order $\mathcal{O}(\mathrm{e}^N)$. While it takes the system only a polynomial time scale $\mathcal{O}(N^p)$ to thermalize, it follows immediately that the time to reach maximal complexity is also of order $\mathcal{O}(\mathrm{e}^N)$. The sequential circuit picture enforces that this complexity growth is linear. Moreover, it was conjectured in [38,73,74] that the slope, representing the growth rate, is given by the explicit relation

$$\frac{\mathrm{d}\mathcal{C}}{\mathrm{d}t} \sim ST, \tag{8.5}$$

where we defined $t \equiv t_L + t_R$ w.r.t. the TFD state (8.1). This formula is motivated by the fact that complexity is an extensive quantity and therefore its rate should be proportional to the thermal entropy S, measuring the degrees of freedom in the system. Furthermore, the units have to be fixed by an energy scale. As such, the temperature T is the only viable candidate. The overall picture that arises from these considerations is summarized in the left panel of Fig. 8.1. After an linear growth for exponentially long times, the complexity is expected to saturate. Very recently, this linear growth and saturation behavior has been proven in a rigorous mathematical way for such a discrete quantum circuit picture [368].

Based on these expectations and properties, two proposals were put forward to describe complexity holographically in the eternal AdS BH setting. They are known as "complexity = volume" [73,74] and "complexity = action" [39,75] conjecture as given in eqs. (2.20) and illustrated in Fig. 8.2. They both capture the phenomenology of the volume growth inside the BH as one moves upward in the Penrose diagram, and they also represent covariant gravitational

observables. In particular, the volume proposal is directly motivated by the rate equation (8.5). Using the thermodynamic quantities in (2.17) for the volume growth in eq. (8.2), one sees directly that the volume of the maximal time slice Σ anchoring at boundary times $t_{L,R}$ satisfies the expected behavior for the complexity growth, cf. the blue curve in the left panel of Fig. 8.2. As a shortcoming, however, an ambiguous length scale l needed to be introduced. To avoid this feature, it was subsequently observed that when multiplying and dividing the volume formula with the AdS radius, one can rewrite the expression in units of an action. The resulting action proposal hence calculates the complexity as the action on the WDW patch, defined by in- and outgoing null rays at the boundary times $t_{L,R}$, cf. the blue region in the right panel of Fig. 8.2. Upon normalization, $\mathcal{C}_A$ satisfies the Lloyd bound

$$\frac{\mathrm{d}\mathcal{C}_A}{\mathrm{d}t} \leq \frac{2M}{\pi} \tag{8.6}$$

in any dimension, where M is the BH mass. This value is seen as an upper bound for the computation rate in any physical system [369]. More detailed studies on the time evolution of holographic complexity in [370] however showed that this value is approached from above, i.e. actually violating the bound at early times. In contrast to the volume proposal, the action definition has no ambiguous scale in it. Nevertheless, the appearance of null boundaries and joint terms in the WDW patch requires a careful separate treatment, which was later provided in [371].

Both the volume and action complexity contain integrals over hyperbolic spacetimes and therefore yield infinite values. The precise structure of the singularities were analyzed in [372,373]. It was found that the leading divergences take the form [372]

$$\mathcal{C}_V(\Sigma) \sim \frac{V(\Sigma)}{\delta^{D-1}}, \qquad \mathcal{C}_A(\Sigma) \sim \log\left(\frac{l}{\delta}\right) \frac{V(\Sigma)}{\delta^{D-1}}. \tag{8.7}$$

Here, δ is a short-distance cutoff scale in the boundary field theory. While in both scenarios the divergences can be interpreted as originating from the UV vacuum structure of the CFT, the action proposal contains an additional logarithmic scale, which provides a clear distinction from the volume result. The scale l therein is, however, again non-unique. Inspired by holographic renormalization procedures, the work [374] proposed a regularization scheme to cancel these divergences.

The outlined pioneering proposals on holographic complexity lead to numerous further analyses in different gravitational theories. For example, the works [375,376] considered the complexity evolution for a time-dependent collapse in Vaidya spacetimes. Further works studied complexity in Jackiw–Teitelboim [377], Einstein-dilaton [378], Einstein–Maxwell-dilaton [379] or Gauss–Bonnet theories [380]. Moreover, due to the ambiguities in the complexity definitions and unclear relations to the Lloyd bound, modified proposals were put forwards, commonly known as "CV2" [381] and "CA2" [382] conjectures, to resolve these problems. Motivated by

thermodynamic relations, the former instead suggests to identify holographic complexity as the spacetime volume of the WDW patch, whereas the latter proposes to calculate only the non-derivative part of the gravitational WDW action. Similarly to the setup for holographic entanglement entropy, the author of [383] outlined how complexity can be calculated for generic subregions in a gravitational spacetime. This proposal was re-interpreted in [384] from a kinematic space approach. Based on the subregion proposal, many works analyzed holographic complexity in different setups. For example, it was shown that complexity can characterize quantum quenches [385–388] and phase transitions [389,390]. In particular, this was discussed in holographic models for QCD [391–393] and holographic superconductors [394,395].

In summary, this chapter exemplified that certain effects or features cannot be captured by entanglement entropy. As emphasized in [396], apart from the volume growth of a ERB, regions or event horizons that are not reached by minimal Ryu–Takayanagi surfaces are further such examples that evade bulk reconstruction. This led the authors of the latter paper to propose *entwinement* as an alternative to complexity. Although entanglement (entropy) and complexity are different concepts and quantities, it was shown recently in [397] that, at least for very small values, tight bounds between them can be found in accordance with a linear growth. Moreover, the recent paper [398] could show, using a path integral approach in $2D$ gravity models, that the BH interior volume indeed grows linearly and then saturates at exponentially late times (w.r.t. the entropy), providing evidence for Susskind's complexity growth conjecture in the volume proposal. While these holographic complexity proposals are physically well motivated, an ultimate decision on the correctness of their interpretations can be only drawn once the QFT side of the duality is better understood. This is the topic of the next chapter, where we outline the fundamental concepts to define notions of complexity in the continuum and review recent progress in the field.

Finally, we would like to point out that already in Susskind's early work [38] a TN interpretation of the quantum circuit picture of complexity was given. However, the translation of this setup into the gravitational setting remained rather vague. The path integral optimization program, which we will discuss below, instead directly aims for a more rigorous interpretation of the underlying AdS/CFT principles in terms of TN encodings.

9 Two QFT viewpoints

Entanglement entropy as a quantum information quantity is well understood in QMB systems as well as CFTs, and was subsequently interpreted holographically in terms of codimension-2 surfaces in the bulk. In contrast, studies on complexity were at first initiated in the context of the AdS/CFT correspondence as discussed in the previous chapter. These analyses, however, left open a definition and clear understanding of complexity in QFTs. The first steps in bridging this gap were taken by two seemingly different approaches, based on a geometric quantum circuit viewpoint, and, alternatively, on the path integral optimization program. In this chapter, we give an overview of these developments, setting the stage for our unification of these concepts in the next chapter.

9.1 Circuit complexity

The question what *complexity* means in the (boundary) CFT (or more generally QFT) was first addressed from a geometric circuit perspective in [45] and [46]. As it becomes obvious from our discussions around eq. (8.3), this requires (i) the definition of a reference and target state, (ii) the selection of a set of gates, and (iii) a distance measure or cost function to evaluate the minimal configuration of gates in the continuous circuit. As usual for QFT quantities, one has to regulate UV divergences, which will provide a way to compare the singularity structure with the holographic results (8.7).

In [45], Jefferson and Myers developed such a geometric approach based on the quantum circuit design of Nielsen and collaborators [399–401]. The basic ingredient is to write the continuous circuit U as a path-ordered exponential in the form

$$U(\sigma) = \mathcal{P} \exp\left(-i \int_0^\sigma \mathrm{d}s\, G(s)\right) \qquad \text{with} \qquad G(s) = \sum_I Y^I(s) O_I. \tag{9.1}$$

Here, s is parameterizing infinitesimal layers on the circuit for some intermediate value $\sigma \in [0, s_f]$, and $G(s)$ are iterating generators. The latter are written as a sum over control functions $Y^I(s)$ and operators (gates) O_I. From a geometric viewpoint, $Y^I(s)$ can be seen as a tangential velocity component along the path s. The path-ordering symbol $\mathcal{P}$ denotes that gates at smaller value of s act first, i.e. the circuit is built from "right to left". In Nielsen's original QMB context, the role of s is played by the time t, whereas $G(s)$ is given by the Hamiltonian

$H(t)$, which is expanded in generalized Pauli matrices acting on qubits. In the present QFT context, we instead assume that the operators act on wavefunctions and that the auxiliary parameter s enumerates these gates.[71] Whereas in Nielsen's proposal the discrete gate setup was reformulated in the language of continuous differential geometry, the generalization to the QFT context requires careful considerations on how to define discrete gates. It then amounts to define a *cost function* $\mathcal{D}$, which measures the length of a path specified by the application of gates onto the reference wavefunction to prepare the desired target state. Its minimization yields the complexity of the optimal circuit. As pointed out in [45], there is a considerable amount of freedom in choosing a particular length functional. A typical choice directly related to gate counting is for example the L^1 norm

$$\mathcal{D}_1 = \int_0^{s_f} \mathrm{d}s \sum_I |Y^I|, \tag{9.2}$$

whereas the L^2 norm is defined as

$$\mathcal{D}_2 = \int_0^{s_f} \mathrm{d}s \sqrt{\sum_{IJ} \eta_{IJ} Y^I Y^J} \tag{9.3}$$

for some positive-definite matrix η_{IJ}. A common generalization is given by the family of cost functions

$$\mathcal{D}_\kappa = \int_0^{s_f} \mathrm{d}s \sum_I |Y^I|^\kappa \tag{9.4}$$

for some positive power $\kappa \geq 1$, which, however, is not reparametrization invariant under changes of s. Demanding $\mathcal{D}$ to be smooth (or at least continuous), positive, homogeneous, and satisfying the triangle inequality, then the cost functional defines a Finsler manifold, which represents a more general class than Riemannian geometry, in the sense that the norm is not necessarily induced by a metric tensor. Hence, the determination of the optimal circuit in the L^2 case is translated into finding extremal curves, i.e. geodesics, whose length is identified with the complexity. As an extension to the upper cost definitions, one can in principle also introduce *penalty factors*, which give different weights to the individual velocity components $Y^I(s)$.

In [45], this general framework was applied to a free D-dimensional scalar field theory, defined by the Hamiltonian

$$H = \frac{1}{2} \int \mathrm{d}^{D-1}x \left[\pi(x)^2 + \vec{\nabla}\phi(x)^2 + m^2 \phi(x)^2 \right], \tag{9.5}$$

which is transformed into a family of coupled harmonic oscillators by regulating it on a lattice

[71] Note that in [402] an interpretation of holographic spacetimes as quantum circuits of path integrations was proposed which related the physical time to the auxiliary parameter.

with spacing δ. Motivated by the cMERA [120], the authors considered a factorized Gaussian state for $|\Psi_R\rangle$ (which leaves different lattice points unentangled) and the groundstate of the theory for $|\Psi_T\rangle$, and chose scaling and entangling gates constructed from the momentum and position operator as a set of unitaries. When solving the geodesic equation for the $\mathcal{D}_2$ cost function, the leading divergence of the associated complexity $\mathcal{C}_2$ was found as $\mathcal{C}_2 \sim (V/\delta^{D-1})^{1/2}$, which differs to the holographic CV result in (8.7) by the square root. In contrast, the κ cost function (9.4) was found to lead to the following behavior

$$\mathcal{C}_\kappa = \frac{V}{\delta^{D-1}} \left| \log\left(\frac{1}{\omega_0 \delta}\right) \right|^\kappa , \tag{9.6}$$

where ω_0 is a scale characterizing the reference state. Interestingly, in the case of $\kappa = 1$, the result resembles the holographic CA proposal in (8.7) upon the identification $l = 1/\omega_0$. This result is remarkable since a free theory with only one degree of freedom is compared to a strongly-coupled holographic theory in the large-N limit.

This picture is backed up by the complementary study in [46]. Therein, the authors study the same underlying theory but in momentum space with a UV cutoff. Instead of Nielsen's gate counting framework, a Fubini-Study approach is employed, which defines a geometry on the state space itself. Here, the line element

$$\mathrm{d}s_{FS}(\sigma) = \mathrm{d}\sigma \sqrt{|\partial_\sigma |\Psi(\sigma)\rangle|^2 - |\langle\Psi(\sigma)| \partial_\sigma |\Psi(\sigma)\rangle|^2} \tag{9.7}$$

is defined for a state $|\Psi(\sigma)\rangle = U(\sigma)|\Psi_R\rangle$ and integrated along the circuit (parametrized by s) whose minimization yields the complexity. In contrast to the Nielsen approach, the complexity is now accumulated through infinitesimal changes of the state along the circuit. Individual gates therefore may have different costs. In particular, overall phase changes do not contribute to the complexity. It should be emphasized that the complexity resulting from the infinitesimal distance (9.7) can be different from the Hilbert space distance of finitely separated states, since the current construction is restricted to unitary gates. Remarkably, up to some normalization factor, the resulting leading divergence takes the same form as in (9.6) when identifying the reference and regulator scales with each other. Interestingly, the optimal path is always given by a straight line circuit and only in case of $\kappa = 1$, the minimal cost is coinciding with the one from the cMERA TN.

Based on these two pioneering approaches, several follow-up works explored circuit complexity in further QFT contexts. For example, the work [403] extended the framework to excited (coherent) states. In [257], the TFD state, which provided the starting point in the AdS/CFT setup, was analyzed. A careful comparison [404] of its complexity time evolution in all holographic and QFT proposals came to the conclusion that the holographic volume conjecture and Nielsen's method on the QFT side are more correlated than the other proposals. Similar analyses extended these circuit approaches to fermionic [405] and charged [406,407] TFD

states. While all these discussions are for pure states, it was proposed that mixed state complexity could be defined either from minimal purifications [408] or based on Fisher information geometry for covariance matrices [409]. Inspired by thermodynamic laws, the works [410,411] analyzed the variation of circuit complexity and found that it depends only on the endpoint of the optimal path, thus realizing a first law of complexity. A renormalization procedure for circuit complexity based on the Suzuki–Trotter decomposition was proposed in [412]. Subsequent studies extended the circuit approach to richer field theory contents. For example, in [413,414] fermionic field theories were considered while [415] analyzed interacting QFTs and relations to the RG group. Recently, the paper [416] studied complexity for CFTs in arbitrary dimensions based on unitary representations of the Lorentzian conformal group. Even in a cosmological context, the authors of [417] have shown that circuit complexity can serve as a probe to distinguish different models of the early universe from primordial perturbations. Despite this tremendous progress, the precise nature of circuit complexity for general QFTs is still not yet understood. Further developments are necessary to fully understand the properties and differences between several approaches or proposals. One such program is based on path integral optimization, which originally was developed independently as we describe in the following section.

9.2 Complexity from path integral optimization

The path integral optimization program [116–118], which we briefly introduced in section 3.7.3, provides an independent framework to define and calculate complexity of QFTs. In that context, we consider the unnormalized thermal density matrix

$$\rho_\beta = \mathrm{e}^{-\beta H}, \tag{9.8}$$

where we assume H to be the Hamiltonian of a $2D$ CFT on a line. When seen as an operator, ρ_β represents a thermal state in the CFT, and projects (for a CFT on a circle) onto the ground state (3.44) in the limit $\beta \to \infty$. On a strip of flat geometry,

$$\mathrm{d}s_0^2 = \epsilon^{-2} \left(\mathrm{d}\tau^2 + \mathrm{d}x^2\right), \tag{9.9}$$

its matrix elements can be calculated from the Euclidean path integral with width β in the τ direction as

$$\langle \phi(\beta, x)| \, \rho_\beta \, |\phi(0, x)\rangle = \int_{\hat{\phi}(0,x)=\phi(0,x)}^{\hat{\phi}(\beta,x)=\phi(\beta,x)} \mathcal{D}\hat{\phi} \; \mathrm{e}^{-S_{\mathrm{CFT}}[\hat{\phi}]} \, . \tag{9.10}$$

Here, the fields of the theory with action S_{CFT} are denoted by $\hat{\phi}$, and ϕ are particular eigenstates of field operators. For example in a $c = 1$ free scalar CFT, this is just the scalar field profile.

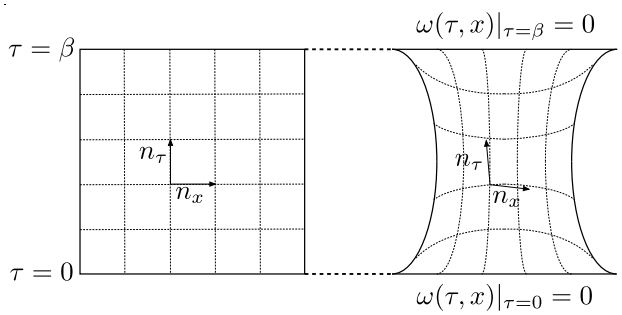

Figure 9.1: Representation of the Euclidean geometry over which the path integral (9.10) is performed. The left panel represents the flat geometry (9.9), while the right panel represents the Weyl-rescaled background (9.11). The boundary conditions at $\tau = 0$ and $\tau = \beta$ are kept fixed, guaranteeing to produce the same operator ρ_β, up to an overall normalization governed by the exponent of the Liouville action (9.13). Figure taken from [5].

When deforming the background geometry by a Weyl factor $\omega(\tau, x)$,

$$\mathrm{d}s_\omega^2 = g_{\mu\nu}\,\mathrm{d}x^\mu\,\mathrm{d}x^\nu = \mathrm{e}^{2\,\omega(\tau,x)}\left(\mathrm{d}\tau^2 + \mathrm{d}x^2\right), \tag{9.11}$$

such that $\omega(\tau = 0, x) = \omega(\tau = \beta, x) = 0$ and $\mathrm{e}^{2\omega(\tau=\epsilon,x)} = 1/\epsilon^2$ (flat space at the boundaries), then the change in the path integral measure is known to take the form [418,419]

$$\left[\mathcal{D}\hat{\phi}\right]_{\mathrm{d}s_\omega^2} = \mathrm{e}^{S_L}\cdot\left[\mathcal{D}\hat{\phi}\right]_{\mathrm{d}s_0^2}. \tag{9.12}$$

In the exponent, S_L is the Liouville action

$$S_L = \frac{c}{24\pi}\int_0^\beta \mathrm{d}\tau \int_{-\infty}^{\infty}\mathrm{d}x\left[\Lambda\,\mathrm{e}^{2\omega} + \dot{\omega}^2 + \omega'^2\right], \tag{9.13}$$

which contains the central charge c in the prefactor, and derivatives of ω w.r.t. τ and x in the integrand, denoted by $\dot{}$ and $'$, respectively. The variable $\Lambda \sim \epsilon^{-2}$ is expressed in terms of the real-space UV cutoff, i.e. lattice spacing ϵ. This overall setup is illustrated in Fig. 9.1.

Since S_L governs the prefactor in (9.12), the authors of [117,118] argue that the Liouville action represents the unique functional $I_\Psi[g(\tau, x)] = S_L[\omega(\tau, x)]$ for $2D$ CFTs whose minimization is equivalent to the optimization of the Euclidean path integral. To perform the optimization, we consider the equation of motion of the Liouville action, $4\partial_z\partial_{\bar{z}}\omega = \mathrm{e}^{2\omega}$, for which we introduced $z \equiv \tau + ix$ and $\bar{z} \equiv \tau - ix$. Its solution reads $\mathrm{e}^{2\omega} = 4(z + \bar{z})^{-2} = \tau^{-2}$, giving rise to the hyperbolic plane metric

$$\mathrm{d}s^2 = \frac{\mathrm{d}\tau^2 + \mathrm{d}x^2}{\tau^2}, \tag{9.14}$$

representing a time slice in AdS_3 as the dual to the CFT_2 vacuum after optimization. Heuristically, the Liouville exponent in (9.12) counts the number of repetitions of discretized path integral operations. This observation lead to the conjecture that its minimum corresponds to

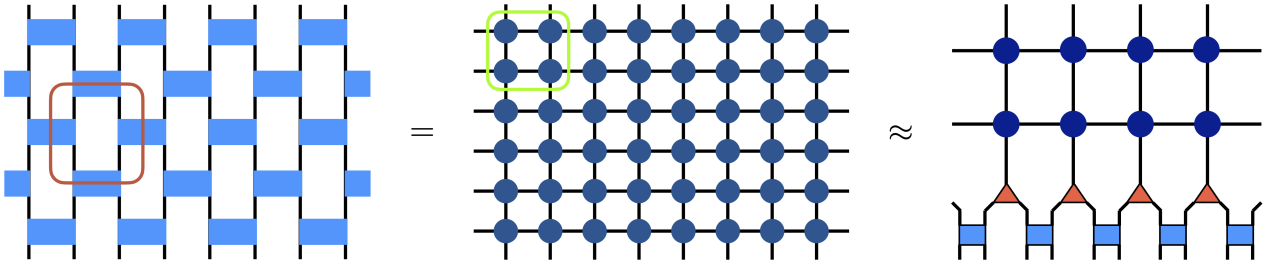

Figure 9.2: Principle of TNR for the discretized Euclidean path integral. The infinite $2D$ TN diagram of $\mathrm{e}^{-\beta H}$ follows from the Suzuki–Trotter decomposition and prepares the groundstate of H in the limit $\beta \to \infty$ (left panel). It consists of 2-site gates $U_i \equiv \mathrm{e}^{-d\tau h_{i,i+1}}$ which are transformed into a uniform TN (small blue circles in the middle panel) by splitting the U_i using SVDs and reassembling them as indicated by the red frame. The TNR step (right panel) removes short-range entanglement by introducing a layer of MERA into the TN and coarsegraining 4 uniform tensors (indicated by the green frame) into one new one (large blue circles in the right panel). The iteration of this process produces the full MERA network.

the computational complexity $\mathcal{C}_{\Psi_0}$ of the ground state Ψ_0. For Weyl-rescaled geometries, it assumes the value

$$\mathcal{C}_{\Psi_0} = \min_{\omega} S_L[\omega(\tau, x)] = \frac{c\, l}{12\pi\epsilon}, \tag{9.15}$$

where we defined $l \equiv \int \mathrm{d}x$. Interestingly, the divergence structure $\sim \epsilon^{-1}$ agrees with the one of the holographic volume proposal in (8.7), independent from the particular CFT under consideration. In the present context, this complexity is also denoted as *path integral complexity*. The optimization procedure which we discussed so far was based on the modification of the background metric over which the Euclidean path integral is performed. As such, it was interpreted in [117,118] as a continuous generalization of the TNR algorithm [99,100] summarized in Fig. 9.2. For the latter we assume that the TN diagram shown in the left panel approximates the ground state wavefunction of the QMB system using the Suzuki–Trotter decomposition of 2-site gates. A judicious reassembling of the tensors transforms this TN into the uniform network shown in the middle panel. The insertion of disentanglers and isometries in the TNR step shown in the right panel sequentially produces the MERA TN. From a computational viewpoint, the MERA circuit contains less tensors and therefore possesses a smaller complexity. In the continuum, this modification of the tensor structure corresponds to the deformation of the background geometry discussed above, yielding versions of the cMERA wavefunction [116]. The concrete amount of complexity in the discrete TN during the TNR procedure was heuristically estimated in [118,121]. In particular, it was argued that the potential term $\sim \int \mathrm{e}^{2\omega}$ measures the number of disentanglers (i.e. unitaries), when attributing a unit area to each tensor, while the kinetic term $\sim \int (\partial\omega)^2$ approximates the number of isometries. Both terms together resemble the Liouville action and therefore provide further evidence that this action represents the relevant functional governing the path integral complexity.

In summary, we have seen that the path integral optimization program provides an alternative

framework to obtain the complexity of ground states in two-dimensional CFTs. The Liouville action is the proposed functional whose minimization yields the complexity by modifying the background metric. Beyond the vacuum case, in which optimized metrics are given by AdS_3 time slices, it was additionally observed in [117,118] that the finite temperature TFD state yields the ERB as the optimized geometry, which was heuristically argued to grow linearly in time in accordance with the holographic counterpart. Overall, the path integral complexity was worked out as an attempt to find a continuous version of TN interpretations of the AdS/CFT correspondence. At this point, the relation to the circuit complexity framework is, however, an open problem. We close this gap through our considerations in the next chapter by showing that, up to an irrelevant overall normalization, S_L represents only an approximation to a cost function for a precise gate counting within the circuit complexity approach.
Before proceeding in this direction, it seems instructive to highlight two further properties of the Liouville action. First, S_L is a properly covariant expression, which in arbitrary coordinates ξ^μ takes the form [418]

$$S_L = \frac{c}{24\pi} \int \mathrm{d}^2\xi \, \sqrt{g} \left[\Lambda + \frac{1}{4} \partial_\mu \chi \partial^\mu \chi \right]. \tag{9.16}$$

Here, the scalar χ is given by the covariant albeit nonlocal expression

$$\chi(\xi) = \int \mathrm{d}^2\tilde{\xi} \, \sqrt{g(\tilde{\xi})} \, \Box^{-1}(\xi, \tilde{\xi}) R(\tilde{\xi}), \tag{9.17}$$

where R is the Ricci scalar and $\Box^{-1}$ the propagator for a massless scalar field. [72] From the expression (9.13), one can deduce that a different relative normalization between the $\dot{\omega}^2$ and ω'^2 terms would not give rise to the covariant form (9.16). The second remark is that the Liouville action can be regarded as consisting of the two leading terms in a derivative expansion w.r.t. ϵ: The cosmological constant term $\Lambda \sim \mathcal{O}(\epsilon^{-2})$ originates from the renormalization of the energy-momentum tensor and diverges in the continuum. On the other hand, the nonlocal term is of order $\mathcal{O}(\epsilon^0)$ and the source of the trace anomaly. Any further terms would come for dimensional reasons with positive powers of ϵ and hence vanish in the continuum limit $\epsilon \to 0$. We therefore ignore such terms in the following circuit approach to the path integral optimization.

[72] For uniqueness, it is imposed that χ vanishes at the boundaries.

10 Path integral optimization as circuit complexity

The discussion of the previous chapter highlighted that the QFT dual of holographic complexity is not yet fully understood. Both the circuit and path integral approach provide a framework to either define a proper cost function or identify the Liouville action as functionals whose minimization yields the complexity of a state. These two viewpoints, however, are based on rather different setups and a possible connection between them seems nontrivial. Moreover, when analyzing the divergence structure as discussed above, the circuit complexity approach seems to favor the holographic action proposal, whereas the path integral complexity shares similarities with the volume proposal. It is therefore highly desirable to try to unify these two concepts, to understand better their relations and decide whether they are indeed competing concepts with different physical implications.

In this chapter we pursue this path by interpreting the Euclidean path integral on Weyl-rescaled geometries as a circuit in the sense of a path ordered exponential, defined by eq. (9.1). At first, we will outline the general setup based on coordinate transformations in section 10.1, and then describe in section 10.2 how the Liouville action can be derived from a particular cost function.

10.1 Euclidean path integrals as circuits

The basis for the circuit identification of Euclidean path integrals is a formula developed in [106,107] in the context of geometrical interpretations of TNs preparing path integrals. In particular, we consider a Euclidean path integral of a $2D$ CFT in generic background coordinates

$$\mathrm{d}s^2 = \left[a(t,y)^2 + b(t,y)^2\right]\mathrm{d}t^2 + 2\,b(t,y)\,\mathrm{d}t\,\mathrm{d}y + \mathrm{d}y^2, \tag{10.1}$$

in which constant Euclidean time t slices are flat lines w.r.t. the coordinate y. The relevant statement then is that this path integral computes, up to an unimportant normalization, the matrix elements of the nonunitary operator

$$V = \mathcal{P}\exp\left\{-\int_{t_i}^{t_f}\mathrm{d}t\int\mathrm{d}y\,\left[a(t,y)\,h(y) + i\,b(t,y)\,p(y)\right]\right\}. \tag{10.2}$$

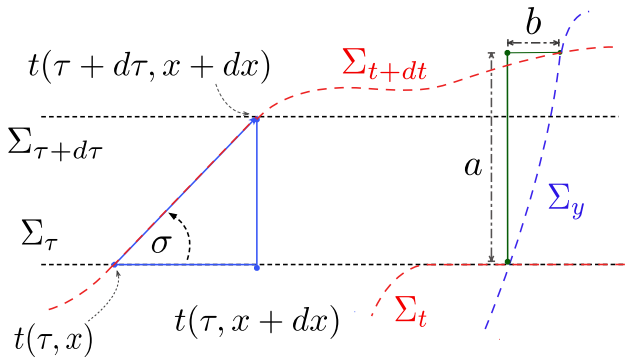

Figure 10.1: Geometric interpretation of the (t, y) coordinate system (10.1) in comparison to the (τ, x) coordinates in (9.11). Σ_τ and Σ_t denote time slices of the respective background geometries. The right side of the figure illustrates the geometrical interpretation of the parameters a and b in the metric (10.1) as distances to intersections of constant coordinate slices. At a given point, the function $\sigma(\tau, x)$ defines the Euclidean angle between tangents to Σ_t and Σ_τ, cf. eq. (10.9). Figure taken from [5].

Here, $h \equiv T_{t_M t_M}$ and $p \equiv T_{t_M y}$ are the Hamiltonian and momentum stress tensor components in Minkowski spacetime with line element $\mathrm{d}s^2 = -\,\mathrm{d}t_M^2 + \mathrm{d}y^2$, and the path ordering refers to the integration over t. A geometric interpretation of this expression in the new (t, y) coordinates is given in Fig. 10.1.

The operator V in eq. (10.2) has the same form as the circuit (9.1) when identifying the time t as the circuit parameter and the energy-momentum tensor components as the gates/operators O_I. In contrast to the usual setting in both QMB systems and QFTs, we now work with both Hermitian (Euclidean) and unitary transformations, generated by the operators h and ip, respectively.[73] The index I differentiates between these two gates and runs over the full range of the y coordinate. The path integral (10.2) can be interpreted as a bilinear map acting on the Hilbert space on a slice of Euclidean time t. To connect it to the Euclidean path integral on a Weyl-rescaled geometry, we need to identify coordinate transformations from the (τ, x) coordinates in the metric (9.11) to the (t, y) coordinates in (10.1). To do so, we at first build up some intuition for a restricted case and then discuss the most general coordinate transformation that achieves this task.

10.1.1 Intuitive understanding of coordinate transformations

Suppose that we perform a transformation only on the spatial coordinate, i.e. $t = \tau$ and $y = y(\tau, x)$, such that $\mathrm{d}y = \dot{y}\,\mathrm{d}\tau + y'\,\mathrm{d}x$. The metric (9.11) transforms under this coordinate change into

$$\mathrm{d}s^2 = \frac{\mathrm{e}^{2\omega(\tau,x(y))}}{y'^2}\left((y'^2 + \dot{y}^2)\,\mathrm{d}\tau^2 - 2\dot{y}\,\mathrm{d}y\,\mathrm{d}\tau + \mathrm{d}y^2\right). \tag{10.3}$$

[73] This can also be understood from the fact that the Wick rotation to Euclidean time places the tt and ty components of the energy-momentum tensor on different footing.

Demanding agreement with the metric form (10.1) amounts to the condition $\mathrm{e}^{2\omega(\tau,x(y))}/y'^2 = 1$, which is solved by the coordinate transformation

$$y = \int_0^x \mathrm{d}\gamma\ \mathrm{e}^{\omega(\tau,\gamma)} + f(\tau) \tag{10.4}$$

for an arbitrary function $f(\tau)$, which we are allowed to set $f(\tau) \equiv 0$. The metric components a and b can be read off as

$$a = y' = \mathrm{e}^{\omega(\tau,x)} \qquad \text{and} \qquad b = -\dot{y} = -\int_0^x \mathrm{d}\gamma\ \mathrm{e}^{\omega(\tau,\gamma)}\,\dot{\omega}(\tau,\gamma). \tag{10.5}$$

The path-ordered exponential (10.2) can be rewritten explicitly using these expressions. Incorporating a Jacobian factor $J = \mathrm{e}^{2\omega}$ when passing to the (τ, x) coordinates, we obtain

$$V = \mathcal{P}\exp\left\{-\int_0^\beta \mathrm{d}\tau \int_{-\infty}^{\infty} \mathrm{d}x \left[h(x) - \left(\mathrm{e}^{-\omega(\tau,x)} \int_0^x \mathrm{d}\gamma\,\dot{\omega}(\tau,\gamma)\,\mathrm{e}^{\omega(\tau,\gamma)}\right) i\,p(x)\right]\right\}. \tag{10.6}$$

This expression can be understood intuitively when viewed as a linear map generated by the path integral on the metric (9.11) from some time slice τ to a time slice $\tau + \delta\tau$. The Hamiltonian time evolution is generated by the first term, whereas the second term accounts for the change of the geometry in the transverse direction when moving from one time slice to the other. To see the latter property, we consider an infinitesimal, position-dependent translation $x \to x + u(x)\,\delta\tau$ and equate the change in the transverse direction with the action of this translation, i.e.

$$\mathrm{e}^{2\omega(\tau+\delta\tau,x)}\,\mathrm{d}x^2 = \mathrm{e}^{2\omega(\tau,x+u(x)\delta\tau)}\,\mathrm{d}(x + u(x)\delta\tau)^2\,. \tag{10.7}$$

Expanding this expression to first order in $\delta\tau$ and solving it for $u(x)$ yields precisely the second term in (10.6) multiplying the generator ip.

10.1.2 The general case

In the most general case, the coordinate transformation can be parametrized by a diffeomorphism $t = t(\tau, x)$, $y = y(\tau, x)$. The same steps as in the previous simpler case give rise to the following solutions for a and b in terms of t and y:

$$a = \frac{\dot{t}\,y' - t'\,\dot{y}}{\dot{t}^2 + t'^2} \qquad \text{and} \qquad b = -\frac{\dot{t}\,\dot{y} + t'\,y'}{\dot{t}^2 + t'^2}. \tag{10.8}$$

The boundary conditions are translated into $y(0,x) = y(\beta,x) = x$, and $t(0,x) \equiv \text{const}$, $t(\beta,x) \equiv \text{const}$. While the functions a and b specify the circuit (10.2), generic choices of them would not prepare, up to normalization, the operator ρ_β in (9.8) on a Weyl-rescaled geometry. Only

the specific relations in (10.8) that follow from the coordinate transformation guarantee this. For the following calculations, we will introduce a convenient variable. We define the angle σ as

$$-\frac{t'}{\dot{t}} = -\frac{\mathrm{d}\tau}{\mathrm{d}x} =: \tan\sigma, \tag{10.9}$$

whose geometric interpretation is explained in Fig. 10.1. Demanding that the overall prefactor in front of the metric (10.1) equals one after the coordinate transformation, relates derivatives of t and y to the Weyl factor ω in the following way

$$y' = \mathrm{e}^{\omega}\sec\sigma - \dot{y}\tan\sigma. \tag{10.10}$$

Based on these relations, we now want to count gates through appropriate cost functionals of a and b. To reformulate the path integral complexity in the circuit complexity approach, our goal is to recover the Liouville action from a particular, so far unknown, cost function. For a proper identification, we aim to reexpress our results in dependence on ω and the new free (gauge) parameter σ.

10.2 Cost functions and the Liouville action

Having identified the circuit (10.2) for the particular functions in (10.8), which prepares the Euclidean path integral, we can define cost functions whose minimization yield the circuit complexity. As discussed in section 9.1, there are many possible choices in the geometrical approach to circuit complexity. We will discuss at first the L^1 and $\kappa = 2$ norm and outline their shortcomings, before moving on to a more general class of cost function, which we find to reproduce the Liouville action.

10.2.1 Properties of L^1 cost functions

The L^1 norm as defined in (9.2) implies in the simplest case a direct counting of a and b in the circuit as

$$\mathcal{D}_1 \simeq \int \mathrm{d}t\,\mathrm{d}y\,(|a| + \eta_b|b|)\,, \tag{10.11}$$

where we do not account for an overall normalization. The counting of a means that we always associate a cost to advancing in the time direction along the circuit. Costs for moving along the transverse direction are counted by b with a penalty factor $\eta_b \geq 0$.[74] Already for the simplified coordinate transformation $\sigma = 0$ in (10.5), this can result in complicate dependencies on ω. From a physical perspective, it makes sense not to assign any cost to uniform space translations. We therefore choose $\eta_b = 0$.

[74] A detailed discussion of penalty factors in this context is available in [45].

More generally, it is a totally valid choice to include also derivative terms in the cost function. However, for a proper identification of circuit complexity, we exclude derivatives w.r.t. the time coordinate, since these would assign a cost to "acceleration" along the path. A more sophisticated version of the L^1 norm hence reads

$$\mathcal{D}_1 \simeq \int \mathrm{d}t\,\mathrm{d}y\,\frac{1}{\epsilon^2}\left(|a| + \epsilon\,\eta_{\partial a}|\partial_y a| + \epsilon\,\eta_{\partial b}|\partial_y b| + \ldots\right). \tag{10.12}$$

Here, we have weighted dimensionful derivative terms with the UV regulator ϵ and accordingly included an overall factor ϵ^{-2} from the integration measure. Possible penalty factors are denotes as $\eta_{\partial a}$ and $\eta_{\partial b}$, and ellipsis stand for terms of order $\mathcal{O}(\epsilon^0)$ and higher, which vanish in the continuum limit. The cost of uniform applications of h is accounted for by $|a|$, while the derivative terms correspond to inhomogeneous translations in space and time. In principle, it would be also possible to include mixed terms of the form $|\partial_y a + \partial_y b|$; we however neglect these in the following discussion.

In the next step we want to express the $\mathcal{D}_1$ cost function (10.12) in the (τ, x) coordinates by taking the Jacobian $J = \dot{t}y' - t'\dot{y} = \mathrm{e}^{\omega}\,\dot{t}\sec\sigma$ into account. The result takes a relatively simple form in terms of ω and σ,

$$\begin{aligned}\mathcal{D}_1 \simeq \int_0^{\beta}\mathrm{d}\tau\int_{-\infty}^{\infty}\mathrm{d}x\,\frac{\mathrm{e}^{\omega}}{\epsilon^2}\Big\{\,&\mathrm{e}^{\omega} + \epsilon\,\eta_{\partial a}\,|(\dot{\omega}-\sigma')\sin\sigma + (\omega'+\dot{\sigma})\cos\sigma| \\ &+ \epsilon\,\eta_{\partial b}\,|(\omega'+\dot{\sigma})\sin\sigma - (\dot{\omega}-\sigma')\cos\sigma| + \ldots\Big\}.\end{aligned} \tag{10.13}$$

Obviously, this cost function is not able to recover the Liouville action. Moreover, it depends explicitly on the foliation into constant time slices via σ and hence is not diffeomorphism-invariant of the metric $g_{\mu\nu}$. Even in the flat space case, $\omega = 0$, $\mathcal{D}_1$ is still nontrivial and foliation-dependent.

To close this section, we now consider the special case of a translation-invariant Weyl factor, $\omega = \omega(\tau)$ and the choice $\sigma = 0$. Eq. (10.13) then reduces to

$$\mathcal{D}_1 \simeq \int_0^{\beta}\mathrm{d}\tau\,\frac{1}{\epsilon}\left\{\mathrm{e}^{2\,\omega} + \epsilon\,\eta_{\partial B}|\,\mathrm{e}^{\omega}\;\dot{\omega}|\right\}, \tag{10.14}$$

where higher-order terms and an unimportant prefactor are neglected. Keeping in mind the boundary condition $\omega = 0$ at $\tau = 0$ and $\tau = \beta$, the optimal path of this cost function can be deduced with relative ease. Observe in particular that the first term is minimized for $\omega \to -\infty$. The kinetic term, on the other hand, is only the absolute value of a total derivative $\frac{\mathrm{d}}{\mathrm{d}\tau}\,\mathrm{e}^{\omega}$ and therefore does not penalize this run-away behavior. It is not sensitive to how fast the function changes but only piecewise to total changes. The optimal circuit is consequently given by an almost infinite dilatation at the boundaries and a piece of Euclidean time evolution with an extremely coarse-grained Hamiltonian in between. This situation is similar to the TNR

outlined above, in whose context the MERA was identified as almost infinite dilations, while the Euclidean time evolution corresponds to a single layer of *Euclideons* [100] (cf. Fig. 9.2).

10.2.2 Properties of $\kappa = 2$ cost functions

Another common choice of cost function is the $\kappa = 2$ norm following from the definition (9.4).[75] Based on the general principles of gate counting as for the L^1 norm, it comprises the following quadratic gate counting

$$\mathcal{D}_{\kappa=2} \simeq \int \mathrm{d}t\, \mathrm{d}y \left\{ \frac{1}{\epsilon^2} a^2 + \eta_{(\partial a)^2} (\partial_y a)^2 + \eta_{(\partial b)^2} (\partial_y b)^2 + \dots \right\}, \tag{10.15}$$

containing possible penalty factors $\eta_{(\partial a)^2}$ and $\eta_{(\partial y)^2}$. Again, higher-order derivatives $\sim \epsilon^n \partial_y^n$ are omitted since they vanish for $\epsilon \to 0$, while mixed terms of the form $\frac{1}{\epsilon} a \partial_y b$ or $\partial_y a \partial_y b$ are possible but we neglect them similarly. In its general form, the $\kappa = 2$ norm can be expressed as

$$\mathcal{D}_{\kappa=2} \simeq \int \mathrm{d}t \sum_{IJ} \eta_{IJ} Y^I Y^J, \tag{10.16}$$

where the metric η_{IJ} takes the form

$$\eta_{IJ} = \begin{pmatrix} (-\partial_y^2 + \frac{1}{\epsilon^2}) \delta(y - y') & 0 \\ 0 & -\partial_y^2 \delta(y - y') \end{pmatrix}. \tag{10.17}$$

The gate counting is reformulated as

$$\mathcal{D}_{\kappa=2} \simeq \int \mathrm{d}t \int \mathrm{d}y \int \mathrm{d}y' \begin{pmatrix} a(y) & b(y) \end{pmatrix} \eta_{IJ} \begin{pmatrix} a(y') \\ b(y') \end{pmatrix}, \tag{10.18}$$

where we have suppressed penalty factors and rewritten the sum $\sum_{IJ}$ as a double integral over y and a summation over a and b. Minimization of the cost function in this form hence corresponds to finding geodesics in a Riemannian geometry.
In Weyl-rescaled coordinates, the $\kappa = 2$ cost function takes the form

$$\mathcal{D}_{\kappa=2} \simeq \int_0^\beta \mathrm{d}\tau \int_{-\infty}^{\infty} \mathrm{d}x \frac{\mathrm{e}^\omega \cos\sigma}{\dot{t}} \left\{ \frac{\mathrm{e}^{2\omega}}{\epsilon^2} + \eta_{(\partial a)^2} (\sigma' - \dot{\omega})^2 + \eta_{(\partial a)^2} (\dot{\sigma} + \omega')^2 \right\} \tag{10.19}$$

for equal penalty factors $\eta_{(\partial a)^2} = \eta_{(\partial b)^2}$. The important lesson here is that this cost function depends explicitly on the diffeomorphism $t(\tau, x)$, i.e. the time foliation in the circuit parametrization, via the derivative $\dot{t}$ appearing in the denominator. Contrary to the previous L^1 norm and the more general class in the next section, we here have ω, σ and t as optimization

[75] In a mathematical strict sense, it is not really a norm. Such subtleties will, however, not be relevant for our explorations.

parameters. Their equations of motion are complicated and do not decouple. An attempt to reproduce the Liouville action in each power of ϵ does not yield consistent conditions for the time slice $t(\tau, x)$.[76] An exception can be found for the special case of a translational invariant circuit $\omega = \omega(\tau)$. In this case, we can choose $\sigma = 0$ and $\dot{t} = \mathrm{e}^{\omega(\tau)}$, which cancels the prefactor in (10.19) and reproduces the Liouville action.

10.2.3 Liouville action from a more general class of cost functions

The outcome of our discussions on the L^1 and $\kappa = 2$ norm is that both these common choices do not recover the Liouville action in the most general case of coordinate transformations. The same conclusions holds for the $\mathcal{D}_2$ cost function, which is even more subtle since the integral over y appears under a square root, which does not yield natural expressions in terms of ω and σ in dependence of τ and x. It turns out that an appropriate choice giving rise to the Liouville action is given by the intermediate definition

$$\mathcal{D}_{1/2} \simeq \int \mathrm{d}t\, \mathrm{d}y \frac{1}{\epsilon^2} \sqrt{a^2 + \epsilon^2 \eta_{(\partial a)^2} (\partial_y a)^2 + \epsilon^2\, \eta_{(\partial b)^2} (\partial_y b)^2 + \ldots}, \tag{10.20}$$

which we denote as $\mathcal{D}_{1/2}$ cost function, referring to a class, which is known as *Schatten p-norms* [420]. We neglect here mixed terms as discussed before, as well as higher-order derivative terms (denoted by ellipses). In full generality, $\mathcal{D}_{1/2}$ does not represent a diffeomorphism-invariant (i.e., σ-independent) cost function. However, for equal penalty factors, $\eta_{(\partial a)^2} = \eta_{(\partial b)^2}$, a Taylor expansion up to next-to-leading order in ϵ yields the result

$$\mathcal{D}_{1/2} \simeq \int \mathrm{d}\tau\, \mathrm{d}x \left\{ \frac{\mathrm{e}^{2\omega}}{\epsilon^2} + \frac{1}{2}\eta_{(\partial a)^2} \left(\dot{\omega}^2 + \omega'^2\right) + \frac{1}{2}\eta_{(\partial a)^2} \left(\dot{\sigma}^2 + \sigma'^2\right) + \eta_{(\partial a)^2} (\omega' \dot{\sigma} - \dot{\omega}\sigma') + \ldots \right\}. \tag{10.21}$$

The last term is only a total derivative. Hence, the resulting equations of motion for ω and σ,

$$-\frac{\mathrm{e}^{2\omega}}{\epsilon^2} + \omega'' + \ddot{\omega} = 0 \qquad \text{and} \qquad \sigma'' + \ddot{\sigma} = 0, \tag{10.22}$$

decouple (here written for unit penalty factor). This means that the optimization over ω is independent from the choice of σ, since the second equation for the latter is solved by any holomorphic or anti-holomorphic function. We can observe that the ω-dependent first part in (10.21) is precisely the Liouville action. As a result, using the $\mathcal{D}_{1/2}$ cost function, we could achieve the task of giving the path integral complexity based on the Liouville action a precise interpretation as an approximation within the circuit complexity approach. This new perspective implies, however, that the Liouville action is not fundamental in quantifying complexity of CFTs, since it only arises after some fine-tuning of a particular cost function.

[76] Note, however, that we neglected for that statement intricate subtleties like total derivatives when comparing to the Liouville action.

This bears a striking resemblance to a similar observation in [402], where the Liouville action was obtained when expanding a bulk gravitational action with a boundary term in AdS_3 with a position dependent cutoff in ϵ in the next-to-leading order. A further analogy comes from the fact that the cost function (10.20) resembles for $\sigma = 0$ a Dirac–Born–Infeld (DBI) action [421] for the field ω. In terms of the field χ in (9.17), it takes the form

$$\mathcal{D}_{\mathrm{DBI}} \simeq \int \mathrm{d}^2\chi \sqrt{\det\left(g_{\mu\nu} + \epsilon^2 \partial_\mu \chi \partial_\nu \chi\right)}. \tag{10.23}$$

10.3 Discussion and outlook

In this chapter we have shown that path integral complexity can be embedded into the circuit approach to complexity by demonstrating that the Liouville action arises as an approximation to a genuine gate counting for a particular class of cost functions. From a broader perspective, we were motivated in our explorations to define circuit complexity in QFT as a direct functional of sources that are present in the underlying Euclidean path integral. In contrast to earlier attempts to circuit complexity in QFTs (cf. section 9.1), we explicitly employed only local gates and treated the background metric as the source.

The genuine cost function $\mathcal{D}_{1/2}$ in (10.20) is not covariant w.r.t. the underlying metric anymore since it is defined for a particular time foliation. However, covariance is recovered in the approximation (10.22), which arises as the next-to-leading order expansion in the UV cutoff. In this way, the Liouville action is obtained. Demanding both covariance and a proper gate counting seems to impose quite severe restrictions on allowed metric functionals. In this context, let us remark that the path integral optimization procedure only varies the cost function w.r.t. the Weyl factor ω. In a general covariant setting, one should, however, also vary the other metric components, which leads to further constraint equations. We also would like to emphasize that the optimization of the Liouville action is not equivalent to the optimization of of the $\mathcal{D}_{1/2}$ cost function. The reason is that solutions of the equations of motion set respectively different terms to order $\mathcal{O}(1)$, causing a breakdown of of the ϵ expansion. This again motivates further explorations on cost functionals for path integral complexity that are covariant to all orders. The DBI form of the cost function in (10.23) could provide a starting point for rigorous analyzes in this direction.

In our studies, we have defined cost functions up to an overall prefactor. This means that we are not sensitive to the central charge appearing in the proper definition of the Liouville action in (9.13). Although it would be possible to include c either ad hoc in the normalization or as penalty factors, we do not see a particular justification for doing so. Hence, our results are valid up to an overall normalization or prefactor.

Based on the works [106,107], which provided the conceptual background for our coordinate transformations, we can interpret our results from a TN perspective. The original path inte-

gral optimization program was derived as a continuous generalization of the TNR algorithm, in which a uniform TN consisting of Euclideons is transformed into the MERA circuit (cf. Fig. 9.2). However, the generalized path ordered exponential (10.2) can implement more general forms of the MERA. In particular, for $a = 1$ and $b \sim y$, one gets a Euclidean MERA on a hyperbolic background geometry, which consists of layers of Euclideons that intersect the usual MERA layers. An example of such a circuit is illustrated in the right panel of Fig. 3.10. This exemplifies that optimal paths can take more complicate forms and do not necessarily correspond to the bare MERA circuit, which was heuristically obtained from optimizing the Liouville action alone. In some preliminary analyses, we tried to discretize the general form of the path-ordered exponential (10.2) uniformly using the TEBD algorithm to prepare the groundstate of a critical Ising Hamiltonian. This, however, revealed the problem that the unitary term in it destroys convergence for any finite value of $\beta < \infty$. A more rigorous analysis on that front could allow to analyze optimal circuits numerically using TN simulations.

Our work has also several implications on complexity in general. As discussed in our review on holographic and QFT proposals for complexity in chapters 8 and 9, a clear proof and understanding on the correctness of these competing proposals is not yet available. However, we want to put forward here the idea that this challenge could be achieved by equating bulk and boundary Euclidean partition functions, whose interface is governed by the boundary QFT sources. This line of reasoning is very much in the spirit of the original operator/field map (cf. section 2.5.2) of the AdS/CFT correspondence. The works [410,422–424] already go in this direction, but our explorations in this chapter, in fact, provide the first rigorous attempt in this vein by constructing genuine cost functions for particular source configurations. Moreover, we want to point out that the original path integral optimization program optimizes the Liouville action alone but neglects higher-order corrections in ϵ. Since we could recover the Liouville action only approximately for a particular cost function, we should expect that optimal circuits or geometries from a genuine circuit approach to QFTs might take a different form than the ones obtained by considering the Liouville action alone as in the path integral complexity.

The line of research in this chapter can be extended in several directions. While we were focusing on the original path integral optimization program for CFTs [116–118], the work [425] extended it to include $T\bar{T}$ deformations, while [426] derived warped spacetimes from a chiral Liouville action, and [427] considered inhomogeneous CFTs. It would be interesting to consider our circuit approach also in these more intricate cases and connect it to the recent holographic proposal of path integral optimization, which is based on the maximization of the Hartle–Hawking wave function [428,429]. Moreover, it seems important to understand the connection to circuit complexity when using the Fubini-Study distance for the cost functional as considered by the works [430–433], which employ explicitly stress tensor insertions as unitary Virasoro generators in $2D$ CFTs. From a more general perspective, the recent work [434] proposes that the full gravitational action represents the complexity of any holographic spacetime

region. In this setup, the Liouville action merely appears as the leading two terms when taking the continuum limit w.r.t. a UV cutoff, and hence the problem of deriving a covariant cost functional which yields the Liouville action alone could be avoided for a circuit interpretation thereof.

11 Summary and discussion

In this thesis we have theoretically studied physical systems at the intersection of holography and quantum field theory (QFT), using methods based on tensor networks (TNs) and, more generally, quantum information science and quantum simulation (QS). We were primarily driven by the quest to understand fundamental matter under extreme conditions, such as in the interior of black holes (BHs) or during heavy-ion collisions (HICs) in nuclear accelerators. Over the last decade, TN based methods and concepts became increasingly important in an interdisciplinary effort to understand such systems. Having been developed originally in the context of condensed matter physics, they also offer computational advantages to study QFTs as in particle physics. They therefore open the avenue to rigorously analyze physical systems under challenging conditions that were previously (including ourselves) studied with applied methods and models from the gauge/gravity duality. At the same time, there are several frameworks that conjecture how TNs can provide a discrete interpretation of the anti-de Sitter/conformal field theory (AdS/CFT) correspondence itself, which provides new insights into quantum gravitational aspects and the emergence of spacetime.

In this vein, we formulated in our overview chapter 1 two motivating questions. First, we asked how TN simulations and related methods can help us in understanding equilibration processes similar to those in HICs. Second, we were interested what role complexity plays at the intersection of TNs, QFT and holography.

After discussing the foundations of the gauge/gravity duality and TNs in part I of this thesis, we addressed the first question in part II. In particular, we studied nontrivial (1+1)-dimensional QFTs arising in the IR limit of quantum spin chain models. In chapter 4, we reviewed motivating aspects of QCD and HICs and identified retarded thermal equilibrium correlators governing linear response theory as an important tool to characterize relaxation and thermalization properties of quantum many-body (QMB) systems and QFTs. In this context, we developed a new method that combines matrix product operator (MPO) simulations for intermediate time scales with a signal analysis procedure using the Prony method. This setup allowed us to extract the analytic correlator structure in the complex frequency plane. The underlying singularity structure can be generically divided into branch cuts and single poles, whereby for the latter one can differentiate between hydrodynamic (long-lived) and transient (decaying) poles. Motivated by previous holographic results and a kinetic theory study, we predicted that for nonintegrable interacting parameter ranges of the Ising QFT (4.40), tran-

sient singularities do not alter their singularity structure in comparison to the integrable free fermion regime. Moreover, we could identify meson poles as a signature of nonperturbative bound states in the system. When the temperature is raised, we observe the appearance of poles corresponding to their mass differences. This study demonstrates that we can extract highly nontrivial dynamical properties of collective QFT states in an ab initio fashion from our TN simulations in combination with signal analysis techniques.

As an extension of this line of research, we then incorporated in chapter 5 scaling operators from an analytic wavelet solution of the multiscale entanglement renormalization ansatz (MERA) to analyze if this coarsegrained discretization scheme allows for a more precise encoding of thermal correlation functions in comparison to the bare Ising model. In this conceptually different setting, we found that to lowest-order in the physical dimension, the MERA based TN simulations allow an extraction of QFT data at most as precise as the bare system. From a broader perspective, it would be interesting to pursue these investigations further for higher physical dimensions, since the related problem of finding optimal discretization schemes of QFTs is also relevant for QS.

These thermal correlator studies highlighted the importance of meson states for the understanding of dynamical properties in QMB systems and QFTs. In chapter 6, we studied a related effect, the melting of meson bound states in the nonintegrable ferromagnetic phase of the Ising QFT, in detail. Our explorations are motivated by QCD, where this phenomenon is important for the understanding of HICs and hence the physics of the early universe. We reviewed phenomenological QCD approaches as well as holographic models, in which the sequential melting process is signalled by a thermal broadening of the in-medium spectral function. In our TN simulations, we instead initiated a new paradigm for its description by analyzing entanglement measures in a static and dynamical situation. In particular, we found that the second Rényi entropy density of a thermal state scales at high temperatures as in a CFT, where no meson masses are present and the only scale is set by the temperature. In the dynamical case, we simulated thermal quantum quenches in the thermodynamic limit and analyzed the growth and behavior of reflected entropies, which can be calculated directly from a translational invariant MPO ansatz. At low effective temperatures, we observe entanglement oscillations, i.e. an oscillatory behavior with frequencies given by the meson masses. In contrast, at high effective temperatures, an observed linear growth behavior is consistent with expectations from a quasiparticle model, which is valid for (integrable) theories without meson states. From these findings, we conclude that mesons have been melted as soon as the temperature is high enough. Even simple entanglement measures can characterize and signal the meson melting effect. We put forward the vision to incorporate this idea also into the QCD context, which, in our opinion, can provide new insights about meson melting as a phenomenon that is not yet completely understood from a detailed microscopic perspective. This idea fits nicely into the recent progress and growing interest of the TN and QS community to address topics originating

from particle physics, in particular for gauge theories.

TN simulations are classical methods based on entanglement properties in a QMB system. As such, they are closely related to QS, in which either digital or analog simulations of quantum systems themselves open the avenue to controlled studies of fundamental physical systems beyond the capability of classical resources. Inspired by our meson studies and the recent rapid progress in experimental technologies, we explored in chapter 7 prospects for identifying relativistic meson spectra on trapped ion devices. Focusing on the E_8 regime of the Ising QFT, we used numerical diagonalization techniques to show that for sufficiently strong long-range suppression, experimentally realizable spin chain models allow for the identification of the low-lying meson excitations even in small systems. We provided a protocol for its detection via absorption spectroscopy. With these theoretical studies, we would like to promote the idea for the experimental realization of our proposal, which can be achieved with existing technologies. We are convinced that this would be an valuable contribution in the understanding of meson physics.

In view of our first motivating question, we can fairly conclude that TN simulations allowed us to learn important lessons about both static and dynamical properties of (1+1)-dimensional QFTs at zero and finite temperature. The same holds for our explorations on QS, which additionally open the prospect to outperform classical computations and therefore shine light on new physical effects and properties. In both cases, the most interesting extension of our work, which we would like to highlight at this point, would be to go beyond the realm of spin chain models and their underlying QFTs. Most relevantly, we would like to motivate future studies in the same spirit but for relativistic lattice gauge theories, which are directly relevant to the standard model in particle physics. While we focused on simulations in (1+1) dimensions, it would be accordingly desirable to perform simulations also in higher dimensions. One obvious computational difficulty arising in this endeavour is the even more severe limitation to early times due to entanglement production under real-time evolutions. However, from the TN perspective, recent years have shown a tremendous progress in both algorithm developments and simulating (relatively simple) gauge theories with 2-dimensional ansätze. Even the first 3-dimensional simulations are available, which could already avoid the sign problem of conventional Monte Carlo methods. In a similar fashion, gauge principles of QFTs were successfully implemented via experimental QS. Based on the recent progress in these directions, we see the potential that our addressed problems and questions can be studied also in more complicate theories with these techniques in the medium-term future. On this route to standard model physics, we see our studies as a first step, which is relevant since it provides a controlled setup to study physical effects with new ideas and concepts for (1+1)-dimensional QFTs in challenging parameter regimes. Moreover, some of our phenomenological observations (such as entanglement measures at high temperatures) and analysis methods (Prony method for a one-dimensional signal originating from arbitrary theories) are directly relevant also for

higher-dimensional computations.

In part III of this thesis we addressed our second motivating question. From the quantum computational viewpoint, we introduced in chapter 8 complexity as a concept to quantify the difficulty to realize a quantum circuit from a reference to a target state. We then reviewed the volume and action proposal as competing conjectured duals to this quantity that probe the interior of the eternal AdS BH. As discussed in chapter 9, the QFT side of this holographic correspondence is less understood. There are two independent proposals: While the circuit approach is based on a geometric gate counting procedure in a continuous circuit (expressed as a path-ordered exponential), the path integral complexity is resting on an optimization of Euclidean path integrals in a Weyl-rescaled background geometry, realizing a continuous generalization of the tensor network renormalization (TNR). In chapter 10 we bridged the gap between these two proposals for $2D$ CFTs. Our calculations are based on a coordinate transformation, which allowed us to reexpress the path-ordered exponential in a generalized form. The Liouville action, which was heuristically argued to govern the path integral complexity, then arises only as an approximation to a judicious gate counting. As a consequence, optimal circuits can take upon discretization more general forms than the MERA, which was obtained from a TNR interpretation of the original path integral optimization procedure.

By constructing cost functions for particular source configurations, we go the first step into equating bulk and boundary Euclidean partition functions, which we argue could provide a way of ultimately proving holographic complexity conjectures. At the same time, we want to stress that, although we related the circuit approach of complexity to the path integral optimization program, the question of the precise definition and meaning of complexity in QFTs is not yet answered. A starting point for achieving this goal could be provided by connecting our geometric gate counting to the Fubini-Study approach, which was complementarily developed within the circuit framework. Moreover, while our analyses were based on $2D$ CFTs, it would be a promising future direction to study also more general QFTs. A natural extension could be to consider for example $T\bar{T}$ deformed CFTs, for which the path integral optimization procedure was recently worked out. Eventually, this research direction could lead to a rigorous circuit interpretation of holographic complexity interpretations, which is directly originating from the QFT viewpoint.

Overall, our discussed topics in this thesis demonstrate that TNs are at the center of of an interdisciplinary and vibrant effort to understand fundamental physics, ranging from holography and quantum information to QFT and QS. We therefore hope that the presented ideas are of service to a broader community of particle, condensed matter and quantum information physicists, and can inspire them to new theoretical and experimental research studies.

A Demonstration of the Prony method in a holographic example

In chapter 4 we employ the Prony method on numerically calculated retarded thermal two-point functions from MPO simulations. The extracted singularity structure in the underlying (1+1)-dimensional QFT has an exact dual holographic interpretation as (2+1)-dimensional BH QNMs in the conformal (CFT) case. In this appendix, instead, we would like to demonstrate the applicability of our signal analysis method to a higher-dimensional holographic scenario as the point of departure, similar to the motivating discussion in section 4.3.

In particular, we consider the holographic model studied in [435]. [77] In this work, the authors analyze the time dependence of shear viscosity in the far from equilibrium initial stage of a HIC from a holographic perspective, resting on a Einstein–Maxwell model. In more detail, the following (3+1)-dimensional action is considered [78]

$$S = \int \mathrm{d}^4x\sqrt{-g}\left(\frac{1}{16\pi G_{\mathrm{N}}^{(4)}}(R+6) - \frac{1}{4}F^{mn}F_{mn}\right) + S_{matter}, \tag{A.1}$$

where the field strength tensor contains an Abelian gauge field. Using an asymptotic AdS spacetime ansatz and the general perturbation theory framework outlined in section 4.3, the authors calculate the time dependent profile of the spatial off-diagonal component $\langle T^{xy}\rangle(t)$ in the dual (2+1)-dimensional QFT. The nontrivial element is the realization of a rapid mass infall on a black brane, which is realized by the time-dependent matter action S_{matter}, and corresponds to an energy deposition on the QFT side. As a result, the system is driven out of equilibrium and (thermodynamic) quantities become time-dependent. Making use of the fact that $\langle T^{xy}\rangle$ is proportional to the correlator $G_R^{xy,xy}$ itself for a localized metric perturbation, this was then used in [435] to calculate the shear viscosity from Kubo's formula in Fourier space.

Here, we instead would like to analyze the function $\langle T^{xy}\rangle(t)$ in real-time with the Prony method. The profile of its absolute value is shown in Fig. A.1. The function exhibits decaying oscillations over many orders of magnitude. From the time $t = -1$ to $t = +1$, energy is deposited into the system. By that, the QNM frequencies become time-dependent, which is

[77] I thank Michael Florian Wondrak and Matthias Kaminski for discussions and provision of the numerical data.

[78] We refer to the original publication [435] for details.

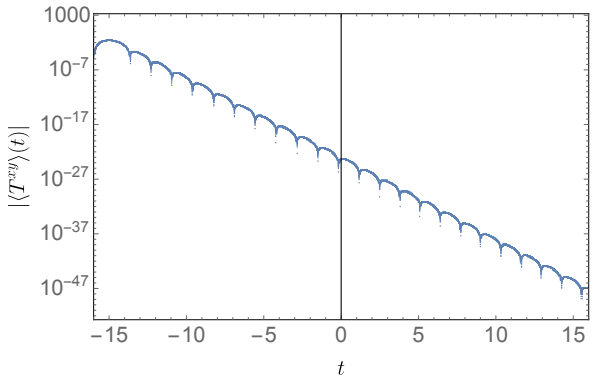

Figure A.1: Time dependence of the energy-momentum tensor component $|\langle T^{xy}\rangle(t)|$ in the holographic model of [435] (in arbitrary units). In the interval $-1 \leq t \leq 1$, the energy density is increased by 10 %, causing a change in the ring-down frequencies.

in great contrast to the MPO equilibrium calculations in chapter 4. We are interested in the question, whether our Prony signal analysis method is capable of identifying this feature. In the present case, the overall time interval $t = -16 \ldots 16$ is available, while the quench period is taking place only in a small time period. We therefore choose a time window $\Delta t = 6.4$ for the signal analysis, which is small enough to capture the pre-quench and post-quench regimes individually, and, on the other hand, large enough to provide a reliable signal identification in the complex frequency plane. The resulting Prony plot is shown in Fig. A.2. One can clearly identify the first three black brane QNMs in the lower half plane. For each level, there are slightly displaced modes identifiable. In particular, the green pole at the first level corresponds to the thermodynamic mode before the quench and the red one to its post-quench counterpart. A similar feature is visible for the higher order singularities of the retarded thermal correlator, albeit with less accuracy due to the faster decay.

To analyze the position of the first QNM ω_1 in more detail, we extract its time-dependent real and imaginary part in Fig. A.3 from the Prony analysis. The "jump" of the frequency towards larger real and lower imaginary values as an effect of the quench is visible. The pre and post-quench regimes are numerically extremely stable: The first QNM is modified from $\mathrm{Re}(\omega_1^{pre}) = 2.33012$ to $\mathrm{Re}(\omega_1^{post}) = 2.40534$ and $\mathrm{Im}(\omega_1^{pre}) = -3.35624$ to $\mathrm{Im}(\omega_1^{post}) = -3.46458$. The position of these values in the complex frequency plane is marked by circles in Fig. A.2. The real part agrees exactly with a simple numerical estimate of the time period from the zeros of the function $\langle T^{xy}\rangle(t)$. Obviously, the Prony method provides the advantage of giving additionally also access to the imaginary part of ω_1 and the values of higher order transient modes.

The time evolution in the quench period $-1 \leq t \leq 1$ can be identified less accurately with the Prony method. One reason is that due to the finite length of the time window, the frequencies cannot be matched with a unique time value. However, from Fig. A.3 it becomes visible that $t_{start} \approx t - 1$, i.e. the starting point of the Prony window agrees with the absolute time upon a

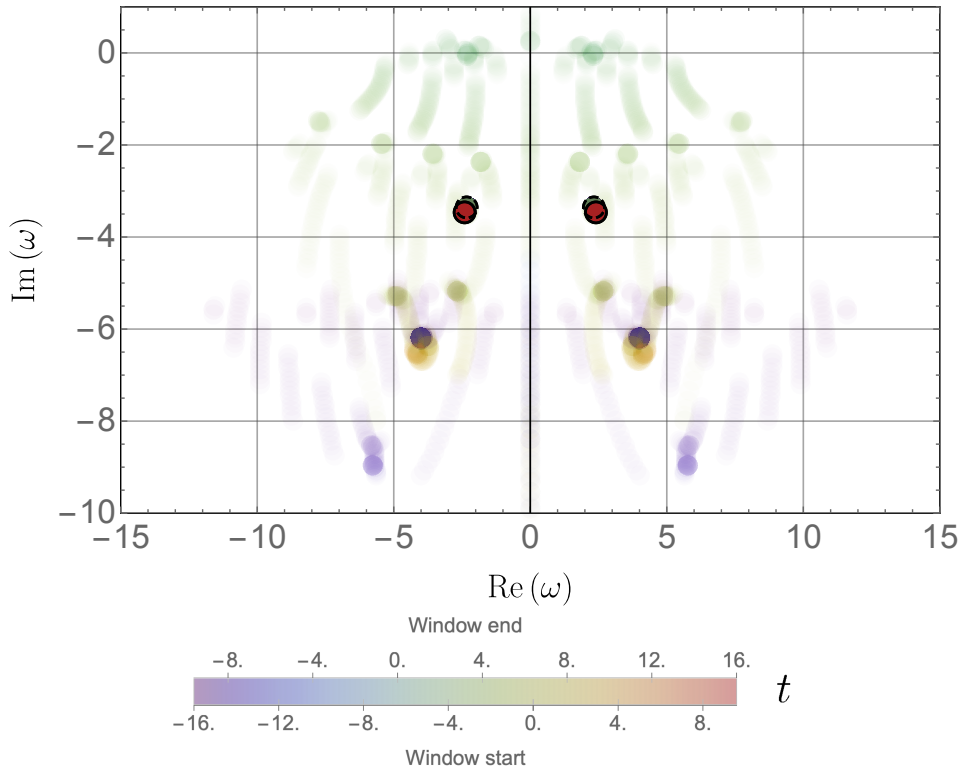

Figure A.2: Prony reconstruction of the energy-momentum tensor component $\langle T^{xy} \rangle(t)$ in the holographic model of [435] in the complex ω plane. Identified modes within a particular time window are shown as dots according to the colorbar. The dashed circle marks the first QNM ω_1 before the quench, the continuous circle after the quench period.

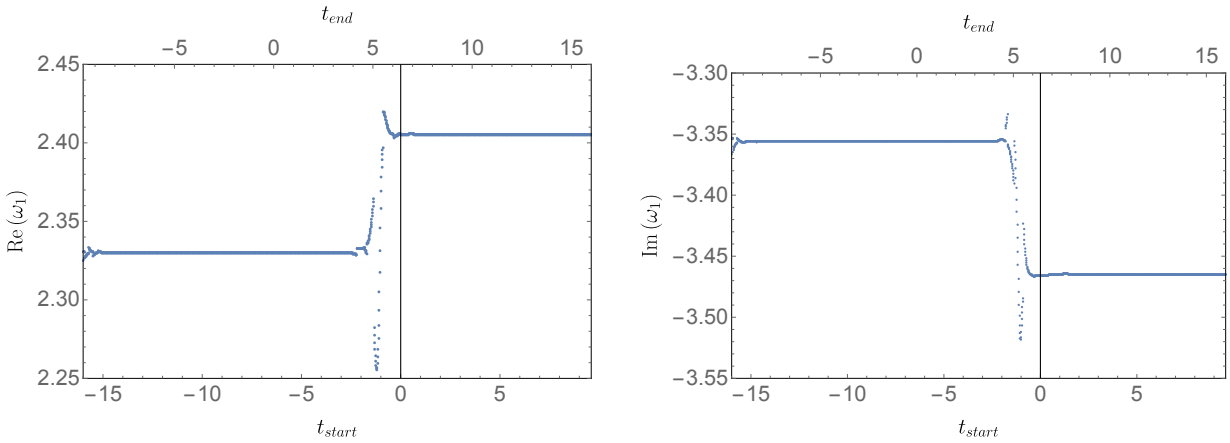

Figure A.3: Real (left) and imaginary (right) part of the first QNM ω_1 in dependence on the signal analysis window. The lower axis indicates the starting point of the Prony time window, the upper axis its endpoint.

small shift. The time-dependent frequencies in the short quench interval are overlapping with the pre and post-quench values in any Prony analysis window covering this period. This effect causes several spurious outliers in the identified frequencies. Numerically, the Prony method seems to favor the identification of the pre-quench mode with larger (negative) imaginary part, since it is less suppressed.

In summary, we have shown that our signal analysis technique provides reliable results even in nonequilibrium situations. Time dependent frequencies can be detected, at least for controlled quench protocols in which the pre and post-quench regimes are long enough to be seen individually.

B Acronyms

AdS	anti-de Sitter
BH	black hole
CFT	conformal field theory
cMERA	continuous multiscale entanglement renormalization ansatz
DMRG	density matrix renormalization group
ERB	Einstein–Rosen bridge
HIC	heavy-ion collision
IR	infra-red
iMPO	infinite matrix product operator
iMPS	infinite matrix product state
iTEBD	infinite time-evolving block decimation
LGT	lattice gauge theory
LR	long-range
MERA	multiscale entanglement renormalization ansatz
MPO	matrix product operator
MPS	matrix product state
NN	nearest-neighbor
obc	open boundary conditions
OPE	operator product expansion
pbc	periodic boundary conditions
PEPS	projected entangled pair states
QCD	quantum chromodynamics
QFT	quantum field theory
QGP	quark-gluon plasma
QMB	quantum many-body
QNM	quasinormal mode
QPM	quasiparticle model
QS	quantum simulation
RG	renormalization group
SUSY	supersymmetry
SVD	singular value decomposition

SYM	super Yang–Mills
TEBD	time-evolving block decimation
TFD	thermofield double
TN	tensor network
TNR	tensor network renormalization
TTN	tree tensor network
UV	ultraviolet
WDW	Wheeler–DeWitt

Bibliography

[1] M. C. Bañuls, M. P. Heller, K. Jansen, J. Knaute, and V. Svensson, *From spin chains to real-time thermal field theory using tensor networks,* Phys. Rev. Res. **2**, 033301 (2020), arXiv:1912.08836 [hep-th]

[2] J. Knaute and P. Hauke, *Relativistic meson spectra on ion-trap quantum simulators,* (2021), arXiv:2107.09071 [cond-mat.str-el]

[3] M. P. Heller, J. Knaute, S. Sing, and V. Svensson, *in preparation,*

[4] M. C. Bañuls, M. P. Heller, K. Jansen, J. Knaute, and V. Svensson, *in preparation,*

[5] H. A. Camargo, M. P. Heller, R. Jefferson, and J. Knaute, *Path Integral Optimization as Circuit Complexity,* Phys. Rev. Lett. **123**, 011601 (2019), arXiv:1904.02713 [hep-th]

[6] S. Banerjee, S. Choudhury, S. Chowdhury, J. Knaute, S. Panda, and K. Shirish, *Thermalization Phenomena in Quenched Quantum Brownian Motion in De Sitter Space,* (2021), arXiv:2104.10692 [hep-th]

[7] B. P. Abbott *et al.* (LIGO Scientific Collaboration and Virgo Collaboration), *Observation of gravitational waves from a binary black hole merger,* Phys. Rev. Lett. **116**, 061102 (2016), arXiv:1602.03837 [gr-qc]

[8] K. Akiyama *et al.* (Event Horizon Telescope), *First M87 Event Horizon Telescope Results. I. The Shadow of the Supermassive Black Hole,* Astrophys. J. Lett. **875**, L1 (2019), arXiv:1906.11238 [astro-ph.GA]

[9] F. Verstraete, V. Murg, and J. Cirac, *Matrix product states, projected entangled pair states, and variational renormalization group methods for quantum spin systems,* Advances in Physics **57**, 143 (2008), arXiv:0907.2796 [quant-ph]

[10] U. Schollwöck, *The density-matrix renormalization group in the age of matrix product states,* Annals of Physics **326**, 96 (2011), arXiv:1008.3477 [cond-mat]

[11] R. Orus, *A Practical Introduction to Tensor Networks: Matrix Product States and Projected Entangled Pair States,* Annals Phys. **349**, 117 (2014), arXiv:1306.2164 [cond-mat.str-el]

[12] J. Eisert, *Entanglement and tensor network states,* in *Autumn School on Correlated Electrons: Emergent Phenomena in Correlated Matter* (2013) arXiv:1308.3318 [quant-ph]

[13] J. C. Bridgeman and C. T. Chubb, *Hand-waving and Interpretive Dance: An Introductory Course on Tensor Networks,* J. Phys. A **50**, 223001 (2017), arXiv:1603.03039 [quant-ph]

[14] P. Silvi, F. Tschirsich, M. Gerster, J. Jünemann, D. Jaschke, M. Rizzi, and S. Montangero, *The Tensor Networks Anthology: Simulation techniques for many-body quantum lattice systems,* SciPost Phys. Lect. Notes **8**, 1 (2019), arXiv:1710.03733 [quant-ph]

[15] S. Montangero, *Introduction to Tensor Network Methods: Numerical simulations of low-dimensional many-body quantum systems* (Springer Nature, 2018)

[16] J. Biamonte, *Lectures on quantum tensor networks,* (2020), arXiv:1912.10049 [quant-ph]

[17] I. Cirac, D. Perez-Garcia, N. Schuch, and F. Verstraete, *Matrix Product States and Projected Entangled Pair States: Concepts, Symmetries, and Theorems,* (2020), arXiv:2011.12127 [quant-ph]

[18] K. Adcox *et al.* (PHENIX), *Formation of dense partonic matter in relativistic nucleus-nucleus collisions at RHIC: Experimental evaluation by the PHENIX collaboration,* Nucl. Phys. **A 757**, 184 (2005), arXiv:nucl-ex/0410003 [nucl-ex]

[19] J. Adams *et al.* (STAR), *Experimental and theoretical challenges in the search for the quark gluon plasma: The STAR Collaboration's critical assessment of the evidence from RHIC collisions,* Nucl. Phys. **A 757**, 102 (2005), arXiv:nucl-ex/0501009 [nucl-ex]

[20] B. B. Back *et al.*, *The PHOBOS perspective on discoveries at RHIC,* Nucl. Phys. **A 757**, 28 (2005), arXiv:nucl-ex/0410022 [nucl-ex]

[21] I. Arsene *et al.* (BRAHMS), *Quark-gluon plasma and color glass condensate at RHIC? The Perspective from the BRAHMS experiment,* Nucl. Phys. **A 757**, 1 (2005), arXiv:nucl-ex/0410020 [nucl-ex]

[22] L. Adamczyk *et al.* (STAR), *Global Λ hyperon polarization in nuclear collisions,* Nature **548**, 62 (2017), arXiv:1701.06657 [nucl-ex]

[23] G. 't Hooft, *Dimensional Reduction in Quantum Gravity,* in *Salamfestschrift* (1993) pp. 284–296, arXiv:gr-qc/9310026 [gr-qc]

[24] L. Susskind, *The world as a hologram,* J. Math. Phys. **36**, 6377 (1995), arXiv:hep-th/9409089 [hep-th]

[25] J. M. Maldacena, *The Large N limit of superconformal field theories and supergravity,* Int. J. Theor. Phys. **38**, 1113 (1999), [Adv. Theor. Math. Phys.2,231(1998)], arXiv:hep-th/9711200 [hep-th]

[26] S. S. Gubser, I. R. Klebanov, and A. M. Polyakov, *Gauge theory correlators from noncritical string theory,* Phys. Lett. **B428**, 105 (1998), arXiv:hep-th/9802109 [hep-th]

[27] E. Witten, *Anti-de Sitter space and holography,* Adv. Theor. Math. Phys. **2**, 253 (1998), arXiv:hep-th/9802150 [hep-th]

[28] M. Ammon and J. Erdmenger, *Gauge/gravity duality* (Cambridge University Press, Cambridge, 2015)

[29] H. Nastase, *Introduction to the AdS/CFT Correspondence* (Cambridge University Press, 2015)

[30] J. Casalderrey-Solana, H. Liu, D. Mateos, K. Rajagopal, and U. A. Wiedemann, *Gauge/String Duality, Hot QCD and Heavy Ion Collisions* (Cambridge University Press, 2014)

[31] P. Kovtun, D. T. Son, and A. O. Starinets, *Viscosity in Strongly Interacting Quantum Field Theories from Black Hole Physics,* Phys. Rev. Lett. **94**, 111601 (2005), arXiv:hep-th/0405231 [hep-th]

[32] W. Florkowski, M. P. Heller, and M. Spalinski, *New theories of relativistic hydrodynamics in the LHC era,* Rept. Prog. Phys. **81**, 046001 (2018), arXiv:1707.02282 [hep-ph]

[33] J. Berges, M. P. Heller, A. Mazeliauskas, and R. Venugopalan, *Thermalization in QCD: theoretical approaches, phenomenological applications, and interdisciplinary connections,* (2020), arXiv:2005.12299 [hep-th]

[34] B. Chen, B. Czech, and Z.-z. Wang, *Quantum Information in Holographic Duality,* (2021), arXiv:2108.09188 [hep-th]

[35] S. Ryu and T. Takayanagi, *Holographic Derivation of Entanglement Entropy from the anti-de Sitter Space/Conformal Field Theory Correspondence,* Phys. Rev. Lett. **96**, 181602 (2006), arXiv:hep-th/0603001 [hep-th]

[36] S. Ryu and T. Takayanagi, *Aspects of holographic entanglement entropy,* JHEP **08**, 045 (2006), arXiv:hep-th/0605073 [hep-th]

[37] L. Susskind, *Three Lectures on Complexity and Black Holes,* (Springer, 2018) arXiv:1810.11563 [hep-th]

[38] L. Susskind, *Entanglement is not enough,* Fortsch. Phys. **64**, 49 (2016), arXiv:1411.0690 [hep-th]

[39] A. R. Brown, D. A. Roberts, L. Susskind, B. Swingle, and Y. Zhao, *Holographic Complexity Equals Bulk Action?* Phys. Rev. Lett. **116**, 191301 (2016), arXiv:1509.07876 [hep-th]

[40] M. C. Bañuls *et al.*, *Simulating Lattice Gauge Theories within Quantum Technologies,* Eur. Phys. J. D **74**, 165 (2020), arXiv:1911.00003 [quant-ph]

[41] G. Magnifico, T. Felser, P. Silvi, and S. Montangero, *Lattice Quantum Electrodynamics in (3+1)-dimensions at finite density with Tensor Networks,* (2020), arXiv:2011.10658 [hep-lat]

[42] G. Vidal, *Class of quantum many-body states that can be efficiently simulated,* Phys. Rev. Lett. **101**, 110501 (2008), arXiv:quant-ph/0610099 [quant-ph]

[43] G. Evenbly and S. R. White, *Entanglement renormalization and wavelets,* Phys. Rev. Lett. **116**, 140403 (2016), arXiv:1602.01166 [cond-mat.str-el]

[44] R. P. Feynman, *Simulating physics with computers,* Int. J. Theor. Phys. **21**, 467 (1982)

[45] R. Jefferson and R. C. Myers, *Circuit complexity in quantum field theory,* JHEP **10**, 107 (2017), arXiv:1707.08570 [hep-th]

[46] S. Chapman, M. P. Heller, H. Marrochio, and F. Pastawski, *Toward a Definition of Complexity for Quantum Field Theory States,* Phys. Rev. Lett. **120**, 121602 (2018), arXiv:1707.08582 [hep-th]

[47] G. 't Hooft, *A planar diagram theory for strong interactions,* Nucl. Phys. **B 72**, 461 (1974)

[48] J. D. Bekenstein, *Black Holes and Entropy,* Phys. Rev. **D 7**, 2333 (1973)

[49] M. Natsuume, *AdS/CFT Duality User Guide,* Lect. Notes Phys. **903**, 1 (2015), arXiv:1409.3575 [hep-th]

[50] E. Papantonopoulos, *From Gravity to Thermal Gauge Theories: The AdS/CFT Correspondence,* Lect. Notes Phys. **828**, 1 (2011)

[51] J. Knaute, *Holographic QCD Phase Diagram and Entanglement Entropy*, Master thesis, Technische Universität Dresden (2017), `https://www.hzdr.de/db/Cms?pOid=55128`

[52] S. Coleman and J. Mandula, *All possible symmetries of the s matrix,* Phys. Rev. **159**, 1251 (1967)

[53] K. Becker, M. Becker, and J. Schwarz, *String Theory and M-Theory: A Modern Introduction* (Cambridge University Press, 2007)

[54] P. Di Francesco, P. Mathieu, and D. Senechal, *Conformal Field Theory*, Graduate Texts in Contemporary Physics (Springer-Verlag, New York, 1997)

[55] E. D'Hoker and D. Z. Freedman, *Supersymmetric Gauge Theories and the AdS/CFT Correspondence,* (2002), arXiv:hep-th/0201253 [hep-th]

[56] J. Polchinski, *String theory. Vol. 1: An introduction to the bosonic string* (Cambridge University Press, 2005)

[57] J. Polchinski, *String theory. Vol. 2: Superstring theory and beyond* (Cambridge University Press, 2005)

[58] J. Polchinski, *Dirichlet Branes and Ramond-Ramond Charges,* Phys. Rev. Lett. **75**, 4724 (1995), arXiv:hep-th/9510017 [hep-th]

[59] O. Aharony, S. S. Gubser, J. M. Maldacena, H. Ooguri, and Y. Oz, *Large N field theories, string theory and gravity,* Phys. Rept. **323**, 183 (2000), arXiv:hep-th/9905111 [hep-th]

[60] D. T. Son and A. O. Starinets, *Minkowski space correlators in AdS / CFT correspondence: Recipe and applications,* JHEP **09**, 042 (2002), arXiv:hep-th/0205051

[61] K. Skenderis and B. C. van Rees, *Real-time gauge/gravity duality,* Phys. Rev. Lett. **101**, 081601 (2008), arXiv:0805.0150 [hep-th]

[62] M. Rangamani and T. Takayanagi, *Holographic Entanglement Entropy,* Lect. Notes Phys. **931**, 1 (2017), arXiv:1609.01287 [hep-th]

[63] V. E. Hubeny, M. Rangamani, and T. Takayanagi, *A covariant holographic entanglement entropy proposal,* JHEP **07**, 062 (2007), arXiv:0705.0016 [hep-th]

[64] X. Dong, A. Lewkowycz, and M. Rangamani, *Deriving covariant holographic entanglement,* JHEP **11**, 028 (2016), arXiv:1607.07506 [hep-th]

[65] M. Van Raamsdonk, *Building up spacetime with quantum entanglement,* Gen. Rel. Grav. **42**, 2323 (2010), [Int. J. Mod. Phys. D 19, 2429 (2010)], arXiv:1005.3035 [hep-th]

[66] B. Swingle and M. Van Raamsdonk, *Universality of Gravity from Entanglement,* (2014), arXiv:1405.2933 [hep-th]

[67] M. Van Raamsdonk, *Spacetime from bits,* Science **370**, 198 (2020)

[68] M. Miyaji and T. Takayanagi, *Surface/State Correspondence as a Generalized Holography,* PTEP **2015**, 073B03 (2015), arXiv:1503.03542 [hep-th]

[69] T. Takayanagi and K. Umemoto, *Entanglement of purification through holographic duality,* Nature Phys. **14**, 573 (2018), arXiv:1708.09393 [hep-th]

[70] P. Nguyen, T. Devakul, M. G. Halbasch, M. P. Zaletel, and B. Swingle, *Entanglement of purification: from spin chains to holography,* JHEP **01**, 098 (2018), arXiv:1709.07424 [hep-th]

[71] Y. Nakata, T. Takayanagi, Y. Taki, K. Tamaoka, and Z. Wei, *New holographic generalization of entanglement entropy,* Phys. Rev. D **103**, 026005 (2021), arXiv:2005.13801 [hep-th]

[72] M. Gerbershagen, *Illuminating entanglement shadows of BTZ black holes by a generalized entanglement measure,* (2021), arXiv:2105.01097 [hep-th]

[73] L. Susskind, *Computational Complexity and Black Hole Horizons,* Fortsch. Phys. **64**, 44 (2016), [Fortsch. Phys.64,24(2016)], arXiv:1403.5695 [hep-th]

[74] D. Stanford and L. Susskind, *Complexity and Shock Wave Geometries,* Phys. Rev. **D90**, 126007 (2014), arXiv:1406.2678 [hep-th]

[75] A. R. Brown, D. A. Roberts, L. Susskind, B. Swingle, and Y. Zhao, *Complexity, action, and black holes,* Phys. Rev. **D93**, 086006 (2016), arXiv:1512.04993 [hep-th]

[76] S. R. White, *Density matrix formulation for quantum renormalization groups,* Phys. Rev. Lett. **69**, 2863 (1992)

[77] J. Eisert, M. Cramer, and M. B. Plenio, *Area laws for the entanglement entropy - a review,* Rev. Mod. Phys. **82**, 277 (2010), arXiv:0808.3773 [quant-ph]

[78] E. H. Lieb and D. W. Robinson, *The finite group velocity of quantum spin systems,* Commun. Math. Phys. **28**, 251 (1972)

[79] M. B. Hastings, *An area law for one-dimensional quantum systems,* J. Stat. Mech. **0708**, P08024 (2007), arXiv:0705.2024 [quant-ph]

[80] P. Calabrese and J. L. Cardy, *Entanglement entropy and quantum field theory,* J. Stat. Mech. **0406**, P06002 (2004), arXiv:hep-th/0405152

[81] M. M. Wolf, F. Verstraete, M. B. Hastings, and J. I. Cirac, *Area Laws in Quantum Systems: Mutual Information and Correlations,* Phys. Rev. Lett. **100**, 070502 (2008), arXiv:0704.3906 [quant-ph]

[82] T. Nishioka, S. Ryu, and T. Takayanagi, *Holographic entanglement entropy: an overview,* J. Phys. **A 42**, 504008 (2009), arXiv:0905.0932 [hep-th]

[83] T. Faulkner, A. Lewkowycz, and J. Maldacena, *Quantum corrections to holographic entanglement entropy,* JHEP **11**, 074 (2013), arXiv:1307.2892 [hep-th]

[84] L. MIRSKY, *SYMMETRIC GAUGE FUNCTIONS AND UNITARILY INVARIANT NORMS,* The Quarterly Journal of Mathematics **11**, 50 (1960), https://academic.oup.com/qjmath/article-pdf/11/1/50/7295335/11-1-50.pdf

[85] `https://github.com/jknaute/TNsimulations`

[86] G. Vidal, *Efficient classical simulation of slightly entangled quantum computations,* Phys. Rev. Lett. **91**, 147902 (2003), arXiv:quant-ph/0301063

[87] G. Vidal, *Efficient simulation of one-dimensional quantum many-body systems,* Phys. Rev. Lett. **93**, 040502 (2004), arXiv:quant-ph/0310089

[88] N. Hatano and M. Suzuki, *Finding Exponential Product Formulas of Higher Orders,* Lect. Notes Phys. **679**, 37 (2005), arXiv:math-ph/0506007

[89] L. Tagliacozzo, T. R. de Oliveira, S. Iblisdir, and J. I. Latorre, *Scaling of entanglement support for Matrix Product States,* Phys. Rev. B **78**, 024410 (2008), arXiv:0712.1976 [cond-mat.stat-mech]

[90] F. Pollmann, S. Mukerjee, A. M. Turner, and J. E. Moore, *Theory of finite-entanglement scaling at one-dimensional quantum critical points,* Phys. Rev. Lett. **102**, 255701 (2009), arXiv:0812.2903 [cond-mat.str-el]

[91] G. Vidal, *Classical simulation of infinite-size quantum lattice systems in one spatial dimension,* Phys. Rev. Lett. **98**, 070201 (2007), arXiv:cond-mat/0605597

[92] R. Orús and G. Vidal, *Infinite time-evolving block decimation algorithm beyond unitary evolution,* Phys. Rev. B **78**, 155117 (2008), arXiv:0711.3960 [cond-mat.stat-mech]

[93] K. G. Wilson, *The renormalization group: Critical phenomena and the kondo problem,* Rev. Mod. Phys. **47**, 773 (1975)

[94] L. P. Kadanoff, *Scaling laws for Ising models near T(c),* Physics Physique Fizika **2**, 263 (1966)

[95] G. Vidal, *Entanglement Renormalization,* Phys. Rev. Lett. **99**, 220405 (2007), arXiv:cond-mat/0512165 [cond-mat]

[96] G. Evenbly and G. Vidal, *Algorithms for entanglement renormalization,* Phys. Rev. B **79**, 144108 (2009), arXiv:0707.1454 [cond-mat.str-el]

[97] G. Evenbly and G. Vidal, *Quantum criticality with the multi-scale entanglement renormalization ansatz,* (2013), arXiv:1109.5334 [quant-ph]

[98] G. Evenbly and G. Vidal, *Algorithms for entanglement renormalization: Boundaries, impurities and interfaces,* Journal of Statistical Physics **157**, 931–978 (2014), arXiv:1312.0303 [quant-ph]

[99] G. Evenbly and G. Vidal, *Tensor network renormalization,* Physical Review Letters **115** (2015), 10.1103/physrevlett.115.180405, arXiv:1412.0732 [cond-mat.str-el]

[100] G. Evenbly and G. Vidal, *Tensor network renormalization yields the multiscale entanglement renormalization ansatz,* Physical Review Letters **115** (2015), 10.1103/physrevlett.115.200401, arXiv:1502.05385 [cond-mat.str-el]

[101] G. Evenbly and G. Vidal, *Entanglement renormalization in two spatial dimensions,* Physical Review Letters **102** (2009), 10.1103/physrevlett.102.180406, arXiv:0811.0879 [cond-mat.str-el]

[102] A. Jahn and J. Eisert, *Holographic tensor network models and quantum error correction: A topical review,* (2021), arXiv:2102.02619 [quant-ph]

[103] B. Swingle, *Entanglement Renormalization and Holography,* Phys. Rev. **D86**, 065007 (2012), arXiv:0905.1317 [cond-mat.str-el]

[104] B. Swingle, *Constructing holographic spacetimes using entanglement renormalization,* (2012), arXiv:1209.3304 [hep-th]

[105] N. Bao, C. Cao, S. M. Carroll, A. Chatwin-Davies, N. Hunter-Jones, J. Pollack, and G. N. Remmen, *Consistency conditions for an AdS multiscale entanglement renormalization ansatz correspondence,* Phys. Rev. D **91**, 125036 (2015), arXiv:1504.06632 [hep-th]

[106] A. Milsted and G. Vidal, *Tensor networks as path integral geometry,* (2018), arXiv:1807.02501 [cond-mat.str-el]

[107] A. Milsted and G. Vidal, *Geometric interpretation of the multi-scale entanglement renormalization ansatz,* (2018), arXiv:1812.00529 [hep-th]

[108] N. Bao, G. Penington, J. Sorce, and A. C. Wall, *Holographic Tensor Networks in Full AdS/CFT,* (2019), arXiv:1902.10157 [hep-th]

[109] P. Caputa, J. Kruthoff, and O. Parrikar, *Building Tensor Networks for Holographic States,* (2020), arXiv:2012.05247 [hep-th]

[110] L. Niermann and T. J. Osborne, *Holographic networks for (1+1)-dimensional de Sitter spacetime,* (2021), arXiv:2102.09223 [hep-th]

[111] S. S. Gubser, J. Knaute, S. Parikh, A. Samberg, and P. Witaszczyk, *p-adic AdS/CFT,* Commun. Math. Phys. **352**, 1019 (2017), arXiv:1605.01061 [hep-th]

[112] L.-Y. Hung, W. Li, and C. M. Melby-Thompson, *p-adic CFT is a holographic tensor network,* JHEP **04**, 170 (2019), arXiv:1902.01411 [hep-th]

[113] A. Bhattacharyya, L.-Y. Hung, Y. Lei, and W. Li, *Tensor network and (p-adic) AdS/CFT,* JHEP **01**, 139 (2018), arXiv:1703.05445 [hep-th]

[114] L. Chen, X. Liu, and L.-Y. Hung, *Emergent Einstein Equation in p-adic CFT Tensor Networks,* (2021), arXiv:2102.12022 [hep-th]

[115] L. Chen, X. Liu, and L.-Y. Hung, *Bending the Bruhat-Tits Tree I:Tensor Network and Emergent Einstein Equations,* (2021), arXiv:2102.12023 [hep-th]

[116] M. Miyaji, T. Takayanagi, and K. Watanabe, *From path integrals to tensor networks for the AdS/CFT correspondence,* Phys. Rev. D **95**, 066004 (2017), arXiv:1609.04645 [hep-th]

[117] P. Caputa, N. Kundu, M. Miyaji, T. Takayanagi, and K. Watanabe, *Anti-de Sitter Space from Optimization of Path Integrals in Conformal Field Theories,* Phys. Rev. Lett. **119**, 071602 (2017), arXiv:1703.00456 [hep-th]

[118] P. Caputa, N. Kundu, M. Miyaji, T. Takayanagi, and K. Watanabe, *Liouville Action as Path-Integral Complexity: From Continuous Tensor Networks to AdS/CFT,* JHEP **11**, 097 (2017), arXiv:1706.07056 [hep-th]

[119] GQFI group at AEI Potsdam, *What is complexity in particle physics?* `https://www.aei.mpg.de/120719/what-is-complexity-in-particle-physics` (2019)

[120] J. Haegeman, T. J. Osborne, H. Verschelde, and F. Verstraete, *Entanglement Renormalization for Quantum Fields in Real Space,* Phys. Rev. Lett. **110**, 100402 (2013), arXiv:1102.5524 [hep-th]

[121] B. Czech, *Einstein Equations from Varying Complexity,* Phys. Rev. Lett. **120**, 031601 (2018), arXiv:1706.00965 [hep-th]

[122] W. Busza, K. Rajagopal, and W. van der Schee, *Heavy Ion Collisions: The Big Picture, and the Big Questions,* Ann. Rev. Nucl. Part. Sci. **68**, 339 (2018), arXiv:1802.04801 [hep-ph]

[123] R. Nandkishore and D. A. Huse, *Many body localization and thermalization in quantum statistical mechanics,* Ann. Rev. Condensed Matter Phys. **6**, 15 (2015), arXiv:1404.0686 [cond-mat.stat-mech]

[124] J. Eisert, M. Friesdorf, and C. Gogolin, *Quantum many-body systems out of equilibrium,* Nature Physics **11**, 124 (2015), arXiv:1408.5148 [quant-ph]

[125] C. Gogolin and J. Eisert, *Equilibration, thermalisation, and the emergence of statistical mechanics in closed quantum systems,* Rept. Prog. Phys. **79**, 056001 (2016), arXiv:1503.07538 [quant-ph]

[126] L. D'Alessio, Y. Kafri, A. Polkovnikov, and M. Rigol, *From quantum chaos and eigenstate thermalization to statistical mechanics and thermodynamics,* Adv. Phys. **65**, 239 (2016), arXiv:1509.06411 [cond-mat.stat-mech]

[127] H. Wilming, T. R. de Oliveira, A. J. Short, and J. Eisert, *Equilibration times in closed quantum many-body systems,* Thermodynamics in the Quantum Regime , 435–455 (2018)

[128] D. A. Abanin, E. Altman, I. Bloch, and M. Serbyn, *Colloquium: Many-body localization, thermalization, and entanglement,* Rev. Mod. Phys. **91**, 021001 (2019), arXiv:1804.11065 [cond-mat.dis-nn]

[129] S. Sachdev, *Quantum Phase Transitions*, 2nd ed. (Cambridge University Press, 2011)

[130] M. Fagotti and F. H. L. Essler, *Reduced density matrix after a quantum quench,* Phys. Rev. B **87**, 245107 (2013), arXiv:1302.6944 [cond-mat.stat-mech]

[131] P. Sabella-Garnier, K. Schalm, T. Vakhtel, and J. Zaanen, *Thermalization/Relaxation in integrable and free field theories: an Operator Thermalization Hypothesis,* (2019), arXiv:1906.02597 [cond-mat.stat-mech]

[132] M. C. Bañuls, K. Cichy, J. I. Cirac, K. Jansen, and S. Kühn, *Tensor Networks and their use for Lattice Gauge Theories,* in *The 36th Annual International Symposium on Lattice Field Theory. 22-28 July* (2018) p. 22, arXiv:1810.12838 [hep-lat]

[133] M. C. Bañuls and K. Cichy, *Review on novel methods for lattice gauge theories,* (2019), arXiv:1910.00257 [hep-lat]

[134] M. C. Bañuls, R. Blatt, J. Catani, A. Celi, J. I. Cirac, M. Dalmonte, L. Fallani, K. Jansen, M. Lewenstein, S. Montangero, C. A. Muschik, B. Reznik, E. Rico, L. Tagliacozzo, K. V. Acoleyen, F. Verstraete, U. J. Wiese, M. Wingate, J. Zakrzewski, and P. Zoller, *Simulating lattice gauge theories within quantum technologies,* (2019), arXiv:1911.00003 [quant-ph]

[135] Y. Shimizu and Y. Kuramashi, *Grassmann tensor renormalization group approach to one-flavor lattice schwinger model,* Phys. Rev. D **90**, 014508 (2014)

[136] Y. Shimizu and Y. Kuramashi, *Critical behavior of the lattice schwinger model with a topological term at $\theta = \pi$ using the grassmann tensor renormalization group,* Phys. Rev. D **90**, 074503 (2014)

[137] E. Rico, T. Pichler, M. Dalmonte, P. Zoller, and S. Montangero, *Tensor networks for lattice gauge theories and atomic quantum simulation,* Phys. Rev. Lett. **112**, 201601 (2014)

[138] T. Pichler, M. Dalmonte, E. Rico, P. Zoller, and S. Montangero, *Real-time dynamics in U(1) lattice gauge theories with tensor networks,* Phys. Rev. X **6**, 011023 (2016)

[139] K. Yagi, T. Hatsuda, and Y. Miake, *Quark-Gluon Plasma: From Big Bang to Little Bang,* Camb. Monogr. Part. Phys. Nucl. Phys. Cosmol. **23** (2005)

[140] C. Patrignani *et al.* (Particle Data Group), *Review of Particle Physics,* Chin. Phys. **C 40**, 100001 (2016)

[141] Y. Aoki, G. Endrodi, Z. Fodor, S. D. Katz, and K. K. Szabo, *The order of the quantum chromodynamics transition predicted by the standard model of particle physics,* Nature **443**, 675 (2006), arXiv:hep-lat/0611014 [hep-lat]

[142] S. Borsanyi, Z. Fodor, C. Hoelbling, S. D. Katz, S. Krieg, and K. K. Szabo, *Full result for the QCD equation of state with 2+1 flavors,* Phys. Lett. **B 730**, 99 (2014), arXiv:1309.5258 [hep-lat]

[143] A. Bazavov *et al.* (HotQCD), *Equation of state in (2+1)-flavor QCD,* Phys. Rev. **D 90**, 094503 (2014), arXiv:1407.6387 [hep-lat]

[144] Y.-J. Lee, A. Yoon, and W. Busza, `https://web.mit.edu/mithig/movies/LHCanmation.mov`

[145] M. Rigobello, S. Notarnicola, G. Magnifico, and S. Montangero, *Entanglement generation in QED scattering processes,* (2021), arXiv:2105.03445 [hep-lat]

[146] P. M. Chesler and L. G. Yaffe, *Boost invariant flow, black hole formation, and far-from-equilibrium dynamics in N = 4 supersymmetric Yang-Mills theory,* Phys. Rev. **D82**, 026006 (2010), arXiv:0906.4426 [hep-th]

[147] M. P. Heller, R. A. Janik, and P. Witaszczyk, *Characteristics of Thermalization of Boost-Invariant Plasma from Holography,* Phys. Rev. Lett. **108**, 201602 (2012), arXiv:1103.3452 [hep-th]

[148] M. Attems, J. Casalderrey-Solana, D. Mateos, D. Santos-Oliván, C. F. Sopuerta, M. Triana, and M. Zilhão, *Paths to equilibrium in non-conformal collisions,* JHEP **06**, 154 (2017), arXiv:1703.09681 [hep-th]

[149] P. Romatschke, *Far From Equilibrium Fluid Dynamics,* (2017), arXiv:1704.08699 [hep-th]

[150] R. Critelli, R. Rougemont, and J. Noronha, *Homogeneous isotropization and equilibration of a strongly coupled plasma with a critical point,* (2017), arXiv:1709.03131 [hep-th]

[151] B. Friman, C. Hohne, J. Knoll, S. Leupold, J. Randrup, R. Rapp, and P. Senger, *The CBM Physics Book: Compressed Baryonic Matter in Laboratory Experiments,* Lect. Notes Phys. **814**, 1 (2011)

[152] D. H. Rischke, *The quark-gluon plasma in equilibrium,* Prog. Part. Nucl. Phys. **52**, 197 (2004), arXiv:nucl-th/0305030 [nucl-th]

[153] H.-T. Ding, F. Karsch, and S. Mukherjee, *Thermodynamics of strong-interaction matter from lattice QCD,* Int. J. Mod. Phys. **E 24**, 1530007 (2015), arXiv:1504.05274 [hep-lat]

[154] P. Braun-Munzinger, V. Koch, T. Schäfer, and J. Stachel, *Properties of hot and dense matter from relativistic heavy ion collisions,* Phys. Rept. **621**, 76 (2016), arXiv:1510.00442 [nucl-th]

[155] J. Knaute, R. Yaresko, and B. Kämpfer, *Holographic QCD phase diagram with critical point from Einstein-Maxwell-dilaton dynamics,* Phys. Lett. **B 778**, 419 (2018), arXiv:1702.06731 [hep-ph]

[156] R. Critelli, J. Noronha, J. Noronha-Hostler, I. Portillo, C. Ratti, and R. Rougemont, *Critical point in the phase diagram of primordial quark-gluon matter from black hole physics,* Phys. Rev. **D 96**, 096026 (2017), arXiv:1706.00455 [nucl-th]

[157] J. Jensen and A. Mackintosh, *Rare Earth Magnetism: Structures and Excitations*, International Series of Monographs on Physics (Clarendon Press, 1991)

[158] E. Berti, V. Cardoso, and A. O. Starinets, *Quasinormal modes of black holes and black branes,* Class. Quant. Grav. **26**, 163001 (2009), arXiv:0905.2975 [gr-qc]

[159] P. K. Kovtun and A. O. Starinets, *Quasinormal modes and holography,* Phys. Rev. D **72**, 086009 (2005), arXiv:hep-th/0506184

[160] S. Grozdanov, N. Kaplis, and A. O. Starinets, *From strong to weak coupling in holographic models of thermalization,* JHEP **07**, 151 (2016), arXiv:1605.02173 [hep-th]

[161] S. A. Hartnoll, A. Lucas, and S. Sachdev, *Holographic quantum matter,* (2016), arXiv:1612.07324 [hep-th]

[162] A. Buchel, M. P. Heller, and R. C. Myers, *Equilibration rates in a strongly coupled nonconformal quark-gluon plasma,* Phys. Rev. Lett. **114**, 251601 (2015), arXiv:1503.07114 [hep-th]

[163] D. Birmingham, I. Sachs, and S. N. Solodukhin, *Conformal field theory interpretation of black hole quasinormal modes,* Phys. Rev. Lett. **88**, 151301 (2002), arXiv:hep-th/0112055 [hep-th]

[164] A. Buchel, R. C. Myers, and A. Sinha, *Beyond $\eta/s = 1/4\pi$,* JHEP **03**, 084 (2009), arXiv:0812.2521 [hep-th]

[165] P. B. Arnold, G. D. Moore, and L. G. Yaffe, *Effective kinetic theory for high temperature gauge theories,* JHEP **01**, 030 (2003), arXiv:hep-ph/0209353

[166] P. Romatschke, *Retarded correlators in kinetic theory: branch cuts, poles and hydrodynamic onset transitions,* Eur. Phys. J. **C76**, 352 (2016), arXiv:1512.02641 [hep-th]

[167] A. Kurkela and U. A. Wiedemann, *Analytic structure of nonhydrodynamic modes in kinetic theory,* Eur. Phys. J. **C79**, 776 (2019), arXiv:1712.04376 [hep-ph]

[168] P. Romatschke, *Azimuthal Anisotropies at High Momentum from Purely Non-Hydrodynamic Transport,* Eur. Phys. J. C **78**, 636 (2018), arXiv:1802.06804 [nucl-th]

[169] D. Tong, *Kinetic Theory,* `https://www.damtp.cam.ac.uk/user/tong/kinetic.html` (2012), University of Cambridge Graduate Course

[170] E. Ising, *Beitrag zur Theorie des Ferromagnetismus,* Zeitschrift für Physik **31**, 253 (1925)

[171] S. Suzuki, J.-i. Inoue, and B. K. Chakrabarti, eds., *Quantum Ising Phases and Transitions in Transverse Ising Models*, Lecture Notes in Physics, Vol. 862 (Springer Verlag, Berlin, 2013)

[172] L. Onsager, *Crystal statistics. 1. A Two-dimensional model with an order disorder transition,* Phys. Rev. **65**, 117 (1944)

[173] P. Pfeuty, *The one-dimensional ising model with a transverse field,* Annals of Physics **57**, 79 (1970)

[174] P. Molignini, *Analyzing the two dimensional Ising model with conformal field theory,* `https://edu.itp.phys.ethz.ch/fs13/cft/SM2_Molignini.pdf` (2013)

[175] P. Jordan and E. P. Wigner, *About the Pauli exclusion principle,* Z. Phys. **47**, 631 (1928)

[176] T. Rakovszky, M. Mestyán, M. Collura, M. Kormos, and G. Takács, *Hamiltonian truncation approach to quenches in the Ising field theory,* Nucl. Phys. **B911**, 805 (2016), arXiv:1607.01068 [cond-mat.stat-mech]

[177] K. Hódsági, M. Kormos, and G. Takács, *Quench dynamics of the Ising field theory in a magnetic field,* SciPost Phys. **5**, 027 (2018), arXiv:1803.01158 [cond-mat.stat-mech]

[178] A. B. Zamolodchikov, *Integrals of Motion and S-Matrix of the (Scaled) $T=T_c$ Ising Model with Magnetic Field,* Int. J. Mod. Phys. **A4**, 4235 (1989)

[179] G. Delfino, P. Grinza, and G. Mussardo, *Decay of particles above threshold in the Ising field theory with magnetic field,* arXiv (2005), 10.1016/j.nuclphysb.2005.12.024, hep-th/0507133

[180] P. Fonseca and A. Zamolodchikov, *Ising spectroscopy. I. Mesons at $T < T_c$,* (2006), arXiv:hep-th/0612304 [hep-th]

[181] A. Zamolodchikov, *Ising Spectroscopy II: Particles and poles at $T > T_c$,* (2013), arXiv:1310.4821 [hep-th]

[182] B. M. McCoy and T. T. Wu, *Two-dimensional Ising Field Theory in a Magnetic Field: Breakup of the Cut in the Two Point Function,* Phys. Rev. D **18**, 1259 (1978)

[183] T. Matsubara, *A New Approach to Quantum-Statistical Mechanics,* Prog. Theor. Phys. **14**, 351 (1955)

[184] M. Banados, C. Teitelboim, and J. Zanelli, *The Black hole in three-dimensional space-time,* Phys. Rev. Lett. **69**, 1849 (1992), arXiv:hep-th/9204099

[185] T. Barthel, U. Schollwöck, and S. R. White, *Spectral functions in one-dimensional quantum systems at finite temperature using the density matrix renormalization group,* Phys. Rev. B **79**, 245101 (2009)

[186] A. E. Feiguin and G. A. Fiete, *Spectral properties of a spin-incoherent luttinger liquid,* Phys. Rev. B **81**, 075108 (2010)

[187] C. Karrasch, J. H. Bardarson, and J. E. Moore, *Finite-temperature dynamical density matrix renormalization group and the drude weight of spin-*1/2 *chains,* Phys. Rev. Lett. **108**, 227206 (2012)

[188] T. Barthel, *Precise evaluation of thermal response functions by optimized density matrix renormalization group schemes,* New Journal of Physics **15**, 073010 (2013)

[189] F. Verstraete, J. J. García-Ripoll, and J. I. Cirac, *Matrix product density operators: Simulation of finite-temperature and dissipative systems,* Phys. Rev. Lett. **93**, 207204 (2004)

[190] M. Zwolak and G. Vidal, *Mixed-state dynamics in one-dimensional quantum lattice systems: A time-dependent superoperator renormalization algorithm,* Phys. Rev. Lett. **93**, 207205 (2004)

[191] M. B. Hastings, *Solving gapped hamiltonians locally,* Phys. Rev. B **73**, 085115 (2006)

[192] A. Molnar, N. Schuch, F. Verstraete, and J. I. Cirac, *Approximating gibbs states of local hamiltonians efficiently with projected entangled pair states,* Phys. Rev. B **91**, 045138 (2015)

[193] G.-C.-F.-M. R. Baron de Prony, *Essai expérimental et analytique sur les lois de la Dilatabilité des fluides élastiques et sur celles de la Force expansive de la vapeur de l'eau et de la vapeur de l'alkool, à différentes températures,* J. de l'École Polytechnique **1**, 24 (1795)

[194] T. Peter, *Generalized Prony Method*, Ph.D. thesis, University of Göttingen (2014), as of 29/05/2020 available online at na.math.uni-goettingen.de/pdf/Pe13.pdf

[195] R. Roy and T. Kailath, *ESPRIT-estimation of signal parameters via rotational invariance techniques,* IEEE Transactions on Acoustics, Speech, and Signal Processing **37**, 984 (1989)

[196] B. Pirvu, V. Murg, J. I. Cirac, and F. Verstraete, *Matrix product operator representations,* New Journal of Physics **12**, 025012 (2010), arXiv:0804.3976 [quant-ph]

[197] M. Ganahl, M. Aichhorn, H. G. Evertz, P. Thunström, K. Held, and F. Verstraete, *Efficient dmft impurity solver using real-time dynamics with matrix product states,* Physical Review B **92** (2015), 10.1103/physrevb.92.155132, arXiv:1405.6728 [cond-mat.str-el]

[198] A. Steffens, C. A. Riofrío, R. Hübener, and J. Eisert, *Quantum field tomography,* New Journal of Physics **16**, 123010 (2014), arXiv:1406.3631 [quant-ph]

[199] F. A. Wolf, I. P. McCulloch, O. Parcollet, and U. Schollwöck, *Chebyshev matrix product state impurity solver for dynamical mean-field theory,* Physical Review B **90** (2014), 10.1103/physrevb.90.115124, arXiv:1407.1622 [cond-mat.str-el]

[200] F. A. Wolf, A. Go, I. P. McCulloch, A. J. Millis, and U. Schollwöck, *Imaginary-time matrix product state impurity solver for dynamical mean-field theory,* Physical Review X **5** (2015), 10.1103/physrevx.5.041032, arXiv:1507.08650 [cond-mat.str-el]

[201] M. Kormos, M. Collura, G. Takács, and P. Calabrese, *Real-time confinement following a quantum quench to a non-integrable model,* Nature Physics **13**, 246 (2017), arXiv:1604.03571 [cond-mat.stat-mech]

[202] L. V. Delacretaz, A. L. Fitzpatrick, E. Katz, and M. T. Walters, *Thermalization and Hydrodynamics of Two-Dimensional Quantum Field Theories,* (2021), arXiv:2105.02229 [hep-th]

[203] G. Evenbly, *An overview of Wavelets and MERA,* `https://pirsa.org/20110035/` (2020), talk presented at the online workshop "Tensor Networks: from Simulations to Holography III"

[204] I. Daubechies, *Ten Lectures on Wavelets,* in *CBMS-NSF Regional Conference Series in Applied Mathematics* (1992)

[205] A. Rothkopf, *Heavy Quarkonium in Extreme Conditions,* Phys. Rept. **858**, 1 (2020), arXiv:1912.02253 [hep-ph]

[206] S. Kim, P. Petreczky, and A. Rothkopf, *Quarkonium in-medium properties from realistic lattice NRQCD,* JHEP **11**, 088 (2018), arXiv:1808.08781 [hep-lat]

[207] D. Lafferty and A. Rothkopf, *Improved Gauss law model and in-medium heavy quarkonium at finite density and velocity,* Phys. Rev. D **101**, 056010 (2020), arXiv:1906.00035 [hep-ph]

[208] T. Matsui and H. Satz, *J/ψ Suppression by Quark-Gluon Plasma Formation,* Phys. Lett. B **178**, 416 (1986)

[209] F. Karsch, D. Kharzeev, and H. Satz, *Sequential charmonium dissociation,* Phys. Lett. B **637**, 75 (2006), arXiv:hep-ph/0512239

[210] M. Laine, O. Philipsen, P. Romatschke, and M. Tassler, *Real-time static potential in hot QCD,* JHEP **03**, 054 (2007), arXiv:hep-ph/0611300

[211] S. Kajimoto, Y. Akamatsu, M. Asakawa, and A. Rothkopf, *Dynamical dissociation of quarkonia by wave function decoherence,* Phys. Rev. D **97**, 014003 (2018), arXiv:1705.03365 [nucl-th]

[212] D. De Boni, *Fate of in-medium heavy quarks via a Lindblad equation,* JHEP **08**, 064 (2017), arXiv:1705.03567 [hep-ph]

[213] R. Zöllner and B. Kämpfer, *Holographically emulating sequential versus instantaneous disappearance of vector mesons in a hot environment,* Phys. Rev. C **94**, 045205 (2016), arXiv:1607.01512 [hep-ph]

[214] R. Zöllner, F. Wunderlich, and B. Kämpfer, *Extended soft-wall model for the QCD phase diagram,* Acta Phys. Polon. Supp. B **10**, 789 (2017), arXiv:1611.04124 [hep-th]

[215] R. Zöllner and B. Kämpfer, *Extended soft wall model with background related to features of QCD thermodynamics,* Eur. Phys. J. A **53**, 139 (2017), arXiv:1701.01398 [hep-ph]

[216] R. Zöllner and B. Kämpfer, *Holography at QCD-T_c,* J. Phys. Conf. Ser. **878**, 012023 (2017), arXiv:1703.02958 [hep-ph]

[217] R. Zöllner and B. Kämpfer, *Holographic vector mesons in a dilaton background,* J. Phys. Conf. Ser. **1024**, 012003 (2018), arXiv:1708.05833 [hep-th]

[218] R. Zöllner and B. Kämpfer, *Phase structures emerging from holography with Einstein gravity – dilaton models at finite temperature,* Eur. Phys. J. Plus **135**, 304 (2020), arXiv:1807.04260 [hep-th]

[219] R. Zöllner and B. Kämpfer, *Holographic vector meson melting in a thermal gravity-dilaton background related to QCD,* Eur. Phys. J. ST **229**, 3585 (2020), arXiv:2002.07200 [hep-ph]

[220] R. Zöllner and B. Kämpfer, *Quarkonia Formation in a Holographic Gravity–Dilaton Background Describing QCD Thermodynamics,* Particles **4**, 159 (2021), arXiv:2007.14287 [hep-ph]

[221] R. Zöllner, *Anwendungen der AdS/CFT-Korrespondenz: Holographische Beschreibung von Vektormesonen in einem heißen Medium*, Ph.D. thesis, Technische Universität Dresden (2020)

[222] A. Karch, E. Katz, D. T. Son, and M. A. Stephanov, *Linear confinement and AdS/QCD,* Phys. Rev. D **74**, 015005 (2006), arXiv:hep-ph/0602229

[223] K. Ghoroku and M. Yahiro, *Holographic model for mesons at finite temperature,* Phys. Rev. D **73**, 125010 (2006), arXiv:hep-ph/0512289

[224] P. Colangelo, F. De Fazio, F. Jugeau, and S. Nicotri, *On the light glueball spectrum in a holographic description of QCD,* Phys. Lett. B **652**, 73 (2007), arXiv:hep-ph/0703316

[225] P. Colangelo, F. De Fazio, F. Giannuzzi, F. Jugeau, and S. Nicotri, *Light scalar mesons in the soft-wall model of AdS/QCD,* Phys. Rev. D **78**, 055009 (2008), arXiv:0807.1054 [hep-ph]

[226] M. Fujita, K. Fukushima, T. Misumi, and M. Murata, *Finite-temperature spectral function of the vector mesons in an AdS/QCD model,* Phys. Rev. D **80**, 035001 (2009), arXiv:0903.2316 [hep-ph]

[227] P. Colangelo, F. Giannuzzi, and S. Nicotri, *Holographic Approach to Finite Temperature QCD: The Case of Scalar Glueballs and Scalar Mesons,* Phys. Rev. D **80**, 094019 (2009), arXiv:0909.1534 [hep-ph]

[228] Y.-Q. Sui, Y.-L. Wu, Z.-F. Xie, and Y.-B. Yang, *Prediction for the Mass Spectra of Resonance Mesons in the Soft-Wall AdS/QCD with a Modified 5D Metric,* Phys. Rev. D **81**, 014024 (2010), arXiv:0909.3887 [hep-ph]

[229] L.-X. Cui, S. Takeuchi, and Y.-L. Wu, *Thermal Mass Spectra of Vector and Axial-Vector Mesons in Predictive Soft-Wall AdS/QCD Model,* JHEP **04**, 144 (2012), arXiv:1112.5923 [hep-ph]

[230] P. Colangelo, F. Giannuzzi, and S. Nicotri, *In-medium hadronic spectral functions through the soft-wall holographic model of QCD,* JHEP **05**, 076 (2012), arXiv:1201.1564 [hep-ph]

[231] M. A. Martin Contreras, S. Diles, and A. Vega, *Heavy quarkonia spectroscopy at zero and finite temperature in bottom-up AdS/QCD,* Phys. Rev. D **103**, 086008 (2021), arXiv:2101.06212 [hep-ph]

[232] I. R. Klebanov, D. Kutasov, and A. Murugan, *Entanglement as a probe of confinement,* Nucl. Phys. **B 796**, 274 (2008), arXiv:0709.2140 [hep-th]

[233] J. Knaute and B. Kämpfer, *Holographic entanglement entropy in the QCD phase diagram with a critical point,* Phys. Rev. **D 96**, 106003 (2017), arXiv:1706.02647 [hep-ph]

[234] P. Calabrese and J. L. Cardy, *Time-dependence of correlation functions following a quantum quench,* Phys. Rev. Lett. **96**, 136801 (2006), arXiv:cond-mat/0601225

[235] P. Calabrese and J. Cardy, *Quantum Quenches in Extended Systems,* J. Stat. Mech. **0706**, P06008 (2007), arXiv:0704.1880 [cond-mat.stat-mech]

[236] S. Sotiriadis and J. Cardy, *Quantum quench in interacting field theory: A Self-consistent approximation,* Phys. Rev. B **81**, 134305 (2010), arXiv:1002.0167 [quant-ph]

[237] L.-Y. Hung, M. Smolkin, and E. Sorkin, *Modification of late time phase structure by quantum quenches,* Phys. Rev. Lett. **109**, 155702 (2012), arXiv:1206.2685 [cond-mat.str-el]

[238] S. R. Das, D. A. Galante, and R. C. Myers, *Universal scaling in fast quantum quenches in conformal field theories,* Phys. Rev. Lett. **112**, 171601 (2014), arXiv:1401.0560 [hep-th]

[239] V. Balasubramanian, A. Bernamonti, J. de Boer, N. Copland, B. Craps, E. Keski-Vakkuri, B. Muller, A. Schafer, M. Shigemori, and W. Staessens, *Holographic Thermalization,* Phys. Rev. D **84**, 026010 (2011), arXiv:1103.2683 [hep-th]

[240] R. C. Myers, M. Rozali, and B. Way, *Holographic Quenches in a Confined Phase,* J. Phys. A **50**, 494002 (2017), arXiv:1706.02438 [hep-th]

[241] H. A. Camargo, P. Caputa, D. Das, M. P. Heller, and R. Jefferson, *Complexity as a novel probe of quantum quenches: universal scalings and purifications,* Phys. Rev. Lett. **122**, 081601 (2019), arXiv:1807.07075 [hep-th]

[242] M. Heyl, *Dynamical quantum phase transitions: a review,* Rept. Prog. Phys. **81**, 054001 (2018), arXiv:1709.07461 [cond-mat.stat-mech]

[243] J. Surace, L. Tagliacozzo, and E. Tonni, *Operator content of entanglement spectra in the transverse field Ising chain after global quenches,* Phys. Rev. B **101**, 241107(R) (2020), arXiv:1909.07381 [cond-mat.stat-mech]

[244] V. Alba and P. Calabrese, *Quantum information scrambling after a quantum quench,* Phys. Rev. B **100**, 115150 (2019), arXiv:1903.09176 [cond-mat.stat-mech]

[245] H. Bernien, S. Schwartz, A. Keesling, H. Levine, A. Omran, H. Pichler, S. Choi, A. S. Zibrov, M. Endres, M. Greiner, and et al., *Probing many-body dynamics on a 51-atom quantum simulator,* Nature **551**, 579–584 (2017)

[246] J. Zhang, G. Pagano, P. W. Hess, A. Kyprianidis, P. Becker, H. Kaplan, A. V. Gorshkov, Z.-X. Gong, and C. Monroe, *Observation of a many-body dynamical phase transition with a 53-qubit quantum simulator,* Nature **551**, 601–604 (2017)

[247] O. A. Castro-Alvaredo, M. Lencsés, I. M. Szécsényi, and J. Viti, *Entanglement Oscillations near a Quantum Critical Point,* Phys. Rev. Lett. **124**, 230601 (2020), arXiv:2001.10007 [cond-mat.stat-mech]

[248] G. Magnifico, M. Dalmonte, P. Facchi, S. Pascazio, F. V. Pepe, and E. Ercolessi, *Real Time Dynamics and Confinement in the $\mathbb{Z}_n$ Schwinger-Weyl lattice model for 1+1 QED,* Quantum **4**, 281 (2020), arXiv:1909.04821 [quant-ph]

[249] T. Chanda, J. Zakrzewski, M. Lewenstein, and L. Tagliacozzo, *Confinement and lack of thermalization after quenches in the bosonic Schwinger model,* Phys. Rev. Lett. **124**, 180602 (2020), arXiv:1909.12657 [cond-mat.stat-mech]

[250] A. Lerose, F. M. Surace, P. P. Mazza, G. Perfetto, M. Collura, and A. Gambassi, *Quasilocalized dynamics from confinement of quantum excitations,* Phys. Rev. B **102**, 041118 (2019), arXiv:1911.07877 [cond-mat.stat-mech]

[251] M. Collura, M. Kormos, and G. Takács, *Dynamical manifestation of the Gibbs paradox after a quantum quench,* Physical Review A **98** (2018), 10.1103/physreva.98.053610, arXiv:1801.05817 [cond-mat.stat-mech]

[252] O. Pomponio, L. Pristyák, and G. Takács, *Quasi-particle spectrum and entanglement generation after a quench in the quantum potts spin chain,* Journal of Statistical Mechanics: Theory and Experiment **2019**, 013104 (2019), arXiv:1810.05539 [cond-mat.stat-mech]

[253] P. Calabrese and J. L. Cardy, *Evolution of entanglement entropy in one-dimensional systems,* J. Stat. Mech. **0504**, P04010 (2005), arXiv:cond-mat/0503393

[254] V. Alba and P. Calabrese, *Entanglement and thermodynamics after a quantum quench in integrable systems,* Proceedings of the National Academy of Sciences **114**, 7947–7951 (2017), arXiv:1608.00614 [cond-mat.str-el]

[255] V. Alba and P. Calabrese, *Entanglement dynamics after quantum quenches in generic integrable systems,* SciPost Phys. **4**, 017 (2018), arXiv:1712.07529 [cond-mat.stat-mech]

[256] A. De Luca and A. Bastianello, *Entanglement front generated by an impurity traveling in an isolated many-body quantum system,* Phys. Rev. B **101**, 085139 (2020), arXiv:1909.07341 [cond-mat.stat-mech]

[257] S. Chapman, J. Eisert, L. Hackl, M. P. Heller, R. Jefferson, H. Marrochio, and R. C. Myers, *Complexity and entanglement for thermofield double states,* SciPost Phys. **6**, 034 (2019), arXiv:1810.05151 [hep-th]

[258] A. Bastianello and M. Collura, *Entanglement spreading and quasiparticle picture beyond the pair structure,* SciPost Physics **8**, 045 (2020), arXiv:2001.01671 [cond-mat.stat-mech]

[259] P. Calabrese, *Entanglement spreading in non-equilibrium integrable systems,* SciPost Phys. Lect. Notes **20**, 1 (2020), arXiv:2008.11080 [cond-mat.stat-mech]

[260] J. Eisert and T. J. Osborne, *General Entanglement Scaling Laws from Time Evolution,* Phys. Rev. Lett. **97**, 150404 (2006), arXiv:quant-ph/0603114

[261] A. J. A. James, R. M. Konik, and N. J. Robinson, *Nonthermal states arising from confinement in one and two dimensions,* Phys. Rev. Lett. **122**, 130603 (2019), arXiv:1804.09990 [cond-mat.stat-mech]

[262] N. J. Robinson, A. J. A. James, and R. M. Konik, *Signatures of rare states and thermalization in a theory with confinement,* Phys. Rev. B **99**, 195108 (2019), arXiv:1808.10782 [cond-mat.stat-mech]

[263] A. Cortés Cubero and N. J. Robinson, *Lack of thermalization in (1+1)-d QCD at large N_c,* (2019), arXiv:1908.00270 [hep-th]

[264] E. Leviatan, F. Pollmann, J. H. Bardarson, and E. Altman, *Quantum thermalization dynamics with Matrix-Product States,* (2017), arXiv:1702.08894 [cond-mat.stat-mech]

[265] M. Lencses, O. Pomponio, and G. Takacs, *Relaxation and entropy generation after quenching quantum spin chains,* SciPost Phys. **9**, 011 (2020), arXiv:2004.09550 [cond-mat.stat-mech]

[266] M. Kormos, *Inhomogeneous quenches in the transverse field Ising chain: scaling and front dynamics,* SciPost Phys. **3**, 020 (2017), arXiv:1704.03744 [cond-mat.stat-mech]

[267] G. Delfino, *Persistent oscillations after quantum quenches: The inhomogeneous case,* Nucl. Phys. B **954**, 115002 (2020), arXiv:2001.05349 [cond-mat.stat-mech]

[268] S. Sotiriadis, P. Calabrese, and J. Cardy, *Quantum quench from a thermal initial state,* EPL (Europhysics Letters) **87**, 20002 (2009), arXiv:0903.0895 [cond-mat.stat-mech]

[269] J. M. Zhang, C. Shen, and W. M. Liu, *Quantum quench dynamics of the bose-hubbard model at finite temperatures,* Phys. Rev. A **83**, 063622 (2011), arXiv:1103.1539 [cond-mat.stat-mech]

[270] A. Bácsi and B. Dóra, *Quantum quench in the luttinger model with finite temperature initial state,* Phys. Rev. B **88**, 155115 (2013), arXiv:1307.7582 [cond-mat.str-el]

[271] M. Collura and D. Karevski, *Quantum quench from a thermal tensor state: Boundary effects and generalized Gibbs ensemble,* Phys. Rev. B **89**, 214308 (2014), arXiv:1402.1944 [cond-mat.stat-mech]

[272] E. Granet, M. Fagotti, and F. H. L. Essler, *Finite temperature and quench dynamics in the Transverse Field Ising Model from form factor expansions,* SciPost Phys. **9**, 033 (2020), arXiv:2003.09014 [cond-mat.stat-mech]

[273] L. Kohn and G. E. Santoro, *Quenching the anderson impurity model at finite temperature: Entanglement and bath dynamics using matrix product states,* (2021), arXiv:2107.02807 [cond-mat.str-el]

[274] T. Brydges, A. Elben, P. Jurcevic, B. Vermersch, C. Maier, B. P. Lanyon, P. Zoller, R. Blatt, and C. F. Roos, *Probing Rényi entanglement entropy via randomized measurements,* Science **364**, 260–263 (2019)

[275] S. Dutta and T. Faulkner, *A canonical purification for the entanglement wedge cross-section,* JHEP **03**, 178 (2021), arXiv:1905.00577 [hep-th]

[276] H.-S. Jeong, K.-Y. Kim, and M. Nishida, *Reflected Entropy and Entanglement Wedge Cross Section with the First Order Correction,* JHEP **12**, 170 (2019), arXiv:1909.02806 [hep-th]

[277] N. Bao and N. Cheng, *Multipartite Reflected Entropy,* JHEP **10**, 102 (2019), arXiv:1909.03154 [hep-th]

[278] J. Chu, R. Qi, and Y. Zhou, *Generalizations of Reflected Entropy and the Holographic Dual,* JHEP **03**, 151 (2020), arXiv:1909.10456 [hep-th]

[279] P. Bueno and H. Casini, *Reflected entropy, symmetries and free fermions,* JHEP **05**, 103 (2020), arXiv:2003.09546 [hep-th]

[280] P. Bueno and H. Casini, *Reflected entropy for free scalars,* JHEP **11**, 148 (2020), arXiv:2008.11373 [hep-th]

[281] J. Kudler-Flam, Y. Kusuki, and S. Ryu, *Correlation measures and the entanglement wedge cross-section after quantum quenches in two-dimensional conformal field theories,* JHEP **04**, 074 (2020), arXiv:2001.05501 [hep-th]

[282] M. Moosa, *Time dependence of reflected entropy in rational and holographic conformal field theories,* JHEP **05**, 082 (2020), arXiv:2001.05969 [hep-th]

[283] J. Kudler-Flam, Y. Kusuki, and S. Ryu, *The quasi-particle picture and its breakdown after local quenches: mutual information, negativity, and reflected entropy,* JHEP **03**, 146 (2021), arXiv:2008.11266 [hep-th]

[284] P. Jain and S. Mahapatra, *Mixed state entanglement measures as probe for confinement,* Phys. Rev. D **102**, 126022 (2020), arXiv:2010.07702 [hep-th]

[285] P. W. Anderson, *More Is Different,* Science **177**, 393 (1972)

[286] P. Coleman, *Introduction to Many-Body Physics* (Cambridge University Press, 2015)

[287] E. Witten, *Symmetry and Emergence,* Nature Phys. **14**, 116 (2018), arXiv:1710.01791 [hep-th]

[288] P. Hauke, F. M. Cucchietti, L. Tagliacozzo, I. Deutsch, and M. Lewenstein, *Can one trust quantum simulators?* Rep. Prog. Phys. **75**, 082401 (2012)

[289] J. I. Cirac and P. Zoller, *Goals and opportunities in quantum simulation,* Nat. Phys. **8**, 264 (2012)

[290] Y. Alexeev *et al.*, *Quantum Computer Systems for Scientific Discovery,* P. R. X. Quantum. **2**, 017001 (2021), arXiv:1912.07577 [quant-ph]

[291] I. Bloch, *Ultracold quantum gases in optical lattices,* Nat. Phys. **1**, 23 (2005)

[292] M. Lewenstein, A. Sanpera, V. Ahufinger, B. Damski, A. Sen(De), and U. Sen, *Ultracold atomic gases in optical lattices: mimicking condensed matter physics and beyond,* Adv. Phys. **56**, 243 (2007), arXiv:cond-mat/0606771 [cond-mat.other]

[293] F. Schäfer, T. Fukuhara, S. Sugawa, Y. Takasu, and Y. Takahashi, *Nature reviews physics,* Tools for quantum simulation with ultracold atoms in optical lattices **2**, 411â425 (2020)

[294] C. Schneider, D. Porras, and T. Schaetz, *Many-Body Physics with Trapped Ions,* (2011), arXiv:1106.2597 [quant-ph]

[295] R. Blatt and C. F. Roos, *Quantum simulations with trapped ions,* Nat. Phys. **8**, 277 (2012)

[296] C. Monroe, W. C. Campbell, L.-M. Duan, Z.-X. Gong, A. V. Gorshkov, P. W. Hess, R. Islam, K. Kim, N. M. Linke, G. Pagano, P. Richerme, C. Senko, and N. Y. Yao, *Programmable quantum simulations of spin systems with trapped ions,* Rev. Mod. Phys. **93**, 025001 (2021)

[297] I. Pogorelov, T. Feldker, C. D. Marciniak, L. Postler, G. Jacob, O. Krieglsteiner, V. Podlesnic, M. Meth, V. Negnevitsky, M. Stadler, B. Höfer, C. Wächter, K. Lakhmanskiy, R. Blatt, P. Schindler, and T. Monz, *Compact ion-trap quantum computing demonstrator,* PRX Quantum **2**, 020343 (2021)

[298] A. Friedenauer, H. Schmitz, J. T. Glueckert, D. Porras, and T. Schaetz, *Simulating a quantum magnet with trapped ions.* Nat. Phys. **4**, 757 (2008)

[299] J. W. Britton, B. C. Sawyer, A. C. Keith, C.-C. J. Wang, J. K. Freericks, H. Uys, M. J. Biercuk, and J. J. Bollinger, *Engineered two-dimensional ising interactions in a trapped-ion quantum simulator with hundreds of spins,* Nature **484**, 489–492 (2012)

[300] P. Richerme, C. Senko, S. Korenblit, J. Smith, A. Lee, R. Islam, W. C. Campbell, and C. Monroe, *Quantum catalysis of magnetic phase transitions in a quantum simulator,* Physical Review Letters **111** (2013), 10.1103/physrevlett.111.100506, arXiv:1303.6983 [quant-ph]

[301] C. Senko, J. Smith, P. Richerme, A. Lee, W. C. Campbell, and C. Monroe, *Coherent imaging spectroscopy of a quantum many-body spin system,* Science **345**, 430–433 (2014), arXiv:1401.5751 [quant-ph]

[302] P. Jurcevic, B. P. Lanyon, P. Hauke, C. Hempel, P. Zoller, R. Blatt, and C. F. Roos, *Quasiparticle engineering and entanglement propagation in a quantum many-body system,* Nature **511**, 202–205 (2014)

[303] P. Jurcevic, P. Hauke, C. Maier, C. Hempel, B. Lanyon, R. Blatt, and C. Roos, *Spectroscopy of interacting quasiparticles in trapped ions,* Physical Review Letters **115** (2015), 10.1103/physrevlett.115.100501, arXiv:1505.02066 [quant-ph]

[304] J. Smith, A. Lee, P. Richerme, B. Neyenhuis, P. W. Hess, P. Hauke, M. Heyl, D. A. Huse, and C. Monroe, *Many-body localization in a quantum simulator with programmable random disorder,* Nature Physics **12**, 907–911 (2016)

[305] M. Gärttner, J. G. Bohnet, A. Safavi-Naini, M. L. Wall, J. J. Bollinger, and A. M. Rey, *Measuring out-of-time-order correlations and multiple quantum spectra in a trapped ion quantum magnet,* Nature Phys. **13**, 781 (2017), arXiv:1608.08938 [quant-ph]

[306] P. Jurcevic, H. Shen, P. Hauke, C. Maier, T. Brydges, C. Hempel, B. Lanyon, M. Heyl, R. Blatt, and C. Roos, *Direct observation of dynamical quantum phase transitions in an interacting many-body system,* Physical Review Letters **119** (2017), 10.1103/physrevlett.119.080501

[307] C. Hempel, C. Maier, J. Romero, J. McClean, T. Monz, H. Shen, P. Jurcevic, B. P. Lanyon, P. Love, R. Babbush, and et al., *Quantum chemistry calculations on a trapped-ion quantum simulator,* Physical Review X **8** (2018), 10.1103/physrevx.8.031022

[308] C. Maier, T. Brydges, P. Jurcevic, N. Trautmann, C. Hempel, B. P. Lanyon, P. Hauke, R. Blatt, and C. F. Roos, *Environment-assisted quantum transport in a 10-qubit network,* Physical Review Letters **122** (2019), 10.1103/physrevlett.122.050501

[309] E. A. Martinez *et al.*, *Real-time dynamics of lattice gauge theories with a few-qubit quantum computer,* Nature **534**, 516 (2016), arXiv:1605.04570 [quant-ph]

[310] C. Kokail *et al.*, *Self-verifying variational quantum simulation of lattice models,* Nature **569**, 355 (2019), arXiv:1810.03421 [quant-ph]

[311] B. Yang, H. Sun, R. Ott, H.-Y. Wang, T. V. Zache, J. C. Halimeh, Z.-S. Yuan, P. Hauke, and J.-W. Pan, *Observation of gauge invariance in a 71-site Bose–Hubbard quantum simulator,* Nature **587**, 392 (2020), arXiv:2003.08945 [cond-mat.quant-gas]

[312] P. Hauke, L. Bonnes, M. Heyl, and W. Lechner, *Probing entanglement in adiabatic quantum optimization with trapped ions,* Frontiers in Physics **3** (2015), 10.3389/fphy.2015.00021

[313] E. Zohar, J. I. Cirac, and B. Reznik, *Quantum Simulations of Lattice Gauge Theories using Ultracold Atoms in Optical Lattices,* Rept. Prog. Phys. **79**, 014401 (2016), arXiv:1503.02312 [quant-ph]

[314] N. Trautmann and P. Hauke, *Quantum simulation of the dynamical Casimir effect with trapped ions,* New J. Phys. **18**, 043029 (2016), arXiv:1512.00990 [quant-ph]

[315] J. Preskill, *Quantum computing in the nisq era and beyond,* Quantum **2**, 79 (2018)

[316] C. Monroe *et al.*, *Programmable quantum simulations of spin systems with trapped ions,* Rev. Mod. Phys. **93**, 025001 (2021), arXiv:1912.07845 [quant-ph]

[317] C. Kokail, R. van Bijnen, A. Elben, B. Vermersch, and P. Zoller, *Entanglement Hamiltonian Tomography in Quantum Simulation,* (2020), arXiv:2009.09000 [quant-ph]

[318] J. Vovrosh and J. Knolle, *Confinement and entanglement dynamics on a digital quantum computer,* Scientific Reports **11** (2021), 10.1038/s41598-021-90849-5

[319] C. Micheletti, P. Hauke, and P. Faccioli, *Polymer physics by quantum computing,* (2021), arXiv:2104.10102 [cond-mat.soft]

[320] J. C. Halimeh, M. V. Damme, L. Guo, J. Lang, and P. Hauke, *Dynamical phase transitions in quantum spin models with antiferromagnetic long-range interactions,* (2021), arXiv:2106.05282 [cond-mat.quant-gas]

[321] M. Greiter, *Fictitious flux confinement: Magnetic pairing in coupled spin chains or planes,* Phys. Rev. B **66**, 054505 (2002)

[322] B. Lake, A. M. Tsvelik, S. Notbohm, D. Alan Tennant, T. G. Perring, M. Reehuis, C. Sekar, G. Krabbes, and B. Büchner, *Confinement of fractional quantum number particles in a condensed-matter system,* Nature Physics **6**, 50–55 (2009)

[323] M. Kormos, M. Collura, G. Takács, and P. Calabrese, *Real-time confinement following a quantum quench to a non-integrable model,* Nature Phys. **13**, 246–249 (2017), arXiv:1604.03571 [cond-mat.stat-mech]

[324] P. P. Mazza, G. Perfetto, A. Lerose, M. Collura, and A. Gambassi, *Suppression of transport in nondisordered quantum spin chains due to confined excitations,* Physical Review B **99** (2019), 10.1103/physrevb.99.180302

[325] L. Vanderstraeten, E. Wybo, N. Chepiga, F. Verstraete, and F. Mila, *Spinon confinement and deconfinement in spin-1 chains,* Phys. Rev. B **101**, 115138 (2020)

[326] F. Liu, R. Lundgren, P. Titum, G. Pagano, J. Zhang, C. Monroe, and A. V. Gorshkov, *Confined Quasiparticle Dynamics in Long-Range Interacting Quantum Spin Chains,* Phys. Rev. Lett. **122**, 150601 (2019), arXiv:1810.02365 [cond-mat.quant-gas]

[327] A. Lerose, B. Žunkovič, A. Silva, and A. Gambassi, *Quasilocalized excitations induced by long-range interactions in translationally invariant quantum spin chains,* Physical Review B **99** (2019), 10.1103/physrevb.99.121112, arXiv:1811.05513 [cond-mat.quant-gas]

[328] J. C. Halimeh, M. Van Damme, V. Zauner-Stauber, and L. Vanderstraeten, *Quasiparticle origin of dynamical quantum phase transitions,* Physical Review Research **2**, 033111 (2020), arXiv:1810.07187 [cond-mat.str-el]

[329] N. Defenu, T. Enss, and J. C. Halimeh, *Dynamical criticality and domain-wall coupling in long-range Hamiltonians,* Phys. Rev. B **100**, 014434 (2019), arXiv:1902.08621 [cond-mat.stat-mech]

[330] W. L. Tan *et al.*, *Domain-wall confinement and dynamics in a quantum simulator,* Nature Phys. **17**, 742 (2021), arXiv:1912.11117 [quant-ph]

[331] R. Verdel, F. Liu, S. Whitsitt, A. V. Gorshkov, and M. Heyl, *Real-time dynamics of string breaking in quantum spin chains,* Phys. Rev. B **102**, 014308 (2020), arXiv:1911.11382 [cond-mat.stat-mech]

[332] F. M. Surace and A. Lerose, *Scattering of mesons in quantum simulators,* (2020), arXiv:2011.10583 [cond-mat.quant-gas]

[333] P. I. Karpov, G. Y. Zhu, M. P. Heller, and M. Heyl, *Spatiotemporal dynamics of particle collisions in quantum spin chains,* (2020), arXiv:2011.11624 [cond-mat.quant-gas]

[334] R. Coldea, D. A. Tennant, E. M. Wheeler, E. Wawrzynska, D. Prabhakaran, M. Telling, K. Habicht, P. Smeibidl, and K. Kiefer, *Quantum Criticality in an Ising Chain: Experimental Evidence for Emergent E_8 Symmetry,* Science **327**, 177–180 (2010), arXiv:1103.3694 [cond-mat.str-el]

[335] H. Zou *et al.*, *E_8 Spectra of Quasi-one-dimensional Antiferromagnet $BaCo_2V_2O_8$ under Transverse Field,* (2020), arXiv:2005.13302 [cond-mat.str-el]

[336] Z. Zhang *et al.*, *Observation of E8 Particles in an Ising Chain Antiferromagnet,* Phys. Rev. B **101**, 220411 (2020), arXiv:2005.13772 [cond-mat.str-el]

[337] K. Amelin, J. Engelmayer, J. Viirok, U. Nagel, T. Rõ om, T. Lorenz, and Z. Wang, *Experimental Observation of Quantum Many-Body Excitations of E_8 Symmetry in the Ising Chain Ferromagnet $CoNb_2O_6$,* Phys. Rev. B **102**, 104431 (2020), arXiv:2006.12956 [cond-mat.str-el]

[338] P. Hauke, D. Marcos, M. Dalmonte, and P. Zoller, *Quantum simulation of a lattice Schwinger model in a chain of trapped ions,* Phys. Rev. X **3**, 041018 (2013)

[339] D. Yang, G. S. Giri, M. Johanning, C. Wunderlich, P. Zoller, and P. Hauke, *Analog quantum simulation of (1+1)-dimensional lattice QED with trapped ions,* Phys. Rev. A **94**, 052321 (2016), arXiv:1604.03124 [quant-ph]

[340] C. Muschik, M. Heyl, E. Martinez, T. Monz, P. Schindler, B. Vogell, M. Dalmonte, P. Hauke, R. Blatt, and P. Zoller, *U(1) wilson lattice gauge theories in digital quantum simulators,* New Journal of Physics **19**, 103020 (2017)

[341] Z. Davoudi, M. Hafezi, C. Monroe, G. Pagano, A. Seif, and A. Shaw, *Towards analog quantum simulations of lattice gauge theories with trapped ions,* Phys. Rev. Res. **2**, 023015 (2020), arXiv:1908.03210 [quant-ph]

[342] D. Paulson *et al.*, *Towards simulating 2D effects in lattice gauge theories on a quantum computer,* (2020), arXiv:2008.09252 [quant-ph]

[343] Z. Davoudi, N. M. Linke, and G. Pagano, *Toward simulating quantum field theories with controlled phonon-ion dynamics: A hybrid analog-digital approach,* (2021), arXiv:2104.09346 [quant-ph]

[344] E. Zohar, *Quantum Simulation of Lattice Gauge Theories in more than One Space Dimension – Requirements, Challenges, Methods,* (2021), arXiv:2106.04609 [quant-ph]

[345] A. Russomanno, M. Fava, and M. Heyl, *Long-range ising chains: eigenstate thermalization and symmetry breaking of excited states,* (2020), arXiv:2012.06505 [cond-mat.stat-mech]

[346] D. Porras and J. I. Cirac, *Effective quantum spin systems with trapped ions,* Phys. Rev. Lett. **92**, 207901 (2004)

[347] N. Trautmann and P. Hauke, *Trapped-ion quantum simulation of excitation transport: Disordered, noisy, and long-range connected quantum networks,* Physical Review A **97** (2018), 10.1103/physreva.97.023606

[348] P. Hauke and L. Tagliacozzo, *Spread of correlations in long-range interacting quantum systems,* Physical Review Letters **111** (2013), 10.1103/physrevlett.111.207202, arXiv:1304.7725 [quant-ph]

[349] J. A. Kjäll, F. Pollmann, and J. E. Moore, *Bound states and E_8 symmetry effects in perturbed quantum Ising chains,* Phys. Rev. B **83**, 020407 (2011), arXiv:1008.3534 [cond-mat.str-el]

[350] N. Wiener, *Generalized harmonic analysis,* Acta Mathematica **55**, 117 (1930)

[351] A. Khintchine, *Korrelationstheorie der stationären stochastischen Prozesse,* Mathematische Annalen **109**, 604 (1934)

[352] M. Lüscher, *Volume dependence of the energy spectrum in massive quantum field theories,* Commun. Math. Phys. **104**, 177 (1986)

[353] X. Wang, H. Zou, K. Hódsági, M. Kormos, G. Takács, and J. Wu, *Spin dynamics of a perturbed quantum critical ising chain,* (2021), arXiv:2103.09128 [cond-mat.str-el]

[354] S.-J. Gu, H.-M. Kwok, W.-Q. Ning, and H.-Q. Lin, *Fidelity susceptibility, scaling, and universality in quantum critical phenomena,* Phys. Rev. B **77**, 245109 (2008), arXiv:0706.2495 [quant-ph]

[355] S.-J. Gu, *Fidelity approach to quantum phase transitions,* International Journal of Modern Physics B **24**, 4371–4458 (2010), arXiv:0811.3127 [quant-ph]

[356] J. Khalouf-Rivera, M. Carvajal, and F. Pérez-Bernal, *Quantum fidelity susceptibility in excited state quantum phase transitions: application to the bending spectra of nonrigid molecules,* (2021), arXiv:2102.12335 [quant-ph]

[357] P. Schindler, D. Nigg, T. Monz, J. T. Barreiro, E. Martinez, S. X. Wang, S. Quint, M. F. Brandl, V. Nebendahl, C. F. Roos, and et al., *A quantum information processor with trapped ions,* New Journal of Physics **15**, 123012 (2013)

[358] P. Nevado and D. Porras, *Hidden frustrated interactions and quantum annealing in trapped-ion spin-phonon chains,* Physical Review A **93** (2016), 10.1103/physreva.93.013625

[359] B. Horstmann, B. Reznik, S. Fagnocchi, and J. Cirac, *Hawking radiation from an acoustic black hole on an ion ring,* Phys. Rev. Lett. **104**, 250403 (2010)

[360] B. Horstmann, R. Schützhold, B. Reznik, S. Fagnocchi, and J. Cirac, *Hawking radiation on an ion ring in the quantum regime,* New J. Phys. **13**, 045008 (2011)

[361] H.-K. Li, E. Urban, C. Noel, A. Chuang, Y. Xia, A. Ransford, B. Hemmerling, Y. Wang, T. Li, H. Häffner, and et al., *Realization of translational symmetry in trapped cold ion rings,* Physical Review Letters **118** (2017), 10.1103/physrevlett.118.053001

[362] D. Zhu, S. Johri, N. M. Linke, K. A. Landsman, N. H. Nguyen, C. H. Alderete, A. Y. Matsuura, T. H. Hsieh, and C. Monroe, *Generation of thermofield double states and critical ground states with a quantum computer,* Proc. Nat. Acad. Sci. **117**, 25402 (2020), arXiv:1906.02699 [quant-ph]

[363] J. Mildenberger, *Trapped-Ion Quantum Simulations of Spin Systems at Non-Vanishing Temperature*, Master thesis, Universität Heidelberg (2019), `https://www.kip.uni-heidelberg.de/Veroeffentlichungen/details.php?id=3997`

[364] J. M. Maldacena, *Eternal black holes in anti-de Sitter,* JHEP **04**, 021 (2003), arXiv:hep-th/0106112

[365] J. Maldacena and L. Susskind, *Cool horizons for entangled black holes,* Fortsch. Phys. **61**, 781 (2013), arXiv:1306.0533 [hep-th]

[366] T. Hartman and J. Maldacena, *Time Evolution of Entanglement Entropy from Black Hole Interiors,* JHEP **05**, 014 (2013), arXiv:1303.1080 [hep-th]

[367] S. Aaronson, *The Complexity of Quantum States and Transformations: From Quantum Money to Black Holes,* (2016) arXiv:1607.05256 [quant-ph]

[368] J. Haferkamp, P. Faist, N. B. T. Kothakonda, J. Eisert, and N. Y. Halpern, *Linear growth of quantum circuit complexity,* (2021), arXiv:2106.05305 [quant-ph]

[369] S. Lloyd, *Ultimate physical limits to computation,* Nature **406**, 1047–1054 (2000), arXiv:quant-ph/9908043

[370] D. Carmi, S. Chapman, H. Marrochio, R. C. Myers, and S. Sugishita, *On the Time Dependence of Holographic Complexity,* JHEP **11**, 188 (2017), arXiv:1709.10184 [hep-th]

[371] L. Lehner, R. C. Myers, E. Poisson, and R. D. Sorkin, *Gravitational action with null boundaries,* Phys. Rev. D **94**, 084046 (2016), arXiv:1609.00207 [hep-th]

[372] D. Carmi, R. C. Myers, and P. Rath, *Comments on Holographic Complexity,* JHEP **03**, 118 (2017), arXiv:1612.00433 [hep-th]

[373] A. Reynolds and S. F. Ross, *Divergences in Holographic Complexity,* Class. Quant. Grav. **34**, 105004 (2017), arXiv:1612.05439 [hep-th]

[374] R.-Q. Yang, C. Niu, and K.-Y. Kim, *Surface Counterterms and Regularized Holographic Complexity,* JHEP **09**, 042 (2017), arXiv:1701.03706 [hep-th]

[375] S. Chapman, H. Marrochio, and R. C. Myers, *Holographic complexity in Vaidya spacetimes. Part I,* JHEP **06**, 046 (2018), arXiv:1804.07410 [hep-th]

[376] S. Chapman, H. Marrochio, and R. C. Myers, *Holographic complexity in Vaidya spacetimes. Part II,* JHEP **06**, 114 (2018), arXiv:1805.07262 [hep-th]

[377] K. Goto, H. Marrochio, R. C. Myers, L. Queimada, and B. Yoshida, *Holographic Complexity Equals Which Action?* JHEP **02**, 160 (2019), arXiv:1901.00014 [hep-th]

[378] S. Mahapatra and P. Roy, *On the time dependence of holographic complexity in a dynamical Einstein-dilaton model,* JHEP **11**, 138 (2018), arXiv:1808.09917 [hep-th]

[379] B. Swingle and Y. Wang, *Holographic Complexity of Einstein-Maxwell-Dilaton Gravity,* JHEP **09**, 106 (2018), arXiv:1712.09826 [hep-th]

[380] Y.-S. An, R.-G. Cai, and Y. Peng, *Time Dependence of Holographic Complexity in Gauss-Bonnet Gravity,* Phys. Rev. D **98**, 106013 (2018), arXiv:1805.07775 [hep-th]

[381] J. Couch, W. Fischler, and P. H. Nguyen, *Noether charge, black hole volume, and complexity,* JHEP **03**, 119 (2017), arXiv:1610.02038 [hep-th]

[382] Z.-Y. Fan and M. Guo, *On the Noether charge and the gravity duals of quantum complexity,* JHEP **08**, 031 (2018), [Erratum: JHEP 09, 121 (2019)], arXiv:1805.03796 [hep-th]

[383] M. Alishahiha, *Holographic Complexity,* Phys. Rev. D **92**, 126009 (2015), arXiv:1509.06614 [hep-th]

[384] R. Abt, J. Erdmenger, M. Gerbershagen, C. M. Melby-Thompson, and C. Northe, *Holographic Subregion Complexity from Kinematic Space,* JHEP **01**, 012 (2019), arXiv:1805.10298 [hep-th]

[385] Z.-Y. Fan and M. Guo, *Holographic complexity under a global quantum quench,* Nucl. Phys. B **950**, 114818 (2020), arXiv:1811.01473 [hep-th]

[386] D. S. Ageev, I. Y. Aref'eva, A. A. Bagrov, and M. I. Katsnelson, *Holographic local quench and effective complexity,* JHEP **08**, 071 (2018), arXiv:1803.11162 [hep-th]

[387] Y. Ling, Y. Liu, and C.-Y. Zhang, *Holographic Subregion Complexity in Einstein-Born-Infeld theory,* Eur. Phys. J. C **79**, 194 (2019), arXiv:1808.10169 [hep-th]

[388] B. Chen, W.-M. Li, R.-Q. Yang, C.-Y. Zhang, and S.-J. Zhang, *Holographic subregion complexity under a thermal quench,* JHEP **07**, 034 (2018), arXiv:1803.06680 [hep-th]

[389] M. Ghodrati, *Complexity growth rate during phase transitions,* Phys. Rev. D **98**, 106011 (2018), arXiv:1808.08164 [hep-th]

[390] P. Roy and T. Sarkar, *Note on subregion holographic complexity,* Phys. Rev. D **96**, 026022 (2017), arXiv:1701.05489 [hep-th]

[391] S.-J. Zhang, *Complexity and phase transitions in a holographic QCD model,* Nucl. Phys. B **929**, 243 (2018), arXiv:1712.07583 [hep-th]

[392] S.-J. Zhang, *Subregion complexity and confinement–deconfinement transition in a holographic QCD model,* Nucl. Phys. B **938**, 154 (2019), arXiv:1808.08719 [hep-th]

[393] M. Lezgi and M. Ali-Akbari, *Note on holographic subregion complexity and QCD phase transition,* Phys. Rev. D **101**, 026022 (2020), arXiv:1908.01303 [hep-th]

[394] D. Momeni, S. A. Hosseini Mansoori, and R. Myrzakulov, *Holographic Complexity in Gauge/String Superconductors,* Phys. Lett. B **756**, 354 (2016), arXiv:1601.03011 [hep-th]

[395] M. Kord Zangeneh, Y. C. Ong, and B. Wang, *Entanglement Entropy and Complexity for One-Dimensional Holographic Superconductors,* Phys. Lett. B **771**, 235 (2017), arXiv:1704.00557 [hep-th]

[396] J. Erdmenger and M. Gerbershagen, *Entwinement as a possible alternative to complexity,* JHEP **03**, 082 (2020), arXiv:1910.05352 [hep-th]

[397] J. Eisert, *Entangling Power and Quantum Circuit Complexity,* Phys. Rev. Lett. **127**, 020501 (2021), arXiv:2104.03332 [quant-ph]

[398] L. V. Iliesiu, M. Mezei, and G. Sárosi, *The volume of the black hole interior at late times,* (2021), arXiv:2107.06286 [hep-th]

[399] M. A. Nielsen, *A geometric approach to quantum circuit lower bounds,* (2005), arXiv:quant-ph/0502070 [quant-ph]

[400] M. A. Nielsen, M. R. Dowling, M. Gu, and A. M. Doherty, *Quantum Computation as Geometry,* Science **311**, 1133 (2006), arXiv:quant-ph/0603161 [quant-ph]

[401] M. A. Nielsen and M. R. Dowling, *The geometry of quantum computation,* (2007), arXiv:quant-ph/0701004 [quant-ph]

[402] T. Takayanagi, *Holographic Spacetimes as Quantum Circuits of Path-Integrations,* JHEP **12**, 048 (2018), arXiv:1808.09072 [hep-th]

[403] M. Guo, J. Hernandez, R. C. Myers, and S.-M. Ruan, *Circuit Complexity for Coherent States,* JHEP **10**, 011 (2018), arXiv:1807.07677 [hep-th]

[404] R.-Q. Yang, C. Niu, C.-Y. Zhang, and K.-Y. Kim, *Comparison of holographic and field theoretic complexities for time dependent thermofield double states,* JHEP **02**, 082 (2018), arXiv:1710.00600 [hep-th]

[405] J. Jiang and X. Liu, *Circuit Complexity for Fermionic Thermofield Double states,* Phys. Rev. D **99**, 026011 (2019), arXiv:1812.00193 [hep-th]

[406] S. Chapman and H. Z. Chen, *Charged Complexity and the Thermofield Double State,* JHEP **02**, 187 (2021), arXiv:1910.07508 [hep-th]

[407] M. Doroudiani, A. Naseh, and R. Pirmoradian, *Complexity for Charged Thermofield Double States,* JHEP **01**, 120 (2020), arXiv:1910.08806 [hep-th]

[408] E. Caceres, S. Chapman, J. D. Couch, J. P. Hernandez, R. C. Myers, and S.-M. Ruan, *Complexity of Mixed States in QFT and Holography,* JHEP **03**, 012 (2020), arXiv:1909.10557 [hep-th]

[409] G. Di Giulio and E. Tonni, *Complexity of mixed Gaussian states from Fisher information geometry,* JHEP **12**, 101 (2020), arXiv:2006.00921 [hep-th]

[410] A. Bernamonti, F. Galli, J. Hernandez, R. C. Myers, S.-M. Ruan, and J. Simón, *First Law of Holographic Complexity,* Phys. Rev. Lett. **123**, 081601 (2019), arXiv:1903.04511 [hep-th]

[411] A. Bernamonti, F. Galli, J. Hernandez, R. C. Myers, S.-M. Ruan, and J. Simón, *Aspects of The First Law of Complexity,* (2020), 10.1088/1751-8121/ab8e66, arXiv:2002.05779 [hep-th]

[412] A. Bhattacharyya, P. Nandy, and A. Sinha, *Renormalized Circuit Complexity,* Phys. Rev. Lett. **124**, 101602 (2020), arXiv:1907.08223 [hep-th]

[413] R. Khan, C. Krishnan, and S. Sharma, *Circuit Complexity in Fermionic Field Theory,* Phys. Rev. D **98**, 126001 (2018), arXiv:1801.07620 [hep-th]

[414] L. Hackl and R. C. Myers, *Circuit complexity for free fermions,* JHEP **07**, 139 (2018), arXiv:1803.10638 [hep-th]

[415] A. Bhattacharyya, A. Shekar, and A. Sinha, *Circuit complexity in interacting QFTs and RG flows,* JHEP **10**, 140 (2018), arXiv:1808.03105 [hep-th]

[416] N. Chagnet, S. Chapman, J. de Boer, and C. Zukowski, *Complexity for Conformal Field Theories in General Dimensions,* (2021), arXiv:2103.06920 [hep-th]

[417] J.-L. Lehners and J. Quintin, *Quantum Circuit Complexity of Primordial Perturbations,* Phys. Rev. D **103**, 063527 (2021), arXiv:2012.04911 [hep-th]

[418] A. M. Polyakov, *Quantum Geometry of Bosonic Strings,* Phys. Lett. B **103**, 207 (1981)

[419] P. H. Ginsparg and G. W. Moore, *Lectures on 2-D gravity and 2-D string theory,* in *Theoretical Advanced Study Institute (TASI 92): From Black Holes and Strings to Particles* (1993) arXiv:hep-th/9304011

[420] J. Watrous, *The Theory of Quantum Information* (Cambridge University Press, Cambridge, 2018)

[421] C. V. Johnson, *D-branes*, Cambridge Monographs on Mathematical Physics (Cambridge University Press, 2005)

[422] M. Miyaji, T. Numasawa, N. Shiba, T. Takayanagi, and K. Watanabe, *Distance between Quantum States and Gauge-Gravity Duality,* Phys. Rev. Lett. **115**, 261602 (2015), arXiv:1507.07555 [hep-th]

[423] A. Belin, A. Lewkowycz, and G. Sarosi, *The boundary dual of the bulk symplectic form,* Phys. Lett. **B789**, 71 (2019), arXiv:1806.10144 [hep-th]

[424] A. Belin, A. Lewkowycz, and G. Sarosi, *Complexity and the bulk volume, a new York time story,* JHEP **03**, 044 (2019), arXiv:1811.03097 [hep-th]

[425] G. Jafari, A. Naseh, and H. Zolfi, *Path Integral Optimization for $T\bar{T}$ Deformation,* Phys. Rev. D **101**, 026007 (2020), arXiv:1909.02357 [hep-th]

[426] M. Ghodrati, *Complexity and emergence of warped AdS_3 space-time from chiral Liouville action,* JHEP **02**, 052 (2020), arXiv:1911.03819 [hep-th]

[427] P. Caputa and I. MacCormack, *Geometry and Complexity of Path Integrals in Inhomogeneous CFTs,* JHEP **01**, 027 (2021), arXiv:2004.04698 [hep-th]

[428] J. Boruch, P. Caputa, and T. Takayanagi, *Path-Integral Optimization from Hartle-Hawking Wave Function,* Phys. Rev. D **103**, 046017 (2021), arXiv:2011.08188 [hep-th]

[429] J. Boruch, P. Caputa, D. Ge, and T. Takayanagi, *Holographic path-integral optimization,* JHEP **07**, 016 (2021), arXiv:2104.00010 [hep-th]

[430] J. M. Magan, *Black holes, complexity and quantum chaos,* JHEP **09**, 043 (2018), arXiv:1805.05839 [hep-th]

[431] P. Caputa and J. M. Magan, *Quantum Computation as Gravity,* Phys. Rev. Lett. **122**, 231302 (2019), arXiv:1807.04422 [hep-th]

[432] M. Flory and M. P. Heller, *Geometry of Complexity in Conformal Field Theory,* Phys. Rev. Res. **2**, 043438 (2020), arXiv:2005.02415 [hep-th]

[433] M. Flory and M. P. Heller, *Conformal field theory complexity from Euler-Arnold equations,* JHEP **12**, 091 (2020), arXiv:2007.11555 [hep-th]

[434] A. R. Chandra, J. de Boer, M. Flory, M. P. Heller, S. Hörtner, and A. Rolph, *Spacetime as a quantum circuit,* JHEP **21**, 207 (2021), arXiv:2101.01185 [hep-th]

[435] M. F. Wondrak, M. Kaminski, and M. Bleicher, *Shear transport far from equilibrium via holography,* Phys. Lett. B **811**, 135973 (2020), arXiv:2002.11730 [hep-ph]

Acknowledgements

First and foremost I offer my sincerest gratitude to my supervisor, Michal P. Heller, who has supported me throughout my thesis with his patience and knowledge. The opportunity to work in the "Gravity, Quantum Fields & Information" (GQFI) group at the Max Planck Institute for Gravitational Physics broadened my horizon to work on fascinating topics at the intersection of several physics areas. I am also grateful for the possibility to have attended stimulating schools, workshops and conferences which gave me the possibility to get inspirations and make valuable contacts. Furthermore, I would like to thank Jens Eisert as my university supervisor for valuable insights into the topic of TNs and the possibility to make contact with his research environment. I thank all my (other) collaborators for their discussions, work and insights which helped us to advance the different projects. My gratitude goes to: Viktor Svensson, Hugo Camargo, Ro Jefferson, Sukhi Singh, Mari Carmen Bañuls, Karl Jansen, Philipp Hauke, Sayantan Choudhury. I also thank the remaining and former QGFI members, who made the time at the institute a joyful experience: Diptarka Das, Ignacio Reyes, Eivind Jørstad, Leo Shaposhnik.